

UCSF

UC San Francisco Electronic Theses and Dissertations

Title

Spatial organization of immune receptors regulate immune cell activation: Insights from reconstituted T cell receptor and Fcγ-receptor systems

Permalink

<https://escholarship.org/uc/item/8vx9x4r3>

Author

Kern, Nadja

Publication Date

2021

Peer reviewed|Thesis/dissertation

Spatial organization of immune receptors regulate immune cell activation:
Insights from reconstituted T cell receptor and Fcγ-receptor systems

by
Nadja Kern

DISSERTATION

Submitted in partial satisfaction of the requirements for degree of
DOCTOR OF PHILOSOPHY

in

Biophysics

in the

GRADUATE DIVISION

of the

UNIVERSITY OF CALIFORNIA, SAN FRANCISCO

Approved:

DocuSigned by:

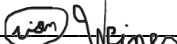


Ronald Vale

DCB8EA4803FF4AA...

Chair

DocuSigned by:



Orion Weiner

DocuSigned by:



Natalia Jura

E438674A382B42F...

Committee Members

Copyright 2021

By

Nadja Kern

DEDICATION

To my family, who incited my passion for science and supported me with all their love.

ACKNOWLEDGEMENTS

I am incredibly grateful for all of the support and mentorship I have received during the last 5 and a half years and have many people to thank for making this work possible and my graduate time so enjoyable.

First, I would like to thank my mentor Ron Vale for all of his guidance throughout my PhD, for allowing me the freedom to work on the questions that I was most passionate about, and especially for creating the wonderful environment that the Vale lab is and has been. It has been a joy both scientifically and personally to have been a part of the Vale lab community. As absolutely everyone in the lab has been truly helpful throughout my PhD, I would like to thank all of the Vale lab members together for making the lab an incredible fun, positive, and inspiring place to work every single day. I have learned from each and every one of you, and can't imagine a better group of people to be surrounded by. I would not be the scientist, the science communicator, or person I am today without the help I received from every Vale lab member, past and present. In particular, I would like to thank Kate Carbone for being my first role model in the lab and for showing me how great the Vale lab and the field of immunology is. Additionally, thank you to the previously called "signaling group" and now "C3" group for their constant advice, motivation, support, and ideas scientifically and otherwise.

A special thank you to Meghan Morrissey, who kindly took the role of my post-doc mentor while she was in the lab and has continued to provide me with invaluable mentorship as she has transitioned to running her own lab at UCSB. Thank you, Meghan, for your unwavering support scientifically, personally, and professionally, and for all of your advice, guidance, and inspiration. Thank you for teaching me essentially everything I know about macrophages, for making my first

paper writing process really fun, and for instilling in me the confidence to finally call myself an immunologist! Your passion for science, outlook on life, and generosity will always inspire me, and I am so thankful I have had the opportunity to learn from you.

Thank you to my thesis committee members, Orion Weiner and Natalia Jura, for all of your advice, fun scientific discussions, creative ideas, and support regarding both my project and professional development. Thank you also to my classmates and the amazing UCSF research community for all of the support, inspiration, and fun scientific discussions.

Thank you to all my incredible friends for all of your support and for the endless laughter and great memories during my graduate time. Thank you all for celebrating the wins with me and for being there for me in whichever way I needed during the lows; whether it was through a phone call, an early morning volleyball session, a climb up some mountain, or a science and life talk over lunch, you were there with what I needed most.

Thank you to my entire amazing family. Thank you for your constant love, motivation, and support through this PhD journey, and for inciting my love for science and research in the first place. To my parents, Mama (Doro) and Papa (Gunther), thank you for the endless scientific discussions, celebrating with me when I had good results, and providing motivation, ideas, and a kick in the butt if needed when experiments failed. I would not be the scientist or person I am now without all of your input, advice, and guidance. Your passion for science and life will always inspire me. To my sister and best friend, Juju (Julia), thank you for always supporting me, for learning to love the cells that go “nom nom nom” because I now love them, and for all of the laughs, love, and adventures.

Thank you to my incredible fiancé Braxton, for his endless love and encouragement. Thank you for understanding that when I say I need 15 minutes in lab it may mean 4 hours. Thank you for pushing me to be the best person and scientist I can be, for supporting me in any way I needed, and for filling each day with joy and laughter. Lastly, thank you to Braxton's side of the family, the Irbys, the Dunstones, and the Angels, for welcoming me into the family with open arms and for their incredible love and support.

STATEMENT REGARDING AUTHOR CONTRIBUTIONS

Statement from Ron Vale:

Chapter 2 of this dissertation includes reprints of material published with co-authors other than Nadja Kern. Nadja contributed through the conceptualization, design, performance, and analysis of experiments shown in Figures 2, 4 and 5, and helped in the writing of the manuscript.

Chapter 2 of this dissertation contains reprints of previously published material as it appears in:

Carbone, C. B., **Kern, N.**, Fernandes, R. A., Hui, E., Su, X., Garcia, K. C., & Vale, R. D. (2017). In vitro reconstitution of T cell receptor-mediated segregation of the CD45 phosphatase. *Proceedings of the National Academy of Sciences*, 114(44), E9338–E9345.

Chapter 3 of this dissertation contains reprints of previously published material as it appears in:

Kern, N., Dong, R., Douglas, S. M., Vale, R. D. & Morrissey, M. A. Tight nanoscale clustering of Fcγ-receptors using DNA origami promotes phagocytosis. *bioRxiv* 2021.03.18.436011 (2021).

ABSTRACT

Spatial organization of immune receptors regulate immune cell activation: Insights from reconstituted T cell receptor and Fc γ -receptor systems

Nadja Kern

As immune cells patrol our body, contacting and surveying the cells around them, they must constantly make the decision of whether or not to activate and surmount an immune response. Importantly, these choices must be made with high fidelity, as the immune cells must quickly eliminate pathogens and diseased cells while limiting damage to healthy cells. This activation decision is regulated by receptors on the immune cells that recognize distinct ligands on the surface of the cells they encounter. A hallmark of successful receptor-ligand interaction is the reorganization of these immune receptors into sub-micron and micron scale clusters, at which activation signals initiate within the immune cell. Although the importance of this receptor reorganization has been long appreciated, the mechanism by which the reorganization is achieved, how receptor reorganization promotes signal activation, and how the spatial organization of receptors regulates or modulates these binary cellular activation decisions has not been well understood. In this dissertation, I used reconstituted signaling systems to understand how the nanoscale spatial organization of the Fc γ receptor (Fc γ R) controls engulfment signaling in macrophages, and how the organization of the T cell receptor (TCR), inhibitory co-receptor, PD-1, and the transmembrane phosphatase, CD45, control signaling in T cells.

TABLE OF CONTENTS

CHAPTER 1

Introduction to TCR and Fc γ R Signaling

1.1 Introduction	1
1.2 References	6

CHAPTER 2

9

In vitro reconstitution of T cell receptor-mediated segregation of the CD45 phosphatase

2.1 Significance	10
2.2 Abstract	10
2.3 Introduction	11
2.4 Results	12
2.5 Discussion	
2.6 Materials and Methods	25
2.7 Supporting Information	30
2.8 Author Contributions	36
2.9 Acknowledgements	36
2.10 References	37

CHAPTER 3

41

Tight nanoscale clustering of Fc γ -receptors using DNA origami promotes phagocytosis

3.1 Abstract	42
3.2 Introduction	43
3.3 Results	44
3.4 Discussion	62
3.5 Materials and Methods	66

3.6 Supporting Information	75
3.7 Acknowledgements	112
3.8 Author Contributions	112
3.9 References	113
CHAPTER 4	120
Concluding Thoughts	
4.1 Looking forward	120
4.2 References	123

LIST OF FIGURES

CHAPTER 2

Figure 2.1	14
Figure 2.2	16
Figure 2.3	17
Figure 2.4	19
Figure 2.5	21
Figure S2.1	32
Figure S2.2	33
Figure S2.3	34
Figure S2.4	35

CHAPTER 3

Figure 3.1	46
Figure 3.2	49
Figure 3.3	52
Figure 3.4	55
Figure 3.5	57
Figure 3.6	60
Figure S3.1	75
Figure S3.2	76
Figure S3.3	78
Figure S3.4	79
Figure S3.5	80
Figure S3.6	82

LIST OF TABLES

CHAPTER 2

Table S2.1	30
------------	----

CHAPTER 3

Table S3.1	85
------------	----

Table S3.2	94
------------	----

Table S3.3	99
------------	----

Table S3.4	103
------------	-----

Table S3.5	107
------------	-----

CHAPTER 1

Introduction to TCR and Fc γ R Signaling

1.1 Introduction

Our immune system plays the vital role of defending our bodies from harmful pathogens and diseased cells. The controlled activation of immune cells is essential for achieving this function, as inactivation may lead to infection or disease, while overactivation could result in the destruction of healthy cells, leading to autoimmune disorder. To this end, immune cells use a myriad of cell surface receptors to survey their surrounding cells and environment. When these receptors bind their cognate ligands, they transduce extracellular signals into intracellular signals. To set robust activation thresholds that effectively differentiate from background signals, immune cells integrate measurements in the identity, number, affinity, and spatial organization of receptor-ligand interactions to determine whether or not the cell activates to surmount an immune response. Despite a wealth of information currently available about the individual molecular components involved in these activation decisions, how the spatial organization of immune receptors and their surrounding signaling proteins affect and regulate activation thresholds remains an open area of investigation.

T Cell Receptor signaling

T cells play a central role in the mammalian adaptive immune response. Consequently, the activation of T cells via the T cell receptor (TCR) is a well-studied example of a signaling system in which the spatial rearrangements of the receptor and surrounding signaling proteins play a significant role in regulating the activation threshold of the T cell. The TCR is a multi-protein complex which is activated through the phosphorylation of its cytosolic immunoreceptor tyrosine-based activation motifs (ITAMs) after binding to peptide major histocompatibility complex (pMHC)

presented by an antigen presenting cell (APC). Upon binding to a pMHC of sufficient strength, the receptors coalesce into microclusters, are phosphorylated by the Src-family kinase Lck, and are able to recruit downstream signaling proteins.¹⁻³ When unbound, the TCR is held in a dephosphorylated state by the transmembrane phosphatase CD45.⁴

As the TCR forms these canonical microclusters at the synapse between the T cell and the APC (immunological synapse), it partitions away from CD45.⁵ Accumulating evidence has supported the kinetic segregation model for TCR activation, which proposes that this partitioning creates a biochemically distinct region around the receptors that shifts the kinase-phosphatase balance to favor phosphorylation of the TCR ITAM domains.^{3,6-8} This is in contrast to a model in which the TCR undergoes a conformational change that enables its phosphorylation.

This spatial partitioning has been proposed to be driven via multiple mechanisms. Elegant experiments in cells and computational studies have demonstrated that the relative sizes of the extracellular domains of the TCR-pMHC complex (~13 nm) and CD45 (25-40 nm) are a critical parameter for this spatial segregation.^{5,9,10} This steric exclusion mechanism proposes that in order to minimize the bending energy of the cell membrane, the proteins will self-partition based on their extracellular size.¹¹⁻¹³ Importantly, this mechanism is proposed to play a role in the activation of not only the TCR, but many different ITAM and immunoreceptor tyrosine-based inhibitory motif (ITIM) containing receptors, including the inhibitory T cell receptor, Programmed Cell Death Protein 1 (PD-1).⁸ However, it has been disputed that distinct lipid domains within the cell membrane that partition Src-family kinases away from CD45, and downstream actin rearrangements in the cell that may actively reorganize transmembrane proteins, also contribute to the partitioning of CD45 from pMHC-bound TCR.¹⁴⁻¹⁶ Therefore, groups have turned to synthetic reconstituted systems in which varying sizes of dimerizing GFP proteins or complementary DNA strands were used to replace TCR-pMHC interactions.^{17,18} These studies

found that protein size alone, absent of additional feedback mechanisms that may be present within the cell, could drive the segregation of proteins in a model membrane. However, these experiments were all performed with artificial proteins which have non-physiological receptor-ligand affinities, leaving the mechanism of segregation between TCR-pMHC and CD45 at the immunological synapse unknown.

In the first part of this dissertation, I worked closely with Kate Carbone to recapitulate TCR-pMHC and PD1-PDL1 binding on model membranes outside of cells to better understand the mechanisms driving the reorganization of these proteins, their segregation from CD45, and the physical parameters that regulate these spatial organizations at the immunological synapse.

Fc γ Receptor signaling in macrophages

Macrophages are an essential part of our innate immune system as they are responsible for patrolling our bodies and clearing any pathogens, harmful, infected, or dead cells. They accomplish this through a process called phagocytosis, in which they engulf and digest their target cells, as well as through the subsequent recruitment and activation of adaptive immune cells. Macrophages recognize harmful targets through specialized receptors which bind to ligands on target surfaces that induce engulfment (“eat me” signals).¹⁹ One of the most common “eat me” signals is the Immunoglobulin G (IgG) antibody, which binds to targets displaying its cognate antigen. Recognition of IgG by the Fc γ receptor family (Fc γ R) of proteins on the macrophage surface drives antibody-dependent cellular phagocytosis (ADCP) of these targets.²⁰

Similar to the TCR in T cells, Fc γ R-driven phagocytosis must be performed efficiently and in a manner that robustly ignores any sub-threshold antibody stimuli that may be bound transiently or nonspecifically to healthy cells. This is an especially hard feat for macrophages, as antibodies are

often found at very high concentrations in the blood (up to mg/mL).²¹ Therefore, the all-or-none decision of engulfment requires the combined activity of signals from multiple Fc γ R-IgG interactions.²² Although it is well established that activation of a single Fc γ R is not sufficient to drive phagocytosis, the mechanisms that underlie this requirement and enable the integration of many signals to dictate the binary cellular decision are unresolved.

Analogous to the TCR, IgG bound Fc γ Rs reorganize into nanoscale clusters upon IgG binding, and this clustering is thought to play an important role in engulfment signaling.²³ This likeness with the TCR is no coincidence, as the Fc γ R is also activated via phosphorylation of its ITAM domains by Src-family kinases upon IgG binding. Once phosphorylated, these receptor clusters recruit the downstream signaling molecules essential for phagocytosis, thus acting as sites of signal initiation in the macrophage.^{24–26} While mounting evidence suggests this clustering to be important for Fc γ R engulfment signaling, little is known about the nanoscale structures of these Fc γ R clusters or how changes in the makeup of these clusters may regulate engulfment thresholds. A better understanding of how these nanoscale antibody patterns effect engulfment decisions would not only provide insight into the molecular mechanisms that govern Fc γ R-mediated macrophage activation but also have important implications for the design of novel and more efficacious immunotherapies targeting the activation of Fc γ Rs.²⁷

Although current experimental methods like nanolithography arrays have provided important insights on how the nanoscale spacing of other immune receptors effects signaling in T cells²⁸, B cells²⁹, mast cells³⁰, and NK cells³¹, these methods lack the ability to pattern ligands on 3 dimensional surfaces and the precision to consistently pattern molecules on the single molecule level. Thus, during my thesis work, I set out to build a synthetic engulfment system which could pattern ligands of engulfment receptors on 3 dimensional targets and be used to investigate the

effects nanoscale spacing has on engulfment in macrophages. To this end, I built a chimeric antigen receptor (CAR) version of the Fc γ R in which the endogenous extracellular domain was replaced with a SNAP tag to which a single stranded DNA (ssDNA) could be covalently attached. This receptor, which we named the DNA CAR γ receptor, can be activated via a complementary base paired ssDNA ligand. Importantly, the rapidly evolving technology of DNA origami enabled me to use this DNA-based engulfment system to directly pattern the DNA ligands with nanometer level precision.

In the second part of this dissertation, I used this synthetic engulfment system to determine the number of ligands and inter-ligand spacing necessary within Fc γ R nanoclusters to activate downstream signaling and engulfment in macrophages. Furthermore, I used this system to gain a mechanistic understanding of the requirement for receptor-ligand clustering in macrophage signaling and phagocytosis.

1.2 References

1. Sherman, E. *et al.* Functional nanoscale organization of signaling molecules downstream of the T cell antigen receptor. *Immunity* **35**, 705–720 (2011).
2. Lillemeier, B. F. *et al.* TCR and Lat are expressed on separate protein islands on T cell membranes and concatenate during activation. *Nat. Immunol.* **11**, 90–96 (2010).
3. Taylor, M. J., Husain, K., Gartner, Z. J., Mayor, S. & Vale, R. D. A DNA-Based T Cell Receptor Reveals a Role for Receptor Clustering in Ligand Discrimination. *Cell* **169**, 108–119.e20 (2017).
4. Hermiston, M. L., Xu, Z. & Weiss, A. CD45: a critical regulator of signaling thresholds in immune cells. *Annu. Rev. Immunol.* **21**, 107–137 (2003).
5. Cordoba, S. P. *et al.* The large ectodomains of CD45 and CD148 regulate their segregation from and inhibition of ligated T-cell receptor. *Blood* **121**, 4295–4302 (2013).
6. Monks, C. R. F., Freiberg, B. A., Kupfer, H., Sciaky, N. & Kupfer, A. Three-dimensional segregation of supramolecular activation clusters in T cells. *Nature* **395**, 82–86 (1998).
7. Grakoui, A. *et al.* The immunological synapse: A molecular machine controlling T cell activation. *Science (80-.)*. **285**, 221–227 (1999).
8. Davis, S. J. & van der Merwe, P. A. The kinetic-segregation model: TCR triggering and beyond. *Nat. Immunol.* **7**, 803–809 (2006).
9. Choudhuri, K., Wiseman, D., Brown, M. H., Gould, K. & van der Merwe, P. A. T-cell receptor triggering is critically dependent on the dimensions of its peptide-MHC ligand. *Nature* **436**, 578–582 (2005).
10. James, J. R. & Vale, R. D. Biophysical mechanism of T-cell receptor triggering in a reconstituted system. *Nature* **487**, 64–9 (2012).
11. Qi, S. Y., Groves, J. T. & Chakraborty, A. K. Synaptic pattern formation during cellular recognition. *Proc. Natl. Acad. Sci. U. S. A.* **98**, 6548–6553 (2001).

12. Burroughs, N. J. & Wülfing, C. Differential segregation in a cell-cell contact interface: The dynamics of the immunological synapse. *Biophys. J.* **83**, 1784–1796 (2002).
13. Weikl, T. R. & Lipowsky, R. Pattern formation during T-cell adhesion. *Biophys. J.* **87**, 3665–3678 (2004).
14. Fernandes, R. A. *et al.* What Controls T Cell Receptor Phosphorylation? *Cell* **142**, 668–669 (2010).
15. Rozdzial, M. M., Malissen, B. & Finkel, T. H. Tyrosine-phosphorylated T cell receptor ζ chain associates with the actin cytoskeleton upon Activation of mature T lymphocytes. *Immunity* **3**, 623–633 (1995).
16. Dinic, J., Riehl, A., Adler, J. & Parmryd, I. The T cell receptor resides in ordered plasma membrane nanodomains that aggregate upon patching of the receptor. *Sci. Rep.* **5**, 1–9 (2015).
17. Schmid, E. M. *et al.* Size-dependent protein segregation at membrane interfaces. *Nat. Phys.* **12**, 704–711 (2016).
18. Chung, M., Koo, B. J. & Boxer, S. G. Formation and analysis of topographical domains between lipid membranes tethered by DNA hybrids of different lengths. *Faraday Discuss.* **161**, 333–45; discussion 419–59 (2013).
19. Freeman, S. A. & Grinstein, S. Phagocytosis: receptors, signal integration, and the cytoskeleton. *Immunol. Rev.* **262**, 193–215 (2014).
20. Nimmerjahn, F. & Ravetch, J. V. Fc γ receptors as regulators of immune responses. *Nat. Rev. Immunol.* (2008). doi:10.1038/nri2206
21. Gonzalez-Quintela, A. *et al.* Serum levels of immunoglobulins (IgG, IgA, IgM) in a general adult population and their relationship with alcohol consumption, smoking and common metabolic abnormalities. *Clin. Exp. Immunol.* **151**, 42–50 (2008).
22. Griffin, F. M., Griffin, J. A., Leider, J. E. & Silverstein, S. C. Studies on the mechanism of phagocytosis. I. Requirements for circumferential attachment of particle-bound ligands to

- specific receptors on the macrophage plasma membrane. *J. Exp. Med.* **142**, 1263–1282 (1975).
23. Goodridge, H. S., Underhill, D. M. & Touret, N. Mechanisms of Fc Receptor and Dectin-1 Activation for Phagocytosis. *Traffic* **13**, 1062–1071 (2012).
 24. Sobota, A. *et al.* Binding of IgG-Opsonized Particles to FcγR Is an Active Stage of Phagocytosis That Involves Receptor Clustering and Phosphorylation. *J. Immunol.* **175**, 4450–4457 (2005).
 25. Lin, J. *et al.* TIRF imaging of Fc gamma receptor microclusters dynamics and signaling on macrophages during frustrated phagocytosis. *BMC Immunol.* **17**, 5 (2016).
 26. Lopes, F. B. *et al.* Membrane nanoclusters of FcγRI segregate from inhibitory SIRPα upon activation of human macrophages. *J. Cell Biol.* jcb.201608094 (2017).
doi:10.1083/jcb.201608094
 27. Nimmerjahn, F. & Ravetch, J. V. Translating basic mechanisms of IgG effector activity into next generation cancer therapies. *IECON Proc. (Industrial Electron. Conf.* **2005**, 1104–1109 (2005).
 28. Cai, H. *et al.* Full control of ligand positioning reveals spatial thresholds for T cell receptor triggering. *Nat. Nanotechnol.* **13**, 610–617 (2018).
 29. Veneziano, R. *et al.* Role of nanoscale antigen organization on B-cell activation probed using DNA origami. *bioRxiv* 2020.02.16.951475 (2020). doi:10.1101/2020.02.16.951475
 30. Sil, D., Lee, J. B., Luo, D., Holowka, D. & Baird, B. Trivalent Ligands with Rigid DNA Spacers Reveal Structural Requirements For IgE Receptor Signaling in RBL Mast Cells. *ACS Chem. Biol.* **2**, 674–684 (2007).
 31. Delcassian, D. *et al.* Nanoscale ligand spacing influences receptor triggering in T cells and NK cells. *Nano Lett.* **13**, 5608–5614 (2013).

CHAPTER 2

***In vitro* reconstitution of T cell receptor-mediated segregation of the CD45 phosphatase**

Catherine B. Carbone¹, Nadja Kern¹, Ricardo A. Fernandes², Enfu Hui¹, Xiaolei Su¹, K. Christopher Garcia², and Ronald D. Vale¹

¹Dept. of Cellular and Molecular Pharmacology and the Howard Hughes Medical Institute, University of California, San Francisco, CA 94158; ²Dept. of Molecular and Cellular Physiology and Structural Biology and the Howard Hughes Medical Institute, Stanford University Medical School, CA 94305

2.1 Significance

The T cell receptor (TCR) and PD-1 signaling cascades have been hypothesized to be triggered by the exclusion of the transmembrane phosphatase CD45 from sites of receptor–ligand engagement at the T cell–antigen-presenting cell interface. We reconstituted TCR–pMHC– and PD1–PD-L1–mediated segregation of CD45 with purified proteins and model membranes, demonstrating that this phenomenon can occur in the absence of any active cellular organization. In this minimal system, two developmentally regulated and different size isoforms of CD45 are differently segregated by TCR–pMHC binding, suggesting a possible mechanism for the fine-tuning of signaling. Collectively, our data show that the binding energy of physiological receptor–ligand pairs is sufficient to create spatial organization in membranes.

2.2 Abstract

T cell signaling initiates upon the binding of peptide-loaded MHC (pMHC) on an antigen-presenting cell to the T cell receptor (TCR) on a T cell. TCR phosphorylation in response to pMHC binding is accompanied by segregation of the transmembrane phosphatase CD45 away from TCR–pMHC complexes. The kinetic segregation hypothesis proposes that CD45 exclusion shifts the local kinase–phosphatase balance to favor TCR phosphorylation. Spatial partitioning may arise from the size difference between the large CD45 extracellular domain and the smaller TCR–pMHC complex, although parsing potential contributions of extracellular protein size, actin activity, and lipid domains is difficult in living cells. Here, we reconstitute segregation of CD45 from bound receptor–ligand pairs using purified proteins on model membranes. Using a model receptor–ligand pair (FRB–FKBP), we first test physical and computational predictions for protein organization at membrane interfaces. We then show that the TCR–pMHC interaction causes partial exclusion of CD45. Comparing two developmentally regulated isoforms of CD45, the larger RABC variant is excluded more rapidly and efficiently (~50%) than the smaller R0 isoform

(~20%), suggesting that CD45 isotypes could regulate signaling thresholds in different T cell subtypes. Similar to the sensitivity of T cell signaling, TCR–pMHC interactions with K_{ds} of ≤ 15 μM were needed to exclude CD45. We further show that the coreceptor PD-1 with its ligand PD-L1, immunotherapy targets that inhibit T cell signaling, also exclude CD45. These results demonstrate that the binding energies of physiological receptor–ligand pairs on the T cell are sufficient to create spatial organization at membrane–membrane interfaces.

2.3 Introduction

Binding of the T cell receptor (TCR) to agonist peptide-MHC (pMHC) triggers a signaling cascade within a T cell leading to reorganization of the cytoskeleton and organelles, transcriptional changes, and cell proliferation. The first step in the cascade is TCR phosphorylation by the Src family tyrosine kinase Lck (2). One model, called “kinetic segregation” (3) for how this initiating phosphorylation is triggered, proposes that the close membrane contact created by TCR–pMHC binding results in exclusion of the transmembrane phosphatase CD45, and the shift of the kinase–phosphatase balance favors net phosphorylation of the TCR by Lck. The basis of this exclusion is thought to be steric, since the large CD45 extracellular domain (CD45 R0 isoform, 25 nm; CD45 RABC isoform, 40 nm) (Table S1) (4–6) may not be able to penetrate the narrow intermembrane spacing generated by the TCR–pMHC complex (13 nm) (Table S1) (7, 8).

Imaging T cells activated *ex vivo* either by B cells (9) or by antigen presented on supported lipid bilayers (SLBs) (10, 11) has revealed that CD45 is indeed partitioned away from the TCR upon pMHC binding. Cellular reconstitutions have demonstrated that the large extracellular domain of CD45 is required for this segregation (12, 13). Additionally, size-dependent segregation of CD45 by orthogonal receptor–ligand pairs that create a similar narrow intermembrane cleft is sufficient for T cell triggering in the absence of TCR–pMHC binding (6, 12).

Despite this strong cellular evidence for size-based partitioning, it has been debated whether the physical properties of CD45 and TCR–pMHC at the membrane–membrane interface alone are sufficient to explain the observed segregation behavior or whether other cellular factors (e.g., actin cytoskeletal or lipid ordering) are also required. Several groups have computationally modeled aspects of size-based organization at membrane interfaces, and two independent mathematical approaches have concluded that spontaneous pattern formation can occur in physiological parameter ranges (14, 15). These models predict the contributions of protein (size, concentration, elasticity, affinity, and kinetics), membrane (stiffness, tension, repulsion), and environmental (thermal fluctuations, cytoskeleton, time) factors in regulating partitioning. Although these models focus primarily on a system with two binding pairs (TCR–pMHC and ICAM-1–LFA-1), some of the predictions can be extrapolated to a system with both ligand-bound and unbound species.

Successful efforts to reconstitute molecular segregation at membrane–membrane interfaces have been made with dimerizing GFP molecules (16) and hybridizing strands of DNA (17). These studies show that laterally mobile molecules at membrane–membrane interfaces organize by height and locally deform the membrane to accommodate different molecular sizes. However, results from high-affinity, artificial receptor–ligand pairs cannot be simply extrapolated to predict results for physiologically relevant molecules at the T cell–APC interface. Here, we have recapitulated TCR–pMHC–mediated partitioning of CD45 on model membranes.

2.4 Results

A chemically-inducible receptor-ligand system for producing CD45 exclusion at a membrane-membrane interface

To mimic a T cell, we used a giant unilamellar vesicle (GUV) containing a nickel-chelating lipid to

which a purified His-tagged, fluorescently-labeled receptor and CD45 could be added (**Fig. 1A**). To mimic the APC, we used a supported lipid bilayer (SLB) containing nickel-chelating lipids to which a His-tagged protein ligand also could be bound. All proteins were linked to their target membrane via either His₁₀ or His₁₂, as detailed in the methods section. As an initial test of this system, we used an artificial receptor (FKBP) and ligand (FRB) that could be induced to form a tight binding interaction (100 fM) upon addition of rapamycin¹. In order to maintain the GUV and SLB in proximity prior to rapamycin addition, the two membranes were passively tethered to one another using two 100-mer single-stranded DNA molecules with a 20 bp region of complementarity^{2,3} (**Table S1**). The elongated extracellular domain of the CD45 R₀ isoform (25 nm)⁴⁻⁶ or the smaller SNAP protein (5 nm, **Table S1**)⁷ were used as test proteins for partitioning.

Upon rapamycin addition, FKBP and FRB concentrated first in small micron-scale clusters at the GUV-SLB interface, which then grew in size over the interface; simultaneously, fluorescently-labeled CD45 R₀ partitioned away from regions of the GUV that became enriched in receptor-ligand (**Fig. 1B and Movie S1**). In contrast to CD45, which was strongly depleted by FRB-FKBP, the SNAP protein (5 nm)⁸ or a lipid dye (Atto390-DOPE) remained evenly distributed throughout the interface after rapamycin addition (**Fig. 1C-D**). We also tested PD-L1 (8 nm, **Table S1**), which also remained evenly distributed throughout the interface after rapamycin addition (**Fig. S1**). The size of FKBP-FRB clusters could be varied by changing the receptor concentration on the GUV membrane; however, the degree of CD45 R₀ exclusion from clusters was similar over the range tested (**Fig. 2A-C**). Across all concentrations of FKBP, at receptor-ligand enriched zones, CD45 R₀ was depleted by $72 \pm 7\%$ (n=22 GUVs pooled from two experiments). Once formed, the receptor -enriched and -depleted zones stably retained their shapes for tens of minutes and receptor-ligand pairs in the enriched zones were largely immobile, as evidenced by

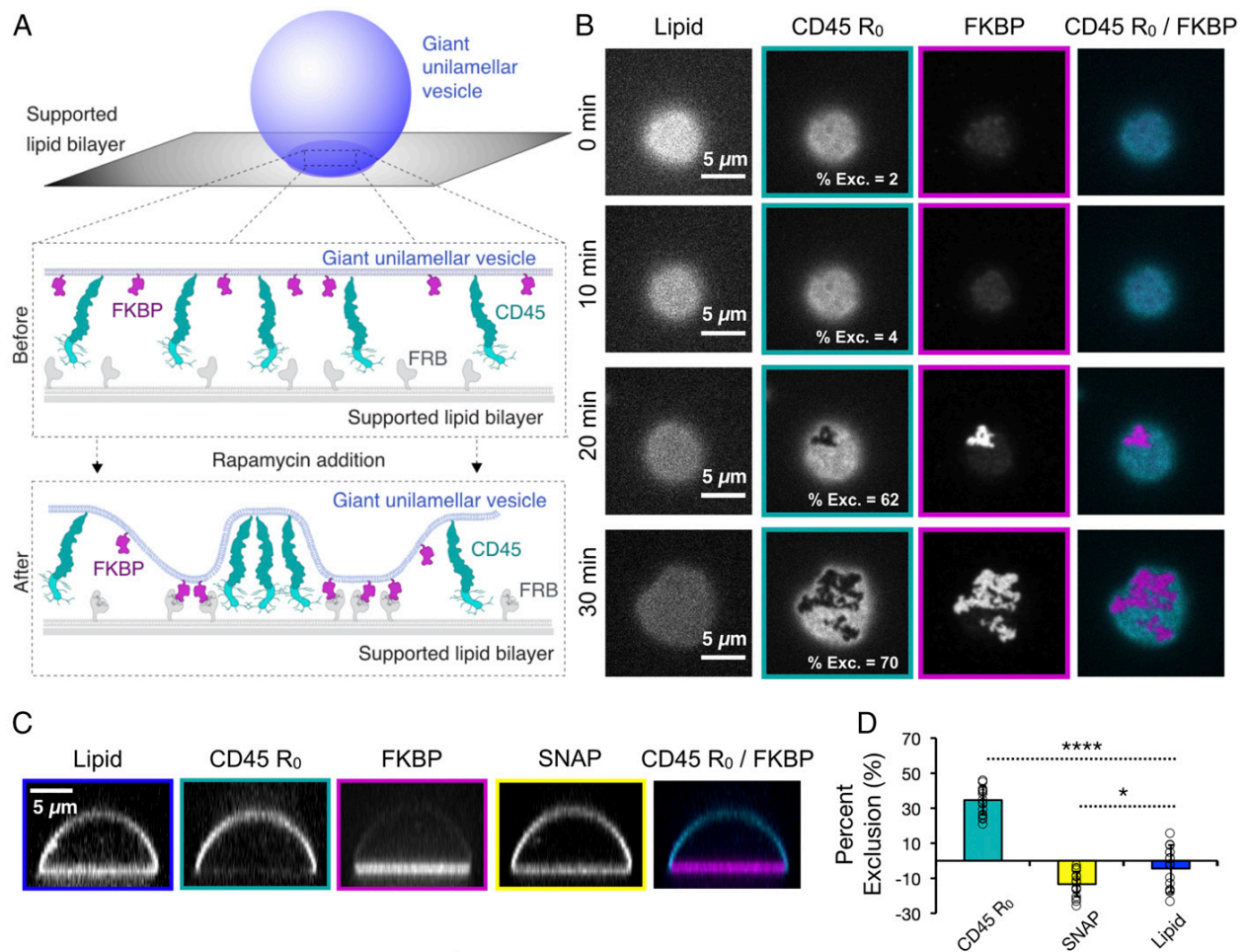


Fig. 2.1. Receptor-ligand binding induces CD45 segregation at membrane interfaces. **(A)** Schematic of rapamycin-induced receptor (FKBP)-ligand (FRB) binding and CD45 R₀ segregation between a giant unilamellar vesicle (GUV) and a supported lipid bilayer (SLB) **(B)** Total internal reflection fluorescence (TIRF) microscopy of a GUV-SLB interface at indicated times after rapamycin addition, showing concentration of FKBP into microdomains that exclude CD45 R₀. Percent exclusion of CD45 R₀ is indicated for each image shown. **(C)** Spinning disk z-sections of GUVs after membrane-apsed interfaces have reached equilibrium, showing localization of FKBP to the membrane interface, localization of CD45 R₀ away from the interface, and uniform distribution of SNAP. **(D)** Quantification of experiment shown in **C**; mean \pm standard deviation ($n=17$ GUVs pooled from two experiments).

fluorescence recovery after photobleaching (FRAP; **Fig. S2**). However, using single molecule TIRF imaging, we observed that single molecules of CD45 R₀ can diffuse across FKBP-FRB -enriched and -depleted zones (**Fig. 2D-E, Movie S2**). This result reveals that individual molecules can exchange across these micron-scale boundaries. In addition to testing the CD45 R₀ isoform for segregation, we also compared the extracellular domain of the CD45 R_{ABC} isoform, which is preferentially expressed early in T cell development⁹, and is about 15 nm larger in size than the shorter and later expressed R₀ isoform (**Table S1**)^{4,5}. With both isoforms present on the same GUV, the larger CD45 R_{ABC} isoform segregated from newly forming FKBP clusters three-fold faster than the R₀ isoform (2.8 ± 0.9 -fold, n=7 GUVs pooled from two experiments, **Fig. 2F-G, Movie S3**). However, the final extent of exclusion between the two CD45 isoforms was similar with this high affinity FRB-FKBP system (**Fig. S3**).

The kinetic segregation model predicts that CD45 is excluded from receptor-ligand complexes based upon a difference in the spacing between the GUV and SLB in the receptor- versus CD45-enriched regions¹⁰. To investigate the topology of the GUV membrane across the interface with nanometer accuracy in the vertical axis, we used scanning angle interference microscopy (SAIM), a technique that calculates the distance of fluorophores from a silicon oxide wafer by collecting sequential images at multiple illumination angles (**Fig. 3A**)¹¹. The SAIM reconstructions revealed membrane deformations at regions of CD45 localization (**Fig. 3B-D**). The calculated difference in membrane spacing between the FRB-FKBP- and CD45 R₀- enriched regions was 18 ± 11 nm (n=4-6 regions from each of 4 GUVs from two experiments, pooled), suggesting a size of ~24 nm for the CD45 R₀ extracellular domain, assuming that FRB-FKBP creates an intermembrane space of 6 nm (**Table S1**)¹². This value is similar to the ~22 nm axial dimension for the CD45 R₀ extracellular domain determined by electron microscopy⁶. Conversely, for GUV-SLB interfaces with FRB-FKBP and SNAP, SAIM reconstructions revealed no changes in membrane spacing across the GUV-SLB interface (**Fig. 3E-G**).

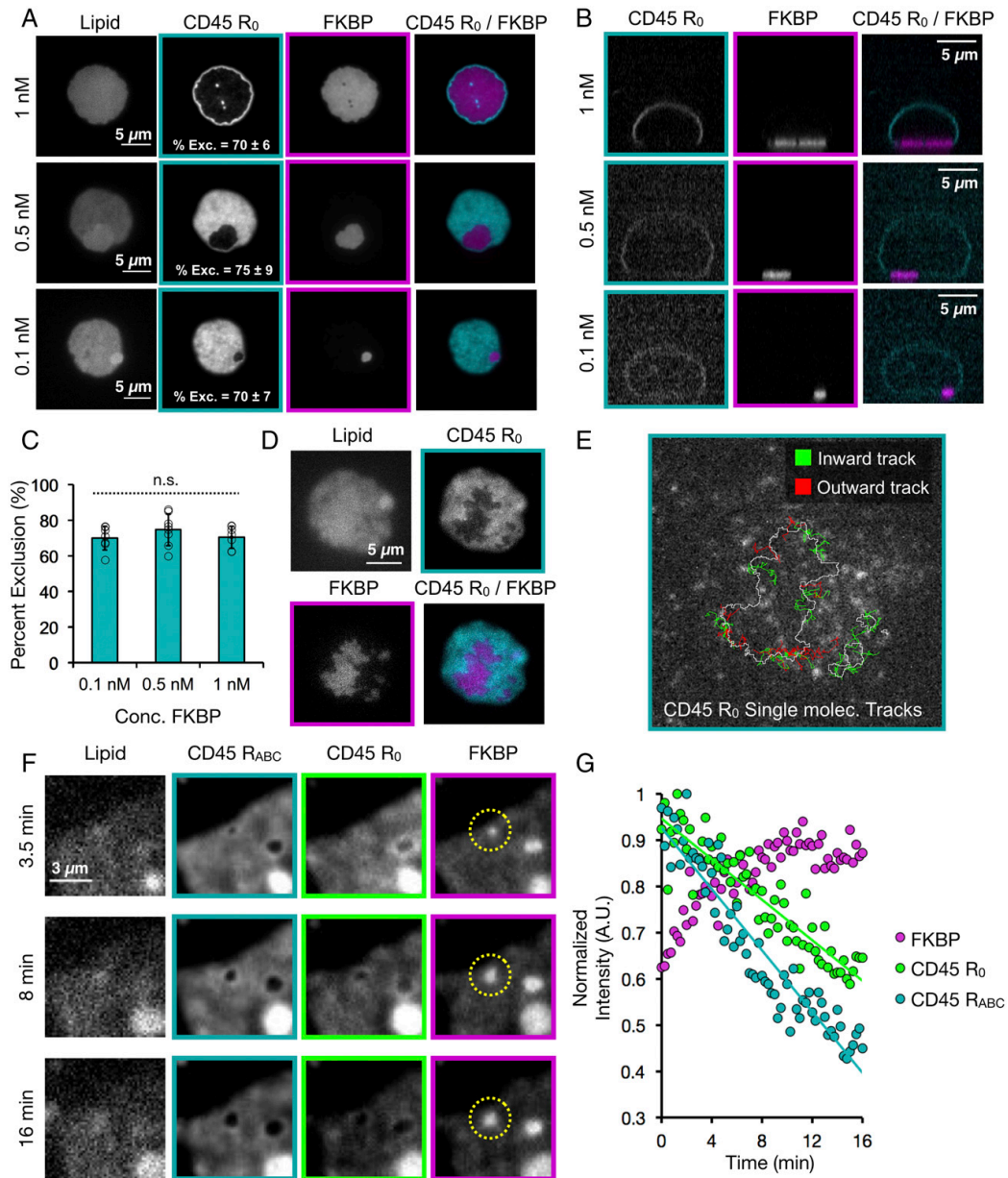


Fig. 2.2. Characterization of partitioned GUV-SLB membrane-membrane interfaces. **(A)** Titration of FKBP concentration (indicated at left of images) with constant CD45 R₀ concentration imaged by TIRF microscopy. Percent exclusion of CD45 R₀ is indicated as mean \pm standard deviation with $n=7-8$ GUVs per condition pooled from three experiments. **(B)** Spinning disk z-sections of GUVs shown in **A**. **(C)** Graphical representation of data shown in **A**. **(D)** Total internal reflection fluorescence (TIRF) microscopy of a GUV-SLB interface showing overall localization of CD45 R₀ and FKBP. **(E)** Single molecule imaging of CD45 R₀ for GUV shown in **D**, border of FKBP enriched zone indicated by white line. Only tracks crossing the exclusion boundary are shown. CD45 R₀ single molecule tracks originating outside FKBP enriched zone are shown as green lines and tracks originating inside the FKBP enriched zone are shown as red lines. **(F)** Total internal reflection fluorescence (TIRF) microscopy of a GUV-SLB interface at 30-sec time points after rapamycin addition showing concentration of FKBP into micro domains that exclude CD45 R₀ and CD45 R_{ABC}. Rate of CD45 R_{ABC} exclusion is 2.8 ± 0.9 times faster than rate of CD45 R₀ exclusion, $n=7$ GUVs from two experiments. **(G)** Quantification of exclusion for representative GUV shown in **F**.

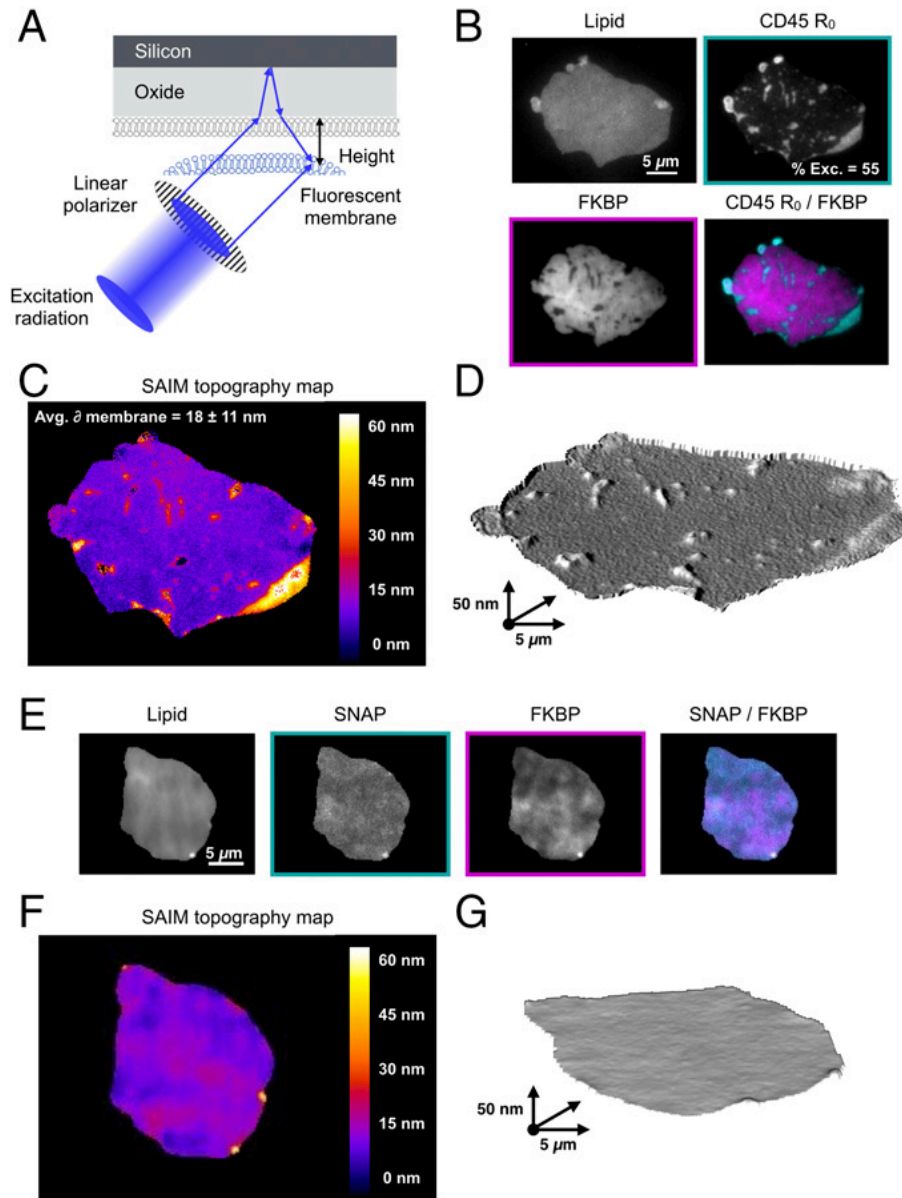


Fig. 2.3. Membrane topology is influenced by local protein composition. **(A)** Schematic of scanning angle interference microscopy showing reflection and interference of excitation light that produces structured illumination patterns used to deduce fluorophore height; adapted from Carbone, et al., 2016. **(B)** Epifluorescence microscopy showing localization of lipid, CD45 R₀ and FKBP on GUV analyzed by SAIM imaging. Percent exclusion of CD45 R₀ indicated for image shown. **(C)** SAIM reconstruction of GUV membrane derived from lipid fluorescence showing an increase in membrane height at CD45 R₀ clusters. Average membrane height change depicted as mean \pm standard deviation, $n=4-6$ clusters from each of 4 GUVs imaged during two separate experiments. **(D)** 3D model of data shown in **c**. Z-scale is exaggerated to clearly depict membrane deformations. **(E)** Epifluorescence microscopy showing localization of lipid, SNAP, and FKBP on GUV analyzed by SAIM imaging. **(F)** SAIM reconstruction of GUV membrane derived from lipid fluorescence **(G)** 3D model of data shown in **F**. Z-scale is exaggerated to clearly depict membrane deformations.

TCR-pMHC –mediated CD45 exclusion

Next, we sought to establish a GUV-SLB interface using the native T cell receptor-ligand pair, TCR-pMHC (**Fig. 4A**). For the TCR, we co-expressed the extracellular domains of the 2B4 α and β chains extended with leucine zippers to stabilize their dimerization¹³; both chains were tagged with His₁₀ for conjugation to the GUV membrane and the β chain contained a ybbR peptide for fluorescent labeling. For the ligand, we used the IE^k MHC, His₁₀-tagged loaded with a high affinity (2.5 μ M Kd) peptide. Similar to the results previously described for FRB-FKBP, we observed the formation of micron-sized TCR clusters that excluded CD45 R₀ (22 \pm 14% exclusion, n=17 GUVs pooled from 2 experiments, **Fig. 4B**) but not the control SNAP domain (**Fig. S3A**).

We also combined both CD45 R_{ABC} and CD45 R₀ isoforms on the same GUV and compared their segregation with the TCR-pMHC system. Upon GUV contact with the SLB, the 2B4 TCR bound the IE^k MHC, and concentrated at the interface where it formed micron-scale clusters that excluded both isoforms of CD45 (**Fig. 4C**). However, unlike the high affinity FKBP-FRB system in which the two CD45 isoforms R₀ and R_{ABC} are excluded to a similar level (Fig. S3), the degree of TCR-pMHC mediated exclusion of the smaller CD45 R₀ isoform (15 \pm 7% exclusion) was lower than the larger CD45 R_{ABC} isoform (38 \pm 9% exclusion) at steady state (45 min, n=13 GUVs pooled from two experiments, **Fig. 4D**).

In vivo, TCR encounters MHCs loaded with a myriad of different peptides; although not absolute, TCR-pMHC affinities of <50 μ M are usually required to trigger a signaling response¹⁴. To examine the effect of TCR-pMHC affinity on CD45 R_{ABC} exclusion, we loaded IE^k MHC with a series of well-characterized peptides with resultant two dimensional Kds of 2.5 μ M, 7.7 μ M, 15 μ M, 50 μ M and null for the 2B4 TCR¹³. At steady state, we observed that pMHCs with affinities to the TCR of 15 μ M and lower excluded CD45 R_{ABC} to similar extents (51 \pm 7% exclusion, n=30 GUVs pooled from two experiments, **Fig. 4E-F**). However, the pMHC with a Kd of 50 μ M and IE^k

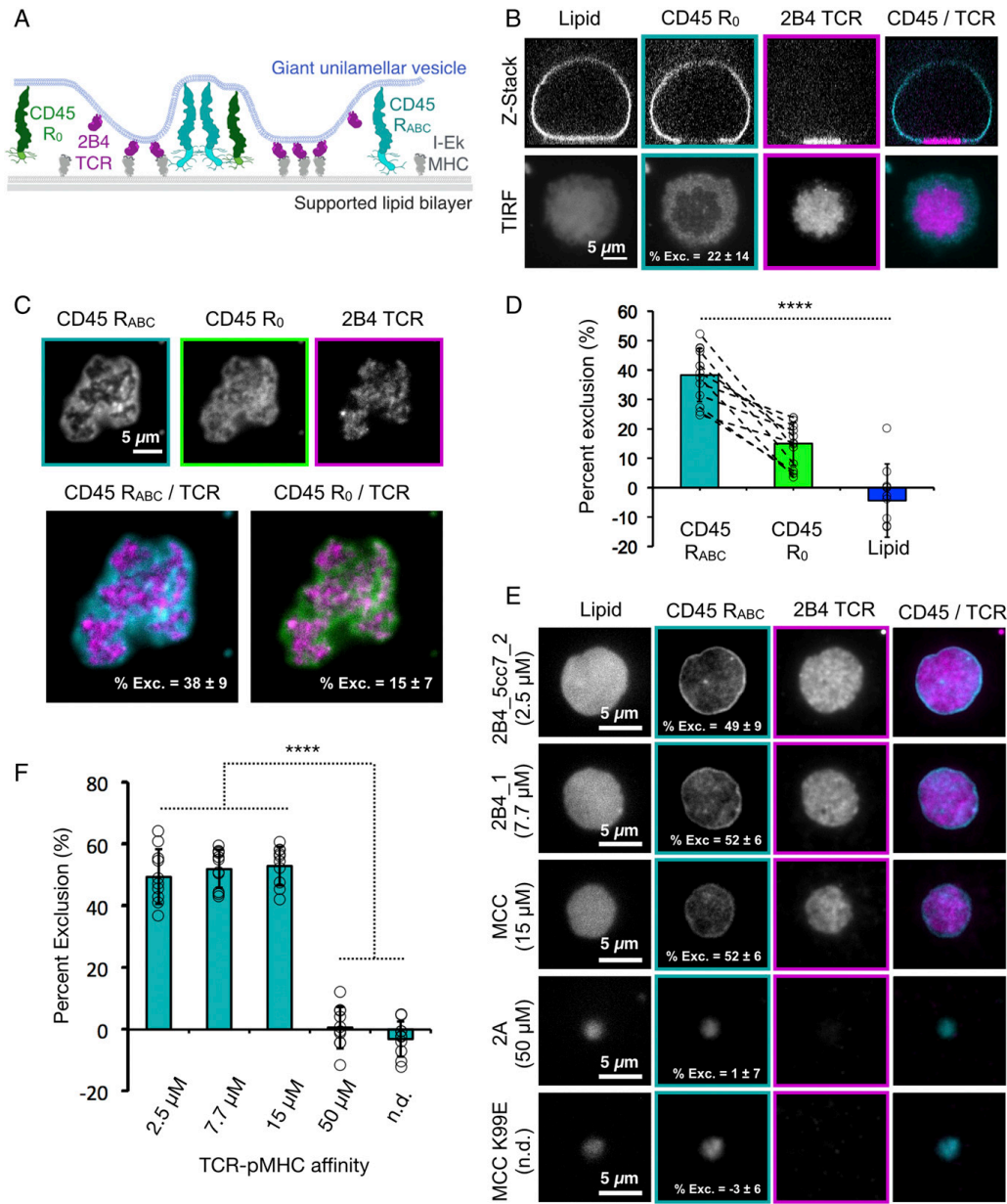


Fig. 2.4. TCR-pMHC binding induces CD45 segregation at GU-SLB interfaces (**A**) Schematic of 2B4 TCR-IE^k MHC binding between a GUV and a SLB, and segregating away from two CD45 isoforms (R₀ and R_{ABC}). (**B**) Top, spinning disk z-sections of GUVs after membrane-apposed interfaces have reached equilibrium, showing localization of 2B4 TCR to membrane interface and exclusion CD45 R₀ away from the interface. Bottom, TIRF images of GUV-SLB interface for GUV shown in panel above. Percent exclusion of CD45 R₀ indicated for image shown. (**C**) Top, segregation of CD45 R₀ and CD45 R_{ABC} on the same GUV membrane away from 2B4 TCR, shown by TIRF microscopy of membrane interface. Percent exclusion of CD45 isoforms indicated as mean ± standard deviation, with n=13 GUVs from two experiments. (**D**) Graphical representation of data shown in **C**. (**E**) Dependence of CD45 R_{ABC} exclusion as a function of TCR-pMHC affinity using peptides with different K_ds, indicated at left of images. Imaged by TIRF microscopy of membrane interfaces. Percent exclusion of CD45 R_{ABC} indicated as mean ± standard deviation, n=10 GUVs per condition from two experiments. (**F**) Graphical representation of data shown in **E**.

loaded with null peptides did not concentrate TCR at the GUV-SLB interface and did not change the distribution of CD45 R_{ABC} ($-1 \pm 6\%$ exclusion, n=20 GUVs pooled from 2 experiments, **Fig. 4E-F**). Thus, in agreement with computational predictions¹⁵, CD45 R_{ABC} exclusion was observed over the same range of affinities that are associated with peptide agonists.

Exclusion of CD45 by PD-1 –PD-L1

T cell signaling involves many receptor-ligand pairs interacting across the two membranes in addition to the TCR-pMHC¹⁶. The co-receptor PD-1 and its ligand PD-L1 create a signaling system that opposes T cell activation by inhibiting CD28 signaling^{17,18}. PD-1 ligation also results in microcluster formation on T cells¹⁹. Like the TCR, PD-1 signaling is initiated through receptor tail phosphorylation by Lck²⁰, and this phosphorylation event may be opposed by the abundant CD45 phosphatase (**Fig. S4A-B**). Therefore we tested the ability of interaction of PD-1 with PD-L1, which forms a complex of similar dimension (9 nm) to TCR-pMHC (**Table S1**)²¹ to partition CD45 in our in vitro liposome system (**Fig. 5A**). As expected from these physical dimensions, PD-1-PD-L1 interaction at the membrane-membrane interfaces formed micron-sized clusters that excluded CD45 R_{ABC} (**Fig. 5B**). The degree of CD45 R_{ABC} exclusion ($60 \pm 14\%$ exclusion, n=14 GUVs from two experiments **Fig. 5B**) was greater than that observed for TCR-pMHC (2.5 μ M peptide), which may be explained by the higher affinity of the PD1-PD-L1 interaction (0.77 μ M)²².

We also combined CD45 R_{ABC} with both TCR-pMHC with PD-1-PD-L1. In this dual receptor-ligand system, the two receptor-ligand complexes co-localized and CD45 R_{ABC} was partitioned away from the combined ligated TCR-PD-1 footprint (**Fig. 5C**). The size (**Table S1**) and affinity

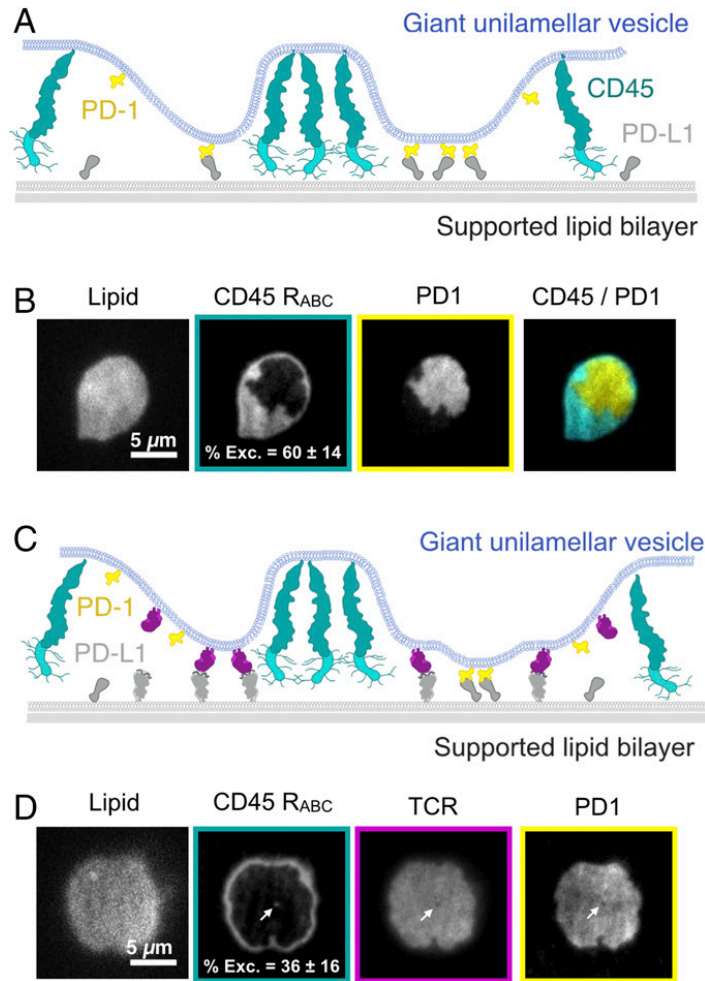


Fig. 2.5. The inhibitory co-receptor PD-1 excludes CD45 and colocalizes with TCR. **(A)** Schematic of PD-1-PD-L1 binding between a GUV and a SLB, with segregation away from CD45_{R_{ABC}}. **(B)** TIRF microscopy showing concentration of PD-1 into microdomains that exclude CD45_{R_{ABC}}. Percent exclusion of CD45_{R_{ABC}} indicated as mean \pm standard deviation, $n=14$ GUVs from two experiments. **(C)** TIRF microscopy showing concentration of TCR and PD-1 into a domain that excludes CD45_{R_{ABC}}. Percent exclusion of CD45_{R_{ABC}} indicated as mean \pm standard deviation, $n=14$ GUVs from two experiments. White arrow highlights small CD45_{R_{ABC}} enriched zone that is depleted for TCR and PD-1.

difference between TCR-pMHC and PD-1-PD-L1 may be small enough to not cause partitioning of these receptor-ligands under the conditions tested in our *in vitro* assay.

2.5 Discussion

In this study, we have established an *in vitro* membrane system that recapitulates receptor-ligand mediated CD45 exclusion. We have found that the binding energy of physiological receptor-ligand interactions is sufficient for CD45 partitioning at a model membrane-membrane interface. We also show that subtle differences in sizes and affinities of the proteins at the interface can give rise to significant changes in spatial organization and discuss the implications of these findings in more detail below.

Spatial organization of TCR and CD45 at the immune cell contacts has been proposed to arise by a nucleation-spreading mechanism¹⁵. By imaging an inducible synthetic receptor-ligand binding interaction in real time, we also conclude that pattern formation arises by the nucleation of small clusters that further spread across the membrane interface over time. These patterns induce changes in membrane topology that reflect the local protein composition and are stable on the order of hours. However, we show that individual molecules can freely exchange between domains. This result is consistent with previous computational simulations, although these models predict patterns will relax to a circular geometry to minimize the length of the domain boundaries^{15,23,24}. In our system, as observed for other physical models of partitioning using DNA-DNA hybridization²⁵ and dimerizing GFP²⁶, patterns have more complex domain structures. The lack of circular geometry in the experimental systems could be due to small inhomogeneities in the supported lipid bilayer compared to perfectly diffusive computational models. Despite this difference, many physical and computational model systems have converged on nucleation and spreading as a general mechanism by which spatial organization arises at membrane-membrane

interfaces.

The mechanism by which receptor-ligand binding induces spatial organization is a subject of active investigation. Our results showing differential exclusion of CD45 R₀ and CD45 R_{ABC} indicate that size-based steric exclusion and membrane deformation are important for exclusion. In addition, protein crowding of receptor-ligand complexes also could provide a driving force for partitioning. Indeed, previous work has shown that patterns formed at analogous membrane-membrane interfaces using dimerizing GFP as the receptor-ligand pair and a small test protein (monomeric Cherry) are due to crowding effects²⁶. In our system, however, we observe that the small SNAP protein is distributed throughout receptor-ligand enriched and depleted zones. These systems employ different proteins at the interface, and it will be interesting to investigate whether specific protein properties (e.g. size, propensity for oligomerization, elasticity, flexibility, packing density of receptor-ligand in partitioned zones, etc) account for these differences in the role of protein crowding in exclusion.

Our work also suggests an important contribution of receptor-ligand affinity in protein exclusion. We observed 70% depletion of CD45 R₀ from FRB-FKBP (100 fM Kd) -enriched zones. The TCR-pMHC interactions, on the other hand, are much lower in affinity, with most agonists generally displaying Kds of 1-100 μ M¹⁴. Strikingly, when we tested CD45 exclusion using TCR-pMHC, we found that exclusion was only 27% for the R₀ isoform and 49% for the R_{ABC} isoform when tested individually. The PD-1-PD-L1 interaction is higher affinity (0.7 μ M) and produces a somewhat higher exclusion (60%) of CD45 R_{ABC}. While the CD45 R₀ isoform exclusion by TCR-pMHC is modest, it nevertheless could be significant for eliciting a signaling response. *In vitro* analysis of the kinase-phosphatase network controlling TCR activation has shown that at physiological protein densities, small perturbations of CD45 can drive large changes in TCR phosphorylation

²⁷. In combination with our results, this suggests that the cellular CD45 concentration may position the TCR precisely at the boundary of a switch-like response in phosphorylation.

Our experimental results also are in reasonable agreement with computational predictions for a lower boundary of receptor-ligand affinity needed for protein exclusion. Computational models by Weikl et al. ¹⁵ predict that, at the ratio of 1 TCR molecule to 8 CD45 molecules used in these experiments, a binding energy of $>4 k_B T$ (corresponding to a K_d of $\sim 20 \mu M$) is required for partitioning. In our system, we find that a pMHC ligand with $15 \mu M$ K_d causes CD45 exclusion whereas a ligand with a K_d of $50 \mu M$ does not. It also has been predicted that increasing the affinity of a receptor-ligand interaction should increase the area fraction of the interface occupied by the receptor-ligand enriched zone by increasing the number of bound complexes at the same protein densities ^{15,25}. However, in our experiments, TCR-pMHC mediated CD45 partitioning occurs as an all-or-nothing process.

Our results also demonstrate that the large extracellular domains of CD45 R_{ABC} and CD45 R₀ are differentially sensitive to the partitioning forces produced by ligand-receptor binding interactions at a membrane-membrane interface. This finding is consistent with results showing that T cells expressing larger CD45 isoforms signal more efficiently ²⁸, although others have contested this conclusion ²⁹. Although the signaling consequences of differential CD45 segregation on immune activation remain to be clarified, our results establish a biophysical difference between two highly conserved CD45 isoforms ³⁰ with regard to their degree of spatial segregation in response to TCR-pMHC interactions. Given that the smaller CD45 isoforms are preferentially expressed in later steps of T cell selection ⁹, our results suggest that T cell signaling may be attenuated by changes in CD45 isoform expression as a mechanism of peripheral tolerance.

We also explore increasing complexity at a membrane interface by introducing two receptor-ligand pairs: TCR-pMHC and PD-1-PD-L1. Interestingly, we find that these two receptor-ligands complexes co-localize with one another and both together exclude CD45. *In vivo*, partial segregation of these two receptor-ligands also has been observed in CD8+ T cells³¹, and a higher degree of co-localization between these receptors was reported in CD4+ T cells¹⁹. Given that the size difference between the TCR-pMHC and PD-1-PD-L1 lies at the biophysical threshold for partitioning²⁶, these results suggest that cellular localization of PD-1 with respect to TCR may be regulated by other factors (e.g. other co-receptors or adaptor proteins) and perhaps even in cell type -specific manner. In addition, it will be interesting to investigate how actin polymer dynamics and lipid-mediated organization³² may enhance or disrupt protein patterning across two membranes.

2.6 Materials and Methods

Materials. Synthetic 1,2-dioleoyl-sn-glycero-3-phosphocholine (POPC; Avanti, 850457), 1,2-dioleoyl-sn-glycero-3-[(N-(5-amino-1-carboxypentyl)iminodiacetic acid)succinyl] (nickel salt, DGS-NTA-Ni; Avanti, 790404) and 1,2-dioleoyl-sn-glycero-3-phosphoethanolamine-N [methoxy(polyethylene glycol)-5000] (ammonium salt, PEG5000-PE; Avanti, 880220) were acquired from Avanti Polar Lipids, Alabama, USA. 1,2-dioleoyl-sn-glycero-3-phosphoethanolamine-Atto390 (DOPE-390; AttoTec, AD390-161) was acquired from Atto-Tec, Germany.

Recombinant protein expression, purification, and labeling. N-terminally His₁₀- and SNAP-tagged FRB and FKBP were subcloned into a pET28a vector and were bacterially expressed in BL21(DE3) strain of *Escherichia coli*. The cells were lysed in an Avestin Emulsiflex system. C-terminally His₁₀- and SNAP- tagged extracellular domains of human CD45 R₀, human CD45 R_{ABC},

and human PD-L1 were subcloned into a pFastBac vector and were expressed in SF9 cells. All proteins were purified by using a HisTrap excel column (GE Healthcare Life Sciences) following the product recommendations. Recombinant C-terminal His₁₀-tagged mouse PD-1 extracellular domain was purchased from Sino Biological.

2B4 TCR V_mC_h chimeras containing an engineered C domain disulfide were cloned into the pAcGP67a insect expression vector (BD Biosciences, 554756) encoding either a C-terminal acidic GCN4-zipper-Biotin acceptor peptide (BAP)-His₆ tag (for α chain) or a C-terminal basic GCN4 zipper-His₆ tag (for β chain)³³. Thus the resulting dimer has a combined His₁₂. Each chain also encoded a 3C protease site between the C-terminus of the TCR ectodomains and the GCN4 zippers to allow for cleavage of zippers. IE^k MHC was cloned into pAcGP67A with acidic/basic zippers and His tags as described for TCRs. IE^k α and 2B4 α chain also encoded ybbr-tag sequence for direct protein labeling. The IE^k β construct was modified with an N-terminal extension containing either the 2A peptide via a Gly-Ser linker or CLIP peptide via a Gly-Ser linker containing a thrombin cleavage site. Proteins were transiently expressed in High Five insect cells (BTI-TN-5B1-4) and purified using His-tag/Nickel according to published protocols¹³.

For fluorescent labeling of SNAP-tagged proteins, 10 μ M protein was incubated with 20 μ M benzylguanine functionalized dye (New England Biolabs) in HBS buffer (50 mM HEPES, 150 mM NaCl, 1 mM TCEP, pH 7.4) for 1 h at room temperature or overnight on ice. For PD-L1 and TCR 10 μ M protein was incubated with 30 μ M tetramethylrhodamine-5-maleimide in HBS buffer for 1 h at room temperature. Excess dyes were removed using Zeba Spin Desalting Columns (ThermoFisher, 89882).

Preparation of SNAP-DNA tethers. Oligonucleotides were ordered from IDT with a 3'/5' terminal amine and labeled with BG-GLA-NHS as previously described³⁴. The adhesion strands used in

this study consisted of a 3' 20mer region (5'- ACTGACTGACTGACTGACTG-3') with a 5' 80mer poly-dT and the complementary sequence (5'- CAGTCAGTCAGTCAGTCAGT-3') also with a 5' 80mer poly-dT. Conjugation to benzyl-guanine was performed as described ³⁴. His₁₀-tagged SNAP was labeled at a concentration of 5 μ M with a 3-fold excess of BG-DNA in HBS (50 mM HEPES, 150 mM NaCl and 1 mM TCEP, pH 7.4).

Electroformation of giant unilamellar vesicles. Lipids were mixed with a molar composition of 94.9% POPC, 5% DGS-NTA, 0.1% DOPE-390 in chloroform (Electron Microscopy Sciences, 12550) and dried under vacuum for 1 h to overnight. Electroformation was performed in 370 mM sucrose according to published protocols ³⁵. GUVs were stored at room temperature and imaged within one week.

Preparation of supported lipid bilayers. Small unilamellar vesicles (SUVs) were prepared from a mixture of 97.5% POPC, 2% DGS-NGA-Ni, and 0.5% PEG5000-PE. The lipid mixture in chloroform was evaporated under argon and further dried under vacuum. The mixture was then rehydrated with phosphate buffered saline pH 7.4 and cycled between -80°C and 37°C 20 times, and then centrifuged for 45 min at 35,000 RCF. SUVs made by this method were stored at 4°C and used within two weeks of formation. Supported lipid bilayers were formed in freshly plasma cleaned custom PDMS chambers on RCA cleaned glass coverslips. 100 μ L of SUV solution containing 0.5 to 1 mg/ml lipid was added to the coverslips and incubated for 30 min. Unadsorbed vesicles were removed and bilayers were blocked by washing three times with reaction buffer (50 mM HEPES, 150 mM NaCl, 1 mM TCEP, 1 mg/mL bovine serum albumen, pH 7.4), and incubating for 20 min.

Optical setup for spinning disk, total internal reflection fluorescence, and scanning angle interference microscopy. Imaging was performed on one of two Nikon TI-E microscopes

equipped with a Nikon 60x Plan Apo VC 1.20 NA water immersion objective, or a Nikon 100x Plan Apo 1.49 NA oil immersion objective, and four laser lines (405, 488, 561, 640 nm), either a Hamamatsu Flash 4.0 or Andor iXon EM-CCD camera, and μ Manager software³⁶. A polarizing filter was placed in the excitation laser path to polarize the light perpendicular to the plane of incidence. Angle of illumination was controlled with either a standard Nikon TIRF motorized positioner or a mirror moved by a motorized actuator (Newport, CMA-25CCCL). Scanning angle microscopy was performed and analyzed as previously described¹¹. For FRAP experiments, a region of $\sim 1 \mu\text{m}^2$ was photobleached using a 405 nm laser modulated by a Rapp UGA-40 photo targeting unit and the fluorescence recovery was monitored over time.

Reconstitution of membrane interfaces. GUVs and SLBs were separately incubated for one hour with the indicated proteins for each experiment. Proteins were diluted in reaction buffer (50 mM HEPES, 150 mM NaCl, 1 mM TCEP, 1 mg/mL bovine serum albumen, pH 7.4) and then mixed 2:1 with GUVs, or added to supported lipid bilayers. SLBs were washed 6 times with $\frac{1}{2}$ total well volume resulting in a final concentration of $\sim 1\%$ input protein remaining. The GUVs were not washed but were diluted 10-fold into the imaging well with the supported lipid bilayer after a one hour incubation. Rapamycin (Sigma, R0395) was added to FRB-FKBP reactions at a final concentration of 5 μM . GUVs were allowed to settle for 30-60 min prior to imaging. SLB fluidity was assessed by visualizing diffusion of unbound GUV proteins that associate with the supported lipid bilayer (e.g. FKBP, TCR, CD45). If $>25\%$ of fluorescent molecules on the SLB were not diffusive, the experiment was repeated with a more fluid bilayer.

Estimated protein densities. Protein densities are estimates based on the conversion factor between protein concentration and molecular density defined by Schmid, et al²⁶. Given our system utilizes an analogous physical setup to their experiments, including the same homemade PDMS-wells with 100 μL volume (described in “Preparation of supported lipid bilayers” section of

the Methods) and protein concentrations in a similar range (1-100nM), we can extrapolate from their measurement of 2,317 +/- 370 molecules/ μm^2 for an SLB with 2.5% DGS-NTA-Ni incubated with 100 nM His₁₀-tagged protein. Because the SLBs used in this study contain 2% DGS-NTA-Ni and GUVs contain 5% DGS-NTA-Ni, this factor (23.17 molec/ μm^2 /nM) was first multiplied by 0.8 or 2, respectively. Protein concentrations (in nM) were then multiplied by the membrane-specific scaling factor to give an estimated final density in molecules/ μm^2 . This estimate may be imperfect due to differences in specific experimental variables affecting total lipid surface area available for protein binding including differences in electroformation. These estimated densities are: FKBP (5-200 molec/ μm^2), CD45 R0 and RABC (1000 molec/ μm^2), TCR (200 molec/ μm^2), PD-L1 (50 molec/ μm^2), SNAP (50 molec/ μm^2), PD-1 (100-300 molec/ μm^2), MHC (200 molec/ μm^2), FRB (20 molec/ μm^2).












Image analysis. Images were analyzed using ImageJ (FIJI)³⁷. The same brightness and contrast were applied to images within the same panels. FIJI rolling ball background subtraction was applied to images before calculating mean fluorescence intensities. Percent exclusion was calculated as one minus the ratio of average intensity inside a receptor enriched zone to the average intensity at the interface outside the receptor-enriched zone. ROIs for inside and outside receptor-enriched zones were selected manually within regions of comparable lipid intensity. All exclusion quantification refers to images acquired using TIRF microscopy. Data from image analysis within FIJI was graphed using Microsoft Excel.

Liposome Assay. Experiments were carried out as previously described¹⁷. Briefly, proteins were purified using baculovirus or bacterial expression system. LUVs and proteins of interest were premixed and incubated at room temperature for 1 h. 2 mM ATP was then injected and rapidly mixed to trigger Lck mediated phosphorylation of CD3 ζ and PD-1. 20 minutes after ATP addition, apyrase was added (t = 0 min) and the reactions were allowed to continue at room temperature.

Equal fractions of the reactions were removed and terminated with SDS sample buffer at the indicated time points. Anti-phosphotyrosine antibody (pY20, Santa Cruz Biotechnology #SC-508) was used to detect phosphorylation by western blotting.

2.7 Supporting Information

Table S2.1. Protein extracellular domain size estimates

	Protein	Size estimate	Notes	References
	FKBP	4 nm	Distance from FKBP Arg 13 to Thr 85 from PDB 3FAP measured in Chimera software.	Liang et al. 1999
	FRB	4 nm	Distance from FRB Gln 152 to Asn 182 from PDB 3FAP measured in Chimera software.	Liang et al. 1999
	FKBP-FRB complex	6 nm	Distance from FKBP Thr 6 to FRB Gln 152 from PDB 3FAP measured in Chimera software.	Liang et al. 1999
	CD45 R ₀	25 nm	Estimate based on published electron microscopy and crystallographic studies.	Woollett et al. 1985, McCall et al. 1992, Chang et al. 2016
	CD45 R _{ABC}	40 nm	Estimate based on published electron microscopy and crystallographic studies.	Woollett et al. 1985, McCall et al. 1992, Chang et al. 2016
	TCR	7 nm	Distance from TCR β Asp 244 to TCR α Thr 92 from PDB 4P2O measured in Chimera software.	Birnbaum et al. 2014
	pMHC	7 nm	Distance from MHC β Pro 165 to Pro 65 from PDB 4P2O measured in Chimera software.	Birnbaum et al. 2014
	TCR-pMHC complex	13 nm	Distance from TCR β Asp 244 to MHC β Pro 165 from PDB 4P2O measured in Chimera software.	Birnbaum et al. 2014
	PD-1	5 nm	Distance from Pro 130 to Ile 148 from PDB 3BIK measured in Chimera software.	Lin et al. 2008
	PD-L1	8 nm	Distance from Gln 47 to Leu 229 from PDB 3BIK measured in Chimera software.	Lin et al. 2008
	PD-1-PD-L1 complex	9 nm	Distance from PD-L1 Leu 229 to PD-1 Ile 148 from PDB 3BIK measured in Chimera software.	Lin et al. 2008
-	SNAP	5 nm	Distance from Ala 50 to Leu 153 from PDB 3KZY measured in Chimera software.	Schmitt et al. 2010

	Protein	Size estimate	Notes	References
-	DNA tether	125 nm	Assuming 0.34 nm per double stranded base pair (20 bp) and 0.67 nm per single stranded base pair (160 bp) plus 5 nm for each of two SNAP proteins. At this length the DNA tether is expected to be quite flexible.	Chi et al, 2013

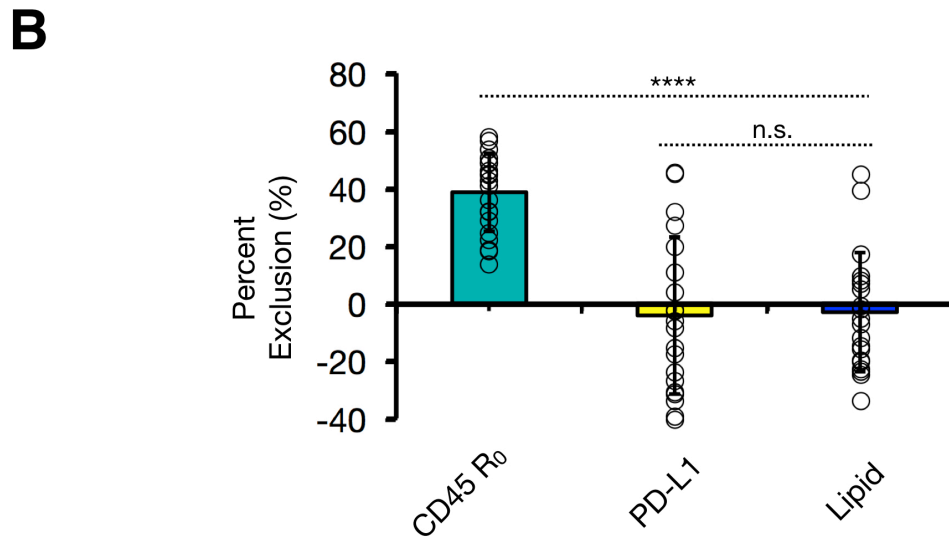
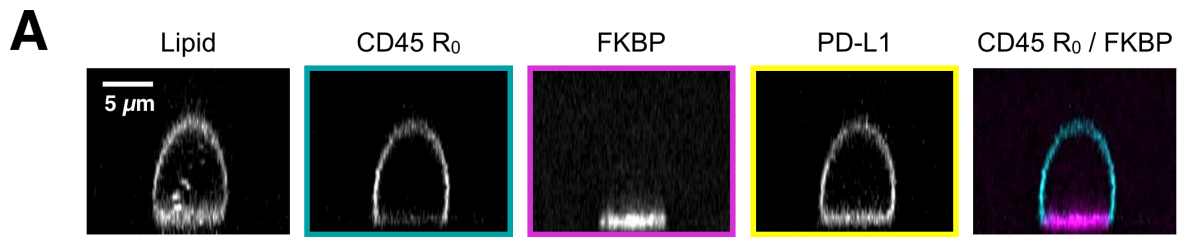


Fig. S2.1. PD-L1 is not excluded from FKBP-bound membrane interfaces. **(A)** Spinning disk z-sections of GUVs after membrane-apposed interfaces have reached equilibrium, showing localization of FKBP to the membrane interface, localization of CD45 R₀ away from the interface, and uniform distribution of PD-L1. **(B)** Quantification of experiment shown in **A**; mean \pm standard deviation (n=20 GUVs pooled from two experiments).

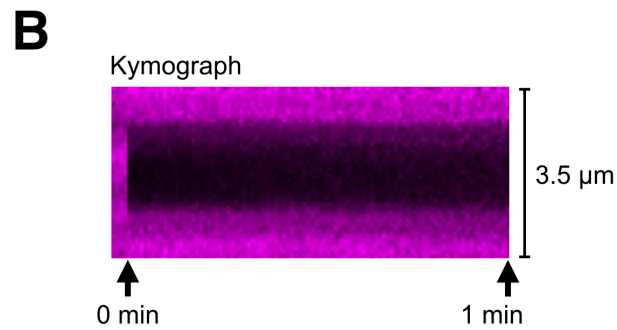
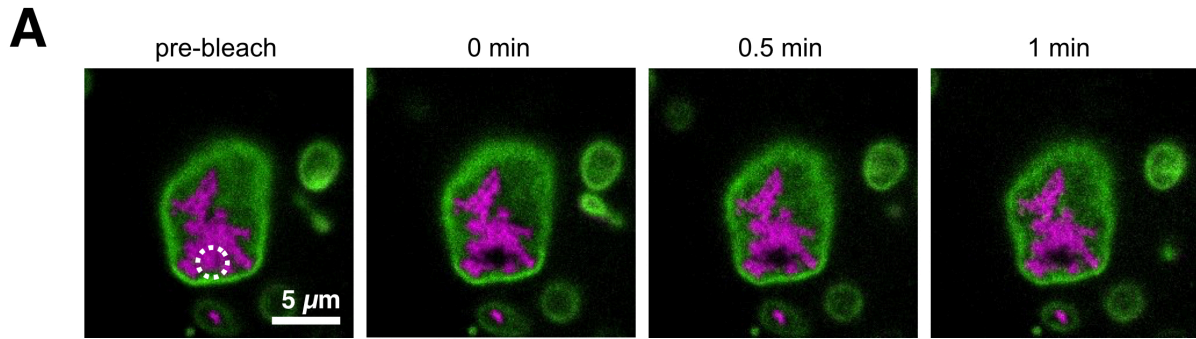


Fig. S2.2. FKBP molecules in partitioned domains do not readily exchange. **(A)** Images for FKBP enriched interfaces before and after photobleaching (dashed white line, bleach site). Scale bars, 5 μm **(B)** Kymograph corresponding to **A**. Data are representative of three independent experiments.

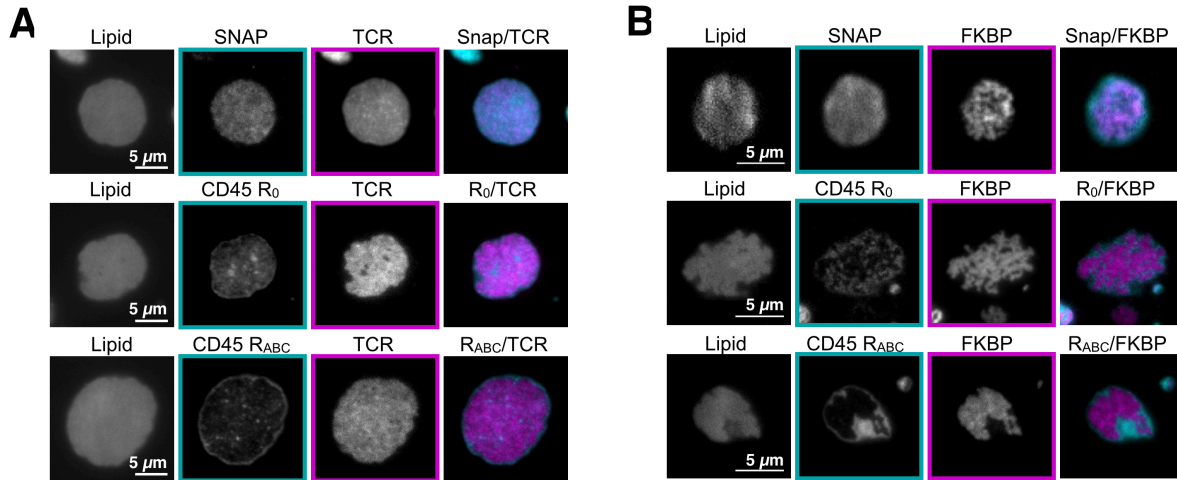


Fig. S2.3. TCR-pMHC and FRB-FKBP exclude CD45 R₀ and CD45 R_{ABC} but not SNAP. **(A)** TIRF microscopy of a GUV-SLB interface at equilibrium showing concentration of TCR into microdomains. Top, SNAP is homogeneously distributed. Middle, CD45 R₀ is weakly excluded. Bottom, CD45 R_{ABC} is strongly excluded. **(B)** TIRF microscopy of a GUV-SLB interface at equilibrium showing concentration of FKBP into micro domains. SNAP is homogeneously distributed. CD45 R₀ and CD45 R_{ABC} are excluded.

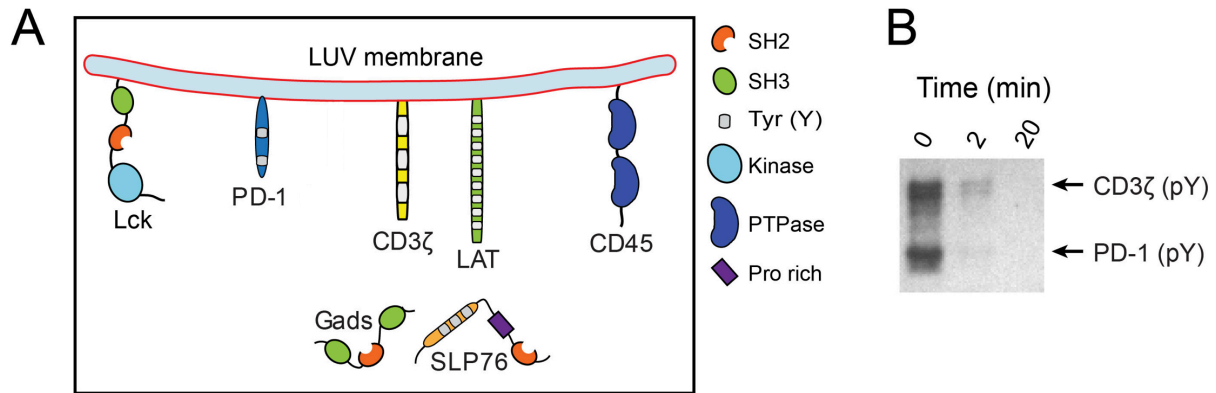


Fig. S2.4. PD-1 is a target for CD45 dephosphorylation. (A) Schematic of LUV reconstitution system for assaying the sensitivity PD-1 to CD45. DGS-NTA-Ni containing LUVs were attached with purified, polyhistidine-tagged cytosolic domains of receptors (CD3 ζ [290 molecules per μm^2]; PD-1 [870 molecules per μm^2]), the adaptor LAT (870 molecules per μm^2), the kinase Lck (290 molecules per μm^2), and the phosphatase CD45 (29 molecules per μm^2). Purified cytosolic factors (Gads [0.3 μM]; SLP76 [0.3 μM]) were added to solution to create a more physiological setting. Pre-addition of ATP triggered net phosphorylation of both CD3 ζ and PD-1 by Lck, despite the presence of CD45, owing to the 10-fold excess of Lck over CD45. (B) A phosphotyrosine western blot showing the time course of CD3 ζ and PD-1 dephosphorylation by CD45, after the addition of the ATP scavenger Apyrase, which rapidly terminated the Lck kinase activity to isolate the CD45 activity. PTPase, protein tyrosine phosphatase; Pro, proline.

2.8 Author Contributions

Author contributions: C.B.C., N.K., E.H., X.S., and R.D.V. designed research; C.B.C., N.K., and E.H. performed research; C.B.C., N.K., R.A.F., E.H., X.S., and K.C.G. contributed new reagents/analytic tools; C.B.C. and N.K. analyzed data; and C.B.C., N.K., and R.D.V. wrote the paper.

2.9 Acknowledgements

We would like to thank N. Stuurman for help with microscopy and image analysis and M. Taylor for guidance with protein purification and DNA tethering. We thank A. Williamson, N. Stuurman, and M. Morrissey for comments on the manuscript. The authors acknowledge funding from the Howard Hughes Medical Institute and National Institutes of Health (R01EB007187, R.D.V.).

2.10 References

1. Banaszynski, L. A., Liu, C. W. & Wandless, T. J. Characterization of the FKBP·Rapamycin·FRB Ternary Complex. *J. Am. Chem. Soc.* **127**, 4715–4721 (2005).
2. Signal Transduction Through a DNA-Based T Cell Receptor.
3. Chi, Q., Wang, G. & Jiang, J. The persistence length and length per base of single-stranded DNA obtained from fluorescence correlation spectroscopy measurements using mean field theory. *Phys. A Stat. Mech. its Appl.* **392**, 1072–1079 (2013).
4. Woollett, G. R., Williams, A. F. & Shotton, D. M. Visualisation by low-angle shadowing of the leucocyte-common antigen. A major cell surface glycoprotein of lymphocytes. *EMBO J.* **4**, 2827–2830 (1985).
5. McCall, M. N., Shotton, D. M. & Barclay, A. N. Expression of soluble isoforms of rat CD45. Analysis by electron microscopy and use in epitope mapping of anti-CD45R monoclonal antibodies. *Immunology* **76**, 310–7 (1992).
6. Chang, V. T. *et al.* Initiation of T cell signaling by CD45 segregation at ‘close contacts’. *Nat. Immunol.* **17**, 574–582 (2016).
7. Gautier, A. *et al.* An Engineered Protein Tag for Multiprotein Labeling in Living Cells. *Chem. Biol.* **15**, 128–136 (2008).
8. Bannwarth, M. *et al.* Crystal structure of SNAP-tag. *doi.org* doi:10.2210/pdb3kzy/pdb
9. Hermiston, M. L., Xu, Z. & Weiss, A. CD45: a critical regulator of signaling thresholds in immune cells. *Annu. Rev. Immunol.* **21**, 107–137 (2003).
10. Davis, S. J. & van der Merwe, P. A. The kinetic-segregation model: TCR triggering and beyond. *Nat. Immunol.* **7**, 803–809 (2006).
11. Carbone, C. B., Vale, R. D. & Stuurman, N. *A data acquisition and analysis pipeline for scanning angle interference microscopy.* (2016). doi:10.1101/050468
12. Liang, J., Choi, J. & Clardy, J. Refined structure of the FKBP12-rapamycin-FRB ternary

- complex at 2.2 Å resolution. *Acta Crystallogr. D. Biol. Crystallogr.* **55**, 736–44 (1999).
13. Birnbaum, M. E. *et al.* Deconstructing the Peptide-MHC Specificity of T Cell Recognition. *Cell* **157**, 1073–1087 (2014).
 14. Gascoigne, N. R. J., Zal, T. & Alam, S. M. T-cell receptor binding kinetics in T-cell development and activation. *Expert Rev. Mol. Med.* **3**, (2001).
 15. Weikl, T. R. & Lipowsky, R. Pattern formation during T-cell adhesion. *Biophys. J.* **87**, 3665–3678 (2004).
 16. Chen, L. & Flies, D. B. Molecular mechanisms of T cell co-stimulation and co-inhibition. *Nat. Rev. Immunol.* **13**, 227–242 (2013).
 17. Hui, E. *et al.* T cell co-stimulatory receptor CD28 is a primary target for PD-1-mediated inhibition. (2016). doi:10.1101/086652
 18. Kamphorst, A. O. *et al.* Rescue of exhausted CD8 T cells by PD-1–targeted therapies is CD28-dependent. *Science (80-.).* **355**, 1423–1427 (2017).
 19. Yokosuka, T. *et al.* Programmed cell death 1 forms negative costimulatory microclusters that directly inhibit T cell receptor signaling by recruiting phosphatase SHP2. *J. Exp. Med.* **209**, 1201–1217 (2012).
 20. Sheppard, K.-A. *et al.* PD-1 inhibits T-cell receptor induced phosphorylation of the ZAP70/CD3 ζ signalosome and downstream signaling to PKC θ . *FEBS Lett.* **574**, 37–41 (2004).
 21. Lin, D. Y. -w. *et al.* The PD-1/PD-L1 complex resembles the antigen-binding Fv domains of antibodies and T cell receptors. *Proc. Natl. Acad. Sci.* **105**, 3011–3016 (2008).
 22. Butte, M. J., Peña-Cruz, V., Kim, M.-J., Freeman, G. J. & Sharpe, A. H. Interaction of human PD-L1 and B7-1. *Mol. Immunol.* **45**, 3567–3572 (2008).
 23. Burroughs, N. J. & Wülfing, C. Differential segregation in a cell-cell contact interface: The dynamics of the immunological synapse. *Biophys. J.* **83**, 1784–1796 (2002).
 24. Krobath, H., Rózycki, B., Lipowsky, R. & Weikl, T. R. Line tension and stability of domains

- in cell-adhesion zones mediated by long and short receptor-ligand complexes. *PLoS One* **6**, (2011).
25. Chung, M., Koo, B. J. & Boxer, S. G. Formation and analysis of topographical domains between lipid membranes tethered by DNA hybrids of different lengths. *Faraday Discuss.* **161**, 333–45; discussion 419-59 (2013).
 26. Schmid, E. M. *et al.* Size-dependent protein segregation at membrane interfaces. *Nat. Phys.* **12**, 704–711 (2016).
 27. Hui, E. & Vale, R. D. In vitro membrane reconstitution of the T-cell receptor proximal signaling network. *Nat. Struct. Mol. Biol.* **21**, 133–42 (2014).
 28. Chui, D., Ong, C. J., Johnson, P., Teh, H. S. & Marth, J. D. Specific CD45 isoforms differentially regulate T cell receptor signaling. *EMBO J.* **13**, 798–807 (1994).
 29. Czyzyk, J., Leitenberg, D., Taylor, T. & Bottomly, K. Combinatorial Effect of T-Cell Receptor Ligation and CD45 Isoform Expression on the Signaling Contribution of the Small GTPases Ras and Rap1. *Mol. Cell. Biol.* **20**, 8740–8747 (2000).
 30. Okumura, M. *et al.* Comparison of CD45 extracellular domain sequences from divergent vertebrate species suggests the conservation of three fibronectin type III domains. *J. Immunol.* **157**, 1569–75 (1996).
 31. Hui, E. *et al.* T cell costimulatory receptor CD28 is a primary target for PD-1–mediated inhibition. *Science (80-.)*. **355**, 1428–1433 (2017).
 32. Köster, D. V & Mayor, S. Cortical actin and the plasma membrane: inextricably intertwined. *Curr. Opin. Cell Biol.* **38**, 81–89 (2016).
 33. Wilson, D. B. *et al.* Immunogenicity. I. Use of peptide libraries to identify epitopes that activate clonotypic CD4+ T cells and induce T cell responses to native peptide ligands. *J. Immunol.* **163**, 6424–34 (1999).
 34. Farlow, J. *et al.* Formation of targeted monovalent quantum dots by steric exclusion. *Nat. Methods* **10**, 1203–1205 (2013).

35. Schmid, E. M., Richmond, D. L. & Fletcher, D. A. *Reconstitution of proteins on electroformed giant unilamellar vesicles. Methods in Cell Biology* **128**, (Elsevier Ltd, 2015).
36. Stuurman, N., Edelstein, A., Amodaj, N., Hoover, K. & Vale, R. Computer control of microscopes using manager. *Current Protocols in Molecular Biology* **CHAPTER**, Unit14.20 (2010).
37. Schindelin, J. *et al.* Fiji: an open-source platform for biological-image analysis. *Nat. Methods* **9**, 676–82 (2012).

CHAPTER 3

Tight nanoscale clustering of Fc γ -receptors using DNA origami promotes phagocytosis

Nadja Kern^{1,2}, Rui Dong^{1,2}, Shawn Douglas¹, Ronald D. Vale^{1,2,3*} and Meghan A. Morrissey^{1,4,5*}

¹ Department of Cellular and Molecular Pharmacology, University of California San Francisco, San Francisco, CA 94158; ² Howard Hughes Medical Institute, University of California San Francisco, San Francisco, CA 94158; ³ Howard Hughes Medical Institute Janelia Research Campus, Ashburn, VA 20147; ⁴ Department of Molecular, Cellular and Developmental Biology, University of California Santa Barbara, CA 93106

*Corresponding Author

⁵Lead contact

3.1 Abstract

Macrophages destroy pathogens and diseased cells through $Fc\gamma$ receptor ($Fc\gamma R$)-driven phagocytosis of antibody-opsonized targets. Phagocytosis requires activation of multiple $Fc\gamma R$ s, but the mechanism controlling the threshold for response is unclear. We developed a DNA origami-based engulfment system that allows precise nanoscale control of the number and spacing of ligands. When the number of ligands remains constant, reducing ligand spacing from 17.5 nm to 7 nm potently enhances engulfment, primarily by increasing efficiency of the engulfment-initiation process. Tighter ligand clustering increases receptor phosphorylation, as well as proximal downstream signals. Increasing the number of signaling domains recruited to a single ligand-receptor complex was not sufficient to recapitulate this effect, indicating that clustering of multiple receptors is required. Our results suggest that macrophages use information about local ligand densities to make critical engulfment decisions, which has implications for the mechanism of antibody-mediated phagocytosis and the design of immunotherapies.

3.2 Introduction

Immune cells eliminate pathogens and diseased cells while limiting damage to healthy cells. Macrophages, professional phagocytes and key effectors of the innate immune system, play an important role in this process by engulfing opsonized targets bearing 'eat me' signals. One of the most common 'eat me' signals is the immunoglobulin G (IgG) antibody, which can bind foreign proteins on infected cells or pathogens. IgG is recognized by Fc γ receptors (Fc γ R) in macrophages that drive antibody-dependent cellular phagocytosis (ADCP) ¹⁻³. ADCP is a key mechanism of action for several cancer immunotherapies including rituximab, trastuzumab, and cetuximab ⁴⁻⁸. Exploring the design parameters of effective antibodies could provide valuable insight into the molecular mechanisms driving ADCP.

Activation of multiple Fc γ Rs is required for a macrophage to engulf a three-dimensional target. Fc γ R-IgG must be present across the entire target to drive progressive closure of the phagocytic cup that surrounds the target ⁹. In addition, a critical antibody threshold across an entire target dictates an all-or-none engulfment response by the macrophage ¹⁰. Although the mechanism of this thresholded response remains unclear, receptor clustering plays a role in regulating digital responses in other immune cells ¹¹⁻¹⁶. Fc γ R clustering may also regulate phagocytosis ¹⁷. High resolution imaging of macrophages has demonstrated that IgG-bound Fc γ Rs form clusters (resolution of >100 nm) within the plasma membrane ¹⁸⁻²⁰. These small clusters, which recruit downstream effector proteins such as Syk-kinase and phosphoinositide 3-kinase, eventually coalesce into larger micron-scale patches as they migrate towards the center of the cell-target synapse ¹⁸⁻²¹.

Prior observational studies could not decouple ligand clustering from other parameters, such as ligand number or receptor mobility. As a result, we do not have a clear picture of how ligand

number or molecular spacing regulate signal activation. To directly assess such questions, we have developed a reconstituted system that utilizes DNA origami to manipulate ligand patterns on a single-molecule level with nanometer resolution. We found that tightly spaced ligands strongly enhanced phagocytosis compared to the same number of more dispersed ligands. Through manipulating the number and spacing of ligands on individual origami pegboards, we found that 8 or more ligands per cluster maximized Fc γ R-driven engulfment, and that macrophages preferentially engulfed targets that had receptor-ligand clusters spaced ≤ 7 nm apart. We demonstrated that tight ligand clustering enhanced receptor phosphorylation, and the generation of PIP $_3$ and actin filaments—critical downstream signaling molecules—at the phagocytic synapse. Together, our results suggest that the nanoscale clustering of receptors may allow macrophages to discriminate between lower density background stimuli and the higher density of ligands on opsonized targets. These results have implications for the design of immunotherapies that involve manipulating Fc γ R-driven engulfment.

3.3 Results

Developing a DNA-based chimeric antigen receptor to study phagocytosis

To study how isolated biochemical and biophysical ligand parameters affect engulfment, we sought to develop a well-defined and tunable engulfment system. Our lab previously developed a synthetic T cell signaling system, in which we replaced the receptor-ligand interaction (TCR-pMHC) with complimentary DNA oligos²². We applied a similar DNA-based synthetic chimeric antigen receptor to study engulfment signaling in macrophages. In our DNA-CAR γ receptor, we replaced the native extracellular ligand binding domain of the Fc γ receptor with an extracellular SNAP-tag that covalently binds a benzyl-guanine-labeled single-stranded DNA (ssDNA) [receptor DNA; Figure 1a;²³]. The SNAP-tag was then joined to the CD86 transmembrane domain followed

by the intracellular signaling domain of the FcR γ chain³. We expressed the DNA-CAR γ in the macrophage-like cell line RAW264.7 and the monocyte-like cell line THP-1.

As an engulfment target, we used silica beads coated with a supported lipid bilayer to mimic the surface of a target cell. The beads were functionalized with biotinylated ssDNA (ligand DNA) containing a sequence complementary to the receptor DNA via biotin-neutravidin interactions (Figure 1a). We used a ligand DNA strand that has 13 complementary base pairs to the receptor DNA, which we chose because the receptor-ligand dwell time (~ 24 sec²²) was comparable to the dwell time of IgG-Fc γ R interactions (~ 30 -150 sec²⁴).

To test whether this synthetic system can drive specific engulfment of ligand-functionalized silica beads, we used confocal microscopy to measure the number of beads that were engulfed by each cell (Figure 1b, c). The DNA-CAR γ drove specific engulfment of DNA-bound beads in both RAW264.7 and THP-1 cells (Figure 1c, S1). The extent of engulfment was similar to IgG-coated beads, and the ligand density required for robust phagocytosis was also comparable to IgG [Figure 1d, S1;^{25,26}]. As a control, we tested a variant of the DNA-CAR that lacked the intracellular domain of the FcR γ chain (DNA-CAR_{adhesion}). Cells expressing the DNA-CAR_{adhesion} failed to induce engulfment of DNA-functionalized beads (Figure 1c), demonstrating that this process depends upon the signaling domain of the Fc γ receptor. Together, these data show that the DNA-CAR γ can drive engulfment of targets in a ligand- and Fc γ R-specific manner.

DNA origami pegboards activate DNA-CAR γ macrophages

DNA origami technology provides the ability to easily build three-dimensional objects that present ssDNA oligonucleotides with defined nanometer-level spatial organization^{15,27-30}. We used DNA origami to manipulate the spatial distribution of DNA-CAR γ ligands in order to determine how

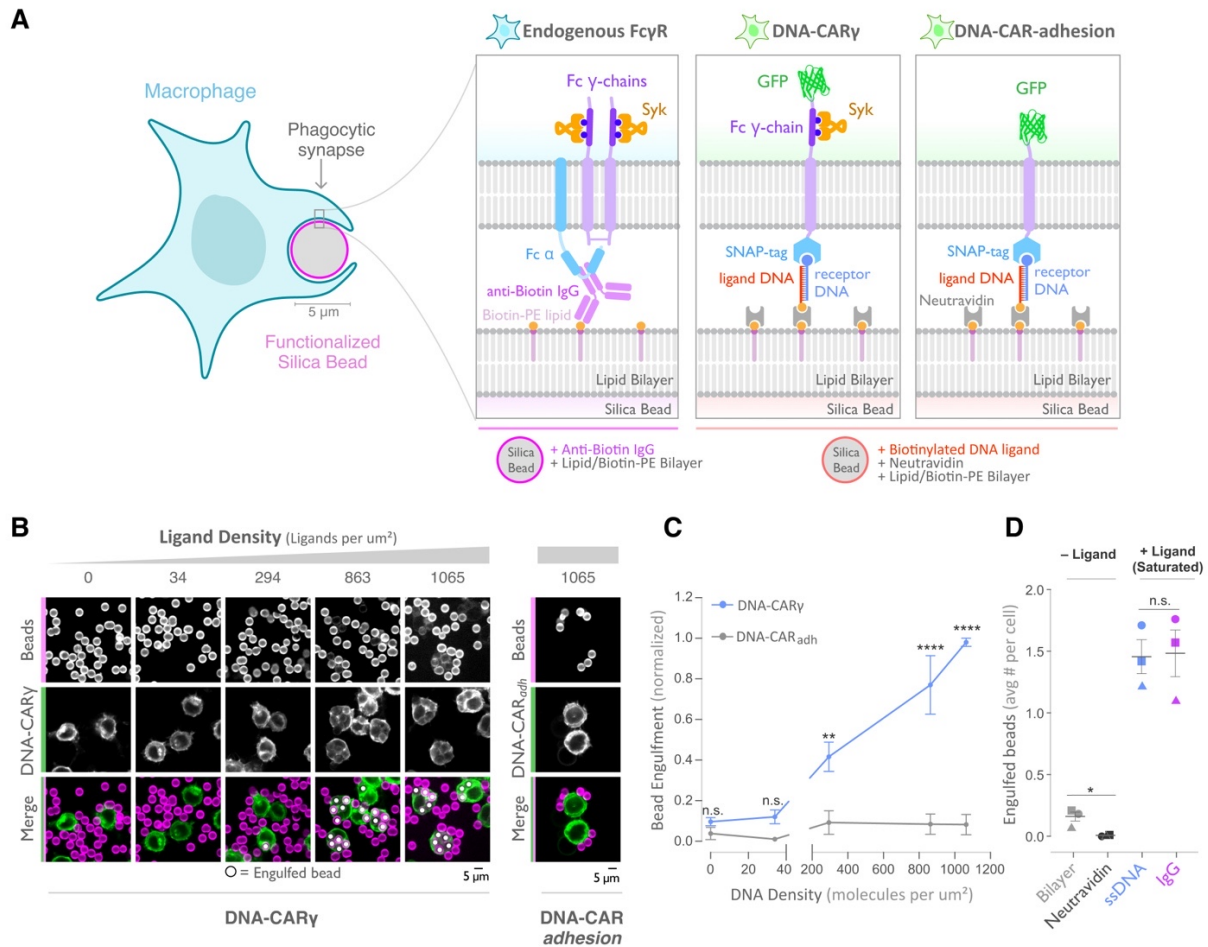


Figure 3.1: A DNA-based system for controlling engulfment

(A) Schematic shows the endogenous (left box) and DNA-based (middle and right boxes) engulfment systems. Engulfment via endogenous Fc γ R_s (left box) is induced through anti-biotin IgG bound to 1-oleoyl-2-(12-biotinyl(aminododecanoyl))-sn-glycero-3-phosphoethanolamine (biotin-PE) lipids incorporated into the bilayer surrounding the silica bead targets. Engulfment induced via the DNA-based system uses chimeric antigen receptors (CAR) expressed in the macrophage and biotinylated ligand DNA that is bound to the lipid bilayer surrounding the silica bead. The DNA-CAR γ (middle box) consists of a ssDNA (receptor DNA) covalently attached to an extracellular SNAP-tag fused to a CD86 transmembrane domain, the intracellular domain of the FcR γ chain, and a fluorescent tag. The DNA-CAR_{adhesion} (right box) is identical but lacks the signaling FcR γ chain. (B) Example images depicting the engulfment assay. Silica beads were coated with a supported lipid bilayer (magenta) and functionalized with neutravidin and the indicated density of ligand DNA (Figure S1a). The functionalized beads were added to RAW264.7 macrophages expressing either the DNA-CAR γ or the DNA-CAR_{adhesion} (green) and fixed after 45 min. The average number of beads engulfed per macrophage was assessed by confocal microscopy. Scale bar denotes 5 μm here and in all subsequent figures. Internalized beads are denoted with a white sphere in the merged images. (C) The number of beads engulfed per cell for DNA-CAR γ (blue) or DNA-CAR_{adhesion} (grey) macrophages was normalized to the maximum bead eating observed in each replicate. Dots and error bars denote the mean \pm SEM of three independent replicates ($n \geq 100$ cells analyzed per experiment). (D) DNA-CAR γ expressing macrophages were incubated with bilayer-coated beads (grey) functionalized with anti-biotin IgG (magenta), neutravidin (black), or neutravidin and saturating amounts of ssDNA (blue). The average number of beads engulfed per cell was assessed. Full data representing the fraction of macrophages

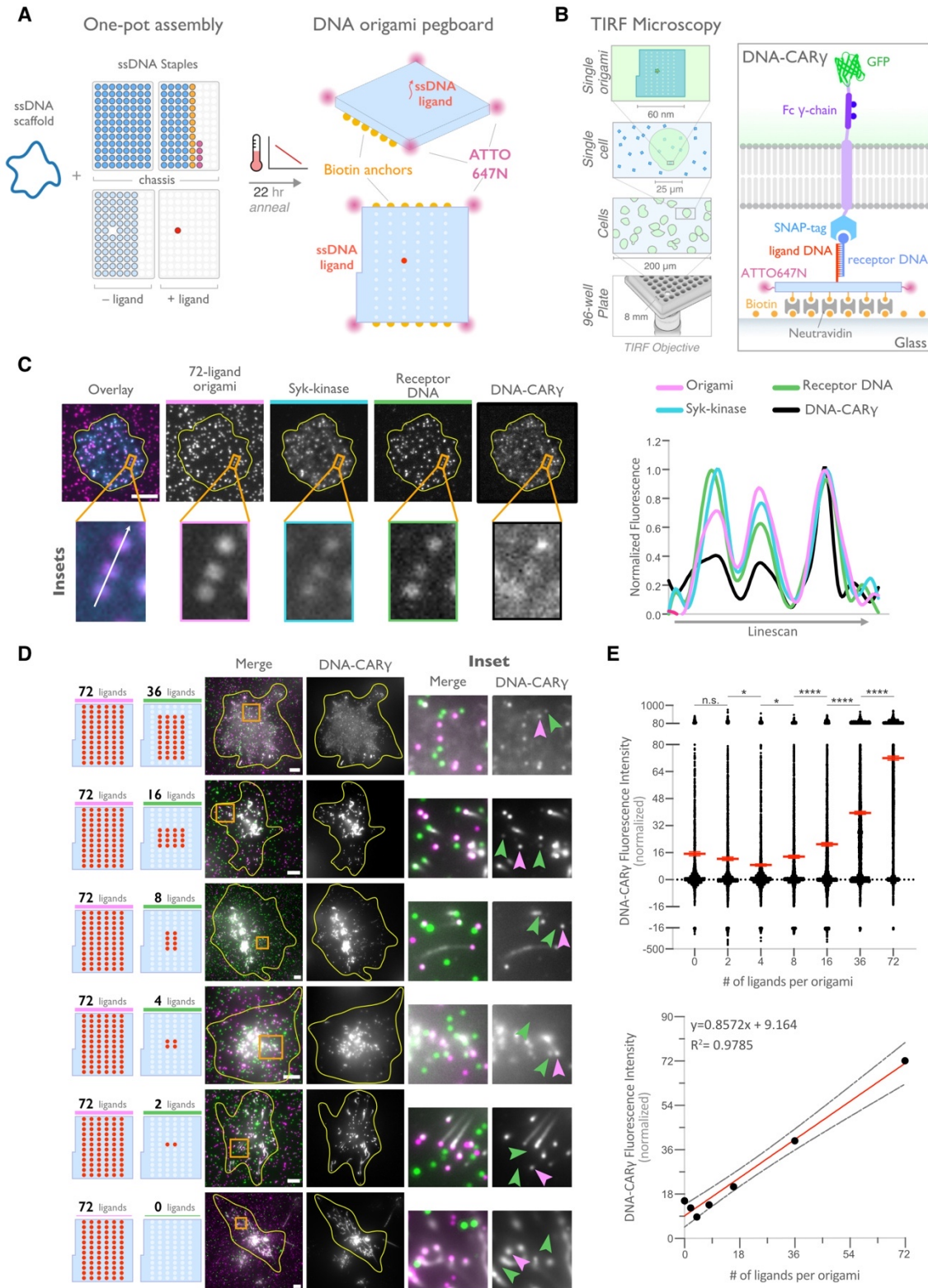
engulfing specific numbers of IgG or ssDNA beads is shown in figure S1. Each data point represents the mean of an independent experiment, denoted by symbol shape, and bars denote the mean \pm SEM. n.s. denotes $p > 0.05$, * indicates $p < 0.05$, ** indicates $p < 0.005$ and **** indicates $p < 0.0001$ by a multiple t-test comparison corrected for multiple comparisons using the Holm-Sidak method (C) or Student's T-test (D).

nanoscale ligand spacing affects engulfment. We used a recently developed two-tiered DNA origami pegboard that encompasses a total of 72 ssDNA positions spaced 7 nm and 3.5 nm apart in the x and y dimensions, respectively (Figure 2a, S2). Each of the 72 ligand positions can be manipulated independently, allowing for full control over the ligand at each position (Figure S2). The DNA origami pegboard also contains fluorophores at each of its four corners to allow for visualization, and 12 biotin-modified oligos on the bottom half of the pegboard to attach it to a neutravidin-containing supported lipid bilayer or glass coverslip (Figure 2a, b, S2).

To determine if the DNA origami pegboards could successfully activate signaling, we first tested whether receptors were recruited to the origami pegboard in a ligand-dependent manner. Using TIRF microscopy, we quantified the fluorescence intensity of the recruited GFP-tagged DNA-CAR γ receptor to origami pegboards presenting 0, 2, 4, 16, 36 or 72 ligands (Figure 2b-e). Using signal from the 72 ligand (72L) origami pegboard as an internal intensity standard of brightness, and thus correcting for differences in illumination between wells, we found that the average fluorescence intensity correlated with the number of ligands presented by individual origami pegboards (Figure 2d, e). In addition, we measured Syk recruitment to individual DNA origami pegboards and found that Syk intensity also increased as a function of the number of ligands present on each origami pegboard (Figure 2c, S3). These results confirmed that our DNA origami system provides a platform that allows quantitative receptor recruitment and the analysis of downstream signaling pathways.

Nanoscale clustering of ligand enhances phagocytosis

Fc γ receptors cluster upon ligand binding, but the functional importance of such clustering for phagocytosis has not been directly addressed, and whether a critical density of receptor-ligand pairs is necessary to initiate Fc γ R signaling is unclear^{18-21,31}. To address these questions, we varied the size of ligand clusters by designing DNA origami pegboards presenting 2-36 ligands.



has 72 positions spaced 7 nm and 3.5 nm apart in the x and y dimensions, which can be modified to expose a single-stranded ligand DNA (red) or no ligand (light blue). A fluorophore is attached at each corner of the pegboard for visualization (pink). The bottom tier of the pegboard displays 12 biotin molecules (yellow) used to attach the origami to neutravidin-coated surfaces. Full representation of the DNA origami pegboard assembly is shown in figure S2. (B) Schematic portraying the TIRF microscopy setup used to image THP-1 cells interacting with origami pegboards functionalized to glass coverslips in (C) and (D) (left). On the right is a zoomed-in side view of an origami pegboard functionalized to a biotin (yellow) and neutravidin (grey) functionalized glass coverslip and interacting with a single DNA-CAR γ receptor. (C) TIRF microscopy images of THP-1 cells show that the DNA-CAR γ (BFP; 5th panel; black in linescan), the receptor DNA bound to the DNA-CAR γ (Cy5; 4th panel; green in linescan), and Syk (mNeonGreen; 3rd panel; cyan in merge and linescan) are recruited to individual 72-ligand origami pegboards (Atto-647; 2nd panel; magenta in merge and linescan). Each diffraction limited magenta spot represents an origami pegboard. The top panels show a single cell (outlined in yellow), and the bottom insets (orange box in top image) show three origami pegboards at higher magnification. The linescan (right, area denoted with a white arrow in merged inset) shows the fluorescence intensity of each of these channels. Intensity was normalized so that 1 is the highest observed intensity and 0 is background for each channel. (D) TIRF microscopy images show DNA-CAR γ expressing THP1s interacting with 72-ligand origami pegboards (pink) and origami pegboards presenting the indicated number of ligands (pegboards labeled in green). Left schematics represent origami pegboard setups for each row of images where red dots denote the presence of a ligand DNA. Middle images depict a single macrophage (outlined in yellow), and right images show the area indicated with an orange box on the left. Examples of DNA-CAR γ -mNeonGreen (grey) recruitment to individual origami pegboards is marked by pink (72L origami pegboard) and green (origami pegboard with the indicated ligand number) arrowheads (right). (E) Quantification of experiment shown in (D). Top graph shows the DNA-CAR γ intensity at the indicated origami pegboard type normalized to the average DNA-CAR γ intensity at 72L origami pegboards in the same well. Each dot represents one origami pegboard and red lines denote the mean \pm SEM of pooled data from three separate replicates. n.s. denotes $p > 0.05$, * indicates $p < 0.05$, and **** indicates $p < 0.0001$ by an ordinary one-way ANOVA with Holm-Sidak's multiple comparison test. A linear regression fit (bottom) of the average fluorescence intensities of each of the origami pegboards suggests that the mean DNA-CAR γ fluorescent intensities are linearly proportional to the number of ligands per DNA origami pegboard. The black dots represent the mean normalized DNA-CAR γ intensity, the red line denotes the linear regression fit, and the grey lines show the 95% confidence intervals.

To ensure a constant total number of ligands and origami pegboards on each bead, we mixed the signaling origami pegboards with 0-ligand “blank” origami pegboards in appropriate ratios (Figure 3a). We confirmed that the surface concentration of origami pegboards on the beads was comparable using fluorescence microscopy (Figure S4). We found that increasing the number of ligands per cluster increased engulfment, but that engulfment plateaued at a cluster size of 8 ligands (Figure 3b). We confirmed that the observed engulfment phenotype was both ligand, receptor, and Fc γ R signaling dependent (Figure 3c, d). Together, these data reveal that Fc γ receptor clustering strongly enhances engulfment, up to a cluster size of 8 ligands.

Spatial organization of ligands in nanoclusters regulates engulfment

Next, we examined whether distance between individual receptor-ligand molecules within a signaling cluster impacts engulfment. For this experiment, we varied the spacing of 4 ligands on the origami pegboard. The 4-ligand tight origami (4T) contains 4 ligands clustered at the center of the pegboard (7 nm by 3.5 nm square), the medium origami (4M) has ligands spaced 21 nm by 17.5 nm apart, and the spread origami (4S) has 4 ligands positioned at the four corners of the pegboard (35 nm by 38.5 nm square) (Figure 4a). We found that the efficiency of macrophage engulfment was approximately 2-fold higher for the 4T functionalized beads when compared to the 4M or 4S beads (Figure 4a). We confirmed via fluorescence microscopy that the concentration of origami pegboards on the surface was similar, and therefore ligand numbers on the beads were similar (Figure S5). DNA CAR constructs that have the FcR γ and α chain transmembrane domains in place of the CD86 transmembrane domain and human THP-1 cells expressing the DNA-CAR γ showed the same ligand spacing dependence (Figure S5). Expression of the various DNA CARs at the cell cortex was comparable, and engulfment of beads functionalized with both the 4T and the 4S origami platforms was dependent on the Fc γ R signaling domain (Figure S5).

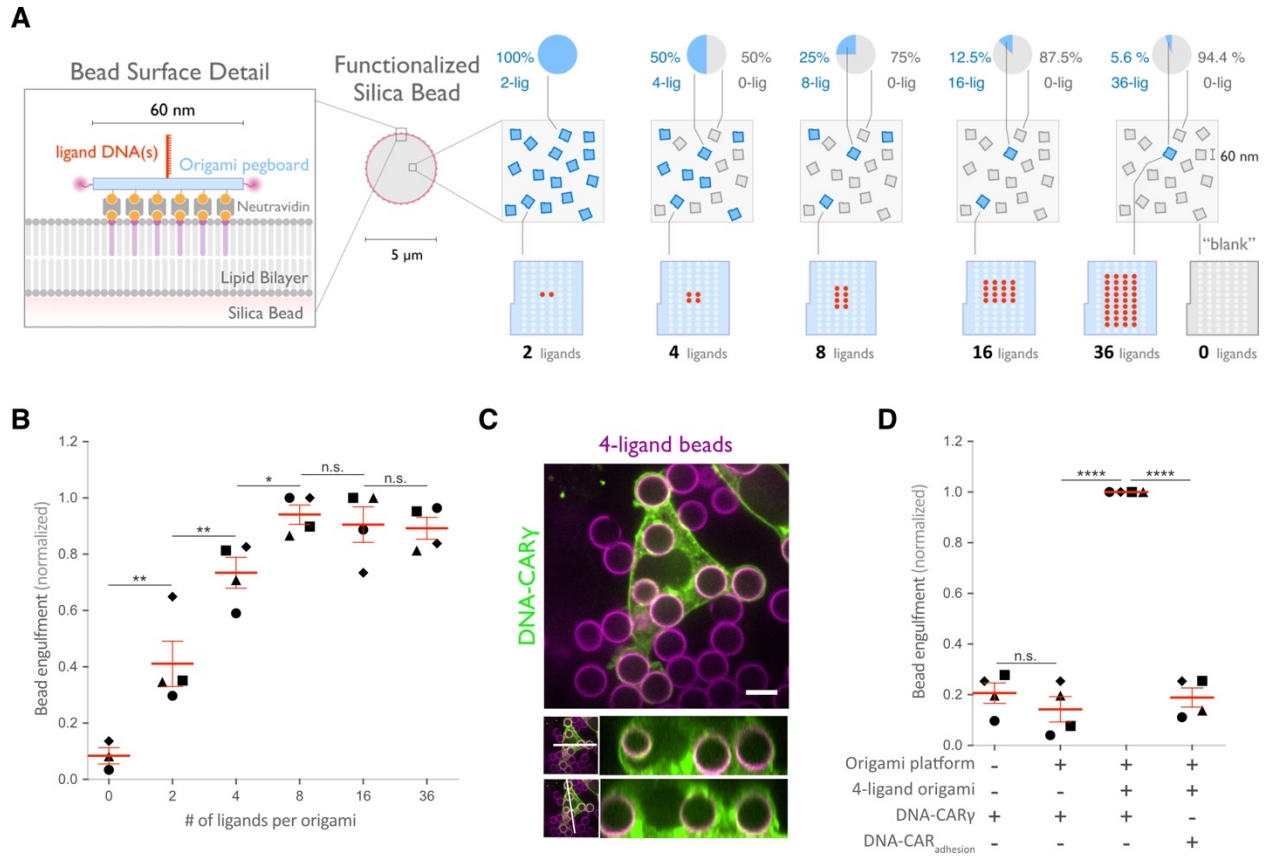


Figure 3.2: DNA origami pegboard induces ligand dependent signaling

(A) Schematic shows the DNA-origami pegboard used in this study (right) and the components used to create it using a one-pot assembly method (left, figure S2). The top of the two-tiered DNA origami pegboard has 72 positions spaced 7 nm and 3.5 nm apart in the x and y dimensions, which can be modified to expose a single-stranded ligand DNA (red) or no ligand (light blue). A fluorophore is attached at each corner of the pegboard for visualization (pink). The bottom tier of the pegboard displays 12 biotin molecules (yellow) used to attach the origami to neutravidin-coated surfaces. Full representation of the DNA origami pegboard assembly is shown in figure S2. (B) Schematic portraying the TIRF microscopy setup used to image THP-1 cells interacting with origami pegboards functionalized to glass coverslips in (C) and (D) (left). On the right is a zoomed-in side view of an origami pegboard functionalized to a biotin (yellow) and neutravidin (grey) functionalized glass coverslip and interacting with a single DNA-CAR γ receptor. (C) TIRF microscopy images of THP-1 cells show that the DNA-CAR γ (BFP; 5th panel; black in linescan), the receptor DNA bound to the DNA-CAR γ (Cy5; 4th panel; green in linescan), and Syk (mNeonGreen; 3rd panel; cyan in merge and linescan) are recruited to individual 72-ligand origami pegboards (Atto-647; 2nd panel; magenta in merge and linescan). Each diffraction limited magenta spot represents an origami pegboard. The top panels show a single cell (outlined in yellow), and the bottom insets (orange box in top image) show three origami pegboards at higher magnification. The linescan (right, area denoted with a white arrow in merged inset) shows the fluorescence intensity of each of these channels. Intensity was normalized so that 1 is the highest observed intensity and 0 is background for each channel. (D) TIRF microscopy images show DNA-CAR γ expressing THP1s interacting with 72-ligand origami pegboards (pink) and origami pegboards presenting the indicated number of ligands (pegboards labeled in green). Left schematics represent origami pegboard setups for each row of images where red dots denote the presence of a ligand DNA. Middle images depict a single macrophage (outlined in yellow), and right images show the area indicated with an

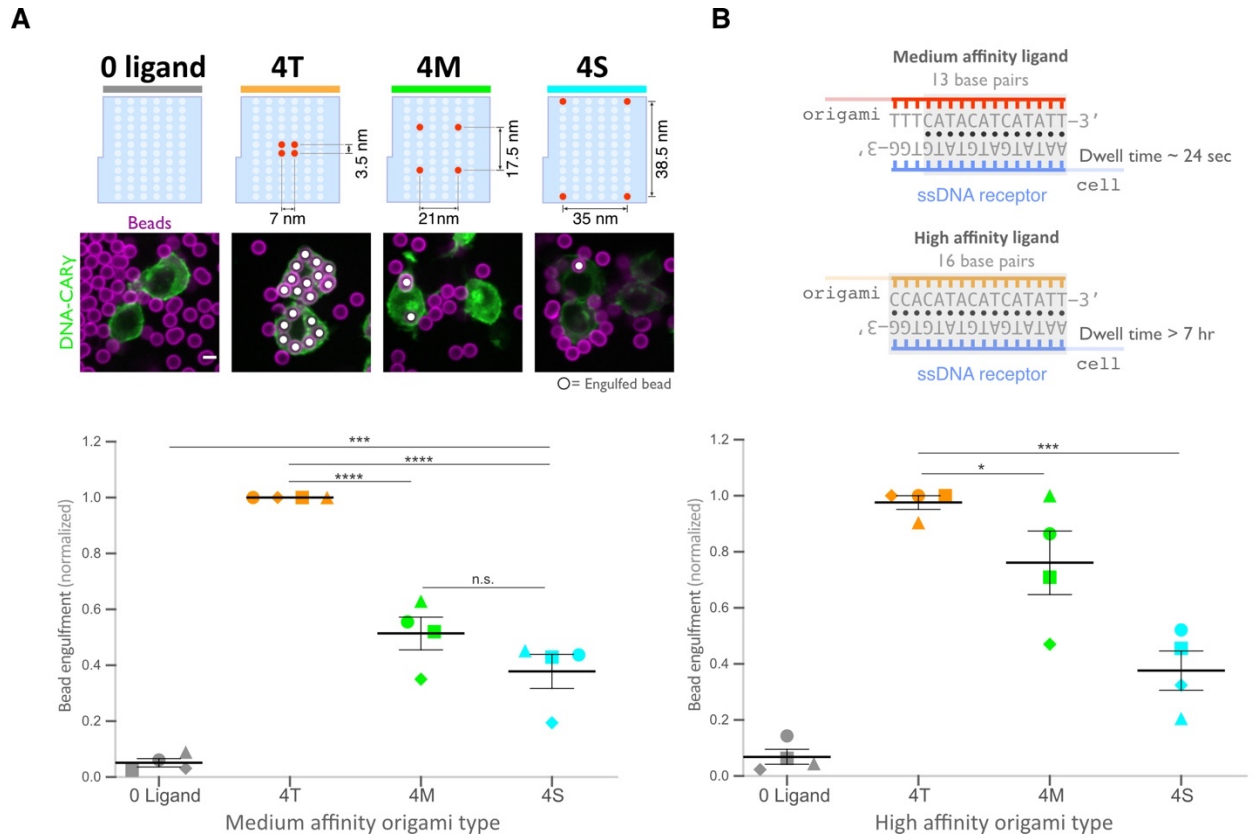
orange box on the left. Examples of DNA-CAR γ -mNeonGreen (grey) recruitment to individual origami pegboards is marked by pink (72L origami pegboard) and green (origami pegboard with the indicated ligand number) arrowheads (right). (E) Quantification of experiment shown in (D). Top graph shows the DNA-CAR γ intensity at the indicated origami pegboard type normalized to the average DNA-CAR γ intensity at 72L origami pegboards in the same well. Each dot represents one origami pegboard and red lines denote the mean \pm SEM of pooled data from three separate replicates. n.s. denotes $p > 0.05$, * indicates $p < 0.05$, and **** indicates $p < 0.0001$ by an ordinary one-way ANOVA with Holm-Sidak's multiple comparison test. A linear regression fit (bottom) of the average fluorescence intensities of each of the origami pegboards suggests that the mean DNA-CAR γ fluorescent intensities are linearly proportional to the number of ligands per DNA origami pegboard. The black dots represent the mean normalized DNA-CAR γ intensity, the red line denotes the linear regression fit, and the grey lines show the 95% confidence intervals.

Together, these results demonstrate that macrophages preferentially engulf targets with tighter ligand clusters.

Tightly spaced ligands could potentially increase phagocytosis by enhancing the avidity of receptor-ligand interactions within each cluster. Such a hypothesis would predict that tightly spaced ligands increase DNA-CAR γ -BFP occupancy at the phagocytic cup. However, when we measured the total fluorescence intensity of receptors at the phagocytic cup, we did not detect a difference in DNA-CAR γ -BFP recruitment to 4T and 4S beads (Figure 6a, b). However, to eliminate any potential contribution of avidity, we created 4T and 4S origami pegboards with very high-affinity 16mer DNA ligands that are predicted to dissociate on a time scale of >7 hr²² (Figure 4b). Using these 16mer high-affinity ligands, we found that 4T origami beads were still preferentially engulfed over 4M or 4S origami beads (Figure 4b, S5). These results suggest that an avidity effect is not the cause of the preferential engulfment of targets having tightly spaced ligands.

Tight ligand spacing enhances engulfment initiation and downstream signaling

We next determined how ligand spacing affects the kinetics of engulfment. Using data from live-cell imaging, we subdivided the engulfment process into three steps: bead binding, engulfment initiation, and engulfment completion (Figure 5a, Supplemental movie 1). To compare engulfment dynamics mediated by 4T and 4S origami pegboards in the same experiment, we labeled each pegboard type with a different colored fluorophore, functionalized a set of beads with each type of pegboard, and added both bead types to macrophages at the same time (Figure 5b, Supplemental movie 2). Macrophages interacted with beads functionalized with the 4T and 4S pegboards with comparable frequency ($46 \pm 7\%$ total bead-cell contacts vs. $54 \pm 7\%$ total bead-cell contacts respectively). However, the probability of engulfment initiation was significantly higher for the 4T ($95 \pm 5\%$ of bead contacts) versus 4S ($61 \pm 9\%$ of bead contacts) beads, and



the probability that initiation events resulted in successful completion of engulfment was higher for 4T ($69 \pm 9\%$ of initiation events) versus 4S ($39 \pm 11\%$ of initiation events) beads (Figure 5a). Initiation events that failed to induce successful engulfment either stalled after progressing partially over the bead or retracted the extended membrane back to the base of the bead. In addition, for beads that were engulfed, the time from contact to engulfment initiation was ~ 300 sec longer for beads functionalized with 4S origami pegboards than beads containing 4T origami pegboards (Figure 5c). However, once initiated, the time from initiation to completion of engulfment did not differ significantly for beads coated with 4T or 4S origami (Figure 5d). Overall, $66 \pm 8\%$ of 4T bead contacts resulted in successful engulfment compared to $24\% \pm 8\%$ for 4S beads (Figure 5e). The DNA-CAR_{adhesion} macrophages rarely met the initiation criteria, suggesting that active signaling from the Fc γ R is required (Figure S6). Together, these data reveal that tighter spacing between ligands within a cluster enhances the probability and kinetics of initiating engulfment, as well as the overall success frequency of completing engulfment, but does not affect the rate of phagosome closure once initiated.

Tightly spaced ligands enhance receptor phosphorylation

We next determined how the 4T or 4S origami pegboards affect signaling downstream of Fc γ R binding by measuring fold enrichment at the phagocytic cup compared to the rest of the cortex of 1) a marker for receptor phosphorylation (the tandem SH2 domains of Syk)^{32,33}, 2) PIP₃ (via recruitment of the PIP₃ binding protein Akt-PH-GFP), and 3) filamentous actin (measured by rhodamine-Phalloidin binding, Figure 6a, b). We found that 4T phagocytic cups recruited more tSH2-Syk than the 4S beads, indicating an increase in receptor phosphorylation by nano-clustered ligands. Generation of PIP₃ and actin filaments at the phagocytic cup also increased at 4T relative to 4S synapses (Figure 6b). This differential recruitment of downstream signaling molecules to 4T versus 4S origami beads was most apparent in early and mid-stage phagocytic cups; late-stage cups showed only a slightly significant difference in tSH2-Syk recruitment and no

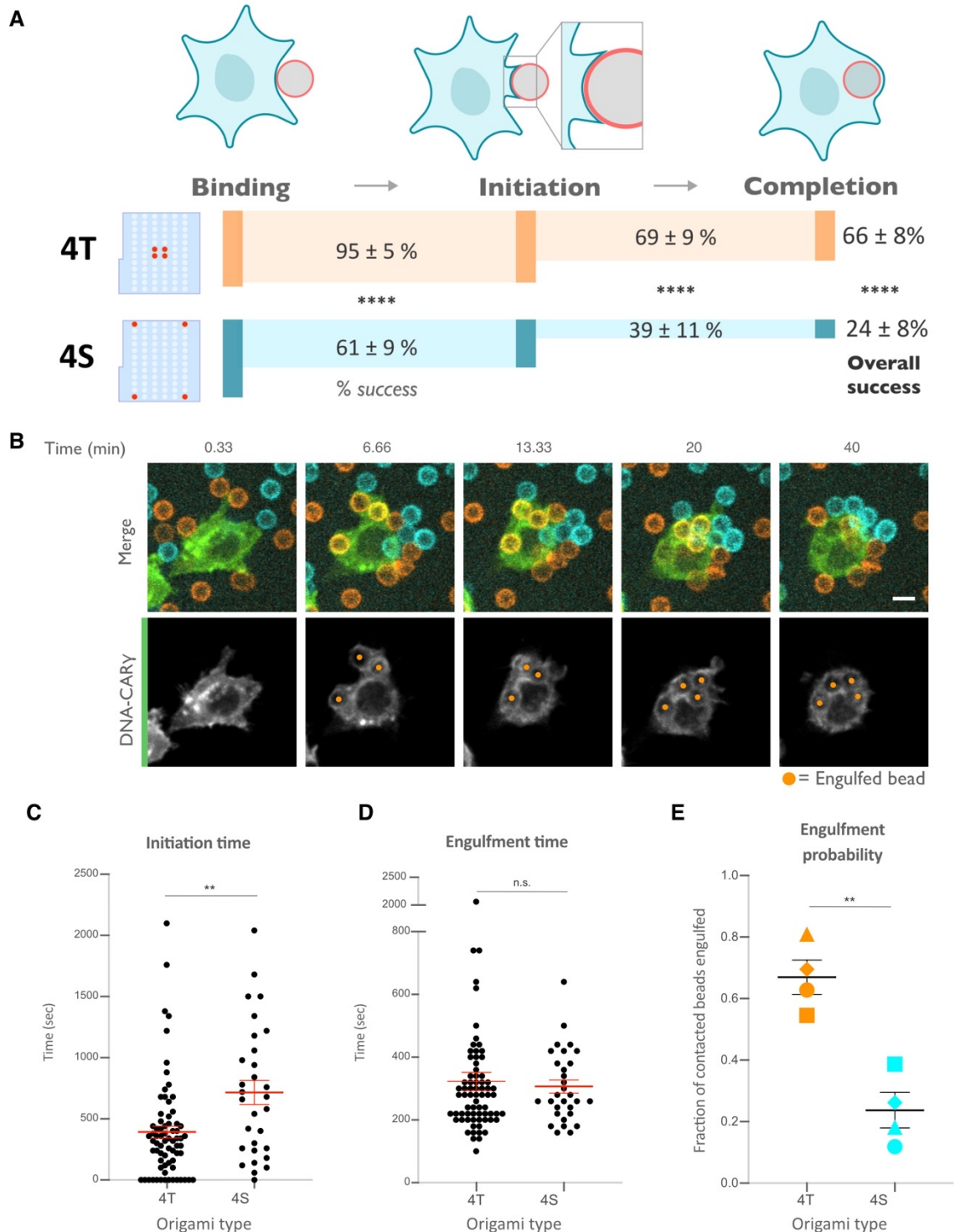


Figure 3.5: Nanoscale ligand clustering controls engulfment initiation

(A) Schematic portraying origami pegboards used to analyze the steps in the engulfment process quantified in (C), (D), and (E). Bead binding is defined as the first frame the macrophage contacts a bead; initiation is the first frame in which the macrophage membrane has begun to extend around the bead, and completion is defined as full internalization. The macrophage membrane was visualized using the DNA CARY, which was present throughout the cell cortex. The % of beads that progress to the next stage of engulfment (% success) is indicated for 4T (orange, origami labeled with Atto550N) and 4S (cyan, origami labeled with

Atto647N) beads. **** denotes $p < 0.0001$ as determined by Fischer's exact test. (B) Still images from a confocal microscopy timelapse showing the macrophage (green) interacting with both the 4T origami pegboard functionalized beads (orange) and the 4S origami pegboard functionalized beads (cyan), but preferentially engulfing the 4T origami pegboard functionalized beads. In the bottom panel (DNA-CAR γ channel), engulfed beads have been indicated by a sphere colored to match its corresponding origami type. (C) Graph depicts quantification of the time from bead contact to engulfment initiation for all beads that were successfully engulfed. Each dot represents one bead with red lines denoting mean \pm SEM. (D) Graph depicts the time from engulfment initiation to completion. Each dot represents one bead with red lines denoting mean \pm SEM. (E) Graph shows the fraction of contacted 4T and 4S beads engulfed (orange and cyan, respectively) by the macrophages. Data represent quantification from 4 independent experiments, denoted by symbol shape, and bars denote the mean \pm SEM. n.s. denotes $p > 0.05$ and ** indicates $p < 0.005$ by Student's T-test comparing the 4T and 4S functionalized beads (C-E).

significant differences in generation of PIP₃ or actin filaments (Figure S7). Together, these data demonstrate that nanoscale ligand spacing affects early downstream signaling events involved in phagocytic cup formation.

We next sought to understand why distributing ligands into tight clusters enhanced receptor phosphorylation and engulfment. One possibility is that the clustering of four complete receptors is needed to drive segregation of the inhibitory phosphatase CD45 and allow sustained phosphorylation of the Fc γ R Immune Receptor Tyrosine-based Activation Motif (ITAM)^{17,26,34,35}. Alternatively, the 4-ligand cluster may be needed to obtain a critical intracellular concentration of Fc γ R ITAM signaling domains. To test for the latter possibility, we designed a synthetic receptor (DNA-CAR-4x γ) that contains four repeats of the intracellular domain of the DNA-CAR γ connected by a GGSG linker between each repeat (Figure 6c). We confirmed that this DNA-CAR-4x γ receptor in which the 3 C-terminal ITAM domains were mutated to phenylalanines (Figure 6c, d). Keeping the number of intracellular ITAMs constant, we compared the engulfment efficiency mediated by two different receptors: 1) the DNA-CAR-4x γ that interacted with beads functionalized with 1-ligand origami, and 2) the DNA-CAR-1x γ -3x Δ ITAM that interacted with beads coated with equivalent amounts of 4T origami (Figure 6c). While the DNA-CAR-1x γ -3x Δ ITAM-expressing macrophages engulfed 4T origami beads, the DNA-CAR-4x γ macrophages failed to engulf the high-affinity 1-ligand origami beads (Figure 6d, Figure S7). To ensure that all four ITAM domains on the DNA-CAR-4x γ were signaling competent, we designed two additional DNA CARs which placed the functional ITAM at the second and fourth position (Figure S7). These receptors were able to induce phagocytosis of 4T origami beads, indicating that the DNA-CAR-4x γ likely contains 4 functional ITAMs. Collectively, these results indicate that the tight clustering of multiple receptors is necessary for engulfment and increasing the number of intracellular signaling modules on a single receptor is not sufficient to surpass the threshold for activation of

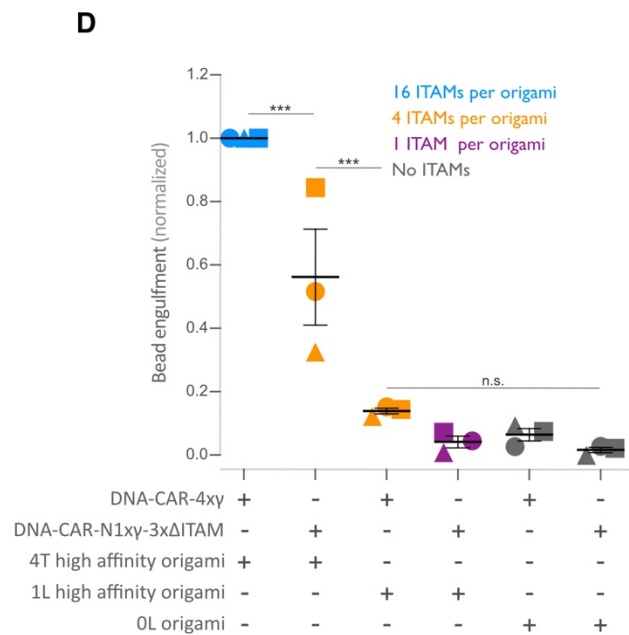
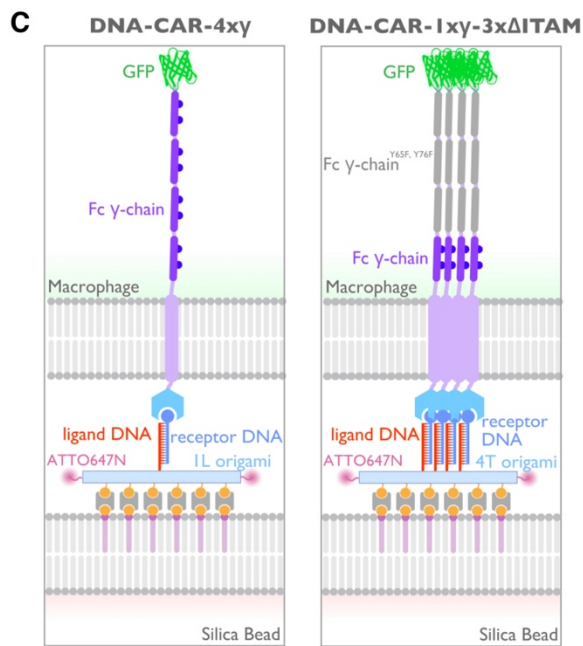
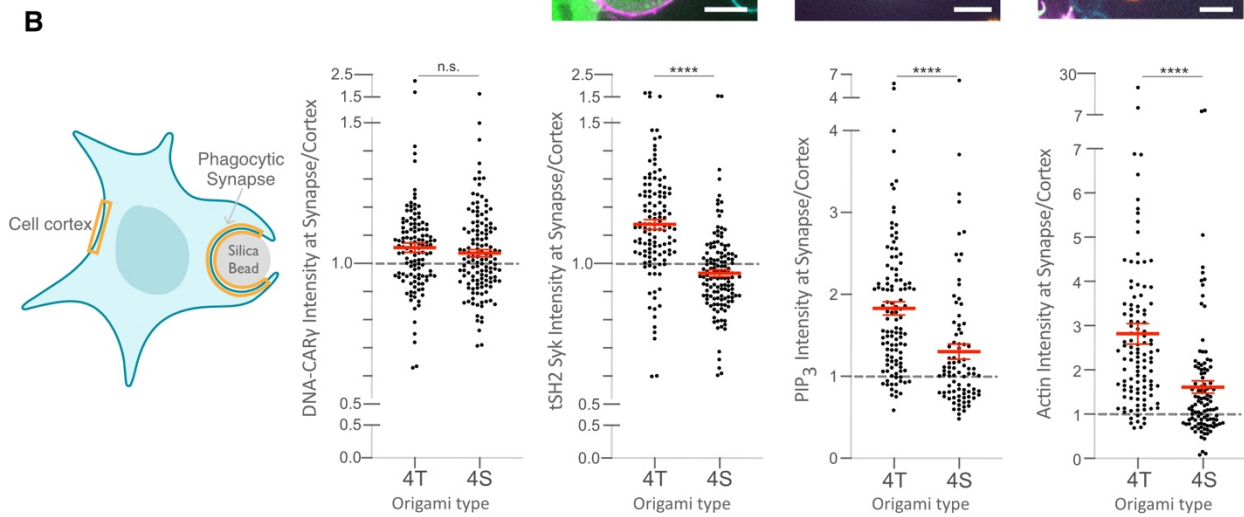
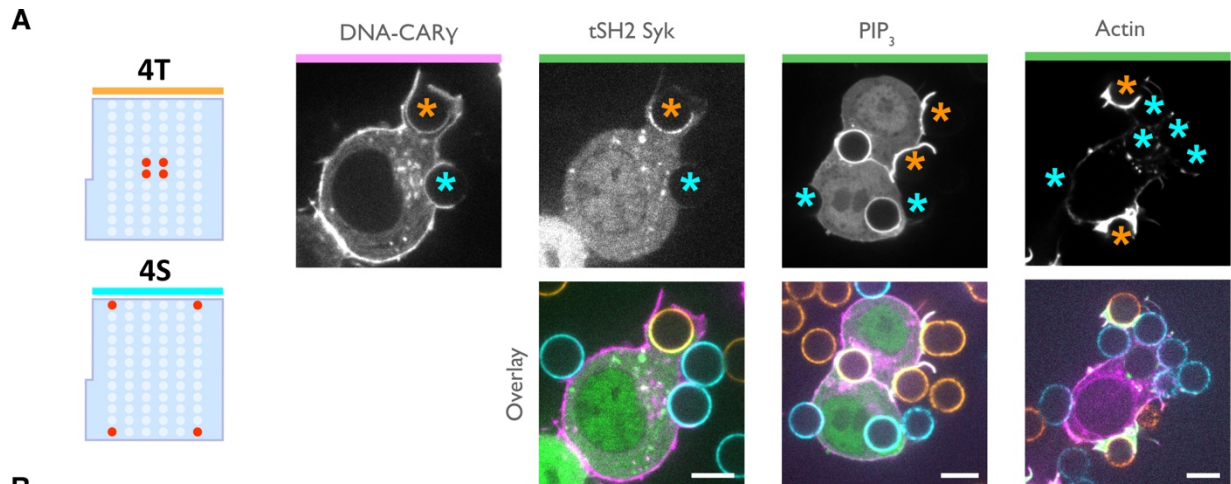


Figure 3.6: Nanoscale ligand spacing controls receptor activation

(A) Beads were functionalized with 4T (orange) or 4S (cyan) origami pegboards at equal amounts, added to macrophages expressing the DNA-CAR γ (magenta) and the indicated signaling reporter protein (green; greyscale on top). Phagocytic synapses were imaged via confocal microscopy. Asterisks indicate whether a 4T (orange) or a 4S (cyan) bead is at the indicated phagocytic synapse in the upper panel. (B) Schematic (left) depicts the areas measured from images shown in (A) to quantify the fluorescence intensity (yellow outlines). Each phagocytic synapse measurement was normalized to the fluorescence intensity of the cell cortex at the same z-plane. Graphs (right) depict the ratio of fluorescence at 4T or 4S functionalized bead synapses to the cortex for the indicated reporter. Each dot represents one bead with red lines denoting mean \pm SEM. (C) Schematic portraying the CAR constructs and origami used in the experiment quantified in (D). The DNA-CAR-4x γ construct (left) consists of four repeats of the intracellular domain of the DNA-CAR γ connected by a GGSG linker. The DNA-CAR-1x γ -3x Δ ITAM (right) is identical to the DNA-CAR-4x γ except that the tyrosines composing the ITAM domains (purple circles) are mutated to phenylalanines in the three C-terminal repeats (grey). Cells expressing either of these constructs were fed beads functionalized with either high affinity 1-ligand origami pegboards (left), high affinity 4T origami pegboards (right), or 0 ligand “blank” origami pegboards (not shown), and engulfment was assessed after 45 min. (D) Graph shows the number of beads engulfed per macrophage normalized to the maximum observed eating in that replicate. Each data point represents the mean from an independent experiment, denoted by symbol shape, and bars denote the mean \pm SEM. Blue points represent a condition where 16 ITAMs are available per origami, orange points represent conditions where 4 ITAMs are available per origami, purple points represent a condition where 1 ITAM is available per origami, and grey points represent conditions where no ITAM is available. n.s. denotes $p > 0.05$, *** denotes $p < 0.0005$, and **** denotes $p < 0.00005$ as determined by the Student's T-test (B) or an Ordinary one-way ANOVA with Holm-Sidak's multiple comparison test (D).

engulfment.

3.4 Discussion

Macrophages integrate information from many Fc γ R-antibody interactions to discriminate between highly opsonized targets and background signal from soluble antibody or sparsely opsonized targets. How the macrophage integrates signals from multiple Fc γ R binding events to make an all-or-none engulfment response is not clear. Here, we use DNA origami nanostructures to manipulate and assess how the nanoscale spatial organization of receptor-ligand interactions modulates Fc γ R signaling and the engulfment process. We found that tight ligand clustering increases the probability of initiating phagocytosis by enhancing Fc γ R phosphorylation.

Phagocytosis requires IgG across the entire target surface to initiate local receptor activation and to 'zipper' close the phagocytic cup^{9,34}. Consistent with this zipper model, incomplete opsonization of a target surface, or micron-scale spaces between IgG patches, decreases engulfment^{9,34}. Initially suggested as an alternative to the zipper model, the trigger model proposed that engulfment occurs once a threshold number of receptors interact with IgG^{9,36,37}. While this model has largely fallen out of favor, more recent studies have found a critical IgG threshold needed to activate the final stages of phagocytosis¹⁰. Our data suggest that there may also be a nanoscale density-dependent trigger for receptor phosphorylation and downstream signaling. Taken together, these results suggest that both tight nanoscale IgG-Fc γ R clustering and a uniform distribution of IgG across the target are needed to direct signaling to 'zipper' close the phagocytic cup. Why might macrophages use this local density dependent trigger to dictate engulfment responses? Macrophages constantly encounter background "eat me" signals³⁸. This hyper-local density measurement may buffer macrophages against background stimuli and

weakly opsonized targets that are unlikely to have adjacent bound antibodies, while still robustly detecting and efficiently engulfing highly-opsonized targets.

Our findings are consistent with previous results demonstrating that Fc γ R crosslinking correlates with increased ITAM phosphorylation^{18,20,39,40}. While our data pinpoints a role for ligand spacing in regulating receptor phosphorylation, it is possible that later steps in the phagocytic signaling pathway are also directly affected by ligand spacing. The mechanism by which dense-ligand clustering promotes receptor phosphorylation remains an open question, although our data rule out a couple of models. Specifically, we demonstrate that nanoscale ligand clustering does not noticeably affect the amount of ligand-bound receptor at the phagocytic cup, and that ligand spacing continues to affect engulfment when avidity effects are diminished through the use of high affinity receptor-ligands. Collectively, these data reveal that changes in receptor binding or recruitment caused by increased avidity are unlikely to account for the increased potency of clustered ligands. Our data also exclude the possibility that receptor clustering simply increases the local intracellular concentration of Fc γ R signaling domains, as arranging Fc γ R ITAMs in tandem did not have the same effect as clustering multiple receptor-ligand interactions. However, it remains possible that the geometry of the intracellular signaling domains could be important for activating or localizing downstream signaling, and that tandem ITAMs on the same polypeptide cannot produce the same engulfment signals as ITAMs on separate parallel polypeptides.

One possible model to explain the observed ligand-density dependence of signaling involves the ordering of lipids around the Fc γ receptor. Segregated liquid-ordered and liquid-disordered membrane domains around immune receptor clusters have been reported to promote receptor phosphorylation⁴¹⁻⁴⁶. Fc γ R clusters are associated with liquid-ordered domains^{39,47,48}. Liquid-ordered domains recruit Src family kinases, which phosphorylate Fc γ Rs, while liquid-disordered

domains are enriched in the transmembrane phosphatase CD45, which dephosphorylates Fc γ Rs^{43,44}. Thus, lipid ordering could provide a mechanism that leads to receptor activation if denser receptor-ligand clusters are more efficient in nucleating or associating with ordered lipid domains.

As an alternative model, a denser cluster of ligated receptors may enhance the steric exclusion of the bulky transmembrane proteins like the phosphatases CD45 and CD148^{17,26,49}. CD45 is heavily glycosylated, making the extracellular domain 25-40 nm tall^{12,50,51}. Because of its size, CD45 is excluded from close cell-cell contacts, such as those mediated by IgG-Fc γ R, which have a dimension of 11.5 nm^{26,35,52-55}. IgG bound to antigens ≤ 10.5 nm from the target surface induces CD45 exclusion and engulfment (estimated total intermembrane distance of ≤ 22 nm²⁶). Our DNA origami structure is estimated to generate similar intermembrane spacing, consisting of hybridized receptor-ligand DNA (~ 9.4 nm), the origami pegboard (6 nm) and neutravidin (4 nm)⁵⁶. A higher receptor-ligand density constrains membrane shape fluctuations⁵⁷⁻⁵⁹, and this constraint may increase CD45 exclusion³⁵. Both the lipid ordering and the steric exclusion models predict at least a partial exclusion of the CD45 from the zone of the receptor cluster. However, the dimension of the tight cluster in particular is very small (7 by 3.5 nm) and measurement of protein concentration at this level is currently not easily achieved, even with super-resolution techniques. Overall, our results establish the molecular and spatial parameters necessary for Fc γ R activation and demonstrate that the spatial organization of IgG-Fc γ R interactions alone can affect engulfment decisions.

How does the spacing requirements for Fc γ R nanoclusters compare to other signaling systems? Engineered multivalent Fc oligomers revealed that IgE ligand geometry alters Fc ϵ receptor signaling in mast cells⁶⁰. DNA origami nanoparticles and planar nanolithography arrays have previously examined optimal inter-ligand distance for the T cell receptor, B cell receptor, NK cell

receptor CD16, death receptor Fas, and integrins^{15,61–64}. Some systems, like integrin-mediated cell adhesion, appear to have very discreet threshold requirements for ligand spacing while others, like T cell activation, appear to continuously improve with reduced intermolecular spacing^{62,64}. Our system may be more similar to the continuous improvement observed in T cell activation, as our most spaced ligands (36.5 nm) are capable of activating some phagocytosis, albeit not as potently as the 4T. Interestingly, as the intermembrane distance between T cell and target increases, the requirement for tight ligand spacing becomes more stringent⁶⁴. This suggests that IgG bound to tall antigens may be more dependent on tight nanocluster spacing than short antigens. Planar arrays have also been used to vary inter-cluster spacing, in addition to inter-ligand spacing^{34,64}. Examining the optimal inter-cluster spacing during phagosome closure may be an interesting direction for future studies.

Our study on the spatial requirements of Fc γ R activation could have implications for the design of therapeutic antibodies or chimeric antigen receptors. Antibody therapies that rely on Fc γ R engagement are used to treat cancer, autoimmune and neurodegenerative diseases^{4–8,65}. Multimerizing Fc domains, or targeting multiple antibodies to the same antigen may increase antibody potency⁶⁶. Interestingly, Rituximab, a successful anti-CD20 therapy that potently induces ADCP, has two binding sites on its target antigen⁶⁷. Selecting clustered antigens, or pharmacologically inducing antigen clustering may also increase antibody potency⁶⁸. These results suggest that oligomerization may lead to more effective therapy; however, a systematic study of the spatial parameters that affect Fc γ R activation has not been undertaken²⁶. Our data suggest that antibody engineering strategies that optimize spacing of multiple antibodies through leucine zippers, cysteine bonds, DNA hybridization^{60,63,69} or multimeric scaffolds^{70–73} could lead to stronger Fc γ R activation and potentially more effective therapies.

3.5 Materials and Methods

Cell culture

RAW264.7 macrophages were purchased from the ATCC and cultured in DMEM (Gibco, Catalog #11965–092) supplemented with 1x Penicillin-Streptomycin-L-Glutamine (Corning, Catalog #30–009 CI), 1 mM sodium pyruvate (Gibco, Catalog #11360-070) and 10% heat-inactivated fetal bovine serum (Atlanta Biologicals, Catalog #S11150H). THP1 cells were also purchased from the ATCC and cultured in RPMI 1640 Medium (Gibco, Catalog #11875-093) supplemented with 1x Pen-Strep-Glutamine and 10% heat-inactivated fetal bovine serum. All cells were certified mycoplasma-free and discarded after 20 passages to minimize variation.

Constructs and antibodies

All relevant information can be found in the key resources table, including detailed descriptions of the amino acid sequences for all constructs.

Lentivirus production and infection

Lentiviral infection was used to express constructs described in the key resources table in either RAW264.7 or THP1 cells. Lentivirus was produced by HEK293T cells or Lenti-X 293T cells (Takara Biosciences, Catalog #632180) transfected with pMD2.G (a gift from Didier Trono, Addgene plasmid # 12259 containing the VSV-G envelope protein), pCMV-dR8.91 (since replaced by second generation compatible pCMV-dR8.2, Addgene plasmid #8455), and a lentiviral backbone vector containing the construct of interest (derived from pHRSIN-CSGW, see key resource table) using lipofectamine LTX (Invitrogen, Catalog # 15338–100). The HEK293T media was harvested 60-72 hr post-transfection, filtered through a 0.45 μm filter, and concentrated using Lenti-X (Takara Biosciences, Catalog #631232) via the standard protocol. Concentrated virus was added directly to the cells and the plate was centrifuged at 2200xg for 45

min at 37°C. Cells were analyzed a minimum of 60 hr later. Cells infected with more than one viral construct were FACs sorted (Sony SH800) before use to enrich for double infected cells.

DNA origami preparation

The DNA origami pegboard utilized for all experiments was generated as described in figure S2. The p8064 DNA scaffold was purchased from IDT (Catalog # 1081314). All unmodified oligonucleotides utilized for the origami were purchased from IDT in 96 well plates with standard desalting purification and resuspension at 100 μ M in water. Fluorophore and biotin conjugated oligonucleotides were also purchased from IDT (HPLC purification). All oligonucleotide sequences are listed in table 1, the assembly is schematized in figure S2, and the Cadnano strand diagram for the pegboard with 72 medium-affinity ligands is included in S2. Core staple oligonucleotides (200 nM) (plates 1 and 2), ligand oligonucleotides (200nM) (plates 3-L, 3MA, and 3HA), biotinylated oligonucleotides (200nM), DNA scaffold (20 nM final concentration), and fluorophore-labeled oligonucleotides (200 nM final concentration) were mixed in 1x folding buffer (5 mM Tris pH 8.0, 1 mM EDTA, 5 mM NaCl, 20 mM MgCl₂). Origami folding reaction was performed in a PCR thermocycler (Bio-Rad MJ Research PTC-240 Tetrad), with initial denaturation at 65 °C for 15 min followed by cooling from 60°C to 40°C with a decrease of 1° C per hr. To purify excess oligonucleotides from fully folded DNA origami, the DNA folding reaction was mixed with an equal volume of PEG precipitation buffer (15% (w/v) PEG-8000, 5 mM Tris-Base pH 8.0, 1 mM EDTA, 500 mM NaCl, 20 mM MgCl₂) and centrifuged at 16,000x rcf for 25 min at room temperature. The supernatant was removed, and the pellet was resuspended in 1x folding buffer. PEG purification was repeated a second time and the final pellet was resuspended at the desired concentration in 1x folding buffer and stored at 4°C.

Preparation of benzylguanine-conjugated DNA oligonucleotides

5'-amine modified (5AmMC6) DNA oligonucleotides were ordered from IDT and diluted in 0.15 M HEPES pH 8.5 to a final concentration of 2 mM. N-hydroxysuccinimide ester (BG-GLA-NHS) functionalized benzylguanine was purchased from NEB (Cat #S9151S) and freshly reconstituted in DMSO to a final concentration of 83 mM. To functionalize the oligonucleotides with benzylguanine, the two solutions were mixed so that the molar ratio of oligonucleotide-amine:benzylguanine-NHS is 1:50, and the final concentration of HEPES is between 50 mM and 100 mM. The reaction was left on a rotator overnight at room temperature. To remove excess benzylguanine-NHS ester, the reaction product was purified the next day with illustra NAP-5 Columns (Cytiva, Cat #17085301), using H₂O for elution. The molar concentration of the benzylguanine conjugated oligonucleotides was determined by measuring the absorbance of the purified reaction at 260 nm with a Nanodrop. This reaction was further condensed with the Savant SpeedVac DNA 130 Integrated Vacuum Concentrator System, resuspended in water to a final concentration of 100 μ M, aliquoted, and stored at -20°C until use.

Functionalization of glass surface with DNA origami

96-well glass bottom MatriPlates were purchased from Brooks (Catalog # MGB096-1-2-LG-L). Before use, plates were incubated in 5% (v/v) Hellmanex III solution (Z805939-1EA; Sigma) overnight, washed extensively with Milli-Q water, dried under the flow of nitrogen gas, and covered with sealing tape (ThermoFisher, Cat # 15036). Wells used for experiment were unsealed, incubated with 200 μ L of Biotin-BSA (ThermoFisher, Cat # 29130) at 0.5 mg/mL in PBS pH 7.4 at RT for 2 hr-overnight. Wells were washed 6x with PBS pH 7.4 to remove excess BSA and incubated for 30 min at room temperature with 100 μ L neutravidin at 250 μ g/mL in PBS pH 7.4 for origami quantification and 50 μ g/mL for cellular experiments. Wells were again washed 6x with PBS pH 7.4 supplemented with 20 mM MgCl₂ and incubated for 1-2 hr with the desired amount of DNA origami diluted in PBS pH 7.4 with 20 mM MgCl₂ and 0.1% BSA.

DNA origami quantification

5 wells of a 96-well glass bottom MatriPlate per origami reaction were prepared as described in 'Functionalization of glass surface with DNA origami'. The purified DNA origami reaction was serially diluted into PBS pH 7.4 with 20 mM MgCl₂ and 0.1% BSA and 5 different concentrations were plated and incubated for 1.5 hr before washing 5x with PBS pH 7.4 with 20 mM MgCl₂ and 0.1% BSA. Fluorescent TIRF images were acquired in the channel with which the origami was labeled. 100 sites per well were imaged using the High Content Screening (HCS) Site Generator plugin in uManager⁷⁴. The number of individual DNA origami per μm^2 in each well were quantified using the Spot Counter plugin in Fiji. This was repeated for all concentrations of origami plated. The final concentration of the origami reaction was measured as number of origami/ μm^2 and was calculated from a linear fit including all concentrations in which individual origami could be identified by the plugin.

TIRF imaging

96-well glass bottom MatriPlates were functionalized with DNA origami as described and then washed into engulfment imaging media (20 mM Hepes pH 7.4, 135 mM NaCl, 4 mM KCl, 1 mM CaCl₂, 10 mM glucose) containing 20 mM MgCl₂. ~100,000 dual infected mNeonGreen-DNA-CAR γ and BFP-Syk THP1 cells per well were pelleted via centrifugation, washed into engulfment imaging media, re-pelleted, and resuspended into 50 μL of engulfment imaging media. 1 μL of 100 μM benzylguanine-labeled receptor DNA stock was added per ~50,000 cells pelleted, and the cell-DNA mixture was incubated at room temperature for 15 min. Cells were subsequently washed twice via centrifugation with 10 mL of imaging buffer to remove excess benzylguanine labeled DNA and resuspended in 200 μL per 100,000 cells of imaging buffer containing 20 mM MgCl₂. Cells were then immediately added to each well and imaged. Data was only collected from a central ROI in the TIRF field. The origami fluorescent intensities along the x and y axis were plotted to ensure there was no drop off in signal and thus no uniformity of illumination.

Quantification of receptor and Syk recruitment to individual origami

Cells that expressed both the mNeonGreen tagged DNA-CAR γ receptor and the BFP-tagged Syk and had interactions with the 72-ligand origami were chosen for analysis in Fiji. An ROI was drawn around the perimeter of the cell-glass surface interaction, which was determined by the presence of receptor fluorescence. The 'Spot Intensity in All Channel' plugin in Fiji was used to identify individual origami pegboards, measure fluorescence intensity of the DNA-CAR γ receptor and Syk at each origami pegboard, and subtract local background fluorescence. The intensity at each origami pegboard was normalized to the average intensity measured at 72-ligand origami pegboards in each well.

Supported lipid bilayer coated silica bead preparation

Chloroform-suspended lipids were mixed in the following molar ratios: 96.8% POPC (Avanti, Catalog # 850457), 2.5% biotinyl cap PE (Avanti, Catalog # 870273), 0.5% PEG5000-PE (Avanti, Catalog # 880230, and 0.2% atto390-DOPE (ATTO-TEC GmbH, Catalog # AD 390–161) for labeled lipid bilayers, or 97% POPC, 2.5% biotinyl cap PE, and 0.5% PEG5000-PE for unlabeled lipid bilayers. The lipid mixes were dried under argon gas and desiccated overnight to remove chloroform. The dried lipids were resuspended in 1 mL PBS, pH 7.2 (Gibco, Catalog # 20012050) and stored under argon gas. Lipids were formed into small unilamellar vesicles via ≥ 30 rounds of freeze-thaws and cleared via ultracentrifugation (TLA120.1 rotor, 35,000 rpm / 53,227 x g, 35 min, 4°C). Lipids were stored at 4°C under argon gas in an eppendorf tube for up to two weeks. To form bilayers on beads, 8.6×10^8 silica beads with a 4.89 μm diameter (10 μl of 10% solids, Bangs Labs, Catalog # SS05N) were washed 2x with water followed by 2x with PBS by spinning at 300rcf and decanting. Beads were then mixed with 1mM SUVs in PBS, vortexed for 10 s at medium speed, covered in foil, and incubated in an end-over-end rotator at room temperature for 0.5-2 hr to allow bilayers to form over the beads. The beads were then washed 3x in PBS to remove excess SUVs, and resuspended in 100uL of 0.2% casein (Sigma, catalog # C5890) in PBS for 15

min at room temperature to block nonspecific binding. Neutravidin (Thermo, Catalog # 31000) was added to the beads at a final concentration of 1 ug/ml for 20-30 minutes, and the beads were subsequently washed 3x in PBS with 0.2% casein and 20mM MgCl₂ to remove unbound neutravidin. The indicated amounts of biotinylated ssDNA or saturating amounts of DNA origami pegboards were added to the beads and incubated for 1 hr at room temperature with end-over-end mixing to allow for coupling. Beads were washed 2 times and resuspended in 100uL PBS with 0.2% casein and 20 mM MgCl₂ to remove uncoupled origami pegboards or ssDNA. When functionalizing SUV-coated beads with anti-biotin AlexaFluor647-IgG (Jackson ImmunoResearch Laboratories Catalog # 200-602-211, Lot # 137445), the IgG was added to the beads at 1uM immediately following the casein blocking step, and beads were incubated for 1 hr at room temperature with end-over-end mixing.

Quantification of ssDNA, IgG, or origami on beads

To estimate the amount of ssDNA bound to each bead, we compared the fluorescence of Atto647-labeled DNA on the bead surface to calibrated fluorescent beads (Quantum AlexaFluor 647, Bangs Lab) using confocal microscopy (Figure S1). To determine saturating conditions of IgG and origami pegboards, we titrated the amount of IgG or origami in the coupling reaction and used confocal microscopy to determine the concentration at which maximum coupling was achieved. A comparable amount of origami pegboard coupling was also confirmed with confocal microscopy for beads used in the same experiment.

Quantification of engulfment

30,000 RAW264.7 macrophages were plated in one well of a 96-well glass bottom MatriPlate (Brooks, Catalog # MGB096-1-2-LG-L) between 12 and 24 hr prior to the experiment. Immediately before adding beads, 100 uL of a 1 uM solution of benzylguanine-conjugated receptor DNA in engulfment imaging media was added, incubated for 10 min at room temperature, and washed

out 4 times with engulfment imaging media containing 20 mM MgCl₂, making sure to leave ~100 uL of media covering the cells between washes, and finally leaving the cells in ~300 uL of media. ~8 x 10⁵ beads were added to the well and engulfment was allowed to proceed for 45 min in the cell incubator. Cells were fixed with 4% PFA for 10 min and washed into PBS. For figures 4c and 6d, 10 nM AlexaFluor647 anti-biotin IgG (Jackson Immuno Labs, Catalog # 200-602-211) diluted into PBS containing 3% BSA was added to each well for 10 minutes to label non-internalized beads. Wells were subsequently washed 3 times with PBS. Images were acquired using the High Content Screening (HCS) Site Generator plugin in μ Manager and at least 100 cells were scored for each condition. When quantifying bead engulfment, cells were selected for analysis based on a threshold of GFP fluorescence, which was held constant throughout analysis for each individual experiment. For figures 3, 4, 6, and S5 the analyzer was blinded during engulfment scoring using the position randomizer plug-in in μ Manager. For the THP1 cells, ~100,000 cells per condition were spun down, washed into engulfment imaging media, and coupled to benzylguanine-labeled receptor DNA as described under TIRF imaging. Cells were resuspended into 300 uL engulfment imaging media containing 20 mM MgCl₂ in an Eppendorf tube, ~8 x 10⁵ beads were added to the tube, and the tube was inverted 8x before plating the solution into a round-bottomed 96 well plate (Corning, Catalog # 38018). Engulfment was allowed to proceed for 45 min in the cell incubator before the plate was briefly spun and the cells were fixed in 4% PFA for 10 min. Cells were subsequently washed 3x with PBS by briefly centrifuging the plate and removing the media, and finally moved into a 96-well glass bottom MatriPlate for imaging.

Quantification of engulfment kinetics

RAW264.7 macrophages were plated and prepared in wells of a 96-well glass bottom MatriPlate as described in 'Quantification of engulfment'. Using Multi-Dimensional Acquisition in μ Manager, 4 positions in the well were marked for imaging at 20 sec intervals through at least 7 z-planes. ~4 x 10⁵ Atto647N-labeled 4S origami functionalized beads and ~4 x 10⁵ Atto550N-labeled 4T

origami functionalized beads were mixed in an Eppendorf tube, added to the well, and immediately imaged. Bead contacts were identified by counting the number of beads that came into contact with the cells throughout the imaging time. Initiation events were identified by active membrane extension events around the bead. Engulfment completion was identified by complete internalization of the bead by the macrophage. The initiation time was quantified as the amount of time between bead contact (the first frame in which the bead contacted the macrophage) and engulfment initiation (the first frame in which membrane extension around the bead was visualized) and was only measured for beads that were completely internalized by the end of the imaging time. The engulfment time was quantified as the amount of time between engulfment initiation and engulfment completion (the first frame in which the bead has been fully internalized by the cell).

Quantification of synapse intensity of DNA-CAR γ receptor, tSH2 Syk, PIP₃ reporter, and actin filaments

Phagocytic cups were selected for analysis based on clear initiation of membrane extension around the bead visualized by GFP fluorescence from the DNA-CAR γ receptor. The phagocytic cup and the cell cortex (areas indicated in schematic in figure 6b) were traced with a line (6 pixels wide for DNA-CAR γ receptor and the tSH2 Syk reporter, and 8 pixels wide for the Akt-PH reporter and phalloidin) at the Z-slice with the clearest cross section of the cup.

Microscopy and analysis

Images were acquired on a spinning disc confocal microscope (Nikon Ti-Eclipse inverted microscope with a Yokogawa CSU-X spinning disk unit and an Andor iXon EM-CCD camera) equipped with a 40 \times 0.95 NA air and a 100 \times 1.49 NA oil immersion objective. The microscope was controlled using μ Manager. For TIRF imaging, images were acquired on the same

microscope with a motorized TIRF arm using a Hamamatsu Flash 4.0 camera and the 100x 1.49 NA oil immersion objective.

Statistics

Statistical analysis was performed in Prism 8 (GraphPad, Inc). The statistical test used is indicated in each relevant figure legend.

3.6 Supporting Information

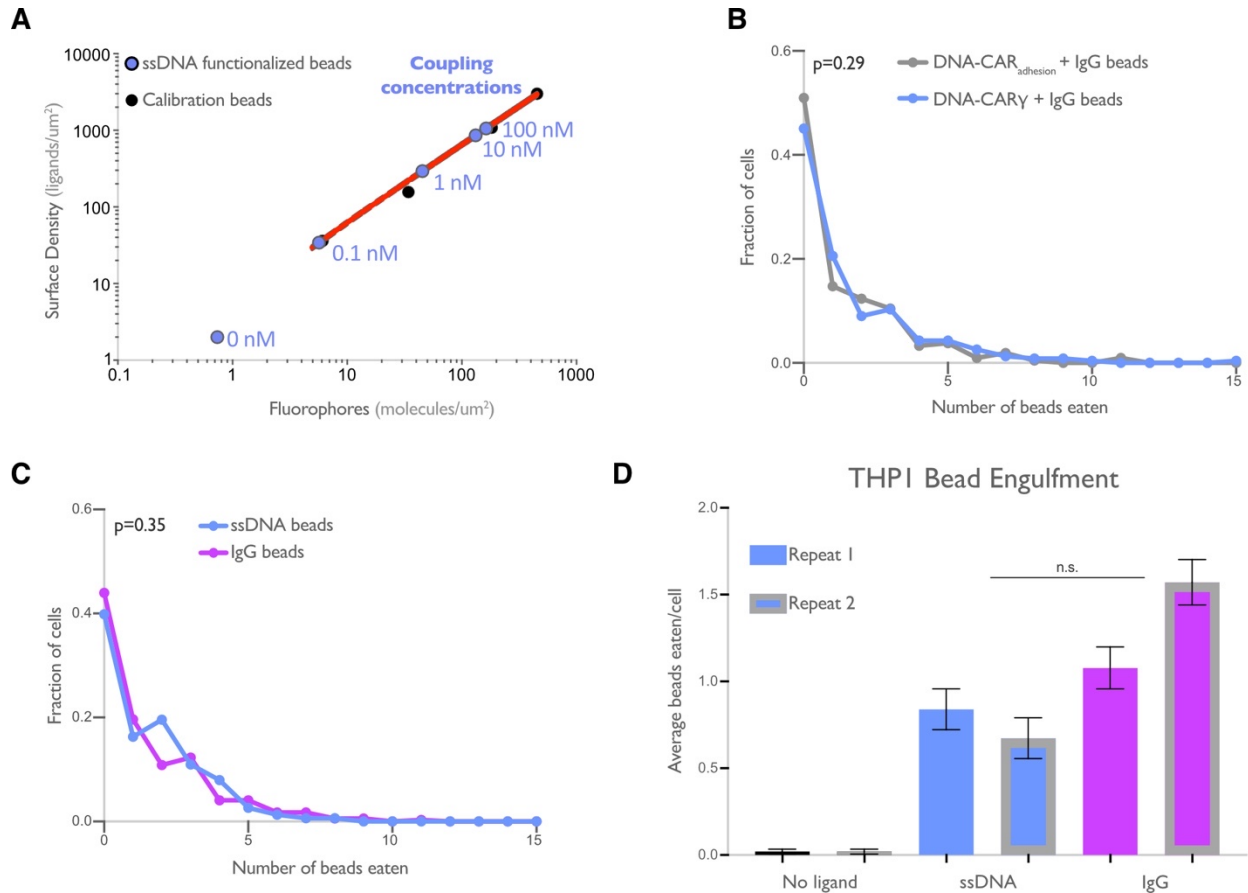


Figure S3.1, related to Figure 1: DNA-based engulfment system reflects endogenous engulfment

(A) Graph depicts the calibration used to determine the surface density of ssDNA on beads used in Figure 1b, c. The intensity of Alexa Fluor 647 fluorescent bead standards (black dots) was measured, and a simple linear regression (red line) was fit to the data. The fluorescence intensity of Alexa Fluor 647-ssDNA coated beads (blue dots) was measured, and the surface density was interpolated using the regression determined from the fluorescent bead standards. The concentration of ssDNA used for each bead coupling condition is indicated next to the blue points on the graph. (B) Macrophages expressing the DNA-CAR γ (blue) or the DNA-CAR_{adhesion} (grey) engulfed similar distributions of IgG functionalized beads. Data is pooled from two independent replicates. (C) Graph depicts the fraction of macrophages engulfing the indicated number of IgG (magenta) or ssDNA (blue) beads from data pooled from the three independent replicates presented in Figure 1d. (D) Graph shows the average number of Neutravidin (black), ligand-DNA (blue), or IgG (magenta) functionalized beads engulfed by the monocyte-like cell line THP1. Lines denote the mean engulfment from each independent replicate and bars denote \pm SEM. P values were calculated using the Mann-Whitney test (B, C) and n.s. denotes $p>0.05$ as determined by the Student's T-test (D).

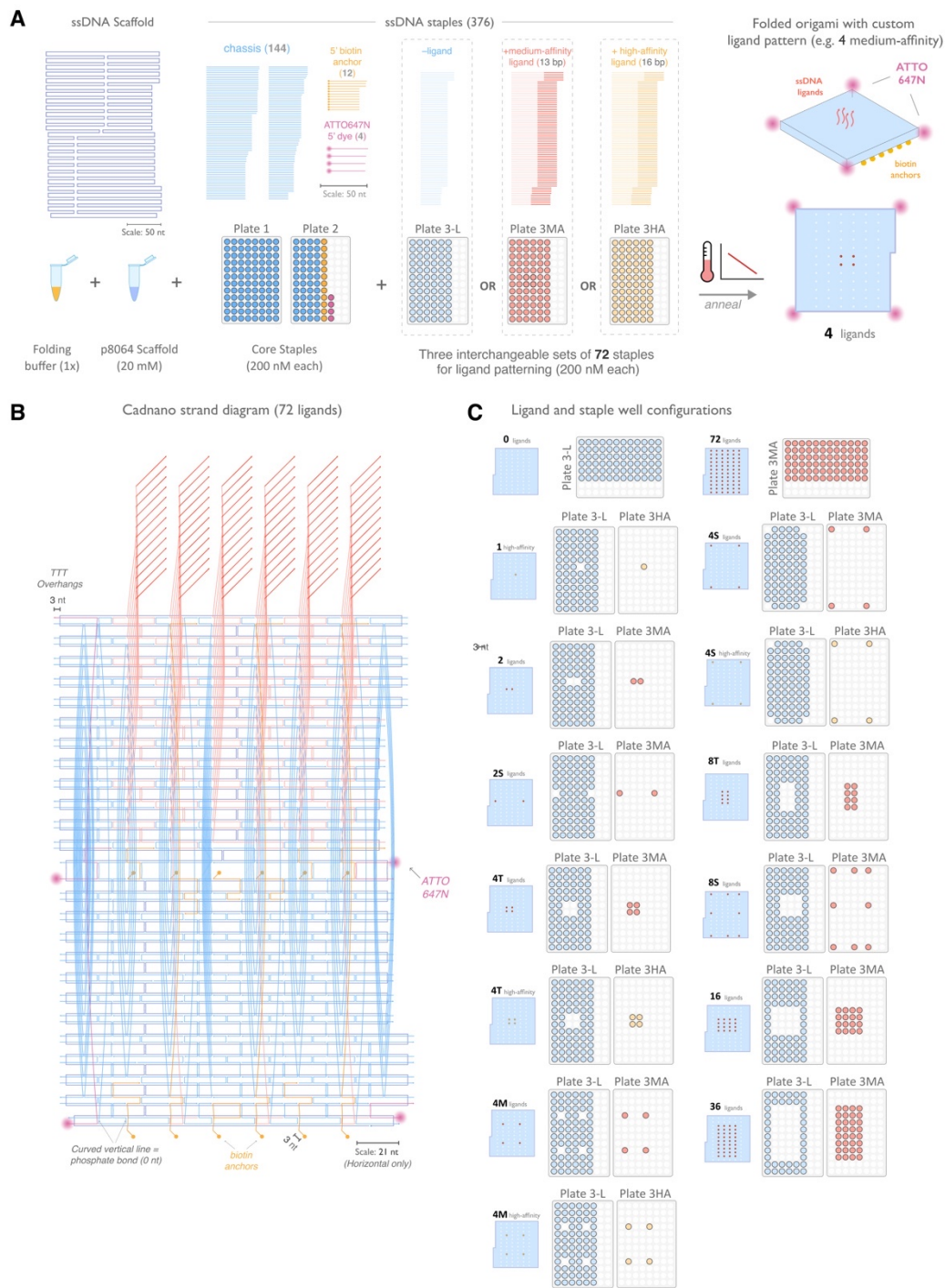


Figure S3.2, related to Figure 2: Design and Assembly of Nanoscale Ligand-Patterning Pegboard built from DNA origami.

(A) 2D schematic of origami scaffold and staples. The p8064 ssDNA scaffold is combined with 160 ssDNA staples that form the chassis, biotin-modified surface anchors, and ATTO647N-labeled dyes, plus a combination of 72 ligand-patterning staples. We used three variants of the ligand-patterning staples: "-ligand" that lacks a 3' single-stranded overhang and terminates flush with the pegboard surface, and a "medium-affinity" (red) and "high-affinity" (yellow) that form 13-bp and 16-bp duplexes with the DNA-CAR

receptors, respectively. Assembly is performed by thermal annealing in a one-pot reaction. (B) Cadnano strand diagram for the pegboard with 72 medium-affinity ligands included. (C) Fourteen pegboard configurations were used in this study. Configurations are labeled by ligand count, spacing, and ligand affinity, and the corresponding plate wells used in each assembly are shown.

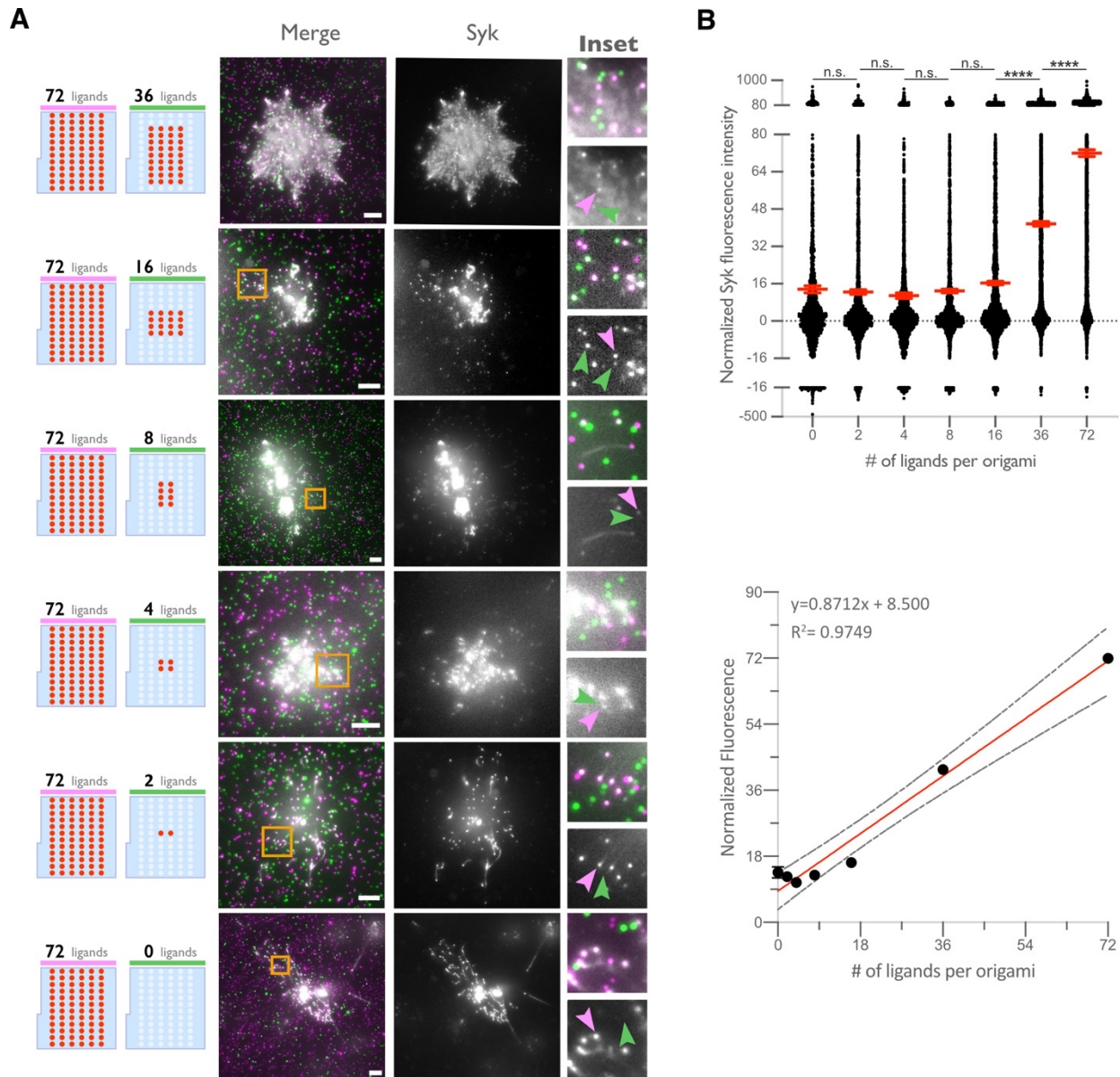


Figure S3.3, related to Figure 2: Syk intensity increases with ligand number in origami cluster

(A) TIRF microscopy images showing DNA-CAR γ -mNeonGreen and Syk-BFP expressing THP1s interacting with 72-ligand origami pegboards (pink) and origami pegboards presenting the indicated number of ligands (green) plated together on a glass surface (schematics shown on the left). Middle images depict a single macrophage, and right images show the area indicated with a yellow box on the left. Examples of Syk-BFP (grey) recruitment to individual origami pegboards is marked by pink (72L origami) and green (indicated ligand number origami) arrowheads (right). (B) Top graph shows the Syk intensity at each indicated origami pegboard type normalized to the average Syk intensity at 72L origami pegboards for each condition. Each dot represents the normalized Syk intensity at one origami and red lines denote the mean \pm SEM of pooled data from three separate replicates. At ligand numbers fewer than 16, we did not detect Syk enrichment over background fluorescence of cytosolic Syk. A linear regression fit (bottom) of the average Syk fluorescence intensity at each origami pegboard type suggests that the mean Syk recruitment is linearly proportional to the number of ligands per DNA origami. n.s. denotes $p>0.05$ and **** indicates $p<0.0001$ by an ordinary one-way ANOVA with Holm-Sidak's multiple comparison test.

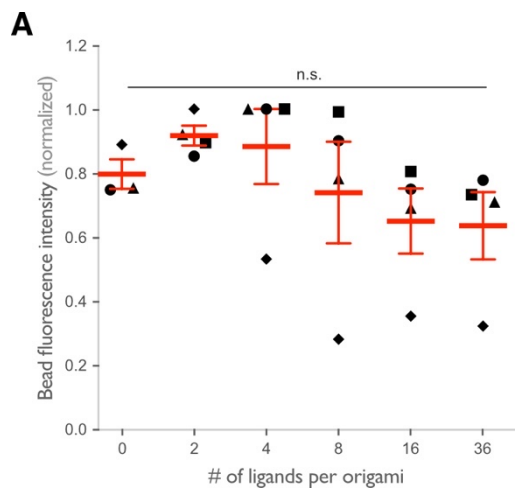


Figure S3.4, related to Figure 3: Origami intensity on beads is comparable across conditions

(A) Graph shows the average Atto647N fluorescence intensity from the beads used in Figure 3a, b measured using confocal microscopy. Each dot represents an independent replicate ($n \geq 100$ cells analyzed per experiment), denoted by symbol shape, with red lines denoting mean \pm SEM. n.s. denotes $p > 0.05$ as determined by an Ordinary one-way ANOVA with Holm-Sidak's multiple comparison test.

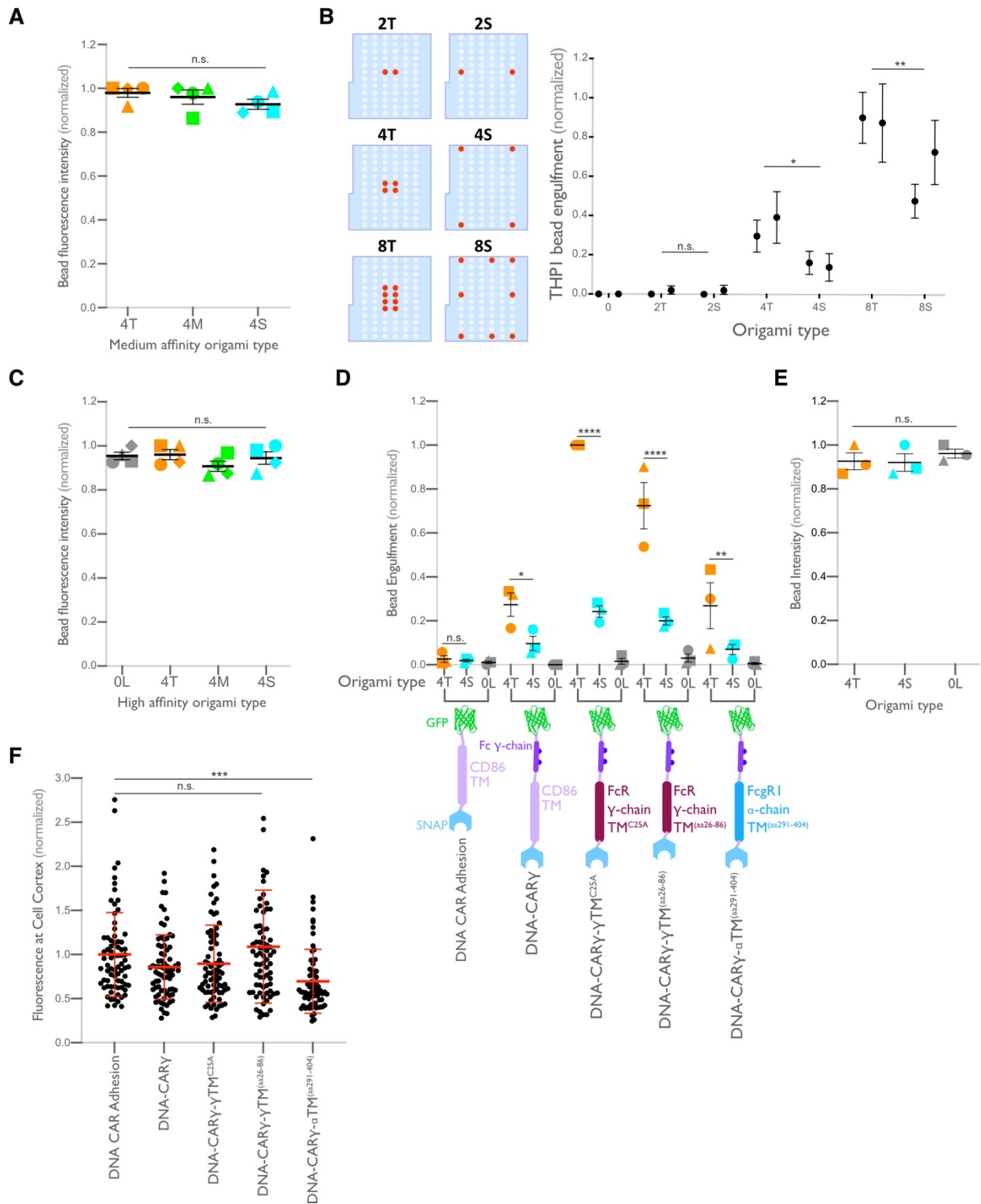


Figure S3.5, related to Figure 4: Ligand clustering enhances engulfment in RAW macrophages expressing DNA CARs with endogenous Fc γ R transmembrane domains and in THP1s

(A) Graph shows the average Atto647N fluorescence intensity from the beads used in Figure 4a measured using confocal microscopy. (B) Beads were functionalized with the indicated ligand-presenting origami pegboards in amounts calculated to equalize the total number of origami pegboards and ligands across conditions. Schematics (left) depict the origami utilized, where the positions presenting a ligand (red dots)

and the positions not occupied by a ligand (light blue) are indicated. Graph (right) depicts the average number of the indicated type of beads internalized per DNA-CAR γ -expressing THP1, normalized to the maximum bead eating in that replicate. (C) Graph shows the average Atto647N647 fluorescence intensity from the beads used in Figure 4b measured using confocal microscopy. (D) Schematics below graph depict the DNA CAR constructs designed with varying transmembrane domains. Beads were functionalized with 4T origami pegboards (orange), 4S origami pegboards (cyan), or 0-ligand 'blank' origami pegboards (grey) and fed to macrophages expressing the DNA CAR receptor depicted below each section of the graph. Graph depicts the number of beads engulfed per macrophage normalized to the maximum observed eating in that replicate. (E) Graph shows the average Atto647N fluorescence intensity from the beads used in (D) measured using confocal microscopy. (F) DNA CAR receptors used in (D) are expressed and trafficked to the membrane at similar levels. Fluorescent intensity at the cell cortex of the DNA CAR-infected macrophage was quantified using the mean intensity of a 2 pixel width linescan at the cell membrane, with the mean intensity of a linescan immediately adjacent to the cell subtracted for local background. The fluorescence intensity was normalized to the average intensity of the DNA CAR_{adhesion} in each experiment. Each dot represents an individual cell and data is pooled from 3 independent experiments, with red lines denoting mean \pm SEM. n.s. denotes $p > 0.05$, * denotes $p < 0.05$, ** denotes $p < 0.005$, *** denotes $p < 0.0005$, and **** indicates $p < 0.0001$ as determined by an Ordinary one-way ANOVA with Holm-Sidak's multiple comparison test (A-F).

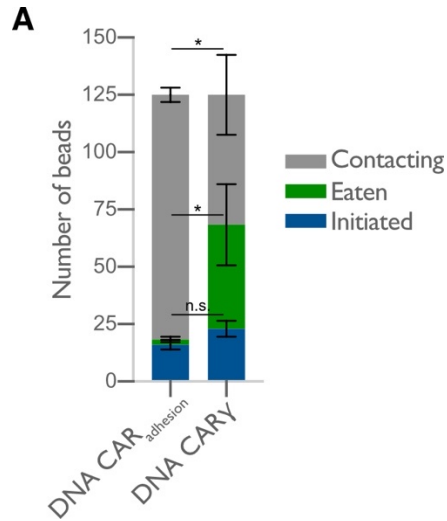


Figure S3.6, related to Figure 5: DNA CAR_{adhesion} fails to induce frequent engulfment initiation attempts

(A) The average number of 4T origami pegboard-functionalized beads contacting (grey), in the initiation stage of engulfment (blue), or fully engulfed (green) by macrophages expressing either the DNA CAR_{adhesion} or the DNA CAR_γ were quantified from fixed still images after 45 minutes of engulfment. 125 beads in contact with DNA CAR expressing macrophages were analyzed in 3 independent replicates. Bars represent the average number of beads identified at each stage and black lines denote \pm SEM between replicates. n.s. denotes $p > 0.05$ and * denotes $p < 0.05$ as determined by an unpaired t-test with Holm-Sidak's multiple comparison test.

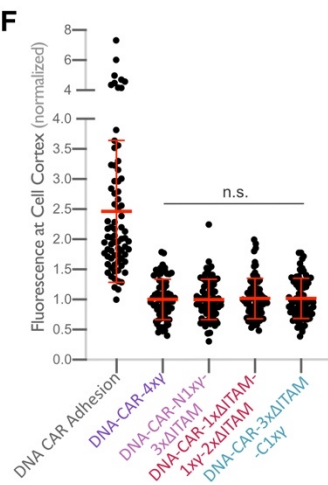
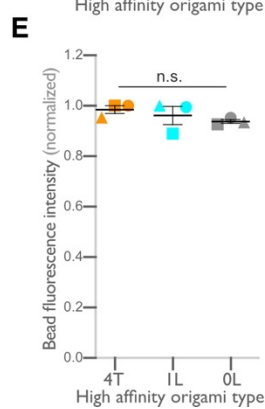
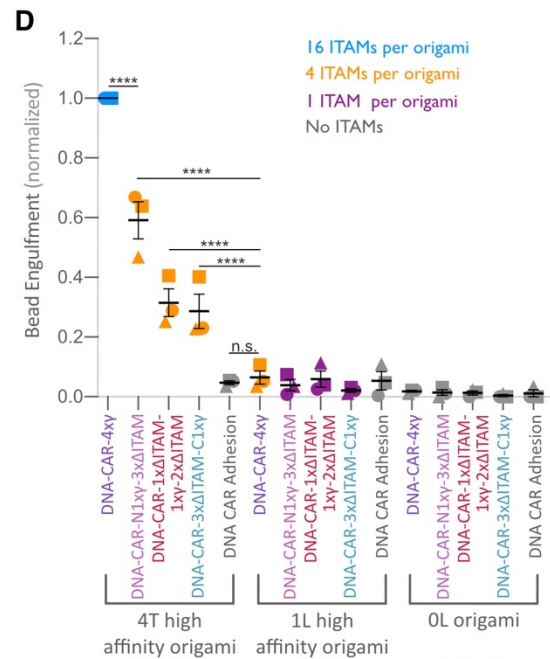
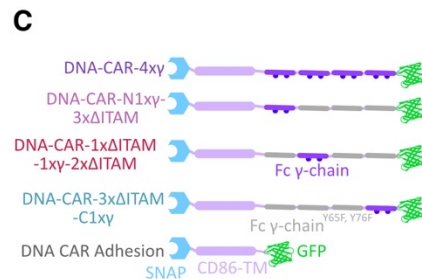
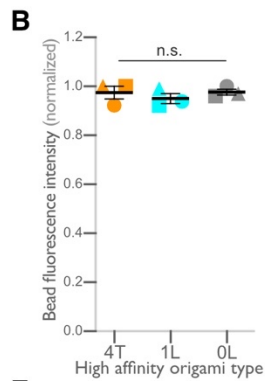
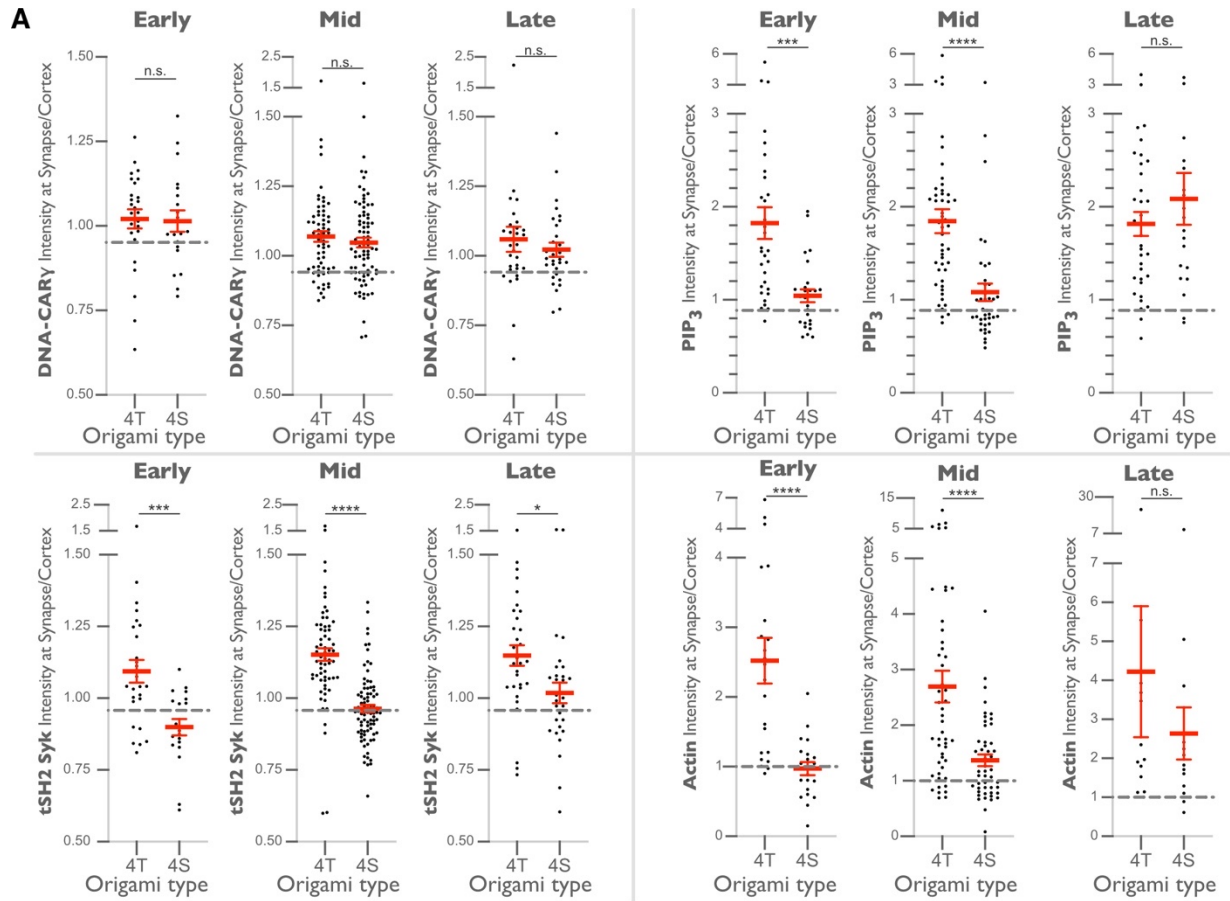


Figure S3.7, related to Figure 6: Differential recruitment of downstream signaling molecules is greater at early and mid-stage phagocytic cups

(A) Data from experiment shown in Figure 6b is separated by early (macrophage membrane extends across <30% of the bead, left), mid (macrophage membrane extends across 30-70% of the bead, middle), and late (macrophage membrane extends across >70% of the bead, right) stage phagocytic cups. Graphs depict the ratio of fluorescence intensity at 4T or 4S functionalized bead synapses compared to the cortex. Each dot represents one bead with red lines denoting mean \pm SEM. n.s. denotes $p > 0.05$, * denotes $p < 0.05$, *** denotes $p < 0.0005$, and **** denotes $p < 0.00005$ by the Student's T-test. (B) Graph shows the average Atto647N fluorescence intensity from the beads used in Figure 6d measured using confocal microscopy. (C) Schematics depict the DNA-CAR-4xy constructs used for experiment quantified in (D). (D) DNA CAR constructs shown in (C) were expressed in RAW macrophages and fed beads functionalized with 4T high affinity origami pegboards, 1 ligand high affinity origami pegboards, or 0 ligand origami pegboards. Graph depicts the number of beads engulfed per macrophage normalized to the maximum observed eating in that replicate. Each data point represents the mean from an independent experiment, denoted by symbol shape, and bars denote the mean \pm SEM. Blue points represent a condition where 16 ITAMs are available per origami, orange points represent conditions where 4 ITAMs are available per origami, purple points represent a condition where 1 ITAM is available per origami, and grey points represent conditions where no ITAM is available. (E) Graph shows the average Atto647N fluorescence intensity from the beads used in (D) measured using confocal microscopy. (F) DNA CAR receptors used in (D) are expressed and trafficked to the membrane at similar levels. Fluorescent intensity at the cell cortex of the DNA CAR infected macrophage was quantified using the mean intensity of a 2 pixel width linescan at the cell membrane, with the mean intensity of a linescan immediately adjacent to the cell subtracted for local background. The fluorescence intensity was normalized to the average intensity of the DNA-CAR-4xy in each experiment. Each dot represents an individual cell and data is pooled from 3 independent experiments, with red lines denoting mean \pm SEM. n.s. denotes $p > 0.05$ and **** indicates $p < 0.0001$ as determined by an Ordinary one-way ANOVA with Holm-Sidak's multiple comparison test (B,D-F).

Table S3.1 Sequences and setup for plates 1+2

Plate Name	Well	Staple ID	Sequence	Length	CN 5' pos	CN 3' pos	Staple Color	Note
Plate1	A1	1	CAGACGAAAAAGAAAGACTGGA TAGCGTAGGCTTGAATACGTAA TGCCACTACGTTT	57	28[4 8]	18[2 0]	#69b 5fc	chassis
Plate1	A2	2	GGTGGCACAATAAAAAGCAATA CCAAAAAGCCTTTCTCATATATT TTAAATGCATTT	57	43[4 2]	48[2 7]	#69b 5fc	chassis
Plate1	A3	3	ATTTTCACATAGTTGTTCCGAAA TCGAGCGGATTGCATCAAATTA TAGTCAGAAGC	56	12[7 6]	33[6 2]	#69b 5fc	chassis
Plate1	A4	4	TACCGATTTCGTCACCAGGAACG GTAATAATAGTAAAATGTTTGT TTGCCAGAGGG	56	16[7 6]	29[6 2]	#69b 5fc	chassis
Plate1	A5	5	GAGGCGAAATATACACAATATA GAGATAGAACCCTGATAGCCCT AAAACACCTCAA	56	18[1 39]	25[1 39]	#69b 5fc	chassis
Plate1	A6	6	GCGAACTTCTGACCTGGTAATG CAATACACGAGCACTGCGCGT CACCCAGAACGTG	56	26[1 53]	33[1 53]	#69b 5fc	chassis
Plate1	A7	7	TACCGCCTCACGCATCCTCGTC TGGCAAGGGTCGAGAACAAGG CAGCAAACGCGC	56	28[1 32]	35[1 32]	#69b 5fc	chassis
Plate1	A8	8	TCACCGTAGGGAAGATAAAGG GACTCCTTGTGTAGGTAAAGAT AGAACCATTTCAA	56	3[42]	47[5 5]	#69b 5fc	chassis
Plate1	A9	9	CCGCCTGTGCGTATTCACAATC CCCGGGCGGTGCCACATCCCC ACCGTCCATCCTC	56	34[1 53]	41[1 53]	#69b 5fc	chassis
Plate1	A10	10	AAGATTATTTAATTCTCCAACCT TTTGATAATTGCATATGCATATA ACAGTTGATT	56	34[4 8]	40[3 5]	#69b 5fc	chassis
Plate1	A11	11	AGTCGGGTGAGCTAGGGGGTT TGGTGCTTATGAGCTCATTGCT TGCCGTCACAGGC	56	35[8 4]	42[8 4]	#69b 5fc	chassis
Plate1	A12	12	ATTTGCCTGAGAGAATGTGCTG CGCCATCGTGGGAGCCATCAA CGGTAATCGTAAA	56	42[1 53]	48[1 40]	#69b 5fc	chassis
Plate1	B1	13	AGAGCCACAGGAGGCATTCCA ACTAAAGTACGGTGTCCCGCC GGGCGCGGTTGCGG	56	6[55]	39[8 3]	#69b 5fc	chassis
Plate1	B2	14	TTTGAGCAAGAAACAATGATTA AGCCTGAGCGATGTTGGGAAG GGCGATCGGTTT	55	0[19 3]	45[1 96]	#69b 5fc	chassis

Plate Name	Well	Staple ID	Sequence	Length	CN 5' pos	CN 3' pos	Staple Color	Note
Plate1	B3	15	TTTCGTCAAAAATGAAAATACG ATTTTCGCTATTGGATAGCTCTC ACGGAAAATTT	55	2[19 3]	43[1 96]	#69b 5fc	chassis
Plate1	B4	16	TTTGCCAAAAGGAATTACGAAT GCAGAAGGGAATCAGTGAATAA GGCTTGCCTTT	55	27[2 3]	22[2 0]	#69b 5fc	chassis
Plate1	B5	17	TTTAGCGAGAGGCTTTTGCCGA TAAATAAACGTAGCCGGAACG AGGCGCAGTTT	55	29[2 3]	20[2 0]	#69b 5fc	chassis
Plate1	B6	18	TTTAAATCAGGTCTTTACCAATG ACCTAATAATGCCACGCATAA CCGATATTTT	55	33[2 3]	16[2 0]	#69b 5fc	chassis
Plate1	B7	19	TTTACTTCAAATATCGCGTAGA GGAAAACACAAATAGAAAGGA ACAATAATTT	55	35[2 3]	14[2 0]	#69b 5fc	chassis
Plate1	B8	20	TTTGTACCTTTAATTGCTCAGGT CAGGATATAATACCGTAACACT GAGTTTCTTT	55	37[2 3]	12[2 0]	#69b 5fc	chassis
Plate1	B9	21	TTTGCTCAACATGTTTTAATGAA TATGGGGTCATACCAGGCGGA TAAGTGCCTTT	55	39[2 3]	10[2 0]	#69b 5fc	chassis
Plate1	B10	22	TTTAAGCCTTAAATCAAGACTTG CGGACAGCGGGTAGAACGTCA GCGTGGTGTTT	55	4[19 3]	41[1 96]	#69b 5fc	chassis
Plate1	B11	23	TTTGGGCGCGAGCTGAAAAGC TATATTTTCATCGCAGAGCCGCC ACCAGAACCTTT	55	43[2 3]	6[20]	#69b 5fc	chassis
Plate1	B12	24	TTTAAGAATTAGCAAAATTTTCAT ACATGAATTAGTTTGCCTTTAG CGTCAGATTT	55	45[2 3]	4[20]	#69b 5fc	chassis
Plate1	C1	25	TTTATACTTTTGCGGGAGAACA TTATTACATACGTAAATATTGAC GGAAATTTTT	55	47[2 3]	2[20]	#69b 5fc	chassis
Plate1	C2	26	TTTAAACCAAGTACCGCACTCC AAGAGCAGCAACCGCAAGCGG ACTTATCAAAC	54	6[19 3]	42[1 68]	#69b 5fc	chassis
Plate1	C3	27	ACAAAGTCCCTGAAAGGTCCT CCGGCACCGCTTCACGCCAGG GTTTTTC	49	0[11 8]	44[1 12]	#69b 5fc	chassis
Plate1	C4	28	TCTTACCAGATAACGATTCTCT CGCCATTCAGGCTCTGGCGAA AGGGGG	49	0[16 0]	44[1 54]	#69b 5fc	chassis
Plate1	C5	29	TTGAGAAATAATTAACATACG GGGAGAGGCGGTTGCCCTGAG AGAGTT	49	10[1 39]	34[1 33]	#69b 5fc	chassis

Plate Name	Well	Staple ID	Sequence	Length	CN 5' pos	CN 3' pos	Staple Color	Note
Plate1	C6	30	TAAGGCGCTATATGACGCTGG GTTGTTCCAGTTTGGGTGCCGT AAAGCA	49	12[1 18]	32[1 12]	#69b 5fc	chassis
Plate1	C7	31	TGACCTAACGCGAGCCCTTCAG ACTCCAACGTCAACACTACGTG AACCA	49	12[1 60]	32[1 54]	#69b 5fc	chassis
Plate1	C8	32	TTTTAACCTTGAATTTTTTGGT GTAGCGGTCACGCGTATAACGT GCTT	49	14[1 39]	30[1 33]	#69b 5fc	chassis
Plate1	C9	33	ACATAAAACATTTATGCTTTGTT CTTTGATTAGTAACTATCGGCC TTGC	49	16[1 60]	28[1 54]	#69b 5fc	chassis
Plate1	C10	34	GAAGCGCCAAAATAGATTAAGA GTCCCAGAAATTTGGCCAGCAG TTGGGC	49	2[13 9]	42[1 33]	#69b 5fc	chassis
Plate1	C11	35	ATTGTGTGATGAACGGTCAGTA TTAAATTTAGGAATACCACAAG ATTCA	49	20[7 6]	25[5 5]	#69b 5fc	chassis
Plate1	C12	36	TGCTCATCCGAACTTGTTACTA AAGAGGCGGGTAACAGGGAGA ACCATC	49	22[4 8]	16[4 2]	#69b 5fc	chassis
Plate1	D1	37	ACAAAGCTAAATTGAAAAATCTA CGTTAGGTAGAATTCAACTAGG CATA	49	22[5 5]	27[4 8]	#69b 5fc	chassis
Plate1	D2	38	GAAAAACCCGAGTAGAGCTAAA AAGGAGCTAAATCGTTGAGTTT TGCCC	49	28[1 11]	34[1 05]	#69b 5fc	chassis
Plate1	D3	39	AGCCATTGCAACAGAAAAGGGA CATTCTTTAAAATGATTATCAG ATGA	49	28[1 25]	21[1 32]	#69b 5fc	chassis
Plate1	D4	40	GAGCGTCAATCAGAACATAAAT TTCGTCTCGTCGCCAGCTTACG GCTGG	49	4[11 8]	40[1 12]	#69b 5fc	chassis
Plate1	D5	41	GCACCCAGCGTTTTTCTGCTCA TAACGGAACGTGCAATGCCAAC GGCAG	49	4[16 0]	40[1 54]	#69b 5fc	chassis
Plate1	D6	42	TCCGTTTAAAATCCCGGCGAAC CAGTCACCAGCTTGTTGGTGTA GATGG	49	41[1 05]	46[9 8]	#69b 5fc	chassis
Plate1	D7	43	TGGCAGCGTTGTGTTTACCT TGGGTATGGTGCCGACCGTAC ATTTTT	49	41[1 26]	47[1 32]	#69b 5fc	chassis
Plate1	D8	44	GTAGGAACATGTAGCCATCCCT TTGCTCGTCATAAGGTGCCCCC TG CAT	49	6[13 9]	38[1 33]	#69b 5fc	chassis

Plate Name	Well	Staple ID	Sequence	Length	CN 5' pos	CN 3' pos	Staple Color	Note
Plate1	D9	45	AAGAAAAGTAATTTTCAGTGTCT CTTCGCGTCCGTGAAGCATAAA GTGTA	49	8[11 8]	36[1 12]	#69b 5fc	chassis
Plate1	D10	46	TGCAGAAATAAAGTCAGCCAGT ACCGAGCTCGAATAAATTGTTA TCCGC	49	8[16 0]	36[1 54]	#69b 5fc	chassis
Plate1	D11	47	TTCAGCGCGTTGAAGTTCAGAG AATCCCCCTCAAATGAAAGCCG G	45	14[5 5]	31[7 2]	#69b 5fc	chassis
Plate1	D12	48	CATTAACAAAAGACGTTTACG TAAGAGCAACACTATAATGGAT T	45	18[5 5]	27[7 2]	#69b 5fc	chassis
Plate1	E1	49	ATAGTGGAGCCGCCACGGGAA CGGGCCTTTCATCTTTTCATAAT	44	43[6 1]	5[90]	#69b 5fc	chassis
Plate1	E2	50	TGAAAGCGTAAGAATTAGTCTT TTGGATTATACTTCTGAATTT	43	27[1 54]	21[1 82]	#69b 5fc	chassis
Plate1	E3	51	TAACCACCACCCCCTATGGTA CAATTTCAATTTGAATTAATTT	43	31[1 54]	17[1 82]	#69b 5fc	chassis
Plate1	E4	52	TGGGCGCCAGGGTGTGATTG AAAATTTTTCAAATATATTTT	43	35[1 54]	13[1 82]	#69b 5fc	chassis
Plate1	E5	53	GAATACCCAAAGACGCCAGTTT GAGGAAATATTTAAATTGTA	42	0[76]	47[7 6]	#69b 5fc	chassis
Plate1	E6	54	CGAGGAATTATTTTGC GCATCA GATCGCACTCCAGCGACGTT	42	0[97]	44[9 8]	#69b 5fc	chassis
Plate1	E7	55	ATTAAGACACCCTCTAATGAGA AACCTGTCTGCCCAGCAGG	42	10[9 7]	34[9 8]	#69b 5fc	chassis
Plate1	E8	56	ACCCTCAAAGTTTTCGAAAATTA GCCCCGAGATAGGGGAACCC	42	12[9 7]	32[9 8]	#69b 5fc	chassis
Plate1	E9	57	TGAATTTATTGTATTAAGGGAA GGGAAGAAAGCGACAGGAG	42	14[9 7]	30[9 8]	#69b 5fc	chassis
Plate1	E10	58	TTTTTCAGAGTGAGACGCCTGA CCCATGGTATAGCTGCTCAG	42	15[4 2]	10[4 2]	#69b 5fc	chassis
Plate1	E11	59	TGAATTTGACAGCAGCCGATTA ATCAGTGAGGCCAGCTCATG	42	16[9 7]	28[9 8]	#69b 5fc	chassis
Plate1	E12	60	CAGAGGCTATACCAGAAATACA CCAGTCACACGACCCAGCAG	42	18[9 7]	26[9 8]	#69b 5fc	chassis
Plate1	F1	61	TGGTTTACAGTAGCGTAAACT CACCGGAAACAATCGTAAAA	42	2[97]	42[9 8]	#69b 5fc	chassis
Plate1	F2	62	TTCATTATAATTTACCAGTCAG GACGTAGCACCGCCTGCAA	42	22[7 6]	25[7 6]	#69b 5fc	chassis
Plate1	F3	63	CCTTAACATTTGAGGATTTAGG CCGTCAATAGATAATTGCGA	42	23[9 8]	24[9 8]	#69b 5fc	chassis
Plate1	F4	64	GTGTTGACGCTCAATCGTCTGA CAGGGCCAGAATCCTGAGAA	42	29[8 1]	29[8 0]	#69b 5fc	chassis

Plate Name	Well	Staple ID	Sequence	Length	CN 5' pos	CN 3' pos	Staple Color	Note
Plate1	F5	65	TTTTTATAAAGGGAAGAAAGGA GCCCCCAAAGAACCTGTTT	42	29[8 4]	34[8 4]	#69b 5fc	chassis
Plate1	F6	66	GATTTAGAGCTTGACGGGGCTA AGCAAATCCCTTATAAATC	42	32[8 3]	33[8 3]	#69b 5fc	chassis
Plate1	F7	67	AGCTGCAAAGCCTGTGCCTGTA CTGCGCCCTGCGGAGGTGTC	42	35[1 05]	40[1 05]	#69b 5fc	chassis
Plate1	F8	68	ACTCACATTAATTGCGTTGCCT GCCGTTTTACGGTCATACC	42	36[8 3]	37[8 3]	#69b 5fc	chassis
Plate1	F9	69	GATAGCACGTTTGCAGTGATGA AGGGGCAAATGGTCAATAAC	42	4[76]	42[4 9]	#69b 5fc	chassis
Plate1	F10	70	AACGTCACAAAATCAAAGCCGT CCGGCAAACGCGGCAGCATC	42	4[97]	40[9 8]	#69b 5fc	chassis
Plate1	F11	71	AGGCGTTTTCGCACTCAATTGT CTAAAGTTAAACGATGCTGA	42	40[8 3]	41[8 3]	#69b 5fc	chassis
Plate1	F12	72	AGTGCCAAGCTTTCAGAGGTAT AGGACGACGACAGTATCGGC	42	44[8 3]	45[8 3]	#69b 5fc	chassis
Plate1	G1	73	TTCAAAAGGGTGAGAAAGGCC GTATAAGCAAATAAAAATTTT	42	49[5 6]	48[5 6]	#69b 5fc	chassis
Plate1	G2	74	ACCGCCTAAACAAAAGCGGGG CGGGTCACTGTTGCGCCTGTG	42	6[97]	38[9 8]	#69b 5fc	chassis
Plate1	G3	75	ACCGTTCAGTTAAGAATGCGG CGGGCGGATGGCTTAGAGCT	42	8[76]	38[4 9]	#69b 5fc	chassis
Plate1	G4	76	GAAAGCGTTCGGAACACTCTGT CTGCCAGCACGCGGGGTGCC	42	8[97]	36[9 8]	#69b 5fc	chassis
Plate1	G5	77	GTGCCTTTTTGATGGCATTGAC CACCTGCATTTTGAATCAA	42	9[42]	4[42]	#69b 5fc	chassis
Plate1	G6	78	GGGTTTTCCGGAATAAGCAAAC GAGCTTCAAAGCGAACGCT	41	10[5 5]	35[6 8]	#69b 5fc	chassis
Plate1	G7	79	TTTCGGAATCGTCATAAATATTC ATTAACGAGCTGACTA	40	31[2 3]	33[4 8]	#69b 5fc	chassis
Plate1	G8	80	TTTTATTTTTGAATGGCTATACG TGCCACAGACAATTT	38	26[1 86]	27[1 86]	#69b 5fc	chassis
Plate1	G9	81	TTTGAGTAGAAGAACTCAAATA ACATCACTTGCCTTTT	38	28[1 86]	29[1 86]	#69b 5fc	chassis
Plate1	G10	82	TTTCGCTACAGGGCGCGTAGC CGCGCTTAATGCGCTTT	38	30[1 86]	31[1 86]	#69b 5fc	chassis
Plate1	G11	83	TTTTATCAGGGCGATGGCCAGG GCGAAAACCGTCTTT	38	32[1 86]	33[1 86]	#69b 5fc	chassis
Plate1	G12	84	TTTGTGAGACGGGCAACAGGTT TTTCTTTTACCATTT	38	34[1 86]	35[1 86]	#69b 5fc	chassis
Plate2	H1	85	TTTAGCTGTTTCCTGTGTGTCG TAATCATGGTCATTTT	38	36[1 86]	37[1 86]	#69b 5fc	chassis
Plate2	H2	86	TTTGGCATCAGATGCCGGGTCA GCAAATCGTTAACTTT	38	38[1 86]	39[1 86]	#69b 5fc	chassis

Plate Name	Well	Staple ID	Sequence	Length	CN 5' pos	CN 3' pos	Staple Color	Note
Plate2	H3	87	TTTACGACGACAATAAACAAAG TAATTCTGTCCAGTTT	38	8[19 3]	9[19 3]	#69b 5fc	chassis
Plate2	H4	88	CACTGCCCGCTTTCCGATGGTG AGCGTAACGATCTA	36	35[6 9]	13[9 0]	#69b 5fc	chassis
Plate2	H5	89	AAGCAGAAAATTAATGCCGGAA CTAGCATAACCAA	35	0[13 2]	47[1 39]	#69b 5fc	chassis
Plate2	H6	90	ACGCAATGTCAAATCACCATCA GCCCCAGTTAAAA	35	0[90]	47[9 7]	#69b 5fc	chassis
Plate2	H7	91	ATCGTTCGAAAGAAGAGAGCGG AAAGAGTCTGTCCA	35	16[1 18]	29[1 25]	#69b 5fc	chassis
Plate2	H8	92	AAGAAACACAAACAATAACAA CTAATAGATTAGA	35	22[1 39]	24[1 19]	#69b 5fc	chassis
Plate2	H9	93	ACATTATATTAATATCTAAAAT ATCTTACCCTCA	35	22[1 60]	25[1 53]	#69b 5fc	chassis
Plate2	H10	94	AATCTTGTGAATTATTTAAGAA CTGGCTCATTAT	35	22[9 7]	24[7 7]	#69b 5fc	chassis
Plate2	H11	95	AATTAACCGTTGTAATCCAGAA GTAACAGTACCTT	35	29[1 33]	19[1 53]	#69b 5fc	chassis
Plate2	H12	96	CGGGCGCTAGGGCGTAGAATC ATGATGAAACAAAC	35	31[1 12]	17[1 32]	#69b 5fc	chassis
Plate2	A1	97	AGTCCACTATTA AAAAATCAAGA ACATAGCGATAGC	35	33[1 33]	15[1 53]	#69b 5fc	chassis
Plate2	A2	98	TTAATGAATCGGCCGCGTCTCT AAATGCTGATGCA	35	35[1 12]	13[1 32]	#69b 5fc	chassis
Plate2	A3	99	GAGCCGGAGCCTCCCAGACGA AGGTTTCACGCAAC	35	36[1 32]	40[1 26]	#69b 5fc	chassis
Plate2	A4	100	TCACAGTTGAGGATTCCACACC TAGAAAAAGCCTG	35	37[1 33]	11[1 53]	#69b 5fc	chassis
Plate2	A5	101	TAAGAGGTCATTTTAGACCGGA GGTGTATCACCGT	35	37[4 9]	11[6 9]	#69b 5fc	chassis
Plate2	A6	102	CTGGTAATGGGTAATCCAGCGA GGCAGAGGCATTT	35	39[1 12]	9[13 2]	#69b 5fc	chassis
Plate2	A7	103	TTACACTGGTGTGTTTACCTGA CCGACAAAAGGTA	35	39[1 54]	9[17 4]	#69b 5fc	chassis
Plate2	A8	104	CTCCGGCCAGAGCAGGTGGTG AAACCAATCAATAA	35	41[1 33]	7[15 3]	#69b 5fc	chassis
Plate2	A9	105	CCATTAGATACATTGAAGTTTTT GAGGCAGGTCAG	35	41[4 9]	7[69]	#69b 5fc	chassis
Plate2	A10	106	ACGTACAGCGCCATTACATCGT ATAGAAGGCTTAT	35	43[1 12]	5[13 2]	#69b 5fc	chassis
Plate2	A11	107	TAGACTTTCTCCGTTTAAATTAG CGAACCTCCCGA	35	43[1 54]	5[17 4]	#69b 5fc	chassis
Plate2	A12	108	GGTGAAGACGCCAGGCGCAAC GTAACA ACTGGCCT	35	43[1 68]	47[1 74]	#69b 5fc	chassis

Plate Name	Well	Staple ID	Sequence	Length	CN 5' pos	CN 3' pos	Staple Color	Note
Plate2	B1	109	GATAACCGACGGCCCTCAGGA GTAACCGATATTTT	35	43[8 4]	47[9 0]	#69b 5fc	chassis
Plate2	B2	110	GAGGGTAGCTATTTTTGAGAGT CGATGAAAAATAA	35	49[1 40]	47[1 60]	#69b 5fc	chassis
Plate2	B3	111	AATATGATATTCAACCGTTCTAC CCCGGTTGTAA	35	49[9 8]	47[1 18]	#69b 5fc	chassis
Plate2	B4	112	TTGAGGGCACCGACTAACATCT CAATTCTACTA	33	2[55]	43[6 0]	#69b 5fc	chassis
Plate2	B5	113	TTTGCGAACGAGTAGATTTAGT TTGACTGTTTA	33	41[2 3]	42[4 2]	#69b 5fc	chassis
Plate2	B6	114	ATTTACATTGGGTGAGGCGGTG TACAGACCAG	32	27[7 3]	21[9 0]	#69b 5fc	chassis
Plate2	B7	115	CGAACGTGCGGTTTTAGACCTC AGCAGCGAAA	32	31[7 3]	17[9 0]	#69b 5fc	chassis
Plate2	B8	116	TTTTTAGTTAATTTTCGTTATAC AAATTTT	30	12[1 82]	11[1 82]	#69b 5fc	chassis
Plate2	B9	117	TTTCTTTTTTAATGGTGAGAAGA GTCATTT	30	16[1 82]	15[1 82]	#69b 5fc	chassis
Plate2	B10	118	TTTTAATGGAAGGGTACAATAA CGGATTTT	30	20[1 82]	19[1 82]	#69b 5fc	chassis
Plate2	B11	119	AATAGCAAAGGCTATCAGGTCA TTGCTTT	29	0[17 4]	49[1 89]	#69b 5fc	chassis
Plate2	B12	120	GCCGCCAATACAGGAGTGTACT GGTATTT	29	7[35]	8[20]	#69b 5fc	chassis
Plate2	C1	121	ATTGCGTATATTCCTACCGAAT CTAAAG	28	20[1 18]	25[1 18]	#69b 5fc	chassis
Plate2	C2	122	TACCATACTGATTGTTAATGCAT CAATA	28	20[1 60]	25[1 60]	#69b 5fc	chassis
Plate2	C3	123	ATTTGTAGCGCATAAAGATAAG AGCCAG	28	20[9 7]	25[9 7]	#69b 5fc	chassis
Plate2	C4	124	AGGCAAAGCAAGGCAACAGCC ATATTAT	28	45[1 40]	3[15 3]	#69b 5fc	chassis
Plate2	C5	125	TTTAAACGTAGAAAAGACCCTG TATTT	27	1[20]	46[2 3]	#69b 5fc	chassis
Plate2	C6	126	TTTGTGCGAGAGGGTTGATTAGA GATTT	27	11[2 0]	36[2 3]	#69b 5fc	chassis
Plate2	C7	127	TTTGTCCACCAGTACAGCCCGAA AGTTT	27	13[2 0]	34[2 3]	#69b 5fc	chassis
Plate2	C8	128	TTTAGGAATTGCGAAATAAATC AATTT	27	15[2 0]	32[2 3]	#69b 5fc	chassis
Plate2	C9	129	TTTATTCGGTCGCTGCCAATAC TGTTT	27	17[2 0]	30[2 3]	#69b 5fc	chassis
Plate2	C10	130	TTTAAGGCACCAACCAACCAAA ATTTT	27	19[2 0]	28[2 3]	#69b 5fc	chassis

Plate Name	Well	Staple ID	Sequence	Length	CN 5' pos	CN 3' pos	Staple Color	Note
Plate2	C11	131	TTTACGGTCAATCATATACATAA CTTT	27	21[2 0]	26[2 3]	#69b 5fc	chassis
Plate2	C12	132	TTTCTGACGAGAAACGAACTAA CGTTT	27	23[2 0]	24[2 3]	#69b 5fc	chassis
Plate2	D1	133	TTTATTCATTAAGGGGCAAGG CATT	27	3[20]	44[2 3]	#69b 5fc	chassis
Plate2	D2	134	TTTCTGGTCTGGTCAACGGGTA TTTTT	27	40[1 96]	7[19 3]	#69b 5fc	chassis
Plate2	D3	135	TTTAGAGACGCAGAAGAGGTTT TGTTT	27	42[1 96]	5[19 3]	#69b 5fc	chassis
Plate2	D4	136	TTTTGCGGGCCTCTTTTTGTTTA ATTT	27	44[1 96]	3[19 3]	#69b 5fc	chassis
Plate2	D5	137	TTTCAACATTAATGCAATAATA ATTT	27	46[1 96]	1[19 3]	#69b 5fc	chassis
Plate2	D6	138	TTTCTGTAGCGCTTTTTTCATT GTTT	27	5[20]	42[2 3]	#69b 5fc	chassis
Plate2	D7	139	TTTACCACCAGAGCCCCAATT CTTTT	27	7[20]	40[2 3]	#69b 5fc	chassis
Plate2	D8	140	TTTATAAGTTTTAACAATGCTGT ATTT	27	9[20]	38[2 3]	#69b 5fc	chassis
Plate2	D9	141	TAACCCTATACACTAAAACAC	21	28[6 2]	19[6 9]	#69b 5fc	chassis
Plate2	D10	142	TTAAACAAATCTCCAAAAAAA	21	32[6 2]	15[6 9]	#69b 5fc	chassis
Plate2	D11	143	GCGGCCATGCCCCCTGCCTAT	21	38[8 3]	9[90]	#69b 5fc	chassis
Plate2	D12	144	GTAGCATTGAGCCATTGTTGGG	21	44[6 2]	3[69]	#69b 5fc	chassis
Plate2	E1	145	????TCTGGTCGAAGGTTCTTT GCCCGAACGTTATT???	40	50[1 64]	23[1 82]	#f793 1e	biotin anchor
Plate2	E2	146	????CAGTGCCACGCTGAAACA GAGCAGATTCCTACATT	39	50[8 0]	28[8 4]	#f793 1e	biotin anchor
Plate2	E3	147	????CGCAAGGGCTAAATCGGT TGTAAGCCTCAGAGCA	39	52[5 9]	45[6 2]	#f793 1e	biotin anchor
Plate2	E4	148	????CAGCAAATGAAAAACGAAC CACAGTAAT	32	50[1 01]	27[1 11]	#f793 1e	biotin anchor
Plate2	E5	149	????CATCACCTTGCTGAATCGC CAGGCCAAC	32	50[1 22]	27[1 32]	#f793 1e	biotin anchor
Plate2	E6	150	????ATATCAATAGGAGCATTTCG ACAACCTCGT	32	50[1 43]	23[1 53]	#f793 1e	biotin anchor
Plate2	E7	151	????TCAGTTGTGGGAAGGGCT TGAGATGGTT	32	50[5 9]	23[6 9]	#f793 1e	biotin anchor
Plate2	E8	152	????TTCGCATTAATTTTTGATA ATCAGAAA	32	52[1 01]	48[9 8]	#f793 1e	biotin anchor

Plate Name	Well	Staple ID	Sequence	Length	CN 5' pos	CN 3' pos	Staple Color	Note
Plate2	E9	153	????ATCAGCTATGGGATCAAAG TCAGAGGGT	32	52[1 22]	1[13 2]	#f793 1e	biotin anchor
Plate2	E10	154	????TAGGAACACAAACGGCGG ATTGGAACC	32	52[1 43]	45[1 39]	#f793 1e	biotin anchor
Plate2	E11	155	????TTCGCGTCCCGTCGCCAC AAGAATTGAG	32	52[1 64]	1[17 4]	#f793 1e	biotin anchor
Plate2	E12	156	????AACGTTATGCATCTACCAC GGAATAAGT	32	52[8 0]	1[90]	#f793 1e	biotin anchor
Plate2	F1	157	?????GAACAACATTATTACAATA AAACACCAGAACGAGTAG	42	25[2 1]	23[4 8]	#730 0de	no dye
Plate2	F2	158	?????GTTGAAAGGAATTGAGAG TTGGCAAATCAACA???	40	24[1 88]	25[1 86]	#730 0de	no dye
Plate2	F3	159	?????CTGAGAGTCTGGTCCTGT AGCCAGCTTTCAT???	39	48[1 91]	47[1 96]	#730 0de	no dye
Plate2	F4	160	?????ATGCCTGAGTAATATTAC GCAGTATGTTAGC???	39	49[2 5]	0[20]	#730 0de	no dye
Plate2	F5		empty					
Plate2	F6		empty					
Plate2	F7		empty					
Plate2	F8		empty					
Plate2	F9		empty					
Plate2	F10		empty					
Plate2	F11		empty					
Plate2	F12		empty					
Plate2	G1		empty					
Plate2	G2		empty					
Plate2	G3		empty					
Plate2	G4		empty					
Plate2	G5		empty					
Plate2	G6		empty					
Plate2	G7		empty					
Plate2	G8		empty					
Plate2	G9		empty					
Plate2	G10		empty					
Plate2	G11		empty					
Plate2	G12		empty					
Plate2	H1		empty					
Plate2	H2		empty					
Plate2	H3		empty					

Plate Name	Well	Staple ID	Sequence	Length	CN 5' pos	CN 3' pos	Staple Color	Note
Plate2	H4		empty					
Plate2	H5		empty					
Plate2	H6		empty					
Plate2	H7		empty					
Plate2	H8		empty					
Plate2	H9		empty					
Plate2	H10		empty					
Plate2	H11		empty					
Plate2	H12		empty					
			SEPARATE TUBE ORDER					
Tube Name	Staple ID	Sequence	Length	CN 5' pos	CN 3' pos	Staple Color	Note	
DyeTube1	157+dye	/5ATTO647NN/TTTCTGAGAGTC TGGTCCTGTAGCCAGCTTTCAT TTT	42	25[21]	23[48]	#7300de	+ATTO 847N dye	
DyeTube2	158+dye	/5ATTO647NN/TTTATGCCTGAG TAATATTACGCAGTATGTTAGCT TT	40	24[188]	25[186]	#7300de	+ATTO 847N dye	
DyeTube3	159+dye	/5ATTO647NN/TTTGTTGAAAGG AATTGAGAGTTGGCAAATCAAC ATTT	39	48[191]	47[196]	#7300de	+ATTO 847N dye	
DyeTube4	160+dye	/5ATTO647NN/TTTGAACAACAT TATTACAATAAAACACCAGAAC GAGTAG	39	49[25]	0[20]	#7300de	+ATTO 847N dye	

Table S3.2 Sequences and setup for plates 3: No ligand

Plate 3-L (No Ligand)						
Plate	Well	Sequence	Length	CN 5' pos	CN 3' pos	CN Color
Plate3-L	A1	CGACATTAGAAACGCAAAAGAACTGGCA	28	2[69]	51[76]	#cee7fe
Plate3-L	A2	AAAACAGGAAGATTGGAGACAAATAACG	28	48[90]	51[97]	#cee7fe
Plate3-L	A3	GTCACAATCAATCATACCAGAAGGAAAC	28	1[98]	51[118]	#cee7fe

Plate 3-L (No Ligand)						
Plate	Well	Sequence	Length	CN 5' pos	CN 3' pos	CN Color
Plate3-L	A4	TGTC AATCATATGTAGCTGATTAGCCGA	28	48[132]	51[139]	#cee7fe
Plate3-L	A5	AACATAAATCAGAGGAAGCCCTTTTTAA	28	2[153]	51[160]	#cee7fe
Plate3-L	A6	AGCAAACAAGAGAAATCTACAATAGCTA	28	48[174]	51[181]	#cee7fe
Plate3-L	A7	TGATTAATGGCAACATATAACAACCGA	28	0[55]	53[76]	#cee7fe
Plate3-L	A8	CCAATGAAAATCACCCAGCGCCAAAGAC	28	4[90]	53[97]	#cee7fe
Plate3-L	A9	TTAACTGAAAGAAAATTCATA	21	2[118]	53[118]	#cee7fe
Plate3-L	A10	TTACCAACCAGTTAATTAGACGGGAGAA	28	4[132]	53[139]	#cee7fe
Plate3-L	A11	GAAAAGTAATTGAGCGCTAATAACAGG	28	0[139]	53[160]	#cee7fe
Plate3-L	A12	TTAGTTGATAAGAAAGCAGCCTTTACAG	28	4[174]	53[181]	#cee7fe
Plate3-L	B1	GAACCGCTTATTAGGCACCGTAATCAGT	28	6[69]	55[76]	#cee7fe
Plate3-L	B2	AAAAGGGAATTAGAGCCAGCAAACCATC	28	2[76]	55[97]	#cee7fe
Plate3-L	B3	ACCGGAACCAGACATTAGCAAGGCCGGA	28	5[98]	55[118]	#cee7fe
Plate3-L	B4	ACCATTACCATTTCCAGAGCCTAATTTGCGCTAAC	35	3[98]	55[139]	#cee7fe
Plate3-L	B5	TTTTTATACGCGAGGCTACAATTTTATC	28	6[153]	55[160]	#cee7fe
Plate3-L	B6	AGAGAATTTATCCCAATCCAATTTTTAGCGACACGGTCATAGCCCCCACCCTC	28	2[160]	55[181]	#cee7fe
Plate3-L	B7	CAGTCTCTATTACCCCTCAGAGCCGCC	28	4[55]	57[76]	#cee7fe
Plate3-L	B8	AATAGCAAGGCCACCACCGGA	21	6[118]	57[97]	#cee7fe
Plate3-L	B9	GATAAGTTTACGAGTCATTACCGCGCCC	28	8[90]	57[118]	#cee7fe
Plate3-L	B10	CTGAATCCCGGTATTCTAAGATTTTCATC	28	8[132]	57[139]	#cee7fe
Plate3-L	B11	ACATGTTTTATCATTTCATCGAGAACAAG	28	4[139]	57[160]	#cee7fe
Plate3-L	B12	GGATTAGGTATAAACAGTAAGCGTCATA	28	8[174]	57[181]	#cee7fe
Plate3-L	C1	GGATTAGGTATAAACAGTAAGCGTCATA	28	10[69]	59[76]	#cee7fe

Plate 3-L (No Ligand)						
Plate	Well	Sequence	Length	CN 5' pos	CN 3' pos	CN Color
Plate3-L	C2	ACCTCAACGATTGGCCTTGATGAATTT	28	6[76]	59[97]	#cee7fe
Plate3-L	C3	CCTATTATTCTGATATAAAGCCAGAATG	28	9[98]	59[118]	#cee7fe
Plate3-L	C4	TAAATCCTCATTAAATATCCCATCCTAATCCTGAAC	35	7[98]	59[139]	#cee7fe
Plate3-L	C5	ACAGTAGAGAGAATCGCGCCTGTTTATC	28	10[153]	59[160]	#cee7fe
Plate3-L	C6	CAAGCCGTCGGCTGTCTTTCCCAGCTAACATGGCTGAGTAACAGTGCCCGATTAGC	28	6[160]	59[181]	#cee7fe
Plate3-L	C7	GAGCCACGTACCGCGGCTGAGACTCCTC	28	8[55]	61[76]	#cee7fe
Plate3-L	C8	GAGCCACGTACCGCGGCTGAGACTCCTC	28	12[90]	61[97]	#cee7fe
Plate3-L	C9	AACGCCAACAAACATGAAAGT	21	10[118]	61[118]	#cee7fe
Plate3-L	C10	GACCGTGCGGAATCTCGCCATATTTAAC	28	12[132]	61[139]	#cee7fe
Plate3-L	C11	AACAATATCGAGCCAGTAATAGGCTTAA	28	8[139]	61[160]	#cee7fe
Plate3-L	C12	TTTTCTTACCAGTATAAAGCCA CAACTTTCAGCCCTGGGATAGCAAGCC C	22	10[182]	61[181]	#cee7fe
Plate3-L	D1	CAACTTTCAGCCCTGGGATAGCAAGCC C	28	14[69]	63[76]	#cee7fe
Plate3-L	D2	AAGAGAACTCAGGAGGTTTACACCCTC	28	10[76]	63[97]	#cee7fe
Plate3-L	D3	GTCGTCTTTCCAAATTCTCAGAACCGCC	28	13[98]	63[118]	#cee7fe
Plate3-L	D4	AGAACCGCCACCAAATAAGAATAAACAC TGATAAA	35	11[98]	63[139]	#cee7fe
Plate3-L	D5	CTGAGAGACAAAGAAATTTAATGGTTTG	28	14[153]	63[160]	#cee7fe
Plate3-L	D6	ACGCTCATTTAGTATCATATGCATCTTC	28	10[160]	63[181]	#cee7fe
Plate3-L	D7	AATAGGATAGCATTCCACAGACAACAGT	28	12[55]	65[76]	#cee7fe
Plate3-L	D8	CTTAAACGCCTTTATCTGTATGGGATTT	28	16[90]	65[97]	#cee7fe
Plate3-L	D9	GGGTTATATGACGTTAGTAAA	21	14[118]	65[118]	#cee7fe
Plate3-L	D10	CCTTGCTTTAGAATCTCCGGCTTAGGTT	28	16[132]	65[139]	#cee7fe
Plate3-L	D11	AAATACCAATCCAATCGCAAGACTACCT	28	12[139]	65[160]	#cee7fe

Plate 3-L (No Ligand)						
Plate	Well	Sequence	Length	CN 5' pos	CN 3' pos	CN Color
Plate3-L	D12	TTTATAGTGAATTTATCAAAAT	22	14[182]	65[181]	#cee7fe
Plate3-L	E1	CATGAGGTGCGGGAAGTTGCGCCGACA A	28	18[69]	67[76]	#cee7fe
Plate3-L	E2	TGCTAAAAGGCTCCAAAAGGAAGCTTGA	28	14[76]	67[97]	#cee7fe
Plate3-L	E3	TCGGAACGAGGGCACTTTGCTTTTCGAG G	28	17[98]	67[118]	#cee7fe
Plate3-L	E4	CGGTTTATCAGCATTAAATTTTCCCT CTGTAA	35	15[98]	67[139]	#cee7fe
Plate3-L	E5	TACAAAATTAATTTCAATATATGTGAG	28	18[153]	67[160]	#cee7fe
Plate3-L	E6	CATAGGTTTAGATTAAGACGCAAACAGT	28	14[160]	67[181]	#cee7fe
Plate3-L	E7	TGACAACCTAAAGGCCGCTTTAAGTTTC	28	16[55]	69[76]	#cee7fe
Plate3-L	E8	TCATCGCCAGCGATTTTGAGGACTAAAG	28	20[90]	69[97]	#cee7fe
Plate3-L	E9	TTACCTGAGTAGCAACGGCTA	21	18[118]	69[118]	#cee7fe
Plate3-L	E10	ACAGAAATCAGATGATTATTCATTTCAA	28	20[132]	69[139]	#cee7fe
Plate3-L	E11	TGAATAAATCAAGAAAACAAATCGCGCA	28	16[139]	69[160]	#cee7fe
Plate3-L	E12	TTTTCGCCTGATTGCTTTGAAT	22	18[182]	69[181]	#cee7fe
Plate3-L	F1	CCCAAATGAGGACACGAAATCCGCGAC C	28	22[69]	71[76]	#cee7fe
Plate3-L	F2	ACTTTTTTCATCTTTGACCCCCTGATAA GGCTGGCTGACCTCAGAGTACAACGGA	28	18[76]	71[97]	#cee7fe
Plate3-L	F3	G	28	21[98]	71[118]	#cee7fe
Plate3-L	F4	AGCGCGAAACAAATTTTCAGGTTTAACG TAAAGAA	35	19[98]	71[139]	#cee7fe
Plate3-L	F5	CATTTTGTATAATCTCAAATTATTTGC	28	22[153]	71[160]	#cee7fe
Plate3-L	F6	ACCAAGTTTACATCGGGAGAATAGAACC	28	18[160]	71[181]	#cee7fe
Plate3-L	F7	TGCTCCAGACCAACTTTGAAACAACGTA	28	20[55]	73[76]	#cee7fe
Plate3-L	F8	AACTTTAATCATTGACAAGAACCGGATA	28	23[77]	73[97]	#cee7fe
Plate3-L	F9	GAATTATCATTATCAAGAGT	21	22[118]	73[118]	#cee7fe

Plate 3-L (No Ligand)						
Plate	Well	Sequence	Length	CN 5' pos	CN 3' pos	CN Color
Plate3-L	F10	AAGTATTAGACTTTCCACCAGAAGGAGCG	28	23[119]	73[139]	#cee7fe
Plate3-L	F11	ACGTAAATGGCAATTCATCAACGGAACA	28	20[139]	73[160]	#cee7fe
Plate3-L	F12	TTTAATTTTAAAAGTTTGAGTA	22	22[182]	73[181]	#cee7fe
Plate3-L	G1	empty				
Plate3-L	G2	empty				
Plate3-L	G3	empty				
Plate3-L	G4	empty				
Plate3-L	G5	empty				
Plate3-L	G6	empty				
Plate3-L	G7	empty				
Plate3-L	G8	empty				
Plate3-L	G9	empty				
Plate3-L	G10	empty				
Plate3-L	G11	empty				
Plate3-L	G12	empty				
Plate3-L	H1	empty				
Plate3-L	H2	empty				
Plate3-L	H3	empty				
Plate3-L	H4	empty				
Plate3-L	H5	empty				
Plate3-L	H6	empty				
Plate3-L	H7	empty				
Plate3-L	H8	empty				
Plate3-L	H9	empty				
Plate3-L	H10	empty				
Plate3-L	H11	empty				
Plate3-L	H12	empty				

Table S3.3 Sequences and setup for plates 3: High-affinity ligand

Plate 3HA (high-affinity 16-bp ligand)						
5T + Ligand:		TTTTTCCACATACATCATATT				
Plate	Well	Sequence	Length	CN 5' pos	CN 3' pos	CN Color
Plate3HA	A1	CGACATTAGAAACGCAAAAGAACTGG CATTTTTCCACATACATCATATT	49	2[69]	51[76]	#ccFB B040
Plate3HA	A2	AAAACAGGAAGATTGGAGACAAATAAC GTTTTTCCACATACATCATATT	49	48[90]	51[97]	#ccFB B040
Plate3HA	A3	GTCACAATCAATCATACCAGAAGGAAA CTTTTTCCACATACATCATATT	49	1[98]	51[118]	#ccFB B040
Plate3HA	A4	TGTCAATCATATGTAGCTGATTAGCCG ATTTTTCCACATACATCATATT	49	48[132]	51[139]	#ccFB B040
Plate3HA	A5	AACATAAATCAGAGGAAGCCCTTTTA ATTTTTCCACATACATCATATT	49	2[153]	51[160]	#ccFB B040
Plate3HA	A6	AGCAAACAAGAGAAATCTACAATAGCT ATTTTTCCACATACATCATATT	49	48[174]	51[181]	#ccFB B040
Plate3HA	A7	TGATTAATGGCAACATATAACAACCG ATTTTTCCACATACATCATATT	49	0[55]	53[76]	#ccFB B040
Plate3HA	A8	CCAATGAAAATCACCCAGCGCCAAAG ACTTTTTCCACATACATCATATT	49	4[90]	53[97]	#ccFB B040
Plate3HA	A9	TTAACTGAAAGAAAATTCATATTTTTCC ACATACATCATATT	42	2[118]	53[118]	#ccFB B040
Plate3HA	A10	TTACCAACCAGTTAATTAGACGGGAGA ATTTTTCCACATACATCATATT	49	4[132]	53[139]	#ccFB B040
Plate3HA	A11	GAAAAGTAATTGAGCGCTAATAAACAG GTTTTTCCACATACATCATATT	49	0[139]	53[160]	#ccFB B040
Plate3HA	A12	TTAGTTGATAAGAAAGCAGCCTTTACA GTTTTTCCACATACATCATATT	49	4[174]	53[181]	#ccFB B040
Plate3HA	B1	GAACCGCTTATTAGGCACCGTAATCA GTTTTTCCACATACATCATATT	49	6[69]	55[76]	#ccFB B040
Plate3HA	B2	AAAAGGGAATTAGAGCCAGCAAACCA TCTTTTTCCACATACATCATATT	49	2[76]	55[97]	#ccFB B040
Plate3HA	B3	ACCGGAACCAGACATTAGCAAGGCCG GATTTTTCCACATACATCATATT	49	5[98]	55[118]	#ccFB B040
Plate3HA	B4	ACCATTACCATTTCCAGAGCCTAATTT GCGCTAACTTTTTCCACATACATCATA TT	56	3[98]	55[139]	#ccFB B040
Plate3HA	B5	TTTTTATACGCGAGGCTACAATTTTAT CTTTTTCCACATACATCATATT	49	6[153]	55[160]	#ccFB B040
Plate3HA	B6	AGAGAATTTATCCCAATCCAATTTTT TTTTTCCACATACATCATATT	49	2[160]	55[181]	#ccFB B040
Plate3HA	B7	AGCGACACGGTCATAGCCCCCACCC TCTTTTTCCACATACATCATATT	49	4[55]	57[76]	#ccFB B040
Plate3HA	B8	CAGTCTCTATTCACCCCTCAGAGCCG CCTTTTTCCACATACATCATATT	49	8[90]	57[97]	#ccFB B040

Plate 3HA (high-affinity 16-bp ligand)						
5T + Ligand:		TTTTTCCACATACATCATATT				
Plate3HA	B9	AATAGCAAGGCCACCACCGGATTTTTCCACATACATCATATT	42	6[118]	57[118]	#ccFB B040
Plate3HA	B10	GATAAGTTTACGAGTCATTACCGCGCCCTTTTTCCACATACATCATATT	49	8[132]	57[139]	#ccFB B040
Plate3HA	B11	CTGAATCCCGGTATTCTAAGATTTTCATCTTTTTCCACATACATCATATT	49	4[139]	57[160]	#ccFB B040
Plate3HA	B12	ACATGTTTTATCATTTCATCGAGAACAA GTTTTTCCACATACATCATATT	49	8[174]	57[181]	#ccFB B040
Plate3HA	C1	GGATTAGGTATAAACAGTAAGCGTCATATTTTTCCACATACATCATATT	49	10[69]	59[76]	#ccFB B040
Plate3HA	C2	ACCCTCAACGATTGGCCTTGATGAATT TTTTTCCACATACATCATATT	49	6[76]	59[97]	#ccFB B040
Plate3HA	C3	CCTATTATTCTGATATAAAGCCAGAAT GTTTTTCCACATACATCATATT	49	9[98]	59[118]	#ccFB B040
Plate3HA	C4	TAAATCCTCATTAAATATCCCATCCTAAT CCTGAACTTTTTCCACATACATCATATT	56	7[98]	59[139]	#ccFB B040
Plate3HA	C5	ACAGTAGAGAGAATCGCGCCTGTTTATCTTTTTCCACATACATCATATT	49	10[153]	59[160]	#ccFB B040
Plate3HA	C6	CAAGCCGTCGGCTGTCTTTCCAGCTAATTTTTCCACATACATCATATT	49	6[160]	59[181]	#ccFB B040
Plate3HA	C7	CATGGCTGAGTAACAGTGCCCGATTA GCTTTTTCCACATACATCATATT	49	8[55]	61[76]	#ccFB B040
Plate3HA	C8	GAGCCACGTACCGCGGCTGAGACTCCTTTTTCCACATACATCATATT	49	12[90]	61[97]	#ccFB B040
Plate3HA	C9	AACGCCAACAAACATGAAAGTTTTTTCACATACATCATATT	42	10[118]	61[118]	#ccFB B040
Plate3HA	C10	GACCGTGCGGAATCTCGCCATATTTAACTTTTTCCACATACATCATATT	49	12[132]	61[139]	#ccFB B040
Plate3HA	C11	AACAATATCGAGCCAGTAATAGGCTTAATTTTTCCACATACATCATATT	49	8[139]	61[160]	#ccFB B040
Plate3HA	C12	TTTTCTTACCAGTATAAAGCCATTTTTCCACATACATCATATT	43	10[182]	61[181]	#ccFB B040
Plate3HA	D1	CAACTTTCAGCCCTGGGATAGCAAGCCCTTTTTCCACATACATCATATT	49	14[69]	63[76]	#ccFB B040
Plate3HA	D2	AAGAGAACTCAGGAGTTTACACCCCTTTTTCCACATACATCATATT	49	10[76]	63[97]	#ccFB B040
Plate3HA	D3	GTCGTCTTCCAAATTCTCAGAACCGCCTTTTTCCACATACATCATATT	49	13[98]	63[118]	#ccFB B040
Plate3HA	D4	AGAACCGCCACCAAATAAGAATAAACACTGATAAATTTTTCCACATACATCATATT	56	11[98]	63[139]	#ccFB B040
Plate3HA	D5	CTGAGAGACAAAGAAATTTAATGGTTGTTTTTCCACATACATCATATT	49	14[153]	63[160]	#ccFB B040
Plate3HA	D6	ACGCTCATTTAGTATCATATGCATCTCTTTTTCCACATACATCATATT	49	10[160]	63[181]	#ccFB B040

Plate 3HA (high-affinity 16-bp ligand)						
5T + Ligand:		TTTTTCCACATACATCATATT				
Plate3HA	D7	AATAGGATAGCATTCCACAGACAACAG TTTTTCCACATACATCATATT	49	12[55]	65[76]	#ccFB B040
Plate3HA	D8	CTTAAACGCCTTTATCTGTATGGGATT TTTTTCCACATACATCATATT	49	16[90]	65[97]	#ccFB B040
Plate3HA	D9	GGGTTATATGACGTTAGTAAATTTTTTC CACATACATCATATT	42	14[11 8]	65[11 8]	#ccFB B040
Plate3HA	D10	CCTTGCTTTAGAATCTCCGGCTTAGGT TTTTTCCACATACATCATATT	49	16[13 2]	65[13 9]	#ccFB B040
Plate3HA	D11	AAATACCAATCCAATCGCAAGACTACC TTTTTCCACATACATCATATT	49	12[13 9]	65[16 0]	#ccFB B040
Plate3HA	D12	TTTATAGTGAATTTATCAAAATTTTTTC CACATACATCATATT	43	14[18 2]	65[18 1]	#ccFB B040
Plate3HA	E1	CATGAGGTGCGGGAAGTTGCGCCGAC AATTTTTCCACATACATCATATT	49	18[69]	67[76]	#ccFB B040
Plate3HA	E2	TGCTAAAAGGCTCCAAAAGGAAGCTT GATTTTTCCACATACATCATATT	49	14[76]	67[97]	#ccFB B040
Plate3HA	E3	TCGGAACGAGGGCACTTTGCTTTCGA GGTTTTTCCACATACATCATATT	49	17[98]	67[11 8]	#ccFB B040
Plate3HA	E4	CGGTTTATCAGCATTAAATTTTTCCC TCTGTAATTTTTCCACATACATCATATT	56	15[98]	67[13 9]	#ccFB B040
Plate3HA	E5	TACAAAATTAATTTCAATATATGTGAG TTTTTCCACATACATCATATT	49	18[15 3]	67[16 0]	#ccFB B040
Plate3HA	E6	CATAGGTTTAGATTAAGACGCAAACAG TTTTTCCACATACATCATATT	49	14[16 0]	67[18 1]	#ccFB B040
Plate3HA	E7	TGACAACCTAAAGGCCGCTTTAAGTTT CTTTTTCCACATACATCATATT	49	16[55]	69[76]	#ccFB B040
Plate3HA	E8	TCATCGCCAGCGATTTTGAGGACTAAA GTTTTTCCACATACATCATATT	49	20[90]	69[97]	#ccFB B040
Plate3HA	E9	TTACCTGAGTAGCAACGGCTATTTTTTC CACATACATCATATT	42	18[11 8]	69[11 8]	#ccFB B040
Plate3HA	E10	ACAGAAATCAGATGATTATTCATTTCA ATTTTTCCACATACATCATATT	49	20[13 2]	69[13 9]	#ccFB B040
Plate3HA	E11	TGAATAAATCAAGAAAACAAATCGCGC ATTTTTCCACATACATCATATT	49	16[13 9]	69[16 0]	#ccFB B040
Plate3HA	E12	TTTTCGCCTGATTGCTTTGAATTTTTTC CACATACATCATATT	43	18[18 2]	69[18 1]	#ccFB B040
Plate3HA	F1	CCCAAATGAGGACACGAAATCCGCGA CCTTTTTCCACATACATCATATT	49	22[69]	71[76]	#ccFB B040
Plate3HA	F2	ACTTTTTTCATCTTTGACCCCCTGATAA TTTTTCCACATACATCATATT	49	18[76]	71[97]	#ccFB B040
Plate3HA	F3	GGCTGGCTGACCTCAGAGTACAACGG AGTTTTTCCACATACATCATATT	49	21[98]	71[11 8]	#ccFB B040
Plate3HA	F4	AGCGCGAAACAAATTTTCAGTTTAAAC GTAAAGAATTTTTCCACATACATCATAT T	56	19[98]	71[13 9]	#ccFB B040

Plate 3HA (high-affinity 16-bp ligand)						
5T + Ligand:		TTTTTCCACATACATCATATT				
Plate3HA	F5	CATTTTGTATAATCTCAAAATTATTTGC TTTTTCCACATACATCATATT	49	22[15 3]	71[16 0]	#ccFB B040
Plate3HA	F6	ACCAAGTTTACATCGGGAGAATAGAAC CTTTTTCCACATACATCATATT	49	18[16 0]	71[18 1]	#ccFB B040
Plate3HA	F7	TGCTCCAGACCAACTTTGAAACAACGT ATTTTTCCACATACATCATATT	49	20[55]	73[76]	#ccFB B040
Plate3HA	F8	AACTTTAATCATTGACAAGAACCGGAT ATTTTTCCACATACATCATATT	49	23[77]	73[97]	#ccFB B040
Plate3HA	F9	GAATTATCATTCAAGAGTTTTTTCC ACATACATCATATT	42	22[11 8]	73[11 8]	#ccFB B040
Plate3HA	F10	AAGTATTAGACTTTCCACCAGAAGGAGC GTTTTTCCACATACATCATATT	49	23[11 9]	73[13 9]	#ccFB B040
Plate3HA	F11	ACGTAAATGGCAATTCATCAACGGAAC ATTTTTCCACATACATCATATT	49	20[13 9]	73[16 0]	#ccFB B040
Plate3HA	F12	TTTAATTTTAAAAGTTTGAGTATTTTC CACATACATCATATT	43	22[18 2]	73[18 1]	#ccFB B040
Plate3HA	G1	empty				
Plate3HA	G2	empty				
Plate3HA	G3	empty				
Plate3HA	G4	empty				
Plate3HA	G5	empty				
Plate3HA	G6	empty				
Plate3HA	G7	empty				
Plate3HA	G8	empty				
Plate3HA	G9	empty				
Plate3HA	G10	empty				
Plate3HA	G11	empty				
Plate3HA	G12	empty				
Plate3HA	H1	empty				
Plate3HA	H2	empty				
Plate3HA	H3	empty				
Plate3HA	H4	empty				
Plate3HA	H5	empty				
Plate3HA	H6	empty				
Plate3HA	H7	empty				
Plate3HA	H8	empty				
Plate3HA	H9	empty				
Plate3HA	H10	empty				
Plate3HA	H11	empty				

Plate 3HA (high-affinity 16-bp ligand)					
5T + Ligand:		TTTTTCCACATACATCATATT			
Plate3HA	H12	empty			

Table S3.4 Sequences and setup for plates 3: Medium-affinity ligand

Plate 3MA (mid-affinity 13-bp ligand)						
7T + Ligand:		TTTTTTTTTCATACATCATATT				
Plate	Well	Sequence	Length	CN 5' pos	CN 3' pos	CN Color
Plate3MA	A1	CGACATTAGAAAACGCAAAGAAGACTGG CATTTTTTTTTTCATACATCATATT	49	2[69]	51[76]	#ccFD 3500
Plate3MA	A2	AAAACAGGAAGATTGGAGACAAATAAC GTTTTTTTTTCATACATCATATT	49	48[90]	51[97]	#ccFD 3500
Plate3MA	A3	GTCACAATCAATCATACCAGAAGGAAA CTTTTTTTTTTCATACATCATATT	49	1[98]	51[118]	#ccFD 3500
Plate3MA	A4	TGTCAATCATATGTAGCTGATTAGCCG ATTTTTTTTTTCATACATCATATT	49	48[132]	51[139]	#ccFD 3500
Plate3MA	A5	AACATAAATCAGAGGAAGCCCTTTTTA ATTTTTTTTTTCATACATCATATT	49	2[153]	51[160]	#ccFD 3500
Plate3MA	A6	AGCAAACAAGAGAAATCTACAATAGCT ATTTTTTTTTTCATACATCATATT	49	48[174]	51[181]	#ccFD 3500
Plate3MA	A7	TGATTAATGGCAACATATAAACAACCG ATTTTTTTTTTCATACATCATATT	49	0[55]	53[76]	#ccFD 3500
Plate3MA	A8	CCAATGAAAATCACCCAGCGCCAAAG ACTTTTTTTTTTCATACATCATATT	49	4[90]	53[97]	#ccFD 3500
Plate3MA	A9	TTAACTGAAAGAAAATTCATATTTTTTT TCATACATCATATT	42	2[118]	53[118]	#ccFD 3500
Plate3MA	A10	TTACCAACCAGTTAATTAGACGGGAGA ATTTTTTTTTTCATACATCATATT	49	4[132]	53[139]	#ccFD 3500
Plate3MA	A11	GAAAAGTAATTGAGCGCTAATAAACAG GTTTTTTTTTCATACATCATATT	49	0[139]	53[160]	#ccFD 3500
Plate3MA	A12	TTAGTTGATAAGAAAGCAGCCTTTACA GTTTTTTTTTCATACATCATATT	49	4[174]	53[181]	#ccFD 3500
Plate3MA	B1	GAACCGCTTATTAGGCACCGTAATCA GTTTTTTTTTCATACATCATATT	49	6[69]	55[76]	#ccFD 3500
Plate3MA	B2	AAAAGGGAATTAGAGCCAGCAAACCA TCTTTTTTTTTTCATACATCATATT	49	2[76]	55[97]	#ccFD 3500
Plate3MA	B3	ACCGGAACCAGACATTAGCAAGGCCG GATTTTTTTTTTCATACATCATATT	49	5[98]	55[118]	#ccFD 3500
Plate3MA	B4	ACCATTACCATTTCCAGAGCCTAATTT GCGCTAACTTTTTTTTTTCATACATCATAT T	56	3[98]	55[139]	#ccFD 3500

Plate 3MA (mid-affinity 13-bp ligand)						
7T + Ligand:		TTTTTTTTTCATACATCATATT				
Plate3MA	B5	TTTTTATACGCGAGGCTACAATTTTAT CTTTTTTTTCATACATCATATT	49	6[153]	55[160]	#ccFD 3500
Plate3MA	B6	AGAGAATTTATCCCAATCCAACATTTTT TTTTTTTTTCATACATCATATT	49	2[160]	55[181]	#ccFD 3500
Plate3MA	B7	AGCGACACGGTCATAGCCCCCACCC TCTTTTTTTTCATACATCATATT	49	4[55]	57[76]	#ccFD 3500
Plate3MA	B8	CAGTCTCTATTACCCCTCAGAGCCG CCTTTTTTTTCATACATCATATT	49	8[90]	57[97]	#ccFD 3500
Plate3MA	B9	AATAGCAAGGCCACCACCGGATTTTTT TTCATACATCATATT	42	6[118]	57[118]	#ccFD 3500
Plate3MA	B10	GATAAGTTTACGAGTCATTACCGCGCC CTTTTTTTTCATACATCATATT	49	8[132]	57[139]	#ccFD 3500
Plate3MA	B11	CTGAATCCCGGTATTCTAAGATTTTCAT CTTTTTTTTCATACATCATATT	49	4[139]	57[160]	#ccFD 3500
Plate3MA	B12	ACATGTTTTATCATTTCATCGAGAACAA GTTTTTTTTTCATACATCATATT	49	8[174]	57[181]	#ccFD 3500
Plate3MA	C1	GGATTAGGTATAAACAGTAAGCGTCAT ATTTTTTTTCATACATCATATT	49	10[69]	59[76]	#ccFD 3500
Plate3MA	C2	ACCCTCAACGATTGGCCTTGATGAATT TTTTTTTTTCATACATCATATT	49	6[76]	59[97]	#ccFD 3500
Plate3MA	C3	CCTATTATTCTGATATAAAGCCAGAAT GTTTTTTTTTCATACATCATATT	49	9[98]	59[118]	#ccFD 3500
Plate3MA	C4	TAAATCCTCATTAATATCCCATCCTAAT CCTGAACTTTTTTTTCATACATCATATT	56	7[98]	59[139]	#ccFD 3500
Plate3MA	C5	ACAGTAGAGAGAATCGCGCCTGTTTAT CTTTTTTTTCATACATCATATT	49	10[153]	59[160]	#ccFD 3500
Plate3MA	C6	CAAGCCGTCGGCTGTCTTTCCAGCT AATTTTTTTTCATACATCATATT	49	6[160]	59[181]	#ccFD 3500
Plate3MA	C7	CATGGCTGAGTAACAGTGCCCGATTA GCTTTTTTTTCATACATCATATT	49	8[55]	61[76]	#ccFD 3500
Plate3MA	C8	GAGCCACGTACCGCGGCTGAGACTCC TCTTTTTTTTCATACATCATATT	49	12[90]	61[97]	#ccFD 3500
Plate3MA	C9	AACGCCAACAAACATGAAAGTTTTTTTT TTCATACATCATATT	42	10[118]	61[118]	#ccFD 3500
Plate3MA	C10	GACCGTGCGGAATCTCGCCATATTTAA CTTTTTTTTCATACATCATATT	49	12[132]	61[139]	#ccFD 3500
Plate3MA	C11	AACAATATCGAGCCAGTAATAGGCTTA ATTTTTTTTCATACATCATATT	49	8[139]	61[160]	#ccFD 3500
Plate3MA	C12	TTTTCTTACCAGTATAAAGCCATTTTTT TTCATACATCATATT	43	10[182]	61[181]	#ccFD 3500
Plate3MA	D1	CAACTTTCAGCCCTGGGATAGCAAGC CCTTTTTTTTCATACATCATATT	49	14[69]	63[76]	#ccFD 3500
Plate3MA	D2	AAGAGAAACTCAGGAGGTTTACACCC TCTTTTTTTTCATACATCATATT	49	10[76]	63[97]	#ccFD 3500

Plate 3MA (mid-affinity 13-bp ligand)						
7T + Ligand:		TTTTTTTTTCATACATCATATT				
Plate3MA	D3	GTCGTCTTCCAAATTCTCAGAACCGC CTTTTTTTTCATACATCATATT	49	13[98]	63[11 8]	#ccFD 3500
Plate3MA	D4	AGAACCGCCACCAAATAAGAATAAACA CTGATAAATTTTTTTTCATACATCATAT T	56	11[98]	63[13 9]	#ccFD 3500
Plate3MA	D5	CTGAGAGACAAAGAAATTTAATGGTTT GTTTTTTTTTCATACATCATATT	49	14[15 3]	63[16 0]	#ccFD 3500
Plate3MA	D6	ACGCTCATTTAGTATCATATGCATCTT CTTTTTTTTCATACATCATATT	49	10[16 0]	63[18 1]	#ccFD 3500
Plate3MA	D7	AATAGGATAGCATTCCACAGACAACAG TTTTTTTTTCATACATCATATT	49	12[55]	65[76]	#ccFD 3500
Plate3MA	D8	CTTAAACGCCTTTATCTGTATGGGATT TTTTTTTTTCATACATCATATT	49	16[90]	65[97]	#ccFD 3500
Plate3MA	D9	GGGTTATATGACGTTAGTAAATTTTTTT TCATACATCATATT	42	14[11 8]	65[11 8]	#ccFD 3500
Plate3MA	D10	CCTTGCTTTAGAATCTCCGGCTTAGGT TTTTTTTTTCATACATCATATT	49	16[13 2]	65[13 9]	#ccFD 3500
Plate3MA	D11	AAATACCAATCCAATCGCAAGACTACC TTTTTTTTTCATACATCATATT	49	12[13 9]	65[16 0]	#ccFD 3500
Plate3MA	D12	TTTATAGTGAATTTATCAAAATTTTTTT TCATACATCATATT	43	14[18 2]	65[18 1]	#ccFD 3500
Plate3MA	E1	CATGAGGTGCGGGAAGTTGCGCCGAC AATTTTTTTTCATACATCATATT	49	18[69]	67[76]	#ccFD 3500
Plate3MA	E2	TGCTAAAAGGCTCCAAAAGGAAGCTT GATTTTTTTTCATACATCATATT	49	14[76]	67[97]	#ccFD 3500
Plate3MA	E3	TCGGAACGAGGGCACTTTGCTTTCGA GGTTTTTTTCATACATCATATT	49	17[98]	67[11 8]	#ccFD 3500
Plate3MA	E4	CGGTTTATCAGCATTAATTAATTTTCCC TCTGTAATTTTTTTTCATACATCATATT	56	15[98]	67[13 9]	#ccFD 3500
Plate3MA	E5	TACAAAAATTAATTTCAATATATGTGAG TTTTTTTTTCATACATCATATT	49	18[15 3]	67[16 0]	#ccFD 3500
Plate3MA	E6	CATAGGTTTAGATTAAGACGCAAACAG TTTTTTTTTCATACATCATATT	49	14[16 0]	67[18 1]	#ccFD 3500
Plate3MA	E7	TGACAACTTAAAGGCCGCTTTAAGTTT CTTTTTTTTCATACATCATATT	49	16[55]	69[76]	#ccFD 3500
Plate3MA	E8	TCATCGCCAGCGATTTTGAGGACTAAA GTTTTTTTTTCATACATCATATT	49	20[90]	69[97]	#ccFD 3500
Plate3MA	E9	TTACCTGAGTAGCAACGGCTATTTTTT TTCATACATCATATT	42	18[11 8]	69[11 8]	#ccFD 3500
Plate3MA	E10	ACAGAAATCAGATGATTATTCATTTCA ATTTTTTTTCATACATCATATT	49	20[13 2]	69[13 9]	#ccFD 3500
Plate3MA	E11	TGAATAAATCAAGAAAACAAATCGCGC ATTTTTTTTCATACATCATATT	49	16[13 9]	69[16 0]	#ccFD 3500
Plate3MA	E12	TTTTCGCCTGATTGCTTTGAATTTTTTT TTCATACATCATATT	43	18[18 2]	69[18 1]	#ccFD 3500

Plate 3MA (mid-affinity 13-bp ligand)						
7T + Ligand:		TTTTTTTTTCATACATCATATT				
Plate3MA	F1	CCCAAATGAGGACACGAAATCCGCGA CCTTTTTTTTTTCATACATCATATT	49	22[69]	71[76]	#ccFD 3500
Plate3MA	F2	ACTTTTTTTCATCTTTGACCCCCTGATAA TTTTTTTTTCATACATCATATT	49	18[76]	71[97]	#ccFD 3500
Plate3MA	F3	GGCTGGCTGACCTCAGAGTACAACGG AGTTTTTTTTTCATACATCATATT	49	21[98]	71[118]	#ccFD 3500
Plate3MA	F4	AGCGCGAAACAAATTTTCAGGTTTAAC GTAAAGAATTTTTTTTTTCATACATCATAT T	56	19[98]	71[139]	#ccFD 3500
Plate3MA	F5	CATTTTGTATAATCTCAAATTTATTTGC TTTTTTTTTCATACATCATATT	49	22[153]	71[160]	#ccFD 3500
Plate3MA	F6	ACCAAGTTTACATCGGGAGAATAGAAC CTTTTTTTTTTCATACATCATATT	49	18[160]	71[181]	#ccFD 3500
Plate3MA	F7	TGCTCCAGACCAACTTTGAAACAACGT ATTTTTTTTTTCATACATCATATT	49	20[55]	73[76]	#ccFD 3500
Plate3MA	F8	AACTTTAATCATTGACAAGAACCGGAT ATTTTTTTTTTCATACATCATATT	49	23[77]	73[97]	#ccFD 3500
Plate3MA	F9	GAATTATCATTCATCAAGATTTTTTTTT TCATACATCATATT	42	22[118]	73[118]	#ccFD 3500
Plate3MA	F10	AAGTATTAGACTTTACCAGAAGGAGC GTTTTTTTTTCATACATCATATT	49	23[119]	73[139]	#ccFD 3500
Plate3MA	F11	ACGTAAATGGCAATTCATCAACGGAAC ATTTTTTTTTTCATACATCATATT	49	20[139]	73[160]	#ccFD 3500
Plate3MA	F12	TTTAATTTTAAAAGTTTGAGTATTTTTTT TCATACATCATATT	43	22[182]	73[181]	#ccFD 3500
Plate3MA	G1	empty				
Plate3MA	G2	empty				
Plate3MA	G3	empty				
Plate3MA	G4	empty				
Plate3MA	G5	empty				
Plate3MA	G6	empty				
Plate3MA	G7	empty				
Plate3MA	G8	empty				
Plate3MA	G9	empty				
Plate3MA	G10	empty				
Plate3MA	G11	empty				
Plate3MA	G12	empty				
Plate3MA	H1	empty				
Plate3MA	H2	empty				
Plate3MA	H3	empty				
Plate3MA	H4	empty				

Plate 3MA (mid-affinity 13-bp ligand)					
7T + Ligand:		TTTTTTTTCATACATCATATT			
Plate3MA	H5	empty			
Plate3MA	H6	empty			
Plate3MA	H7	empty			
Plate3MA	H8	empty			
Plate3MA	H9	empty			
Plate3MA	H10	empty			
Plate3MA	H11	empty			
Plate3MA	H12	empty			

Table S3.5 Key resources

REAGENT or RESOURCE	SOURCE	IDENTIFIER	ADDITIONAL INFO
Antibodies			
AlexaFluor 647 anti-biotin IgG	Jackson Immuno Labs	Cat# 200-602-211	
AlexaFluor 488 anti-biotin IgG	Jackson Immuno Labs	Cat# 200-542-211	
Oligonucleotides			
Receptor DNA strand	this paper	Benzylguanine-5'-AATATGATGTATGTGG -3'	Oligonucleotide was ordered from IDT with a 5' terminal amine. Conjugation to benzylguanine was performed as described (Farlow et al., 2013).
DNA ligand strand	IDT	Biotin-5'- TTTT-TTTCATACATCATATT - 3'-Atto647	

REAGENT or RESOURCE	SOURCE	IDENTIFIER	ADDITIONAL INFO
p8064 DNA scaffold	IDT	Cat # 1081314	
All other oligonucleotides used for origami pegboard are listed in Table 1			
Chemicals, Peptides, and Recombinant Proteins			
Alexa Fluor 488 Phalloidin	Thermo/Molecular Probes	Cat# A12379	
Biotinyl Cap PE	Avanti	Cat# 870273	
POPC	Avanti	Cat# 850457	
PEG5000-PE	Avanti	Cat# 880230	
Atto390 DOPE	ATTO-TEC GmbH	Cat# AD 390-161	
Lipofectamine LTX	ThermoFisher	Cat#15338030	
Lenti-X Concentrator	Takara Biosciences	Cat# 631231	
Pierce Biotinylated Bovine Serum Albumin (Biotin-LC-BSA)	ThermoScientific	Cat#29130	
Neutravidin	ThermoScientific	Cat# 31050	
Experimental Models: Cell Lines			
Lenti-X 293T cell line	Takara Biosciences	Cat# 632180	For lentivirus production
HEK293T cells	UCSF Cell Culture Facility		For lentivirus production
Raw264.7 Macrophages	ATCC	Cat# ATCC® TIB-71™	
THP1 Monocytes	ATCC	Cat# ATCC® TIB-202™	
Recombinant DNA			

REAGENT or RESOURCE	SOURCE	IDENTIFIER	ADDITIONAL INFO
pHR-DNA-CAR γ	this paper	In PhR vector. Signal peptide: (MQSGTHWRVGLGLCLLSVGVWG QD) Derived from CD3 ϵ Extracellular: HA tag plus a linker (LPETGGGGGG), SNAPf (from the pSNAPf plasmid, New England Biolabs) Linker: GGSGGSGGS, TM and intracellular: CD86TM (aa 236-271), cytoplasmic domain (aa 45-86) of the Fc γ -chain UniProtKB - P20491 (FCERG_MOUSE) linker: GSGS, Fluorophore: mGFP or BFP	
pHR-Syk-BFP	adapted from DOI: 10.1016/j.immuni.2020.07.008	CDS: aa1-629 UniProtKB - P48025 (KSYK_MOUSE), Linker: ADPVAT, Fluorophore: BFP	
pHR-DNA-CARadhesion	DOI: 10.1016/j.immuni.2020.07.008	In PhR vector. Signal peptide: (MQSGTHWRVGLGLCLLSVGVWG QD) Derived from CD3 ϵ Extracellular: HA tag plus a linker (LPETGGGGGG), SNAPf (from the pSNAPf plasmid, New England Biolabs) Linker: GGSGGSGGS, TM and intracellular: CD86TM (aa 236-271), linker: SADASGG, Fluorophore: eGFP	
pHR-mNeonGreen-tSH2 Syk	adapted from DOI: 10.1016/j.cell.2018.05.059	CDS: aa2-261 UniProtKB - P48025 (KSYK_MOUSE), Linker: GGGSGGGG, Fluorophore: mNeonGreen	
pHR-Akt PH domain	this paper	CDS: aa1-164 UniProtKB - P31749 (AKT1_HUMAN), Linker: HMTSPVAT, Fluorophore: mGFP	

REAGENT or RESOURCE	SOURCE	IDENTIFIER	ADDITIONAL INFO
pHR-DNA-CAR4 γ	this paper	<p>In PhR vector. Signal peptide: (MQSGTHWRV LGLCLLSVGVWG QD) Derived from CD3ϵ</p> <p>Extracellular: HA tag plus a linker (LPETGGGGGG), SNAPf (from the pSNAPf plasmid, New England Biolabs) Linker: GSGSGSGGS, TM and intracellular: CD86TM (aa 236-271), 4 repeats of the cytoplasmic domain (aa 45-86) of the Fc γ-chain UniProtKB - P20491 (FCERG_MOUSE) with a GSGS linker between each repeat, Linker: GSGS, Fluorophore: mGFP</p>	
pHR-DNA-CAR-1 γ -3x Δ ITAM	this paper	<p>In PhR vector. Signal peptide: (MQSGTHWRV LGLCLLSVGVWG QD) Derived from CD3ϵ</p> <p>Extracellular: HA tag plus a linker (LPETGGGGGG), SNAPf (from the pSNAPf plasmid, New England Biolabs) Linker: GSGSGSGGS, TM and intracellular: CD86TM (aa 236-271), the cytoplasmic domain (aa 45-86) of the Fc γ-chain UniProtKB - P20491 (FCERG_MOUSE) followed by 3 repeats of the cytoplasmic domain (aa 45-86) of the Fc γ-chain UniProtKB - P20491 (FCERG_MOUSE) with aa65 and aa76 mutated from YtoF and a GSGS linker between each repeat, Linker: GSGS, Fluorophore: mGFP</p>	

REAGENT or RESOURCE	SOURCE	IDENTIFIER	ADDITIONAL INFO
pHR-DNA-CAR γ human	this paper	In PhR vector. Signal peptide: (MQSGTHWRVGLGLCLLSVGVWG QD) Derived from CD3 ϵ Extracellular: HA tag plus a linker (LPETGGGGGG), SNAPf (from the pSNAPf plasmid, New England Biolabs) Linker: GGSGGSGGS, TM and intracellular: CD86 TM (aa 236-271), cytoplasmic domain (aa 45-86) of the Fc γ -chain UniProtKB - P30273 (FCERG_HUMAN) linker: GSGS, Fluorophore: mGFP or BFP	
pMD2.G lentiviral plasmid	D. Stainier, Max Planck; VSV-G envelope	Addgene 12259	
pCMV-dR8.91	DOI: 10.1038/nature11220.	Current Addgene 8455	
pHRSIN-CSGW	DOI: 10.1038/nature11220.		
Software and Algorithms			
ImageJ	NIH		
Affinity Designer			
Fiji	https://fiji.sc/		
Prism	GraphPad	8	
Micromanager	DOI:10.14440/jbm.2014.36		
Other			
5 μ m silica microspheres	Bangs	Cat# SS05N	
MatriPlate	Brooks	Cat# MGB096-1-2-LG-L	
96 well round bottomed plates	Corning	Cat# 38018	
Illustra NAP-5 columns	Cytiva	Cat# 17085301	

3.7 Acknowledgements

We thank N. Stuurman for help with microscopy and developing the 'image randomizer' plug-in for blinding our analysis as well as the 'Spot Intensity in All Channel' plugin for quantification of our TIRF experiments. We also thank K. McKinley, T. Skokan, C. Gladkova, J. Sheu-Gruttadauria for discussions and critical feedback on this manuscript. M.A.M. was supported by the National Institute of General Medical Sciences of the National Institutes of Health under award number F32GM120990. Funding was provided by the Howard Hughes Medical Institute to R.D.V.

3.8 Author Contributions

N.K., R.D.V., and M.A.M. designed research; N.K. performed research; N.K., R.D., S.D. and M.A.M. contributed new reagents/analytic tools; N.K. analyzed data; and N.K., R.D.V., and M.A.M wrote the paper.

3.9 References

1. Erwig, L. P. & Gow, N. A. R. Interactions of fungal pathogens with phagocytes. *Nature Reviews Microbiology* **14**, 163–176 (2016).
2. Dilillo, D. J., Tan, G. S., Palese, P. & Ravetch, J. V. Broadly neutralizing hemagglutinin stalk-specific antibodies require FcR interactions for protection against influenza virus in vivo. *Nat. Med.* **20**, 143–151 (2014).
3. Nimmerjahn, F. & Ravetch, J. V. Fcγ receptors as regulators of immune responses. *Nat. Rev. Immunol.* (2008). doi:10.1038/nri2206
4. Uchida, J. *et al.* The innate mononuclear phagocyte network depletes B lymphocytes through Fc receptor-dependent mechanisms during anti-CD20 antibody immunotherapy. *J. Exp. Med.* **199**, 1659–1669 (2004).
5. Weiskopf, K. *et al.* Engineered SIRPα variants as immunotherapeutic adjuvants to anticancer antibodies. *Science (80-.)*. **341**, 88–91 (2013).
6. Chao, M. P. *et al.* Anti-CD47 Antibody Synergizes with Rituximab to Promote Phagocytosis and Eradicate Non-Hodgkin Lymphoma. *Cell* **142**, 699–713 (2010).
7. Weiskopf, K. & Weissman, I. L. Macrophages are critical effectors of antibody therapies for cancer. *mAbs* **7**, 303–310 (2015).
8. Watanabe, M. *et al.* Antibody dependent cellular phagocytosis (ADCP) and antibody dependent cellular cytotoxicity (ADCC) of breast cancer cells mediated by bispecific antibody, MDX-210. *Breast Cancer Res. Treat.* **53**, 199–207 (1999).
9. Griffin, F. M., Griffin, J. A., Leider, J. E. & Silverstein, S. C. Studies on the mechanism of phagocytosis. I. Requirements for circumferential attachment of particle-bound ligands to specific receptors on the macrophage plasma membrane. *J. Exp. Med.* **142**, 1263–1282 (1975).
10. Zhang, Y., Hoppe, A. D. & Swanson, J. A. Coordination of Fc receptor signaling regulates

- cellular commitment to phagocytosis. *Proc. Natl. Acad. Sci. U. S. A.* **107**, 19332–19337 (2010).
11. Ma, Y., Lim, Y., Benda, A., Goyette, J. & Gaus, K. Clustering of CD3 ζ is sufficient to initiate T cell receptor signaling. (2020). doi:10.1101/2020.02.17.953463
 12. Davis, S. J. & van der Merwe, P. A. The kinetic-segregation model: TCR triggering and beyond. *Nat. Immunol.* **7**, 803–809 (2006).
 13. Holowka, D. & Baird, B. Antigen-Mediated IGE Receptor Aggregation and Signaling: A Window on Cell Surface Structure and Dynamics. *Annu. Rev. Biophys. Biomol. Struct.* **25**, 79–112 (1996).
 14. Kato, Y. *et al.* Multifaceted Effects of Antigen Valency on B Cell Response Composition and Differentiation *In Vivo*. (2020). doi:10.1016/j.immuni.2020.08.001
 15. Veneziano, R. *et al.* Role of nanoscale antigen organization on B-cell activation probed using DNA origami. *bioRxiv* 2020.02.16.951475 (2020). doi:10.1101/2020.02.16.951475
 16. Berger, R. M. L. *et al.* Nanoscale Organization of FasL on DNA Origami as a Versatile Platform to Tune Apoptosis Signaling in Cells. doi:10.1101/2020.07.05.187203
 17. Goodridge, H. S., Underhill, D. M. & Touret, N. Mechanisms of Fc Receptor and Dectin-1 Activation for Phagocytosis. *Traffic* **13**, 1062–1071 (2012).
 18. Sobota, A. *et al.* Binding of IgG-Opsonized Particles to Fc γ R Is an Active Stage of Phagocytosis That Involves Receptor Clustering and Phosphorylation. *J. Immunol.* **175**, 4450–4457 (2005).
 19. Lopes, F. B. *et al.* Membrane nanoclusters of Fc γ R1 segregate from inhibitory SIRP α upon activation of human macrophages. *J. Cell Biol.* jcb.201608094 (2017). doi:10.1083/jcb.201608094
 20. Lin, J. *et al.* TIRF imaging of Fc gamma receptor microclusters dynamics and signaling on macrophages during frustrated phagocytosis. *BMC Immunol.* **17**, 5 (2016).
 21. Jaumouillé, V. *et al.* Actin cytoskeleton reorganization by syk regulates fcy receptor

- responsiveness by increasing its lateral mobility and clustering. *Dev. Cell* **29**, 534–546 (2014).
22. Taylor, M. J., Husain, K., Gartner, Z. J., Mayor, S. & Vale, R. D. A DNA-Based T Cell Receptor Reveals a Role for Receptor Clustering in Ligand Discrimination. *Cell* **169**, 108-119.e20 (2017).
 23. Morrissey, M. A. *et al.* Chimeric antigen receptors that trigger phagocytosis. *Elife* (2018). doi:10.7554/eLife.36688
 24. Li, P. *et al.* Affinity and kinetic analysis of Fcγ receptor IIIa (CD16a) binding to IgG ligands. *J. Biol. Chem.* **282**, 6210–6221 (2007).
 25. Morrissey, M. A., Kern, N. & Vale, R. D. CD47 Ligation Repositions the Inhibitory Receptor SIRPA to Suppress Integrin Activation and Phagocytosis. *Immunity* **53**, 290-302.e6 (2020).
 26. Bakalar, M. H. *et al.* Size-Dependent Segregation Controls Macrophage Phagocytosis of Antibody-Opsonized Targets. *Cell* (2018). doi:10.1016/j.cell.2018.05.059
 27. Rothmund, P. W. K. Folding DNA to create nanoscale shapes and patterns. *Nature* **440**, 297–302 (2006).
 28. Seeman, N. C. Nanomaterials Based on DNA. *Annu. Rev. Biochem.* **79**, 65–87 (2010).
 29. Hong, F., Zhang, F., Liu, Y. & Yan, H. *DNA Origami: Scaffolds for Creating Higher Order Structures. Chemical Reviews* **117**, (2017).
 30. Shaw, A. *et al.* Binding to nanopatterned antigens is dominated by the spatial tolerance of antibodies. *Nat. Nanotechnol.* **14**, 184–190 (2019).
 31. Duchemin, A. M., Ernst, L. K. & Anderson, C. L. Clustering of the high affinity Fc receptor for immunoglobulin G (FcγRI) results in phosphorylation of its associated γ-chain. *J. Biol. Chem.* **269**, 12111–12117 (1994).
 32. Bakalar, M. H. *et al.* Size-Dependent Segregation Controls Macrophage Phagocytosis of Antibody-Opsonized Targets. *Cell* **174**, 131-142.e13 (2018).

33. Morrissey, M. A. *et al.* Chimeric antigen receptors that trigger phagocytosis. *Elife* **7**, (2018).
34. Freeman, S. A. *et al.* Integrins Form an Expanding Diffusional Barrier that Coordinates Phagocytosis. *Cell* **164**, 128–140 (2016).
35. Schmid, E. M. *et al.* Size-dependent protein segregation at membrane interfaces. *Nat. Phys.* **12**, 704–711 (2016).
36. Swanson, J. A. & Baer, S. C. Phagocytosis by zippers and triggers. *Trends Cell Biol.* **5**, 89–93 (1995).
37. Ben M'Barek, K. *et al.* Phagocytosis of immunoglobulin-coated emulsion droplets. *Biomaterials* **51**, 270–277 (2015).
38. Gonzalez-Quintela, A. *et al.* Serum levels of immunoglobulins (IgG, IgA, IgM) in a general adult population and their relationship with alcohol consumption, smoking and common metabolic abnormalities. *Clin. Exp. Immunol.* **151**, 42–50 (2008).
39. Kwiatkowska, K. & Sobota, A. The clustered Fcγ receptor II is recruited to Lyn-containing membrane domains and undergoes phosphorylation in a cholesterol-dependent manner. *Eur. J. Immunol.* **31**, 989–998 (2001).
40. Huang, M. M. *et al.* Activation of FcγRII induces tyrosine phosphorylation of multiple proteins including FcγRII. *J. Biol. Chem.* **267**, 5467–5473 (1992).
41. Simons, K. & Ikonen, E. Functional rafts in cell membranes. *Nature* **387**, 569–572 (1997).
42. Eggeling, C. *et al.* Direct observation of the nanoscale dynamics of membrane lipids in a living cell. *Nature* **457**, 1159–1162 (2009).
43. Stone, M. B., Shelby, S. A., Nñez, M. F., Wisser, K. & Veatch, S. L. Protein sorting by lipid phase-like domains supports emergent signaling function in b lymphocyte plasma membranes. *Elife* **6**, 1–33 (2017).
44. Sohn, H. W., Tolar, P., Jin, T. & Pierce, S. K. Fluorescence resonance energy transfer in living cells reveals dynamic membrane changes in the initiation of B cell signaling. *Proc.*

- Natl. Acad. Sci. U. S. A.* **103**, 8143–8148 (2006).
45. Dinic, J., Riehl, A., Adler, J. & Parmryd, I. The T cell receptor resides in ordered plasma membrane nanodomains that aggregate upon patching of the receptor. *Sci. Rep.* **5**, 1–9 (2015).
 46. Kabouridis, P. S. Lipid rafts in T cell receptor signalling (review). *Molecular Membrane Biology* **23**, 49–57 (2006).
 47. Beekman, J. M., van der Linden, J. A., van de Winkel, J. G. J. & Leusen, J. H. W. FcγRI (CD64) resides constitutively in lipid rafts. *Immunol. Lett.* **116**, 149–155 (2008).
 48. Katsumata, O. *et al.* Association of FcγRII with Low-Density Detergent-Resistant Membranes Is Important for Cross-Linking-Dependent Initiation of the Tyrosine Phosphorylation Pathway and Superoxide Generation. *J. Immunol.* **167**, 5814–5823 (2001).
 49. Zhu, J. W., Brdicka, T., Katsumoto, T. R., Lin, J. & Weiss, A. Structurally Distinct Phosphatases CD45 and CD148 Both Regulate B Cell and Macrophage Immunoreceptor Signaling. *Immunity* **28**, 183–196 (2008).
 50. McCall, M. N., Shotton, D. M. & Barclay, A. N. Expression of soluble isoforms of rat CD45. Analysis by electron microscopy and use in epitope mapping of anti-CD45R monoclonal antibodies. *Immunology* **76**, 310–7 (1992).
 51. Woollett, G. R., Williams, A. F. & Shotton, D. M. Visualisation by low-angle shadowing of the leucocyte-common antigen. A major cell surface glycoprotein of lymphocytes. *EMBO J.* **4**, 2827–2830 (1985).
 52. Burroughs, N. J. *et al.* Boltzmann energy-based image analysis demonstrates that extracellular domain size differences explain protein segregation at immune synapses. *PLoS Comput. Biol.* **7**, (2011).
 53. Lu, J., Ellsworth, J. L., Hamacher, N., Oak, S. W. & Sun, P. D. Crystal structure of Fcγ receptor I and its implication in high affinity γ-immunoglobulin binding. *J. Biol. Chem.* **286**,

- 40608–40613 (2011).
54. Carbone, C. B. *et al.* In vitro reconstitution of T cell receptor-mediated segregation of the CD45 phosphatase. *Proc. Natl. Acad. Sci. U. S. A.* **114**, E9338–E9345 (2017).
 55. Chung, M., Koo, B. J. & Boxer, S. G. Formation and analysis of topographical domains between lipid membranes tethered by DNA hybrids of different lengths. *Faraday Discuss.* **161**, 333–45; discussion 419–59 (2013).
 56. Rosano, C., Arosio, P. & Bolognesi, M. The X-ray three-dimensional structure of avidin. *Biomol. Eng.* **16**, 5–12 (1999).
 57. Krobath, H., Rózycki, B., Lipowsky, R. & Weikl, T. R. Binding cooperativity of membrane adhesion receptors. *Soft Matter* **5**, 3354–3361 (2009).
 58. Rózycki, B., Lipowsky, R. & Weikl, T. R. Segregation of receptor-ligand complexes in cell adhesion zones: Phase diagrams and the role of thermal membrane roughness. *New J. Phys.* **12**, (2010).
 59. Krobath, H., Rózycki, B., Lipowsky, R. & Weikl, T. R. Line tension and stability of domains in cell-adhesion zones mediated by long and short receptor-ligand complexes. *PLoS One* **6**, (2011).
 60. Sil, D., Lee, J. B., Luo, D., Holowka, D. & Baird, B. Trivalent Ligands with Rigid DNA Spacers Reveal Structural Requirements For IgE Receptor Signaling in RBL Mast Cells. *ACS Chem. Biol.* **2**, 674–684 (2007).
 61. Berger, R. M. L. *et al.* Nanoscale Organization of FasL on DNA Origami as a Versatile Platform to Tune Apoptosis Signaling in Cells. *bioRxiv* 2020.07.05.187203 (2020).
doi:10.1101/2020.07.05.187203
 62. Arnold, M. *et al.* Activation of integrin function by nanopatterned adhesive interfaces. *ChemPhysChem* **5**, 383–388 (2004).
 63. Delcassian, D. *et al.* Nanoscale ligand spacing influences receptor triggering in T cells and NK cells. *Nano Lett.* **13**, 5608–5614 (2013).

64. Cai, H. *et al.* Full control of ligand positioning reveals spatial thresholds for T cell receptor triggering. *Nat. Nanotechnol.* **13**, 610–617 (2018).
65. Nimmerjahn, F. & Ravetch, J. V. Translating basic mechanisms of IgG effector activity into next generation cancer therapies. *IECON Proc. (Industrial Electron. Conf.* **2005**, 1104–1109 (2005).
66. Zhang, X. *et al.* Anti-CD20 Antibody with Multimerized Fc Domains: A Novel Strategy To Deplete B Cells and Augment Treatment of Autoimmune Disease. *J. Immunol.* **196**, 1165–1176 (2016).
67. Zhao, K. *et al.* Structure of CD20 in complex with the therapeutic monoclonal antibody rituximab. *Science (80-.).* **367**, 1218–1223 (2020).
68. Chew, H. Y. *et al.* Endocytosis Inhibition in Humans to Improve Responses to ADCC-Mediating Antibodies. *Cell* **180**, 895-914.e27 (2020).
69. Seifert, O. *et al.* Tetravalent Antibody-scTRAIL Fusion Proteins with Improved Properties. *Mol. Cancer Ther.* **13**, 101–111 (2014).
70. Huang, X. *et al.* DNA scaffolds enable efficient and tunable functionalization of biomaterials for immune cell modulation. *Nat. Nanotechnol.* (2020). doi:10.1038/s41565-020-00813-z
71. Ueda, G. *et al.* Tailored design of protein nanoparticle scaffolds for multivalent presentation of viral glycoprotein antigens. *Elife* **9**, 1–30 (2020).
72. Fallas, J. A. *et al.* Computational design of self-assembling cyclic protein homo-oligomers. *Nat. Chem.* **9**, 353–360 (2017).
73. Divine, R. *et al.* Designed proteins assemble antibodies into modular nanocages. *bioRxiv* (2020). doi:10.1101/2020.12.01.406611
74. Stuurman, N., Edelstein, A., Amodaj, N., Hoover, K. & Vale, R. Computer control of microscopes using manager. *Current Protocols in Molecular Biology* **CHAPTER**, Unit14.20 (2010).

CHAPTER 4

Concluding Thoughts

4.1 Looking Forward

The work presented in this thesis provides a much clearer picture of how the molecular-scale organization of Fc γ R nanoclusters regulate macrophage activation and an increased understanding of the steric exclusion mechanisms driving CD45 segregation from TCR clusters. However, the mechanisms underlying how both T cells and macrophages use this spatial information to make such specific yet robust activation decisions are not yet fully understood. Additionally, how parameters like receptor-ligand size, mobility, or affinity regulate the organization of proteins at different immunological synapses, and how spatial regulation cooperates with other immune cell regulation mechanisms remain open questions.

The work presented in chapter 3 of this dissertation demonstrates that tight Fc γ R clustering promotes receptor phosphorylation and phagocytosis. As the exclusion of phosphatases CD45 and CD148 has been demonstrated to be essential for Fc γ R phosphorylation and phagocytosis,¹ we suggest that the increased receptor phosphorylation in tight clusters is driven by an increase in the exclusion of these phosphatases. Although this model fits within the current literature, the scale at which we are currently able to form this pre-defined spacing remains below the diffraction limit of fluorescence microscopes. Therefore, we could not directly visualize and measure CD45 or CD148 exclusion from these nanoclusters with current technologies. As DNA origami technology advances, increasing the size of the origami pegboards to be able to maintain this same level of precision on the spacing but over a larger area would allow us to directly test and visualize this hypothesis. Alternatively, slight improvements in ultra-high resolution imaging techniques could enable this farther analysis.

The work shown in chapter 2 of this dissertation demonstrates that CD45 exclusion can be driven from nanoscale TCR-pMHC clusters merely based on the size of the extracellular domain of the phosphatase. Given that the TCR shares many properties with the Fc γ R, we hypothesize that this increase in CD45 exclusion from tight clusters compared to more sparse clusters could be due to an increase in this steric exclusion. Data mostly in the TCR field has shown that higher-receptor ligand densities result in less deformations in the intermembrane space,^{2,3} and thus could increase the extent of phosphatase exclusion from the receptors. Alternatively, we suggest a mechanism in which the lipid organization around tight clusters enhances receptor phosphorylation. It has been shown both for the TCR and the Fc γ R that receptor clusters associate with or induce the formation of ordered lipid domains that are enriched in Src-family kinases.⁴⁻⁸ These ordered lipid domains then act as phosphorylation hotspots, as phosphatases like CD45 are excluded from the domains, farther enhancing the likelihood that receptors within these domains are phosphorylated.^{9,10} Work by Bag et al recently demonstrated that a combination of lipid-based, protein-based, and steric interactions drove Fc ϵ receptor (Fc ϵ R) phosphorylation and signaling in mast cells.⁸ As the Fc ϵ R contains the same common cytosolic γ chain as the Fc γ R, it is highly likely that tight nanoclustering of IgG-Fc γ R interactions promotes many of these factors and that they synergistically promote receptor phosphorylation.

Future work separately manipulating the lipid ordering, extent of steric exclusion of phosphatases, and protein-protein interactions in a well-controlled system could help our understanding of the relative roles of each of these parameters for both Fc γ R and TCR signaling. Additionally, a better quantitative understanding of how each parameter may be regulated by changes in protein size, affinity of interactions, and identity of transmembrane domains to modulate cellular activation thresholds will significantly increase our understanding of how immune cells integrate all of the extracellular information they receive to make their critical all-or-none-activation decisions. This

in depth knowledge of the endogenous systems will enable rational design of new engineered chimeric antigen receptors for cell based therapies as well as antibody based immunotherapies.

Lastly, much of this work focuses on the nanoscale spatial organization of receptor-ligand and surrounding protein interactions, as these play a large role in dictating receptor activation. However, immune cells also take in and integrate information about the larger-scale spacing of proteins throughout the entire immunological synapse when making activation decisions. For example, the micron-scale spacing between individual TCR clusters as well as Fc γ R clusters has been shown to regulate T cell and macrophage activation.^{11,12} Again, expanding DNA origami platforms in a manner that would enable both the control of inter-ligand spacing within clusters as well as inter-cluster spacing would enable the precise study of both of these parameters are integrated in cellular decisions. Alternatively, this current hurdle would be overcome if nanolithography techniques evolve to match the precision that DNA origami patterning provides or enable patterning of 3 dimensional surfaces. Either of these technological advances would especially prove helpful for the study of phagocytosis, as phagocytosis is a process that must be spatially controlled in all 3 dimensions to proceed successfully, and thus study of this process on 3 dimensional targets is essential.

As our understanding of TCR and Fc γ R signaling advances, we have uncovered paradigms that are generalizable between these and many other immune receptors. Farther study of these receptors will keep improving our understanding of the basic biophysical parameters that regulate their activation, but also progress our knowledge of how each individual receptor may have evolved to function optimally within each type of immune cell or for each of its intended functions.

4.2 References

1. Zhu, J. W., Brdicka, T., Katsumoto, T. R., Lin, J. & Weiss, A. Structurally Distinct Phosphatases CD45 and CD148 Both Regulate B Cell and Macrophage Immunoreceptor Signaling. *Immunity* **28**, 183–196 (2008).
2. Krobath, H., Rózycki, B., Lipowsky, R. & Weikl, T. R. Line tension and stability of domains in cell-adhesion zones mediated by long and short receptor-ligand complexes. *PLoS One* **6**, (2011).
3. Rózycki, B., Lipowsky, R. & Weikl, T. R. Segregation of receptor-ligand complexes in cell adhesion zones: Phase diagrams and the role of thermal membrane roughness. *New J. Phys.* **12**, (2010).
4. Dinic, J., Riehl, A., Adler, J. & Parmryd, I. The T cell receptor resides in ordered plasma membrane nanodomains that aggregate upon patching of the receptor. *Sci. Rep.* **5**, 1–9 (2015).
5. Beekman, J. M., van der Linden, J. A., van de Winkel, J. G. J. & Leusen, J. H. W. FcγRI (CD64) resides constitutively in lipid rafts. *Immunol. Lett.* **116**, 149–155 (2008).
6. Katsumata, O. *et al.* Association of FcγRII with Low-Density Detergent-Resistant Membranes Is Important for Cross-Linking-Dependent Initiation of the Tyrosine Phosphorylation Pathway and Superoxide Generation. *J. Immunol.* **167**, 5814–5823 (2001).
7. Kwiatkowska, K. & Sobota, A. The clustered Fcγ receptor II is recruited to Lyn-containing membrane domains and undergoes phosphorylation in a cholesterol-dependent manner. *Eur. J. Immunol.* **31**, 989–998 (2001).
8. Bag, N., Wagenknecht-Wiesner, A., Lee, A., Shi, S. & Holowka, D. A. Lipid-based, protein-based, and steric interactions synergize to facilitate transmembrane signaling stimulated by antigen-clustering of IgE receptors. *Bioarxiv*

doi:10.1101/2020.12.26.424347

9. Sohn, H. W., Tolar, P., Jin, T. & Pierce, S. K. Fluorescence resonance energy transfer in living cells reveals dynamic membrane changes in the initiation of B cell signaling. *Proc. Natl. Acad. Sci. U. S. A.* **103**, 8143–8148 (2006).
10. Stone, M. B., Shelby, S. A., Nññez, M. F., Wisser, K. & Veatch, S. L. Protein sorting by lipid phase-like domains supports emergent signaling function in b lymphocyte plasma membranes. *Elife* **6**, 1–33 (2017).
11. Cai, H. *et al.* Full control of ligand positioning reveals spatial thresholds for T cell receptor triggering. *Nat. Nanotechnol.* **13**, 610–617 (2018).
12. Freeman, S. A. *et al.* Integrins Form an Expanding Diffusional Barrier that Coordinates Phagocytosis. *Cell* **164**, 128–140 (2016).

Copyright 2021

By

Nadja Kern

DEDICATION

To my family, who incited my passion for science and supported me with all their love.

ACKNOWLEDGEMENTS

I am incredibly grateful for all of the support and mentorship I have received during the last 5 and a half years and have many people to thank for making this work possible and my graduate time so enjoyable.

First, I would like to thank my mentor Ron Vale for all of his guidance throughout my PhD, for allowing me the freedom to work on the questions that I was most passionate about, and especially for creating the wonderful environment that the Vale lab is and has been. It has been a joy both scientifically and personally to have been a part of the Vale lab community. As absolutely everyone in the lab has been truly helpful throughout my PhD, I would like to thank all of the Vale lab members together for making the lab an incredible fun, positive, and inspiring place to work every single day. I have learned from each and every one of you, and can't imagine a better group of people to be surrounded by. I would not be the scientist, the science communicator, or person I am today without the help I received from every Vale lab member, past and present. In particular, I would like to thank Kate Carbone for being my first role model in the lab and for showing me how great the Vale lab and the field of immunology is. Additionally, thank you to the previously called "signaling group" and now "C3" group for their constant advice, motivation, support, and ideas scientifically and otherwise.

A special thank you to Meghan Morrissey, who kindly took the role of my post-doc mentor while she was in the lab and has continued to provide me with invaluable mentorship as she has transitioned to running her own lab at UCSB. Thank you, Meghan, for your unwavering support scientifically, personally, and professionally, and for all of your advice, guidance, and inspiration. Thank you for teaching me essentially everything I know about macrophages, for making my first

paper writing process really fun, and for instilling in me the confidence to finally call myself an immunologist! Your passion for science, outlook on life, and generosity will always inspire me, and I am so thankful I have had the opportunity to learn from you.

Thank you to my thesis committee members, Orion Weiner and Natalia Jura, for all of your advice, fun scientific discussions, creative ideas, and support regarding both my project and professional development. Thank you also to my classmates and the amazing UCSF research community for all of the support, inspiration, and fun scientific discussions.

Thank you to all my incredible friends for all of your support and for the endless laughter and great memories during my graduate time. Thank you all for celebrating the wins with me and for being there for me in whichever way I needed during the lows; whether it was through a phone call, an early morning volleyball session, a climb up some mountain, or a science and life talk over lunch, you were there with what I needed most.

Thank you to my entire amazing family. Thank you for your constant love, motivation, and support through this PhD journey, and for inciting my love for science and research in the first place. To my parents, Mama (Doro) and Papa (Gunther), thank you for the endless scientific discussions, celebrating with me when I had good results, and providing motivation, ideas, and a kick in the butt if needed when experiments failed. I would not be the scientist or person I am now without all of your input, advice, and guidance. Your passion for science and life will always inspire me. To my sister and best friend, Juju (Julia), thank you for always supporting me, for learning to love the cells that go “nom nom nom” because I now love them, and for all of the laughs, love, and adventures.

Thank you to my incredible fiancé Braxton, for his endless love and encouragement. Thank you for understanding that when I say I need 15 minutes in lab it may mean 4 hours. Thank you for pushing me to be the best person and scientist I can be, for supporting me in any way I needed, and for filling each day with joy and laughter. Lastly, thank you to Braxton's side of the family, the Irbys and the Dunstones, for welcoming me into the family with open arms and for their incredible love and support.

STATEMENT REGARDING AUTHOR CONTRIBUTIONS

Statement from Ron Vale:

Chapter 2 of this dissertation includes reprints of material published with co-authors other than Nadja Kern. Nadja contributed through the conceptualization, design, performance, and analysis of experiments shown in Figures 2, 4 and 5, and helped in the writing of the manuscript.

Chapter 2 of this dissertation contains reprints of previously published material as it appears in:

Carbone, C. B., **Kern, N.**, Fernandes, R. A., Hui, E., Su, X., Garcia, K. C., & Vale, R. D. (2017). In vitro reconstitution of T cell receptor-mediated segregation of the CD45 phosphatase. *Proceedings of the National Academy of Sciences*, 114(44), E9338–E9345.

Chapter 3 of this dissertation contains ongoing work and unpublished material:

Kern, N., Dong, R., Douglas, S., Vale, R.D., and Morrissey, M.A.

Title: Tight nanoscale clustering of Fc γ -receptors using DNA origami promotes phagocytosis

ABSTRACT

Spatial organization of immune receptors regulate immune cell activation: Insights from reconstituted T cell receptor and Fc γ -receptor systems

Nadja Kern

As immune cells patrol our body, contacting and surveying the cells around them, they must constantly make the decision of whether or not to activate and surmount an immune response. Importantly, these choices must be made with high fidelity, as the immune cells must quickly eliminate pathogens and diseased cells while limiting damage to healthy cells. This activation decision is regulated by receptors on the immune cells that recognize distinct ligands on the surface of the cells they encounter. A hallmark of successful receptor-ligand interaction is the reorganization of these immune receptors into sub-micron and micron scale clusters, at which activation signals initiate within the immune cell. Although the importance of this receptor reorganization has been long appreciated, the mechanism by which the reorganization is achieved, how receptor reorganization promotes signal activation, and how the spatial organization of receptors regulates or modulates these binary cellular activation decisions has not been well understood. In this dissertation, I used reconstituted signaling systems to understand how the nanoscale spatial organization of the Fc γ receptor (Fc γ R) controls engulfment signaling in macrophages, and how the organization of the T cell receptor (TCR), inhibitory co-receptor, PD-1, and the transmembrane phosphatase, CD45, control signaling in T cells.

TABLE OF CONTENTS

CHAPTER 1

Introduction to TCR and Fc γ R Signaling

1.1 Introduction	1
1.2 References	6

CHAPTER 2

9

In vitro reconstitution of T cell receptor-mediated segregation of the CD45 phosphatase

2.1 Significance	10
2.2 Abstract	10
2.3 Introduction	11
2.4 Results	12
2.5 Discussion	
2.6 Materials and Methods	25
2.7 Supporting Information	30
2.8 Author Contributions	36
2.9 Acknowledgements	36
2.10 References	37

CHAPTER 3

41

Tight nanoscale clustering of Fc γ -receptors using DNA origami promotes phagocytosis

3.1 Abstract	42
3.2 Introduction	43
3.3 Results	44
3.4 Discussion	62
3.5 Materials and Methods	66

3.6 Supporting Information	75
3.7 Acknowledgements	112
3.8 Author Contributions	112
3.9 References	113
CHAPTER 4	120
Concluding Thoughts	
4.1 Looking forward	120
4.2 References	123

LIST OF FIGURES

CHAPTER 2

Figure 2.1	14
Figure 2.2	16
Figure 2.3	17
Figure 2.4	19
Figure 2.5	21
Figure S2.1	32
Figure S2.2	33
Figure S2.3	34
Figure S2.4	35

CHAPTER 3

Figure 3.1	46
Figure 3.2	49
Figure 3.3	52
Figure 3.4	55
Figure 3.5	57
Figure 3.6	60
Figure S3.1	75
Figure S3.2	76
Figure S3.3	78
Figure S3.4	79
Figure S3.5	80
Figure S3.6	82

LIST OF TABLES

CHAPTER 2

Table S2.1	30
------------	----

CHAPTER 3

Table S3.1	85
------------	----

Table S3.2	94
------------	----

Table S3.3	99
------------	----

Table S3.4	103
------------	-----

Table S3.5	107
------------	-----

CHAPTER 1

Introduction to TCR and Fc γ R Signaling

1.1 Introduction

Our immune system plays the vital role of defending our bodies from harmful pathogens and diseased cells. The controlled activation of immune cells is essential for achieving this function, as inactivation may lead to infection or disease, while overactivation could result in the destruction of healthy cells, leading to autoimmune disorder. To this end, immune cells use a myriad of cell surface receptors to survey their surrounding cells and environment. When these receptors bind their cognate ligands, they transduce extracellular signals into intracellular signals. To set robust activation thresholds that effectively differentiate from background signals, immune cells integrate measurements in the identity, number, affinity, and spatial organization of receptor-ligand interactions to determine whether or not the cell activates to surmount an immune response. Despite a wealth of information currently available about the individual molecular components involved in these activation decisions, how the spatial organization of immune receptors and their surrounding signaling proteins affect and regulate activation thresholds remains an open area of investigation.

T Cell Receptor signaling

T cells play a central role in the mammalian adaptive immune response. Consequently, the activation of T cells via the T cell receptor (TCR) is a well-studied example of a signaling system in which the spatial rearrangements of the receptor and surrounding signaling proteins play a significant role in regulating the activation threshold of the T cell. The TCR is a multi-protein complex which is activated through the phosphorylation of its cytosolic immunoreceptor tyrosine-based activation motifs (ITAMs) after binding to peptide major histocompatibility complex (pMHC)

presented by an antigen presenting cell (APC). Upon binding to a pMHC of sufficient strength, the receptors coalesce into microclusters, are phosphorylated by the Src-family kinase Lck, and are able to recruit downstream signaling proteins.¹⁻³ When unbound, the TCR is held in a dephosphorylated state by the transmembrane phosphatase CD45.⁴

As the TCR forms these canonical microclusters at the synapse between the T cell and the APC (immunological synapse), it partitions away from CD45.⁵ Accumulating evidence has supported the kinetic segregation model for TCR activation, which proposes that this partitioning creates a biochemically distinct region around the receptors that shifts the kinase-phosphatase balance to favor phosphorylation of the TCR ITAM domains.^{3,6-8} This is in contrast to a model in which the TCR undergoes a conformational change that enables its phosphorylation.

This spatial partitioning has been proposed to be driven via multiple mechanisms. Elegant experiments in cells and computational studies have demonstrated that the relative sizes of the extracellular domains of the TCR-pMHC complex (~13 nm) and CD45 (25-40 nm) are a critical parameter for this spatial segregation.^{5,9,10} This steric exclusion mechanism proposes that in order to minimize the bending energy of the cell membrane, the proteins will self-partition based on their extracellular size.¹¹⁻¹³ Importantly, this mechanism is proposed to play a role in the activation of not only the TCR, but many different ITAM and immunoreceptor tyrosine-based inhibitory motif (ITIM) containing receptors, including the inhibitory T cell receptor, Programmed Cell Death Protein 1 (PD-1).⁸ However, it has been disputed that distinct lipid domains within the cell membrane that partition Src-family kinases away from CD45, and downstream actin rearrangements in the cell that may actively reorganize transmembrane proteins, also contribute to the partitioning of CD45 from pMHC-bound TCR.¹⁴⁻¹⁶ Therefore, groups have turned to synthetic reconstituted systems in which varying sizes of dimerizing GFP proteins or complementary DNA strands were used to replace TCR-pMHC interactions.^{17,18} These studies

found that protein size alone, absent of additional feedback mechanisms that may be present within the cell, could drive the segregation of proteins in a model membrane. However, these experiments were all performed with artificial proteins which have non-physiological receptor-ligand affinities, leaving the mechanism of segregation between TCR-pMHC and CD45 at the immunological synapse unknown.

In the first part of this dissertation, I worked closely with Kate Carbone to recapitulate TCR-pMHC and PD1-PDL1 binding on model membranes outside of cells to better understand the mechanisms driving the reorganization of these proteins, their segregation from CD45, and the physical parameters that regulate these spatial organizations at the immunological synapse.

Fc γ Receptor signaling in macrophages

Macrophages are an essential part of our innate immune system as they are responsible for patrolling our bodies and clearing any pathogens, harmful, infected, or dead cells. They accomplish this through a process called phagocytosis, in which they engulf and digest their target cells, as well as through the subsequent recruitment and activation of adaptive immune cells. Macrophages recognize harmful targets through specialized receptors which bind to ligands on target surfaces that induce engulfment (“eat me” signals).¹⁹ One of the most common “eat me” signals is the Immunoglobulin G (IgG) antibody, which binds to targets displaying its cognate antigen. Recognition of IgG by the Fc γ receptor family (Fc γ R) of proteins on the macrophage surface drives antibody-dependent cellular phagocytosis (ADCP) of these targets.²⁰

Similar to the TCR in T cells, Fc γ R-driven phagocytosis must be performed efficiently and in a manner that robustly ignores any sub-threshold antibody stimuli that may be bound transiently or nonspecifically to healthy cells. This is an especially hard feat for macrophages, as antibodies are

often found at very high concentrations in the blood (up to mg/mL).²¹ Therefore, the all-or-none decision of engulfment requires the combined activity of signals from multiple Fc γ R-IgG interactions.²² Although it is well established that activation of a single Fc γ R is not sufficient to drive phagocytosis, the mechanisms that underlie this requirement and enable the integration of many signals to dictate the binary cellular decision are unresolved.

Analogous to the TCR, IgG bound Fc γ Rs reorganize into nanoscale clusters upon IgG binding, and this clustering is thought to play an important role in engulfment signaling.²³ This likeness with the TCR is no coincidence, as the Fc γ R is also activated via phosphorylation of its ITAM domains by Src-family kinases upon IgG binding. Once phosphorylated, these receptor clusters recruit the downstream signaling molecules essential for phagocytosis, thus acting as sites of signal initiation in the macrophage.^{24–26} While mounting evidence suggests this clustering to be important for Fc γ R engulfment signaling, little is known about the nanoscale structures of these Fc γ R clusters or how changes in the makeup of these clusters may regulate engulfment thresholds. A better understanding of how these nanoscale antibody patterns effect engulfment decisions would not only provide insight into the molecular mechanisms that govern Fc γ R-mediated macrophage activation but also have important implications for the design of novel and more efficacious immunotherapies targeting the activation of Fc γ Rs.²⁷

Although current experimental methods like nanolithography arrays have provided important insights on how the nanoscale spacing of other immune receptors effects signaling in T cells²⁸, B cells²⁹, mast cells³⁰, and NK cells³¹, these methods lack the ability to pattern ligands on 3 dimensional surfaces and the precision to consistently pattern molecules on the single molecule level. Thus, during my thesis work, I set out to build a synthetic engulfment system which could pattern ligands of engulfment receptors on 3 dimensional targets and be used to investigate the

effects nanoscale spacing has on engulfment in macrophages. To this end, I built a chimeric antigen receptor (CAR) version of the Fc γ R in which the endogenous extracellular domain was replaced with a SNAP tag to which a single stranded DNA (ssDNA) could be covalently attached. This receptor, which we named the DNA CAR γ receptor, can be activated via a complementary base paired ssDNA ligand. Importantly, the rapidly evolving technology of DNA origami enabled me to use this DNA-based engulfment system to directly pattern the DNA ligands with nanometer level precision.

In the second part of this dissertation, I used this synthetic engulfment system to determine the number of ligands and inter-ligand spacing necessary within Fc γ R nanoclusters to activate downstream signaling and engulfment in macrophages. Furthermore, I used this system to gain a mechanistic understanding of the requirement for receptor-ligand clustering in macrophage signaling and phagocytosis.

1.2 References

1. Sherman, E. *et al.* Functional nanoscale organization of signaling molecules downstream of the T cell antigen receptor. *Immunity* **35**, 705–720 (2011).
2. Lillemeier, B. F. *et al.* TCR and Lat are expressed on separate protein islands on T cell membranes and concatenate during activation. *Nat. Immunol.* **11**, 90–96 (2010).
3. Taylor, M. J., Husain, K., Gartner, Z. J., Mayor, S. & Vale, R. D. A DNA-Based T Cell Receptor Reveals a Role for Receptor Clustering in Ligand Discrimination. *Cell* **169**, 108–119.e20 (2017).
4. Hermiston, M. L., Xu, Z. & Weiss, A. CD45: a critical regulator of signaling thresholds in immune cells. *Annu. Rev. Immunol.* **21**, 107–137 (2003).
5. Cordoba, S. P. *et al.* The large ectodomains of CD45 and CD148 regulate their segregation from and inhibition of ligated T-cell receptor. *Blood* **121**, 4295–4302 (2013).
6. Monks, C. R. F., Freiberg, B. A., Kupfer, H., Sciaky, N. & Kupfer, A. Three-dimensional segregation of supramolecular activation clusters in T cells. *Nature* **395**, 82–86 (1998).
7. Grakoui, A. *et al.* The immunological synapse: A molecular machine controlling T cell activation. *Science (80-.)*. **285**, 221–227 (1999).
8. Davis, S. J. & van der Merwe, P. A. The kinetic-segregation model: TCR triggering and beyond. *Nat. Immunol.* **7**, 803–809 (2006).
9. Choudhuri, K., Wiseman, D., Brown, M. H., Gould, K. & van der Merwe, P. A. T-cell receptor triggering is critically dependent on the dimensions of its peptide-MHC ligand. *Nature* **436**, 578–582 (2005).
10. James, J. R. & Vale, R. D. Biophysical mechanism of T-cell receptor triggering in a reconstituted system. *Nature* **487**, 64–9 (2012).
11. Qi, S. Y., Groves, J. T. & Chakraborty, A. K. Synaptic pattern formation during cellular recognition. *Proc. Natl. Acad. Sci. U. S. A.* **98**, 6548–6553 (2001).

12. Burroughs, N. J. & Wülfing, C. Differential segregation in a cell-cell contact interface: The dynamics of the immunological synapse. *Biophys. J.* **83**, 1784–1796 (2002).
13. Weikl, T. R. & Lipowsky, R. Pattern formation during T-cell adhesion. *Biophys. J.* **87**, 3665–3678 (2004).
14. Fernandes, R. A. *et al.* What Controls T Cell Receptor Phosphorylation? *Cell* **142**, 668–669 (2010).
15. Rozdzial, M. M., Malissen, B. & Finkel, T. H. Tyrosine-phosphorylated T cell receptor ζ chain associates with the actin cytoskeleton upon Activation of mature T lymphocytes. *Immunity* **3**, 623–633 (1995).
16. Dinic, J., Riehl, A., Adler, J. & Parmryd, I. The T cell receptor resides in ordered plasma membrane nanodomains that aggregate upon patching of the receptor. *Sci. Rep.* **5**, 1–9 (2015).
17. Schmid, E. M. *et al.* Size-dependent protein segregation at membrane interfaces. *Nat. Phys.* **12**, 704–711 (2016).
18. Chung, M., Koo, B. J. & Boxer, S. G. Formation and analysis of topographical domains between lipid membranes tethered by DNA hybrids of different lengths. *Faraday Discuss.* **161**, 333–45; discussion 419–59 (2013).
19. Freeman, S. A. & Grinstein, S. Phagocytosis: receptors, signal integration, and the cytoskeleton. *Immunol. Rev.* **262**, 193–215 (2014).
20. Nimmerjahn, F. & Ravetch, J. V. Fc γ receptors as regulators of immune responses. *Nat. Rev. Immunol.* (2008). doi:10.1038/nri2206
21. Gonzalez-Quintela, A. *et al.* Serum levels of immunoglobulins (IgG, IgA, IgM) in a general adult population and their relationship with alcohol consumption, smoking and common metabolic abnormalities. *Clin. Exp. Immunol.* **151**, 42–50 (2008).
22. Griffin, F. M., Griffin, J. A., Leider, J. E. & Silverstein, S. C. Studies on the mechanism of phagocytosis. I. Requirements for circumferential attachment of particle-bound ligands to

- specific receptors on the macrophage plasma membrane. *J. Exp. Med.* **142**, 1263–1282 (1975).
23. Goodridge, H. S., Underhill, D. M. & Touret, N. Mechanisms of Fc Receptor and Dectin-1 Activation for Phagocytosis. *Traffic* **13**, 1062–1071 (2012).
 24. Sobota, A. *et al.* Binding of IgG-Opsonized Particles to FcγR Is an Active Stage of Phagocytosis That Involves Receptor Clustering and Phosphorylation. *J. Immunol.* **175**, 4450–4457 (2005).
 25. Lin, J. *et al.* TIRF imaging of Fc gamma receptor microclusters dynamics and signaling on macrophages during frustrated phagocytosis. *BMC Immunol.* **17**, 5 (2016).
 26. Lopes, F. B. *et al.* Membrane nanoclusters of FcγRI segregate from inhibitory SIRPα upon activation of human macrophages. *J. Cell Biol.* jcb.201608094 (2017).
doi:10.1083/jcb.201608094
 27. Nimmerjahn, F. & Ravetch, J. V. Translating basic mechanisms of IgG effector activity into next generation cancer therapies. *IECON Proc. (Industrial Electron. Conf.* **2005**, 1104–1109 (2005).
 28. Cai, H. *et al.* Full control of ligand positioning reveals spatial thresholds for T cell receptor triggering. *Nat. Nanotechnol.* **13**, 610–617 (2018).
 29. Veneziano, R. *et al.* Role of nanoscale antigen organization on B-cell activation probed using DNA origami. *bioRxiv* 2020.02.16.951475 (2020). doi:10.1101/2020.02.16.951475
 30. Sil, D., Lee, J. B., Luo, D., Holowka, D. & Baird, B. Trivalent Ligands with Rigid DNA Spacers Reveal Structural Requirements For IgE Receptor Signaling in RBL Mast Cells. *ACS Chem. Biol.* **2**, 674–684 (2007).
 31. Delcassian, D. *et al.* Nanoscale ligand spacing influences receptor triggering in T cells and NK cells. *Nano Lett.* **13**, 5608–5614 (2013).

CHAPTER 2

***In vitro* reconstitution of T cell receptor-mediated segregation of the CD45 phosphatase**

Catherine B. Carbone¹, Nadja Kern¹, Ricardo A. Fernandes², Enfu Hui¹, Xiaolei Su¹, K. Christopher Garcia², and Ronald D. Vale¹

¹Dept. of Cellular and Molecular Pharmacology and the Howard Hughes Medical Institute, University of California, San Francisco, CA 94158; ²Dept. of Molecular and Cellular Physiology and Structural Biology and the Howard Hughes Medical Institute, Stanford University Medical School, CA 94305

2.1 Significance

The T cell receptor (TCR) and PD-1 signaling cascades have been hypothesized to be triggered by the exclusion of the transmembrane phosphatase CD45 from sites of receptor–ligand engagement at the T cell–antigen-presenting cell interface. We reconstituted TCR–pMHC– and PD1–PD-L1–mediated segregation of CD45 with purified proteins and model membranes, demonstrating that this phenomenon can occur in the absence of any active cellular organization. In this minimal system, two developmentally regulated and different size isoforms of CD45 are differently segregated by TCR–pMHC binding, suggesting a possible mechanism for the fine-tuning of signaling. Collectively, our data show that the binding energy of physiological receptor–ligand pairs is sufficient to create spatial organization in membranes.

2.2 Abstract

T cell signaling initiates upon the binding of peptide-loaded MHC (pMHC) on an antigen-presenting cell to the T cell receptor (TCR) on a T cell. TCR phosphorylation in response to pMHC binding is accompanied by segregation of the transmembrane phosphatase CD45 away from TCR–pMHC complexes. The kinetic segregation hypothesis proposes that CD45 exclusion shifts the local kinase–phosphatase balance to favor TCR phosphorylation. Spatial partitioning may arise from the size difference between the large CD45 extracellular domain and the smaller TCR–pMHC complex, although parsing potential contributions of extracellular protein size, actin activity, and lipid domains is difficult in living cells. Here, we reconstitute segregation of CD45 from bound receptor–ligand pairs using purified proteins on model membranes. Using a model receptor–ligand pair (FRB–FKBP), we first test physical and computational predictions for protein organization at membrane interfaces. We then show that the TCR–pMHC interaction causes partial exclusion of CD45. Comparing two developmentally regulated isoforms of CD45, the larger RABC variant is excluded more rapidly and efficiently (~50%) than the smaller R0 isoform

(~20%), suggesting that CD45 isotypes could regulate signaling thresholds in different T cell subtypes. Similar to the sensitivity of T cell signaling, TCR–pMHC interactions with K_{ds} of $\leq 15 \mu\text{M}$ were needed to exclude CD45. We further show that the coreceptor PD-1 with its ligand PD-L1, immunotherapy targets that inhibit T cell signaling, also exclude CD45. These results demonstrate that the binding energies of physiological receptor–ligand pairs on the T cell are sufficient to create spatial organization at membrane–membrane interfaces.

2.3 Introduction

Binding of the T cell receptor (TCR) to agonist peptide-MHC (pMHC) triggers a signaling cascade within a T cell leading to reorganization of the cytoskeleton and organelles, transcriptional changes, and cell proliferation. The first step in the cascade is TCR phosphorylation by the Src family tyrosine kinase Lck (2). One model, called “kinetic segregation” (3) for how this initiating phosphorylation is triggered, proposes that the close membrane contact created by TCR–pMHC binding results in exclusion of the transmembrane phosphatase CD45, and the shift of the kinase–phosphatase balance favors net phosphorylation of the TCR by Lck. The basis of this exclusion is thought to be steric, since the large CD45 extracellular domain (CD45 R0 isoform, 25 nm; CD45 RABC isoform, 40 nm) (Table S1) (4–6) may not be able to penetrate the narrow intermembrane spacing generated by the TCR–pMHC complex (13 nm) (Table S1) (7, 8).

Imaging T cells activated *ex vivo* either by B cells (9) or by antigen presented on supported lipid bilayers (SLBs) (10, 11) has revealed that CD45 is indeed partitioned away from the TCR upon pMHC binding. Cellular reconstitutions have demonstrated that the large extracellular domain of CD45 is required for this segregation (12, 13). Additionally, size-dependent segregation of CD45 by orthogonal receptor–ligand pairs that create a similar narrow intermembrane cleft is sufficient for T cell triggering in the absence of TCR–pMHC binding (6, 12).

Despite this strong cellular evidence for size-based partitioning, it has been debated whether the physical properties of CD45 and TCR–pMHC at the membrane–membrane interface alone are sufficient to explain the observed segregation behavior or whether other cellular factors (e.g., actin cytoskeletal or lipid ordering) are also required. Several groups have computationally modeled aspects of size-based organization at membrane interfaces, and two independent mathematical approaches have concluded that spontaneous pattern formation can occur in physiological parameter ranges (14, 15). These models predict the contributions of protein (size, concentration, elasticity, affinity, and kinetics), membrane (stiffness, tension, repulsion), and environmental (thermal fluctuations, cytoskeleton, time) factors in regulating partitioning. Although these models focus primarily on a system with two binding pairs (TCR–pMHC and ICAM-1–LFA-1), some of the predictions can be extrapolated to a system with both ligand-bound and unbound species.

Successful efforts to reconstitute molecular segregation at membrane–membrane interfaces have been made with dimerizing GFP molecules (16) and hybridizing strands of DNA (17). These studies show that laterally mobile molecules at membrane–membrane interfaces organize by height and locally deform the membrane to accommodate different molecular sizes. However, results from high-affinity, artificial receptor–ligand pairs cannot be simply extrapolated to predict results for physiologically relevant molecules at the T cell–APC interface. Here, we have recapitulated TCR–pMHC–mediated partitioning of CD45 on model membranes.

2.4 Results

A chemically-inducible receptor-ligand system for producing CD45 exclusion at a membrane-membrane interface

To mimic a T cell, we used a giant unilamellar vesicle (GUV) containing a nickel-chelating lipid to which a purified His-tagged, fluorescently-labeled receptor and CD45 could be added (**Fig. 1A**). To mimic the APC, we used a supported lipid bilayer (SLB) containing nickel-chelating lipids to which a His-tagged protein ligand also could be bound. All proteins were linked to their target membrane via either His₁₀ or His₁₂, as detailed in the methods section. As an initial test of this system, we used an artificial receptor (FKBP) and ligand (FRB) that could be induced to form a tight binding interaction (100 fM) upon addition of rapamycin¹. In order to maintain the GUV and SLB in proximity prior to rapamycin addition, the two membranes were passively tethered to one another using two 100-mer single-stranded DNA molecules with a 20 bp region of complementarity^{2,3} (**Table S1**). The elongated extracellular domain of the CD45 R₀ isoform (25 nm)⁴⁻⁶ or the smaller SNAP protein (5 nm, **Table S1**)⁷ were used as test proteins for partitioning.

Upon rapamycin addition, FKBP and FRB concentrated first in small micron-scale clusters at the GUV-SLB interface, which then grew in size over the interface; simultaneously, fluorescently-labeled CD45 R₀ partitioned away from regions of the GUV that became enriched in receptor-ligand (**Fig. 1B and Movie S1**). In contrast to CD45, which was strongly depleted by FRB-FKBP, the SNAP protein (5 nm)⁸ or a lipid dye (Atto390-DOPE) remained evenly distributed throughout the interface after rapamycin addition (**Fig. 1C-D**). We also tested PD-L1 (8 nm, **Table S1**), which also remained evenly distributed throughout the interface after rapamycin addition (**Fig. S1**). The size of FKBP-FRB clusters could be varied by changing the receptor concentration on the GUV membrane; however, the degree of CD45 R₀ exclusion from clusters was similar over the range tested (**Fig. 2A-C**). Across all concentrations of FKBP, at receptor-ligand enriched zones, CD45 R₀ was depleted by $72 \pm 7\%$ (n=22 GUVs pooled from two experiments). Once formed, the receptor -enriched and -depleted zones stably retained their shapes for tens of minutes and receptor-ligand pairs in the enriched zones were largely immobile, as evidenced by

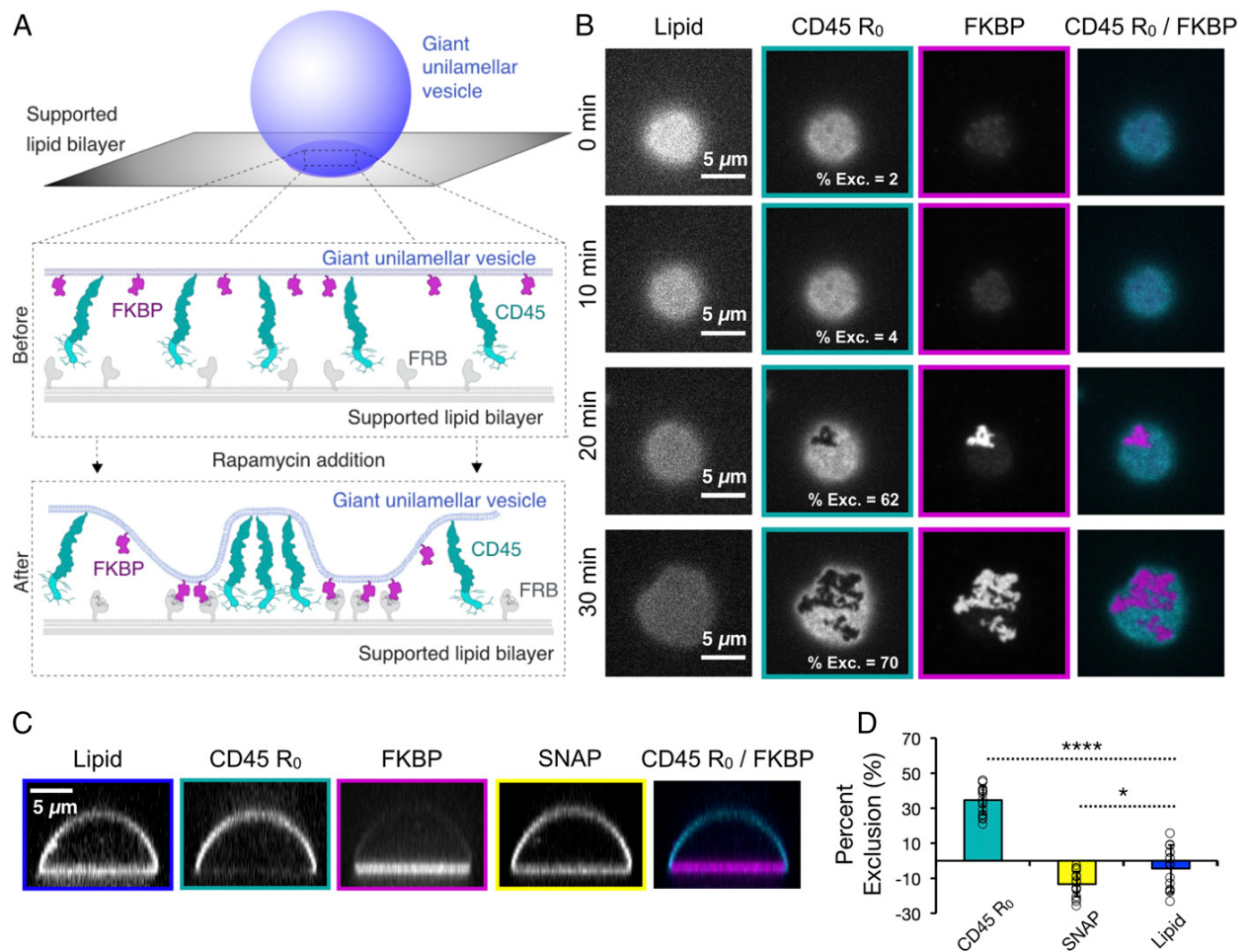


Fig. 2.1. Receptor-ligand binding induces CD45 segregation at membrane interfaces. **(A)** Schematic of rapamycin-induced receptor (FKBP)-ligand (FRB) binding and CD45 R₀ segregation between a giant unilamellar vesicle (GUV) and a supported lipid bilayer (SLB) **(B)** Total internal reflection fluorescence (TIRF) microscopy of a GUV-SLB interface at indicated times after rapamycin addition, showing concentration of FKBP into microdomains that exclude CD45 R₀. Percent exclusion of CD45 R₀ is indicated for each image shown. **(C)** Spinning disk z-sections of GUVs after membrane-apsed interfaces have reached equilibrium, showing localization of FKBP to the membrane interface, localization of CD45 R₀ away from the interface, and uniform distribution of SNAP. **(D)** Quantification of experiment shown in **C**; mean \pm standard deviation ($n=17$ GUVs pooled from two experiments).

fluorescence recovery after photobleaching (FRAP; **Fig. S2**). However, using single molecule TIRF imaging, we observed that single molecules of CD45 R₀ can diffuse across FKBP-FRB -enriched and -depleted zones (**Fig. 2D-E, Movie S2**). This result reveals that individual molecules can exchange across these micron-scale boundaries. In addition to testing the CD45 R₀ isoform for segregation, we also compared the extracellular domain of the CD45 R_{ABC} isoform, which is preferentially expressed early in T cell development⁹, and is about 15 nm larger in size than the shorter and later expressed R₀ isoform (**Table S1**)^{4,5}. With both isoforms present on the same GUV, the larger CD45 R_{ABC} isoform segregated from newly forming FKBP clusters three-fold faster than the R₀ isoform (2.8 ± 0.9 -fold, n=7 GUVs pooled from two experiments, **Fig. 2F-G, Movie S3**). However, the final extent of exclusion between the two CD45 isoforms was similar with this high affinity FRB-FKBP system (**Fig. S3**).

The kinetic segregation model predicts that CD45 is excluded from receptor-ligand complexes based upon a difference in the spacing between the GUV and SLB in the receptor- versus CD45-enriched regions¹⁰. To investigate the topology of the GUV membrane across the interface with nanometer accuracy in the vertical axis, we used scanning angle interference microscopy (SAIM), a technique that calculates the distance of fluorophores from a silicon oxide wafer by collecting sequential images at multiple illumination angles (**Fig. 3A**)¹¹. The SAIM reconstructions revealed membrane deformations at regions of CD45 localization (**Fig. 3B-D**). The calculated difference in membrane spacing between the FRB-FKBP- and CD45 R₀- enriched regions was 18 ± 11 nm (n=4-6 regions from each of 4 GUVs from two experiments, pooled), suggesting a size of ~24 nm for the CD45 R₀ extracellular domain, assuming that FRB-FKBP creates an intermembrane space of 6 nm (**Table S1**)¹². This value is similar to the ~22 nm axial dimension for the CD45 R₀ extracellular domain determined by electron microscopy⁶. Conversely, for GUV-SLB interfaces with FRB-FKBP and SNAP, SAIM reconstructions revealed no changes in membrane spacing across the GUV-SLB interface (**Fig. 3E-G**).

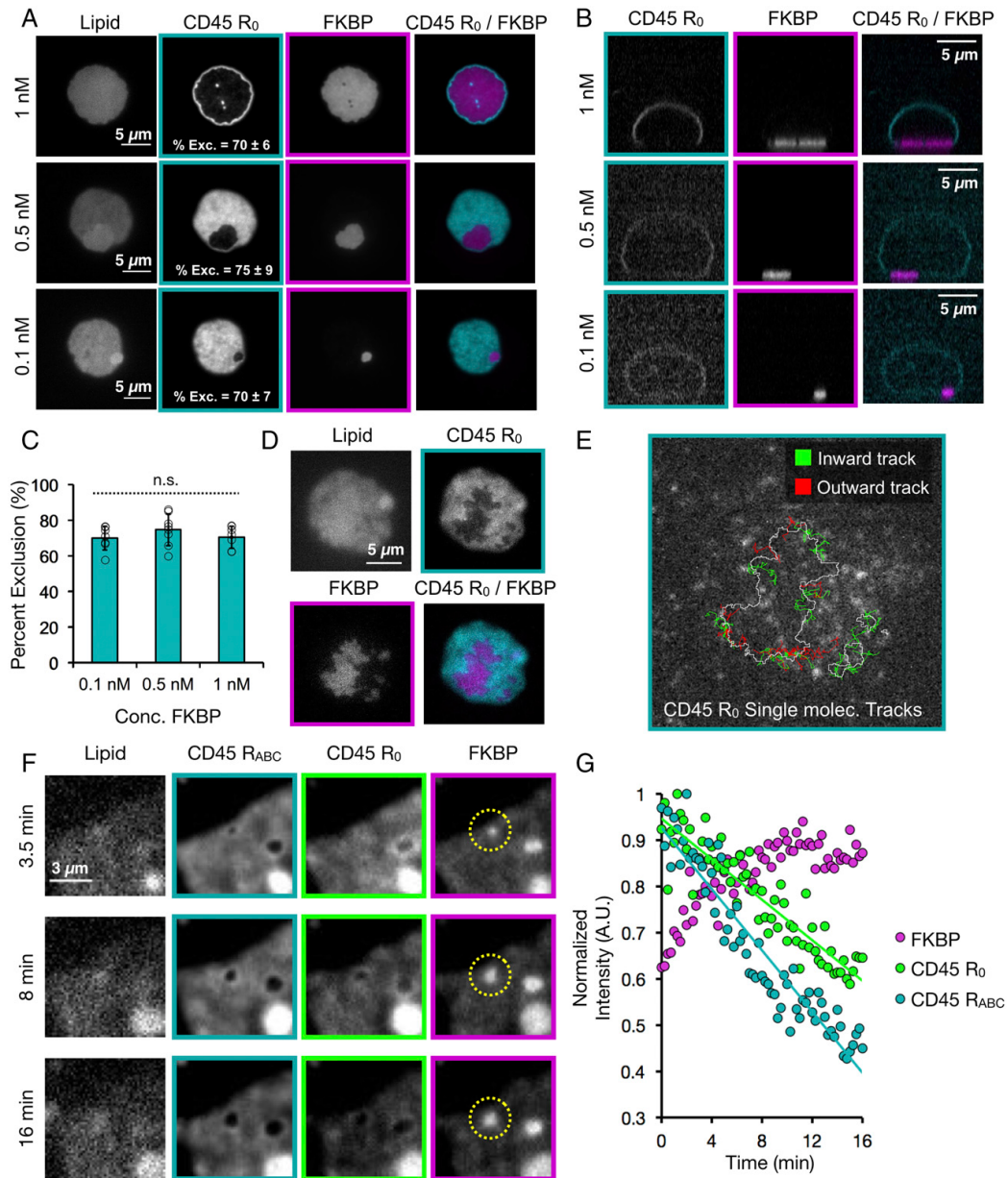


Fig. 2.2. Characterization of partitioned GUV-SLB membrane-membrane interfaces. **(A)** Titration of FKBP concentration (indicated at left of images) with constant CD45 R₀ concentration imaged by TIRF microscopy. Percent exclusion of CD45 R₀ is indicated as mean ± standard deviation with n=7-8 GUVs per condition pooled from three experiments. **(B)** Spinning disk z-sections of GUVs shown in **A**. **(C)** Graphical representation of data shown in **A**. **(D)** Total internal reflection fluorescence (TIRF) microscopy of a GUV-SLB interface showing overall localization of CD45 R₀ and FKBP. **(E)** Single molecule imaging of CD45 R₀ for GUV shown in **D**, border of FKBP enriched zone indicated by white line. Only tracks crossing the exclusion boundary are shown. CD45 R₀ single molecule tracks originating outside FKBP enriched zone are shown as green lines and tracks originating inside the FKBP enriched zone are shown as red lines. **(F)** Total internal reflection fluorescence (TIRF) microscopy of a GUV-SLB interface at 30-sec time points after rapamycin addition showing concentration of FKBP into micro domains that exclude CD45 R₀ and CD45 R_{ABC}. Rate of CD45 R_{ABC} exclusion is 2.8 ± 0.9 times faster than rate of CD45 R₀ exclusion, n=7 GUVs from two experiments. **(G)** Quantification of exclusion for representative GUV shown in **F**.

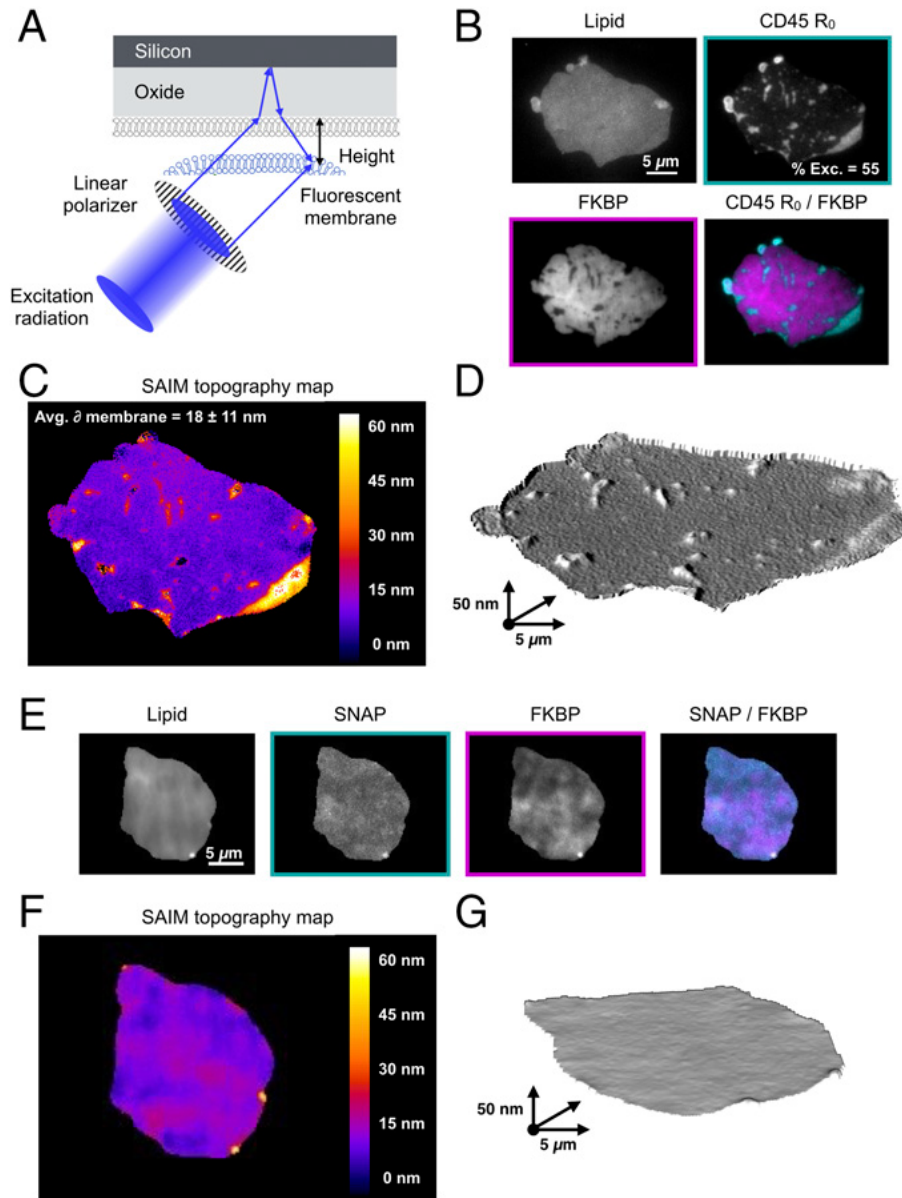


Fig. 2.3. Membrane topology is influenced by local protein composition. **(A)** Schematic of scanning angle interference microscopy showing reflection and interference of excitation light that produces structured illumination patterns used to deduce fluorophore height; adapted from Carbone, et al., 2016. **(B)** Epifluorescence microscopy showing localization of lipid, CD45 R₀ and FKBP on GUV analyzed by SAIM imaging. Percent exclusion of CD45 R₀ indicated for image shown. **(C)** SAIM reconstruction of GUV membrane derived from lipid fluorescence showing an increase in membrane height at CD45 R₀ clusters. Average membrane height change depicted as mean \pm standard deviation, $n=4-6$ clusters from each of 4 GUVs imaged during two separate experiments. **(D)** 3D model of data shown in **c**. Z-scale is exaggerated to clearly depict membrane deformations. **(E)** Epifluorescence microscopy showing localization of lipid, SNAP, and FKBP on GUV analyzed by SAIM imaging. **(F)** SAIM reconstruction of GUV membrane derived from lipid fluorescence **(G)** 3D model of data shown in **F**. Z-scale is exaggerated to clearly depict membrane deformations.

TCR-pMHC –mediated CD45 exclusion

Next, we sought to establish a GUV-SLB interface using the native T cell receptor-ligand pair, TCR-pMHC (**Fig. 4A**). For the TCR, we co-expressed the extracellular domains of the 2B4 α and β chains extended with leucine zippers to stabilize their dimerization¹³; both chains were tagged with His₁₀ for conjugation to the GUV membrane and the β chain contained a ybbR peptide for fluorescent labeling. For the ligand, we used the IE^k MHC, His₁₀-tagged loaded with a high affinity (2.5 μ M Kd) peptide. Similar to the results previously described for FRB-FKBP, we observed the formation of micron-sized TCR clusters that excluded CD45 R₀ (22 \pm 14% exclusion, n=17 GUVs pooled from 2 experiments, **Fig. 4B**) but not the control SNAP domain (**Fig. S3A**).

We also combined both CD45 R_{ABC} and CD45 R₀ isoforms on the same GUV and compared their segregation with the TCR-pMHC system. Upon GUV contact with the SLB, the 2B4 TCR bound the IE^k MHC, and concentrated at the interface where it formed micron-scale clusters that excluded both isoforms of CD45 (**Fig. 4C**). However, unlike the high affinity FKBP-FRB system in which the two CD45 isoforms R₀ and R_{ABC} are excluded to a similar level (Fig. S3), the degree of TCR-pMHC mediated exclusion of the smaller CD45 R₀ isoform (15 \pm 7% exclusion) was lower than the larger CD45 R_{ABC} isoform (38 \pm 9% exclusion) at steady state (45 min, n=13 GUVs pooled from two experiments, **Fig. 4D**).

In vivo, TCR encounters MHCs loaded with a myriad of different peptides; although not absolute, TCR-pMHC affinities of <50 μ M are usually required to trigger a signaling response¹⁴. To examine the effect of TCR-pMHC affinity on CD45 R_{ABC} exclusion, we loaded IE^k MHC with a series of well-characterized peptides with resultant two dimensional Kds of 2.5 μ M, 7.7 μ M, 15 μ M, 50 μ M and null for the 2B4 TCR¹³. At steady state, we observed that pMHCs with affinities to the TCR of 15 μ M and lower excluded CD45 R_{ABC} to similar extents (51 \pm 7% exclusion, n=30 GUVs pooled from two experiments, **Fig. 4E-F**). However, the pMHC with a Kd of 50 μ M and IE^k

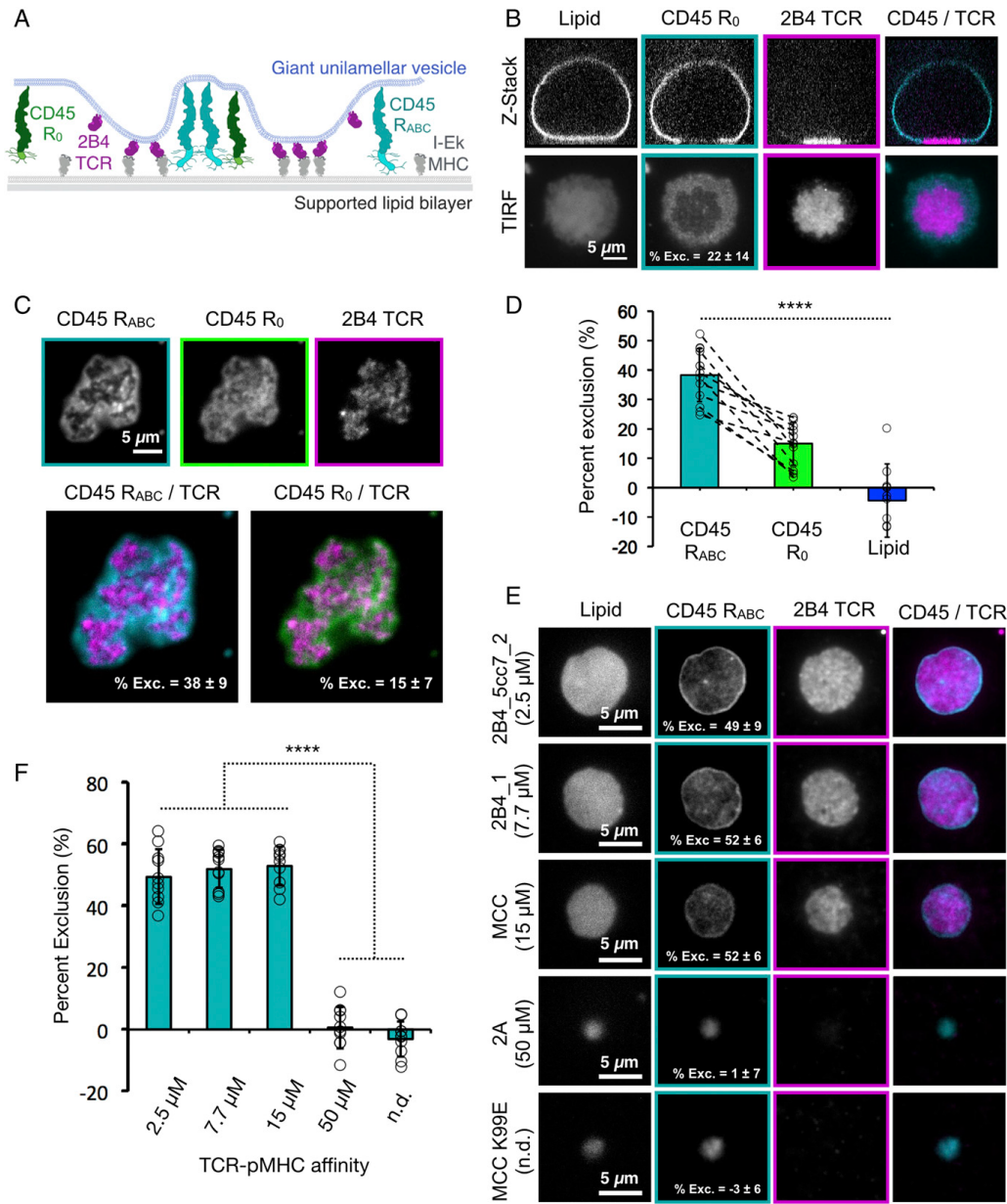


Fig. 2.4. TCR-pMHC binding induces CD45 segregation at GU-SLB interfaces (A) Schematic of 2B4 TCR-IE^k MHC binding between a GUV and a SLB, and segregating away from two CD45 isoforms (R₀ and R_{ABC}). (B) Top, spinning disk z-sections of GUVs after membrane-apposed interfaces have reached equilibrium, showing localization of 2B4 TCR to membrane interface and exclusion CD45 R₀ away from the interface. Bottom, TIRF images of GUV-SLB interface for GUV shown in panel above. Percent exclusion of CD45 R₀ indicated for image shown. (C) Top, segregation of CD45 R₀ and CD45 R_{ABC} on the same GUV membrane away from 2B4 TCR, shown by TIRF microscopy of membrane interface. Percent exclusion of CD45 isoforms indicated as mean ± standard deviation, with n=13 GUVs from two experiments. (D) Graphical representation of data shown in C. (E) Dependence of CD45 R_{ABC} exclusion as a function of TCR-pMHC affinity using peptides with different K_ds, indicated at left of images. Imaged by TIRF microscopy of membrane interfaces. Percent exclusion of CD45 R_{ABC} indicated as mean ± standard deviation, n=10 GUVs per condition from two experiments. (F) Graphical representation of data shown in E.

loaded with null peptides did not concentrate TCR at the GUV-SLB interface and did not change the distribution of CD45 R_{ABC} ($-1 \pm 6\%$ exclusion, $n=20$ GUVs pooled from 2 experiments, **Fig. 4E-F**). Thus, in agreement with computational predictions¹⁵, CD45 R_{ABC} exclusion was observed over the same range of affinities that are associated with peptide agonists.

Exclusion of CD45 by PD-1 –PD-L1

T cell signaling involves many receptor-ligand pairs interacting across the two membranes in addition to the TCR-pMHC¹⁶. The co-receptor PD-1 and its ligand PD-L1 create a signaling system that opposes T cell activation by inhibiting CD28 signaling^{17,18}. PD-1 ligation also results in microcluster formation on T cells¹⁹. Like the TCR, PD-1 signaling is initiated through receptor tail phosphorylation by Lck²⁰, and this phosphorylation event may be opposed by the abundant CD45 phosphatase (**Fig. S4A-B**). Therefore we tested the ability of interaction of PD-1 with PD-L1, which forms a complex of similar dimension (9 nm) to TCR-pMHC (**Table S1**)²¹ to partition CD45 in our in vitro liposome system (**Fig. 5A**). As expected from these physical dimensions, PD-1-PD-L1 interaction at the membrane-membrane interfaces formed micron-sized clusters that excluded CD45 R_{ABC} (**Fig. 5B**). The degree of CD45 R_{ABC} exclusion ($60 \pm 14\%$ exclusion, $n=14$ GUVs from two experiments **Fig. 5B**) was greater than that observed for TCR-pMHC (2.5 μ M peptide), which may be explained by the higher affinity of the PD1-PD-L1 interaction (0.77 μ M)²².

We also combined CD45 R_{ABC} with both TCR-pMHC with PD-1-PD-L1. In this dual receptor-ligand system, the two receptor-ligand complexes co-localized and CD45 R_{ABC} was partitioned away from the combined ligated TCR-PD-1 footprint (**Fig. 5C**). The size (**Table S1**) and affinity

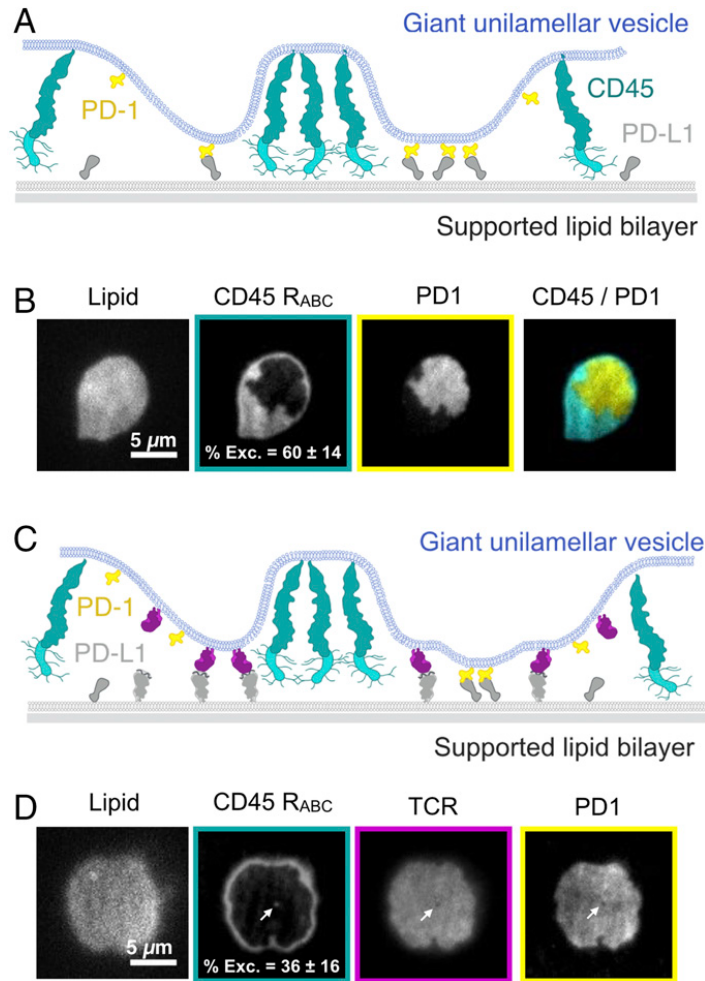


Fig. 2.5. The inhibitory co-receptor PD-1 excludes CD45 and colocalizes with TCR. **(A)** Schematic of PD-1-PD-L1 binding between a GUV and a SLB, with segregation away from CD45 R_{ABC}. **(B)** TIRF microscopy showing concentration of PD-1 into microdomains that exclude CD45 R_{ABC}. Percent exclusion of CD45 R_{ABC} indicated as mean \pm standard deviation, n=14 GUVs from two experiments. **(C)** TIRF microscopy showing concentration of TCR and PD-1 into a domain that excludes CD45 R_{ABC}. Percent exclusion of CD45 R_{ABC} indicated as mean \pm standard deviation, n=14 GUVs from two experiments. White arrow highlights small CD45 R_{ABC} enriched zone that is depleted for TCR and PD-1.

difference between TCR-pMHC and PD-1-PD-L1 may be small enough to not cause partitioning of these receptor-ligands under the conditions tested in our *in vitro* assay.

2.5 Discussion

In this study, we have established an *in vitro* membrane system that recapitulates receptor-ligand mediated CD45 exclusion. We have found that the binding energy of physiological receptor-ligand interactions is sufficient for CD45 partitioning at a model membrane-membrane interface. We also show that subtle differences in sizes and affinities of the proteins at the interface can give rise to significant changes in spatial organization and discuss the implications of these findings in more detail below.

Spatial organization of TCR and CD45 at the immune cell contacts has been proposed to arise by a nucleation-spreading mechanism¹⁵. By imaging an inducible synthetic receptor-ligand binding interaction in real time, we also conclude that pattern formation arises by the nucleation of small clusters that further spread across the membrane interface over time. These patterns induce changes in membrane topology that reflect the local protein composition and are stable on the order of hours. However, we show that individual molecules can freely exchange between domains. This result is consistent with previous computational simulations, although these models predict patterns will relax to a circular geometry to minimize the length of the domain boundaries^{15,23,24}. In our system, as observed for other physical models of partitioning using DNA-DNA hybridization²⁵ and dimerizing GFP²⁶, patterns have more complex domain structures. The lack of circular geometry in the experimental systems could be due to small inhomogeneities in the supported lipid bilayer compared to perfectly diffusive computational models. Despite this difference, many physical and computational model systems have converged on nucleation and spreading as a general mechanism by which spatial organization arises at membrane-membrane

interfaces.

The mechanism by which receptor-ligand binding induces spatial organization is a subject of active investigation. Our results showing differential exclusion of CD45 R₀ and CD45 R_{ABC} indicate that size-based steric exclusion and membrane deformation are important for exclusion. In addition, protein crowding of receptor-ligand complexes also could provide a driving force for partitioning. Indeed, previous work has shown that patterns formed at analogous membrane-membrane interfaces using dimerizing GFP as the receptor-ligand pair and a small test protein (monomeric Cherry) are due to crowding effects²⁶. In our system, however, we observe that the small SNAP protein is distributed throughout receptor-ligand enriched and depleted zones. These systems employ different proteins at the interface, and it will be interesting to investigate whether specific protein properties (e.g. size, propensity for oligomerization, elasticity, flexibility, packing density of receptor-ligand in partitioned zones, etc) account for these differences in the role of protein crowding in exclusion.

Our work also suggests an important contribution of receptor-ligand affinity in protein exclusion. We observed 70% depletion of CD45 R₀ from FRB-FKBP (100 fM Kd) -enriched zones. The TCR-pMHC interactions, on the other hand, are much lower in affinity, with most agonists generally displaying Kds of 1-100 μ M¹⁴. Strikingly, when we tested CD45 exclusion using TCR-pMHC, we found that exclusion was only 27% for the R₀ isoform and 49% for the R_{ABC} isoform when tested individually. The PD-1-PD-L1 interaction is higher affinity (0.7 μ M) and produces a somewhat higher exclusion (60%) of CD45 R_{ABC}. While the CD45 R₀ isoform exclusion by TCR-pMHC is modest, it nevertheless could be significant for eliciting a signaling response. *In vitro* analysis of the kinase-phosphatase network controlling TCR activation has shown that at physiological protein densities, small perturbations of CD45 can drive large changes in TCR phosphorylation

²⁷. In combination with our results, this suggests that the cellular CD45 concentration may position the TCR precisely at the boundary of a switch-like response in phosphorylation.

Our experimental results also are in reasonable agreement with computational predictions for a lower boundary of receptor-ligand affinity needed for protein exclusion. Computational models by Weikl et al. ¹⁵ predict that, at the ratio of 1 TCR molecule to 8 CD45 molecules used in these experiments, a binding energy of $>4 k_B T$ (corresponding to a K_d of $\sim 20 \mu M$) is required for partitioning. In our system, we find that a pMHC ligand with $15 \mu M$ K_d causes CD45 exclusion whereas a ligand with a K_d of $50 \mu M$ does not. It also has been predicted that increasing the affinity of a receptor-ligand interaction should increase the area fraction of the interface occupied by the receptor-ligand enriched zone by increasing the number of bound complexes at the same protein densities ^{15,25}. However, in our experiments, TCR-pMHC mediated CD45 partitioning occurs as an all-or-nothing process.

Our results also demonstrate that the large extracellular domains of CD45 R_{ABC} and CD45 R_0 are differentially sensitive to the partitioning forces produced by ligand-receptor binding interactions at a membrane-membrane interface. This finding is consistent with results showing that T cells expressing larger CD45 isoforms signal more efficiently ²⁸, although others have contested this conclusion ²⁹. Although the signaling consequences of differential CD45 segregation on immune activation remain to be clarified, our results establish a biophysical difference between two highly conserved CD45 isoforms ³⁰ with regard to their degree of spatial segregation in response to TCR-pMHC interactions. Given that the smaller CD45 isoforms are preferentially expressed in later steps of T cell selection ⁹, our results suggest that T cell signaling may be attenuated by changes in CD45 isoform expression as a mechanism of peripheral tolerance.

We also explore increasing complexity at a membrane interface by introducing two receptor-ligand pairs: TCR-pMHC and PD-1-PD-L1. Interestingly, we find that these two receptor-ligands complexes co-localize with one another and both together exclude CD45. *In vivo*, partial segregation of these two receptor-ligands also has been observed in CD8+ T cells³¹, and a higher degree of co-localization between these receptors was reported in CD4+ T cells¹⁹. Given that the size difference between the TCR-pMHC and PD-1-PD-L1 lies at the biophysical threshold for partitioning²⁶, these results suggest that cellular localization of PD-1 with respect to TCR may be regulated by other factors (e.g. other co-receptors or adaptor proteins) and perhaps even in cell type -specific manner. In addition, it will be interesting to investigate how actin polymer dynamics and lipid-mediated organization³² may enhance or disrupt protein patterning across two membranes.

2.6 Materials and Methods

Materials. Synthetic 1,2-dioleoyl-sn-glycero-3-phosphocholine (POPC; Avanti, 850457), 1,2-dioleoyl-sn-glycero-3-[(N-(5-amino-1-carboxypentyl)iminodiacetic acid)succinyl] (nickel salt, DGS-NTA-Ni; Avanti, 790404) and 1,2-dioleoyl-sn-glycero-3-phosphoethanolamine-N [methoxy(polyethylene glycol)-5000] (ammonium salt, PEG5000-PE; Avanti, 880220) were acquired from Avanti Polar Lipids, Alabama, USA. 1,2-dioleoyl-sn-glycero-3-phosphoethanolamine-Atto390 (DOPE-390; AttoTec, AD390-161) was acquired from Atto-Tec, Germany.

Recombinant protein expression, purification, and labeling. N-terminally His₁₀- and SNAP-tagged FRB and FKBP were subcloned into a pET28a vector and were bacterially expressed in BL21(DE3) strain of *Escherichia coli*. The cells were lysed in an Avestin Emulsiflex system. C-terminally His₁₀- and SNAP- tagged extracellular domains of human CD45 R₀, human CD45 R_{ABC},

and human PD-L1 were subcloned into a pFastBac vector and were expressed in SF9 cells. All proteins were purified by using a HisTrap excel column (GE Healthcare Life Sciences) following the product recommendations. Recombinant C-terminal His₁₀-tagged mouse PD-1 extracellular domain was purchased from Sino Biological.

2B4 TCR V_mC_h chimeras containing an engineered C domain disulfide were cloned into the pAcGP67a insect expression vector (BD Biosciences, 554756) encoding either a C-terminal acidic GCN4-zipper-Biotin acceptor peptide (BAP)-His₆ tag (for α chain) or a C-terminal basic GCN4 zipper-His₆ tag (for β chain)³³. Thus the resulting dimer has a combined His₁₂. Each chain also encoded a 3C protease site between the C-terminus of the TCR ectodomains and the GCN4 zippers to allow for cleavage of zippers. IE^k MHC was cloned into pAcGP67A with acidic/basic zippers and His tags as described for TCRs. IE^k α and 2B4 α chain also encoded ybbr-tag sequence for direct protein labeling. The IE^k β construct was modified with an N-terminal extension containing either the 2A peptide via a Gly-Ser linker or CLIP peptide via a Gly-Ser linker containing a thrombin cleavage site. Proteins were transiently expressed in High Five insect cells (BTI-TN-5B1-4) and purified using His-tag/Nickel according to published protocols¹³.

For fluorescent labeling of SNAP-tagged proteins, 10 μ M protein was incubated with 20 μ M benzylguanine functionalized dye (New England Biolabs) in HBS buffer (50 mM HEPES, 150 mM NaCl, 1 mM TCEP, pH 7.4) for 1 h at room temperature or overnight on ice. For PD-L1 and TCR 10 μ M protein was incubated with 30 μ M tetramethylrhodamine-5-maleimide in HBS buffer for 1 h at room temperature. Excess dyes were removed using Zeba Spin Desalting Columns (ThermoFisher, 89882).

Preparation of SNAP-DNA tethers. Oligonucleotides were ordered from IDT with a 3'/5' terminal amine and labeled with BG-GLA-NHS as previously described³⁴. The adhesion strands used in

this study consisted of a 3' 20mer region (5'- ACTGACTGACTGACTGACTG-3') with a 5' 80mer poly-dT and the complementary sequence (5'- CAGTCAGTCAGTCAGTCAGT-3') also with a 5' 80mer poly-dT. Conjugation to benzyl-guanine was performed as described ³⁴. His₁₀-tagged SNAP was labeled at a concentration of 5 μ M with a 3-fold excess of BG-DNA in HBS (50 mM HEPES, 150 mM NaCl and 1 mM TCEP, pH 7.4).

Electroformation of giant unilamellar vesicles. Lipids were mixed with a molar composition of 94.9% POPC, 5% DGS-NTA, 0.1% DOPE-390 in chloroform (Electron Microscopy Sciences, 12550) and dried under vacuum for 1 h to overnight. Electroformation was performed in 370 mM sucrose according to published protocols ³⁵. GUVs were stored at room temperature and imaged within one week.

Preparation of supported lipid bilayers. Small unilamellar vesicles (SUVs) were prepared from a mixture of 97.5% POPC, 2% DGS-NGA-Ni, and 0.5% PEG5000-PE. The lipid mixture in chloroform was evaporated under argon and further dried under vacuum. The mixture was then rehydrated with phosphate buffered saline pH 7.4 and cycled between -80°C and 37°C 20 times, and then centrifuged for 45 min at 35,000 RCF. SUVs made by this method were stored at 4°C and used within two weeks of formation. Supported lipid bilayers were formed in freshly plasma cleaned custom PDMS chambers on RCA cleaned glass coverslips. 100 μ L of SUV solution containing 0.5 to 1 mg/ml lipid was added to the coverslips and incubated for 30 min. Unadsorbed vesicles were removed and bilayers were blocked by washing three times with reaction buffer (50 mM HEPES, 150 mM NaCl, 1 mM TCEP, 1 mg/mL bovine serum albumen, pH 7.4), and incubating for 20 min.

Optical setup for spinning disk, total internal reflection fluorescence, and scanning angle interference microscopy. Imaging was performed on one of two Nikon TI-E microscopes

equipped with a Nikon 60x Plan Apo VC 1.20 NA water immersion objective, or a Nikon 100x Plan Apo 1.49 NA oil immersion objective, and four laser lines (405, 488, 561, 640 nm), either a Hamamatsu Flash 4.0 or Andor iXon EM-CCD camera, and μ Manager software³⁶. A polarizing filter was placed in the excitation laser path to polarize the light perpendicular to the plane of incidence. Angle of illumination was controlled with either a standard Nikon TIRF motorized positioner or a mirror moved by a motorized actuator (Newport, CMA-25CCCL). Scanning angle microscopy was performed and analyzed as previously described¹¹. For FRAP experiments, a region of $\sim 1 \mu\text{m}^2$ was photobleached using a 405 nm laser modulated by a Rapp UGA-40 photo targeting unit and the fluorescence recovery was monitored over time.

Reconstitution of membrane interfaces. GUVs and SLBs were separately incubated for one hour with the indicated proteins for each experiment. Proteins were diluted in reaction buffer (50 mM HEPES, 150 mM NaCl, 1 mM TCEP, 1 mg/mL bovine serum albumen, pH 7.4) and then mixed 2:1 with GUVs, or added to supported lipid bilayers. SLBs were washed 6 times with $\frac{1}{2}$ total well volume resulting in a final concentration of $\sim 1\%$ input protein remaining. The GUVs were not washed but were diluted 10-fold into the imaging well with the supported lipid bilayer after a one hour incubation. Rapamycin (Sigma, R0395) was added to FRB-FKBP reactions at a final concentration of 5 μM . GUVs were allowed to settle for 30-60 min prior to imaging. SLB fluidity was assessed by visualizing diffusion of unbound GUV proteins that associate with the supported lipid bilayer (e.g. FKBP, TCR, CD45). If $>25\%$ of fluorescent molecules on the SLB were not diffusive, the experiment was repeated with a more fluid bilayer.

Estimated protein densities. Protein densities are estimates based on the conversion factor between protein concentration and molecular density defined by Schmid, et al²⁶. Given our system utilizes an analogous physical setup to their experiments, including the same homemade PDMS-wells with 100 μL volume (described in “Preparation of supported lipid bilayers” section of

the Methods) and protein concentrations in a similar range (1-100nM), we can extrapolate from their measurement of 2,317 +/- 370 molecules/ μm^2 for an SLB with 2.5% DGS-NTA-Ni incubated with 100 nM His₁₀-tagged protein. Because the SLBs used in this study contain 2% DGS-NTA-Ni and GUVs contain 5% DGS-NTA-Ni, this factor (23.17 molec/ μm^2 /nM) was first multiplied by 0.8 or 2, respectively. Protein concentrations (in nM) were then multiplied by the membrane-specific scaling factor to give an estimated final density in molecules/ μm^2 . This estimate may be imperfect due to differences in specific experimental variables affecting total lipid surface area available for protein binding including differences in electroformation. These estimated densities are: FKBP (5-200 molec/ μm^2), CD45 R0 and RABC (1000 molec/ μm^2), TCR (200 molec/ μm^2), PD-L1 (50 molec/ μm^2), SNAP (50 molec/ μm^2), PD-1 (100-300 molec/ μm^2), MHC (200 molec/ μm^2), FRB (20 molec/ μm^2).












Image analysis. Images were analyzed using ImageJ (FIJI)³⁷. The same brightness and contrast were applied to images within the same panels. FIJI rolling ball background subtraction was applied to images before calculating mean fluorescence intensities. Percent exclusion was calculated as one minus the ratio of average intensity inside a receptor enriched zone to the average intensity at the interface outside the receptor-enriched zone. ROIs for inside and outside receptor-enriched zones were selected manually within regions of comparable lipid intensity. All exclusion quantification refers to images acquired using TIRF microscopy. Data from image analysis within FIJI was graphed using Microsoft Excel.

Liposome Assay. Experiments were carried out as previously described¹⁷. Briefly, proteins were purified using baculovirus or bacterial expression system. LUVs and proteins of interest were premixed and incubated at room temperature for 1 h. 2 mM ATP was then injected and rapidly mixed to trigger Lck mediated phosphorylation of CD3 ζ and PD-1. 20 minutes after ATP addition, apyrase was added (t = 0 min) and the reactions were allowed to continue at room temperature.

Equal fractions of the reactions were removed and terminated with SDS sample buffer at the indicated time points. Anti-phosphotyrosine antibody (pY20, Santa Cruz Biotechnology #SC-508) was used to detect phosphorylation by western blotting.

2.7 Supporting Information

Table S2.1. Protein extracellular domain size estimates

	Protein	Size estimate	Notes	References
	FKBP	4 nm	Distance from FKBP Arg 13 to Thr 85 from PDB 3FAP measured in Chimera software.	Liang et al. 1999
	FRB	4 nm	Distance from FRB Gln 152 to Asn 182 from PDB 3FAP measured in Chimera software.	Liang et al. 1999
	FKBP-FRB complex	6 nm	Distance from FKBP Thr 6 to FRB Gln 152 from PDB 3FAP measured in Chimera software.	Liang et al. 1999
	CD45 R ₀	25 nm	Estimate based on published electron microscopy and crystallographic studies.	Woollett et al. 1985, McCall et al. 1992, Chang et al. 2016
	CD45 R _{ABC}	40 nm	Estimate based on published electron microscopy and crystallographic studies.	Woollett et al. 1985, McCall et al. 1992, Chang et al. 2016
	TCR	7 nm	Distance from TCR β Asp 244 to TCR α Thr 92 from PDB 4P2O measured in Chimera software.	Birnbaum et al. 2014
	pMHC	7 nm	Distance from MHC β Pro 165 to Pro 65 from PDB 4P2O measured in Chimera software.	Birnbaum et al. 2014
	TCR-pMHC complex	13 nm	Distance from TCR β Asp 244 to MHC β Pro 165 from PDB 4P2O measured in Chimera software.	Birnbaum et al. 2014
	PD-1	5 nm	Distance from Pro 130 to Ile 148 from PDB 3BIK measured in Chimera software.	Lin et al. 2008
	PD-L1	8 nm	Distance from Gln 47 to Leu 229 from PDB 3BIK measured in Chimera software.	Lin et al. 2008
	PD-1-PD-L1 complex	9 nm	Distance from PD-L1 Leu 229 to PD-1 Ile 148 from PDB 3BIK measured in Chimera software.	Lin et al. 2008
-	SNAP	5 nm	Distance from Ala 50 to Leu 153 from PDB 3KZY measured in Chimera software.	Schmitt et al. 2010

-	DNA tether	125 nm	Assuming 0.34 nm per double stranded base pair (20 bp) and 0.67 nm per single stranded base pair (160 bp) plus 5 nm for each of two SNAP proteins. At this length the DNA tether is expected to be quite flexible.	Chi et al, 2013
---	---------------	--------	--	-----------------

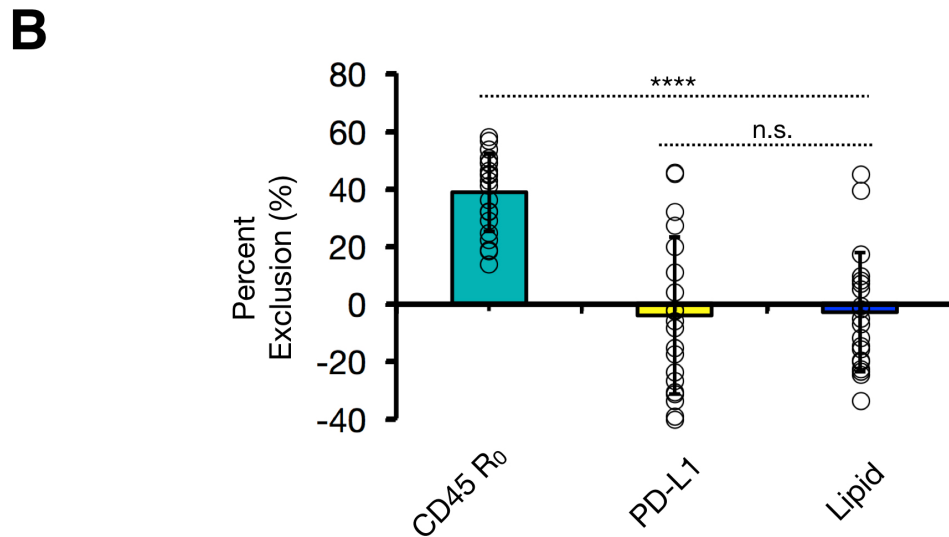
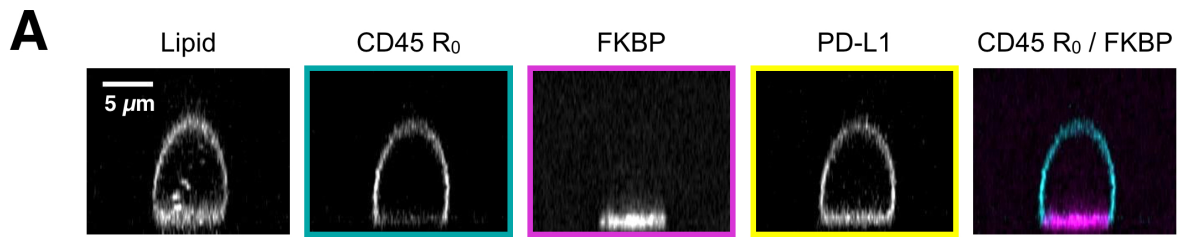


Fig. S2.1. PD-L1 is not excluded from FKBP-bound membrane interfaces. **(A)** Spinning disk z-sections of GUVs after membrane-apposed interfaces have reached equilibrium, showing localization of FKBP to the membrane interface, localization of CD45 R₀ away from the interface, and uniform distribution of PD-L1. **(B)** Quantification of experiment shown in **A**; mean \pm standard deviation (n=20 GUVs pooled from two experiments).

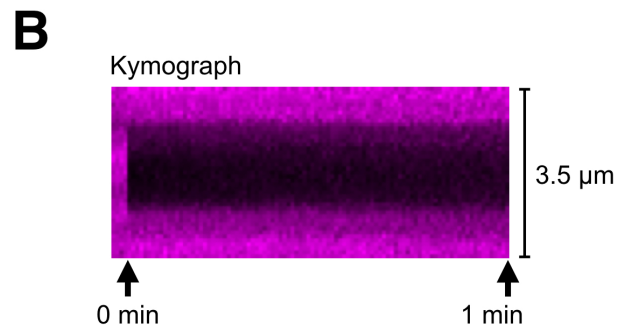
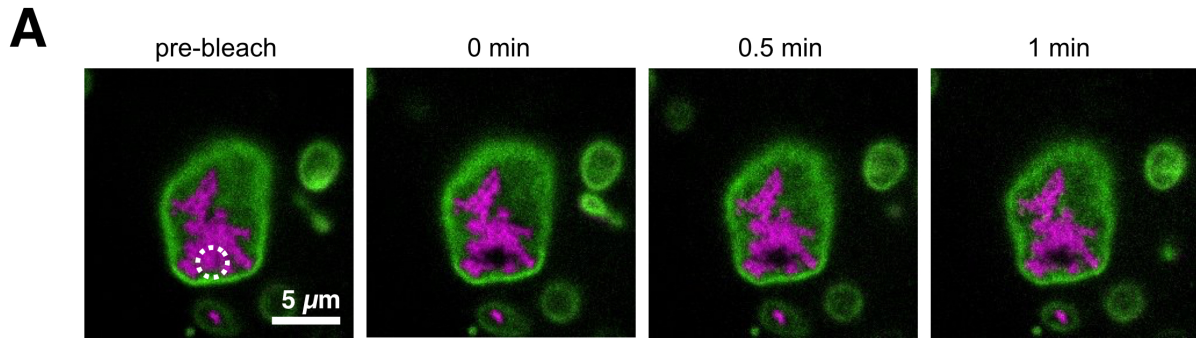


Fig. S2.2. FKBP molecules in partitioned domains do not readily exchange. **(A)** Images for FKBP enriched interfaces before and after photobleaching (dashed white line, bleach site). Scale bars, 5 μ m **(B)** Kymograph corresponding to **A**. Data are representative of three independent experiments.

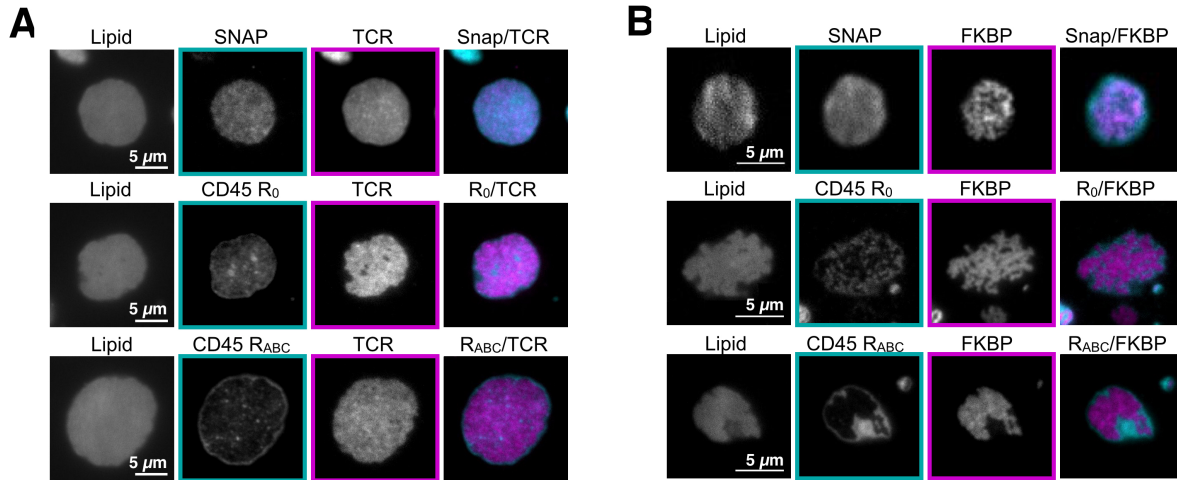


Fig. S2.3. TCR-pMHC and FRB-FKBP exclude CD45 R₀ and CD45 R_{ABC} but not SNAP. **(A)** TIRF microscopy of a GUV-SLB interface at equilibrium showing concentration of TCR into microdomains. Top, SNAP is homogeneously distributed. Middle, CD45 R₀ is weakly excluded. Bottom, CD45 R_{ABC} is strongly excluded. **(B)** TIRF microscopy of a GUV-SLB interface at equilibrium showing concentration of FKBP into micro domains. SNAP is homogeneously distributed. CD45 R₀ and CD45 R_{ABC} are excluded.

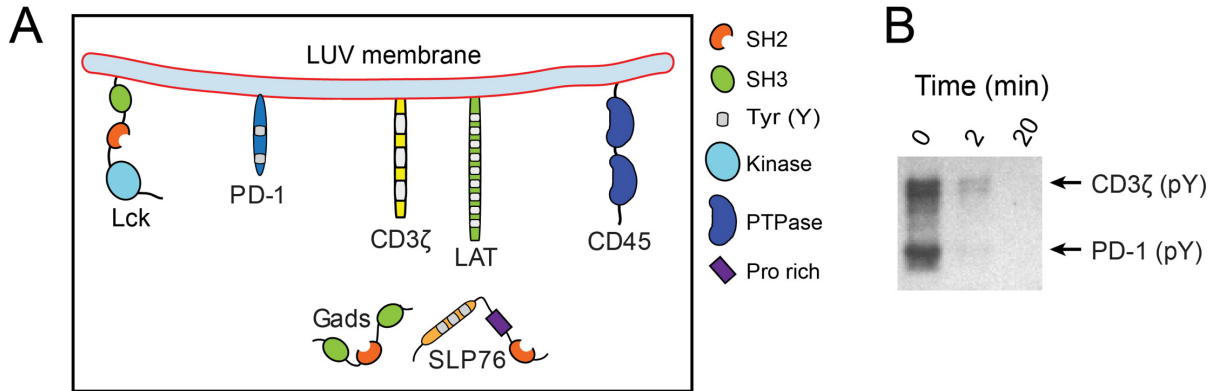


Fig. S2.4. PD-1 is a target for CD45 dephosphorylation. (A) Schematic of LUV reconstitution system for assaying the sensitivity PD-1 to CD45. DGS-NTA-Ni containing LUVs were attached with purified, polyhistidine-tagged cytosolic domains of receptors (CD3ζ [290 molecules per μm^2]; PD-1 [870 molecules per μm^2]), the adaptor LAT (870 molecules per μm^2), the kinase Lck (290 molecules per μm^2), and the phosphatase CD45 (29 molecules per μm^2). Purified cytosolic factors (Gads [0.3 μM]; SLP76 [0.3 μM]) were added to solution to create a more physiological setting. Pre-addition of ATP triggered net phosphorylation of both CD3ζ and PD-1 by Lck, despite the presence of CD45, owing to the 10-fold excess of Lck over CD45. (B) A phosphotyrosine western blot showing the time course of CD3ζ and PD-1 dephosphorylation by CD45, after the addition of the ATP scavenger Apyrase, which rapidly terminated the Lck kinase activity to isolate the CD45 activity. PTPase, protein tyrosine phosphatase; Pro, proline.

2.8 Author Contributions

Author contributions: C.B.C., N.K., E.H., X.S., and R.D.V. designed research; C.B.C., N.K., and E.H. performed research; C.B.C., N.K., R.A.F., E.H., X.S., and K.C.G. contributed new reagents/analytic tools; C.B.C. and N.K. analyzed data; and C.B.C., N.K., and R.D.V. wrote the paper.

2.9 Acknowledgements

We would like to thank N. Stuurman for help with microscopy and image analysis and M. Taylor for guidance with protein purification and DNA tethering. We thank A. Williamson, N. Stuurman, and M. Morrissey for comments on the manuscript. The authors acknowledge funding from the Howard Hughes Medical Institute and National Institutes of Health (R01EB007187, R.D.V.).

2.10 References

1. Banaszynski, L. A., Liu, C. W. & Wandless, T. J. Characterization of the FKBP·Rapamycin·FRB Ternary Complex. *J. Am. Chem. Soc.* **127**, 4715–4721 (2005).
2. Signal Transduction Through a DNA-Based T Cell Receptor.
3. Chi, Q., Wang, G. & Jiang, J. The persistence length and length per base of single-stranded DNA obtained from fluorescence correlation spectroscopy measurements using mean field theory. *Phys. A Stat. Mech. its Appl.* **392**, 1072–1079 (2013).
4. Woollett, G. R., Williams, A. F. & Shotton, D. M. Visualisation by low-angle shadowing of the leucocyte-common antigen. A major cell surface glycoprotein of lymphocytes. *EMBO J.* **4**, 2827–2830 (1985).
5. McCall, M. N., Shotton, D. M. & Barclay, A. N. Expression of soluble isoforms of rat CD45. Analysis by electron microscopy and use in epitope mapping of anti-CD45R monoclonal antibodies. *Immunology* **76**, 310–7 (1992).
6. Chang, V. T. *et al.* Initiation of T cell signaling by CD45 segregation at ‘close contacts’. *Nat. Immunol.* **17**, 574–582 (2016).
7. Gautier, A. *et al.* An Engineered Protein Tag for Multiprotein Labeling in Living Cells. *Chem. Biol.* **15**, 128–136 (2008).
8. Bannwarth, M. *et al.* Crystal structure of SNAP-tag. *doi.org* doi:10.2210/pdb3kzy/pdb
9. Hermiston, M. L., Xu, Z. & Weiss, A. CD45: a critical regulator of signaling thresholds in immune cells. *Annu. Rev. Immunol.* **21**, 107–137 (2003).
10. Davis, S. J. & van der Merwe, P. A. The kinetic-segregation model: TCR triggering and beyond. *Nat. Immunol.* **7**, 803–809 (2006).
11. Carbone, C. B., Vale, R. D. & Stuurman, N. *A data acquisition and analysis pipeline for scanning angle interference microscopy.* (2016). doi:10.1101/050468
12. Liang, J., Choi, J. & Clardy, J. Refined structure of the FKBP12-rapamycin-FRB ternary

- complex at 2.2 Å resolution. *Acta Crystallogr. D. Biol. Crystallogr.* **55**, 736–44 (1999).
13. Birnbaum, M. E. *et al.* Deconstructing the Peptide-MHC Specificity of T Cell Recognition. *Cell* **157**, 1073–1087 (2014).
 14. Gascoigne, N. R. J., Zal, T. & Alam, S. M. T-cell receptor binding kinetics in T-cell development and activation. *Expert Rev. Mol. Med.* **3**, (2001).
 15. Weikl, T. R. & Lipowsky, R. Pattern formation during T-cell adhesion. *Biophys. J.* **87**, 3665–3678 (2004).
 16. Chen, L. & Flies, D. B. Molecular mechanisms of T cell co-stimulation and co-inhibition. *Nat. Rev. Immunol.* **13**, 227–242 (2013).
 17. Hui, E. *et al.* T cell co-stimulatory receptor CD28 is a primary target for PD-1-mediated inhibition. (2016). doi:10.1101/086652
 18. Kamphorst, A. O. *et al.* Rescue of exhausted CD8 T cells by PD-1–targeted therapies is CD28-dependent. *Science (80-.)*. **355**, 1423–1427 (2017).
 19. Yokosuka, T. *et al.* Programmed cell death 1 forms negative costimulatory microclusters that directly inhibit T cell receptor signaling by recruiting phosphatase SHP2. *J. Exp. Med.* **209**, 1201–1217 (2012).
 20. Sheppard, K.-A. *et al.* PD-1 inhibits T-cell receptor induced phosphorylation of the ZAP70/CD3 ζ signalosome and downstream signaling to PKC θ . *FEBS Lett.* **574**, 37–41 (2004).
 21. Lin, D. Y. -w. *et al.* The PD-1/PD-L1 complex resembles the antigen-binding Fv domains of antibodies and T cell receptors. *Proc. Natl. Acad. Sci.* **105**, 3011–3016 (2008).
 22. Butte, M. J., Peña-Cruz, V., Kim, M.-J., Freeman, G. J. & Sharpe, A. H. Interaction of human PD-L1 and B7-1. *Mol. Immunol.* **45**, 3567–3572 (2008).
 23. Burroughs, N. J. & Wülfing, C. Differential segregation in a cell-cell contact interface: The dynamics of the immunological synapse. *Biophys. J.* **83**, 1784–1796 (2002).
 24. Krobath, H., Rózycki, B., Lipowsky, R. & Weikl, T. R. Line tension and stability of domains

- in cell-adhesion zones mediated by long and short receptor-ligand complexes. *PLoS One* **6**, (2011).
25. Chung, M., Koo, B. J. & Boxer, S. G. Formation and analysis of topographical domains between lipid membranes tethered by DNA hybrids of different lengths. *Faraday Discuss.* **161**, 333–45; discussion 419-59 (2013).
 26. Schmid, E. M. *et al.* Size-dependent protein segregation at membrane interfaces. *Nat. Phys.* **12**, 704–711 (2016).
 27. Hui, E. & Vale, R. D. In vitro membrane reconstitution of the T-cell receptor proximal signaling network. *Nat. Struct. Mol. Biol.* **21**, 133–42 (2014).
 28. Chui, D., Ong, C. J., Johnson, P., Teh, H. S. & Marth, J. D. Specific CD45 isoforms differentially regulate T cell receptor signaling. *EMBO J.* **13**, 798–807 (1994).
 29. Czyzyk, J., Leitenberg, D., Taylor, T. & Bottomly, K. Combinatorial Effect of T-Cell Receptor Ligation and CD45 Isoform Expression on the Signaling Contribution of the Small GTPases Ras and Rap1. *Mol. Cell. Biol.* **20**, 8740–8747 (2000).
 30. Okumura, M. *et al.* Comparison of CD45 extracellular domain sequences from divergent vertebrate species suggests the conservation of three fibronectin type III domains. *J. Immunol.* **157**, 1569–75 (1996).
 31. Hui, E. *et al.* T cell costimulatory receptor CD28 is a primary target for PD-1–mediated inhibition. *Science (80-.).* **355**, 1428–1433 (2017).
 32. Köster, D. V & Mayor, S. Cortical actin and the plasma membrane: inextricably intertwined. *Curr. Opin. Cell Biol.* **38**, 81–89 (2016).
 33. Wilson, D. B. *et al.* Immunogenicity. I. Use of peptide libraries to identify epitopes that activate clonotypic CD4+ T cells and induce T cell responses to native peptide ligands. *J. Immunol.* **163**, 6424–34 (1999).
 34. Farlow, J. *et al.* Formation of targeted monovalent quantum dots by steric exclusion. *Nat. Methods* **10**, 1203–1205 (2013).

35. Schmid, E. M., Richmond, D. L. & Fletcher, D. A. *Reconstitution of proteins on electroformed giant unilamellar vesicles. Methods in Cell Biology* **128**, (Elsevier Ltd, 2015).
36. Stuurman, N., Edelstein, A., Amodaj, N., Hoover, K. & Vale, R. Computer control of microscopes using manager. *Current Protocols in Molecular Biology* **CHAPTER**, Unit14.20 (2010).
37. Schindelin, J. *et al.* Fiji: an open-source platform for biological-image analysis. *Nat. Methods* **9**, 676–82 (2012).

CHAPTER 3

Tight nanoscale clustering of Fc γ -receptors using DNA origami promotes phagocytosis

Nadja Kern^{1,2}, Rui Dong^{1,2}, Shawn Douglas¹, Ronald D. Vale^{1,2,3*} and Meghan A. Morrissey^{1,4,5*}

¹ Department of Cellular and Molecular Pharmacology, University of California San Francisco, San Francisco, CA 94158; ² Howard Hughes Medical Institute, University of California San Francisco, San Francisco, CA 94158; ³ Howard Hughes Medical Institute Janelia Research Campus, Ashburn, VA 20147; ⁴ Department of Molecular, Cellular and Developmental Biology, University of California Santa Barbara, CA 93106

*Corresponding Author

⁵Lead contact

3.1 Abstract

Macrophages destroy pathogens and diseased cells through $Fc\gamma$ receptor ($Fc\gamma R$)-driven phagocytosis of antibody-opsonized targets. Phagocytosis requires activation of multiple $Fc\gamma R$ s, but the mechanism controlling the threshold for response is unclear. We developed a DNA origami-based engulfment system that allows precise nanoscale control of the number and spacing of ligands. When the number of ligands remains constant, reducing ligand spacing from 17.5 nm to 7 nm potently enhances engulfment, primarily by increasing efficiency of the engulfment-initiation process. Tighter ligand clustering increases receptor phosphorylation, as well as proximal downstream signals. Increasing the number of signaling domains recruited to a single ligand-receptor complex was not sufficient to recapitulate this effect, indicating that clustering of multiple receptors is required. Our results suggest that macrophages use information about local ligand densities to make critical engulfment decisions, which has implications for the mechanism of antibody-mediated phagocytosis and the design of immunotherapies.

3.2 Introduction

Immune cells eliminate pathogens and diseased cells while limiting damage to healthy cells. Macrophages, professional phagocytes and key effectors of the innate immune system, play an important role in this process by engulfing opsonized targets bearing 'eat me' signals. One of the most common 'eat me' signals is the immunoglobulin G (IgG) antibody, which can bind foreign proteins on infected cells or pathogens. IgG is recognized by Fc γ receptors (Fc γ R) in macrophages that drive antibody-dependent cellular phagocytosis (ADCP) ¹⁻³. ADCP is a key mechanism of action for several cancer immunotherapies including rituximab, trastuzumab, and cetuximab ⁴⁻⁸. Exploring the design parameters of effective antibodies could provide valuable insight into the molecular mechanisms driving ADCP.

Activation of multiple Fc γ Rs is required for a macrophage to engulf a three-dimensional target. Fc γ R-IgG must be present across the entire target to drive progressive closure of the phagocytic cup that surrounds the target ⁹. In addition, a critical antibody threshold across an entire target dictates an all-or-none engulfment response by the macrophage ¹⁰. Although the mechanism of this thresholded response remains unclear, receptor clustering plays a role in regulating digital responses in other immune cells ¹¹⁻¹⁶. Fc γ R clustering may also regulate phagocytosis ¹⁷. High resolution imaging of macrophages has demonstrated that IgG-bound Fc γ Rs form clusters (resolution of >100 nm) within the plasma membrane ¹⁸⁻²⁰. These small clusters, which recruit downstream effector proteins such as Syk-kinase and phosphoinositide 3-kinase, eventually coalesce into larger micron-scale patches as they migrate towards the center of the cell-target synapse ¹⁸⁻²¹.

Prior observational studies could not decouple ligand clustering from other parameters, such as ligand number or receptor mobility. As a result, we do not have a clear picture of how ligand

number or molecular spacing regulate signal activation. To directly assess such questions, we have developed a reconstituted system that utilizes DNA origami to manipulate ligand patterns on a single-molecule level with nanometer resolution. We found that tightly spaced ligands strongly enhanced phagocytosis compared to the same number of more dispersed ligands. Through manipulating the number and spacing of ligands on individual origami pegboards, we found that 8 or more ligands per cluster maximized Fc γ R-driven engulfment, and that macrophages preferentially engulfed targets that had receptor-ligand clusters spaced ≤ 7 nm apart. We demonstrated that tight ligand clustering enhanced receptor phosphorylation, and the generation of PIP $_3$ and actin filaments—critical downstream signaling molecules—at the phagocytic synapse. Together, our results suggest that the nanoscale clustering of receptors may allow macrophages to discriminate between lower density background stimuli and the higher density of ligands on opsonized targets. These results have implications for the design of immunotherapies that involve manipulating Fc γ R-driven engulfment.

3.3 Results

Developing a DNA-based chimeric antigen receptor to study phagocytosis

To study how isolated biochemical and biophysical ligand parameters affect engulfment, we sought to develop a well-defined and tunable engulfment system. Our lab previously developed a synthetic T cell signaling system, in which we replaced the receptor-ligand interaction (TCR-pMHC) with complimentary DNA oligos²². We applied a similar DNA-based synthetic chimeric antigen receptor to study engulfment signaling in macrophages. In our DNA-CAR γ receptor, we replaced the native extracellular ligand binding domain of the Fc γ receptor with an extracellular SNAP-tag that covalently binds a benzyl-guanine-labeled single-stranded DNA (ssDNA) [receptor DNA; Figure 1a;²³]. The SNAP-tag was then joined to the CD86 transmembrane domain followed

by the intracellular signaling domain of the FcR γ chain³. We expressed the DNA-CAR γ in the macrophage-like cell line RAW264.7 and the monocyte-like cell line THP-1.

As an engulfment target, we used silica beads coated with a supported lipid bilayer to mimic the surface of a target cell. The beads were functionalized with biotinylated ssDNA (ligand DNA) containing a sequence complementary to the receptor DNA via biotin-neutravidin interactions (Figure 1a). We used a ligand DNA strand that has 13 complementary base pairs to the receptor DNA, which we chose because the receptor-ligand dwell time (~ 24 sec²²) was comparable to the dwell time of IgG-Fc γ R interactions (~ 30 -150 sec²⁴).

To test whether this synthetic system can drive specific engulfment of ligand-functionalized silica beads, we used confocal microscopy to measure the number of beads that were engulfed by each cell (Figure 1b, c). The DNA-CAR γ drove specific engulfment of DNA-bound beads in both RAW264.7 and THP-1 cells (Figure 1c, S1). The extent of engulfment was similar to IgG-coated beads, and the ligand density required for robust phagocytosis was also comparable to IgG [Figure 1d, S1;^{25,26}]. As a control, we tested a variant of the DNA-CAR that lacked the intracellular domain of the FcR γ chain (DNA-CAR_{adhesion}). Cells expressing the DNA-CAR_{adhesion} failed to induce engulfment of DNA-functionalized beads (Figure 1c), demonstrating that this process depends upon the signaling domain of the Fc γ receptor. Together, these data show that the DNA-CAR γ can drive engulfment of targets in a ligand- and Fc γ R-specific manner.

DNA origami pegboards activate DNA-CAR γ macrophages

DNA origami technology provides the ability to easily build three-dimensional objects that present ssDNA oligonucleotides with defined nanometer-level spatial organization^{15,27-30}. We used DNA origami to manipulate the spatial distribution of DNA-CAR γ ligands in order to determine how

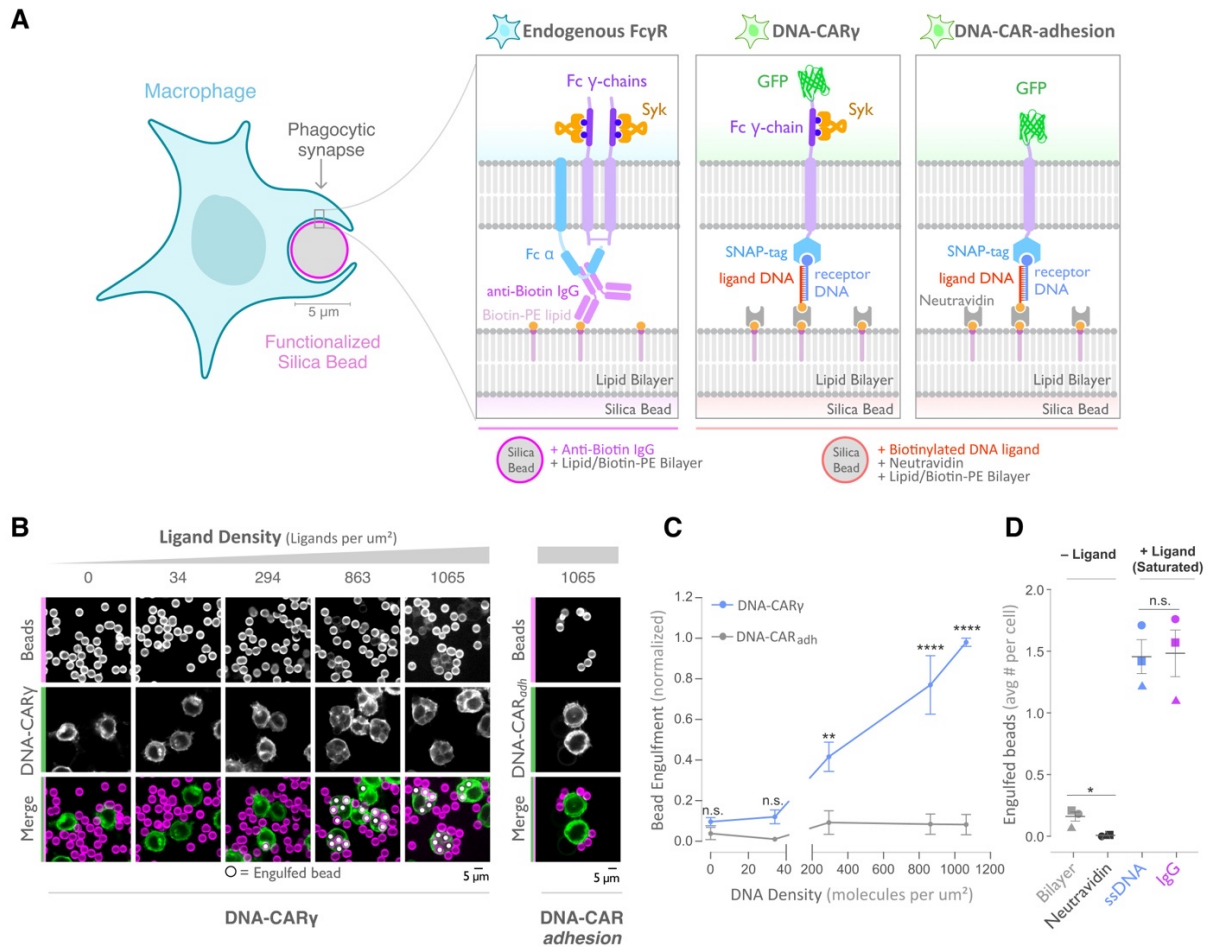


Figure 3.1: A DNA-based system for controlling engulfment

(A) Schematic shows the endogenous (left box) and DNA-based (middle and right boxes) engulfment systems. Engulfment via endogenous Fc γ R_s (left box) is induced through anti-biotin IgG bound to 1-oleoyl-2-(12-biotinyl(aminododecanoyl))-sn-glycero-3-phosphoethanolamine (biotin-PE) lipids incorporated into the bilayer surrounding the silica bead targets. Engulfment induced via the DNA-based system uses chimeric antigen receptors (CAR) expressed in the macrophage and biotinylated ligand DNA that is bound to the lipid bilayer surrounding the silica bead. The DNA-CAR γ (middle box) consists of a ssDNA (receptor DNA) covalently attached to an extracellular SNAP-tag fused to a CD86 transmembrane domain, the intracellular domain of the FcR γ chain, and a fluorescent tag. The DNA-CAR_{adhesion} (right box) is identical but lacks the signaling FcR γ chain. (B) Example images depicting the engulfment assay. Silica beads were coated with a supported lipid bilayer (magenta) and functionalized with neutravidin and the indicated density of ligand DNA (Figure S1a). The functionalized beads were added to RAW264.7 macrophages expressing either the DNA-CAR γ or the DNA-CAR_{adhesion} (green) and fixed after 45 min. The average number of beads engulfed per macrophage was assessed by confocal microscopy. Scale bar denotes 5 μ m here and in all subsequent figures. Internalized beads are denoted with a white sphere in the merged images. (C) The number of beads engulfed per cell for DNA-CAR γ (blue) or DNA-CAR_{adhesion} (grey) macrophages was normalized to the maximum bead eating observed in each replicate. Dots and error bars denote the mean \pm SEM of three independent replicates ($n \geq 100$ cells analyzed per experiment). (D) DNA-CAR γ expressing macrophages were incubated with bilayer-coated beads (grey) functionalized with anti-biotin IgG (magenta), neutravidin (black), or neutravidin and saturating amounts of ssDNA (blue). The average number of beads engulfed per cell was assessed. Full data representing the fraction of macrophages

engulfing specific numbers of IgG or ssDNA beads is shown in figure S1. Each data point represents the mean of an independent experiment, denoted by symbol shape, and bars denote the mean \pm SEM. n.s. denotes $p > 0.05$, * indicates $p < 0.05$, ** indicates $p < 0.005$ and **** indicates $p < 0.0001$ by a multiple t-test comparison corrected for multiple comparisons using the Holm-Sidak method (C) or Student's T-test (D).

nanoscale ligand spacing affects engulfment. We used a recently developed two-tiered DNA origami pegboard that encompasses a total of 72 ssDNA positions spaced 7 nm and 3.5 nm apart in the x and y dimensions, respectively (Figure 2a, S2). Each of the 72 ligand positions can be manipulated independently, allowing for full control over the ligand at each position (Figure S2). The DNA origami pegboard also contains fluorophores at each of its four corners to allow for visualization, and 12 biotin-modified oligos on the bottom half of the pegboard to attach it to a neutravidin-containing supported lipid bilayer or glass coverslip (Figure 2a, b, S2).

To determine if the DNA origami pegboards could successfully activate signaling, we first tested whether receptors were recruited to the origami pegboard in a ligand-dependent manner. Using TIRF microscopy, we quantified the fluorescence intensity of the recruited GFP-tagged DNA-CAR γ receptor to origami pegboards presenting 0, 2, 4, 16, 36 or 72 ligands (Figure 2b-e). Using signal from the 72 ligand (72L) origami pegboard as an internal intensity standard of brightness, and thus correcting for differences in illumination between wells, we found that the average fluorescence intensity correlated with the number of ligands presented by individual origami pegboards (Figure 2d, e). In addition, we measured Syk recruitment to individual DNA origami pegboards and found that Syk intensity also increased as a function of the number of ligands present on each origami pegboard (Figure 2c, S3). These results confirmed that our DNA origami system provides a platform that allows quantitative receptor recruitment and the analysis of downstream signaling pathways.

Nanoscale clustering of ligand enhances phagocytosis

Fc γ receptors cluster upon ligand binding, but the functional importance of such clustering for phagocytosis has not been directly addressed, and whether a critical density of receptor-ligand pairs is necessary to initiate Fc γ R signaling is unclear^{18-21,31}. To address these questions, we varied the size of ligand clusters by designing DNA origami pegboards presenting 2-36 ligands.

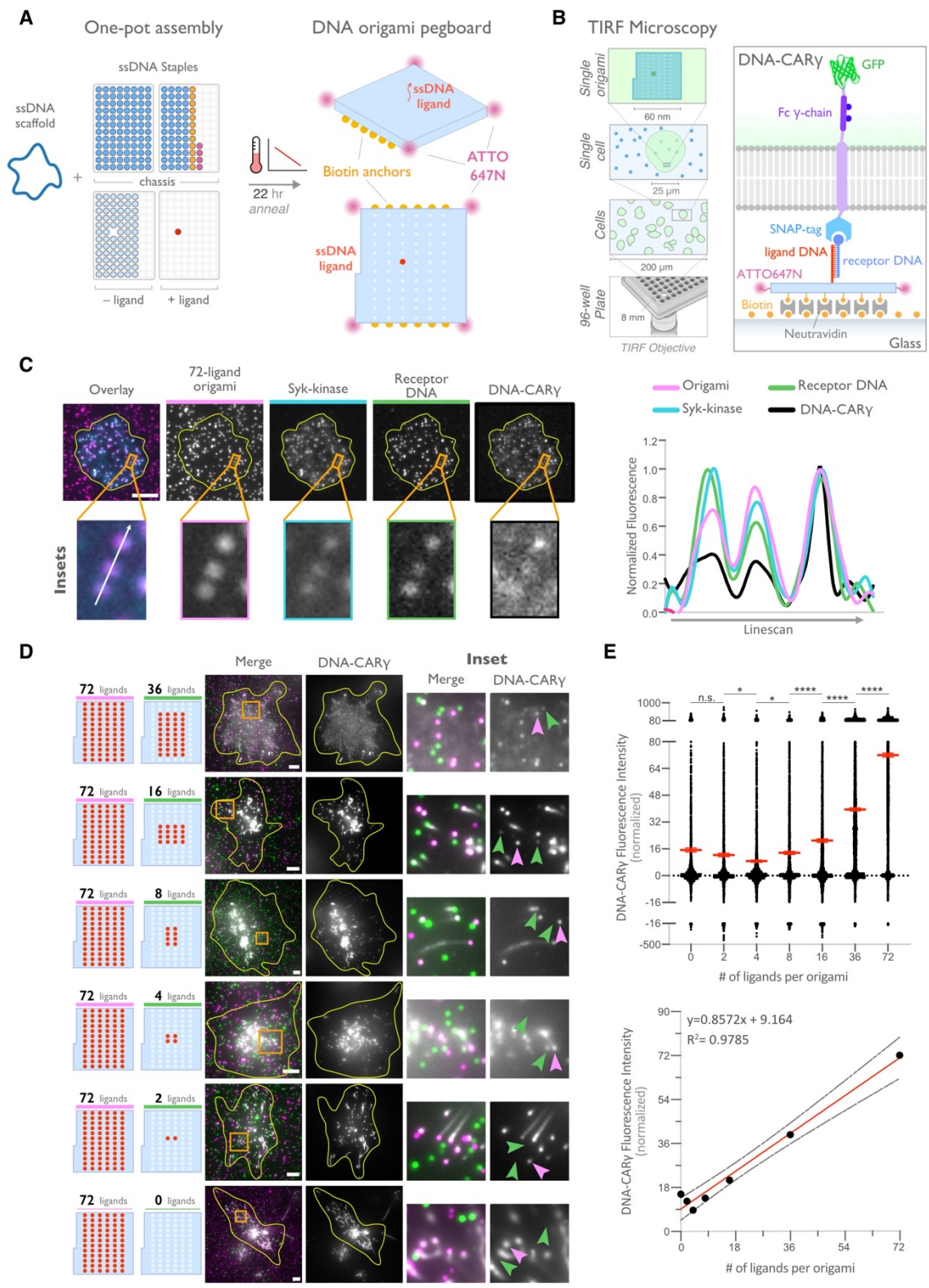


Figure 3.2: DNA origami pegboard induces ligand dependent signaling

(A) Schematic shows the DNA-origami pegboard used in this study (right) and the components used to create it using a one-pot assembly method (left, figure S2). The top of the two-tiered DNA origami pegboard

has 72 positions spaced 7 nm and 3.5 nm apart in the x and y dimensions, which can be modified to expose a single-stranded ligand DNA (red) or no ligand (light blue). A fluorophore is attached at each corner of the pegboard for visualization (pink). The bottom tier of the pegboard displays 12 biotin molecules (yellow) used to attach the origami to neutravidin-coated surfaces. Full representation of the DNA origami pegboard assembly is shown in figure S2. (B) Schematic portraying the TIRF microscopy setup used to image THP-1 cells interacting with origami pegboards functionalized to glass coverslips in (C) and (D) (left). On the right is a zoomed-in side view of an origami pegboard functionalized to a biotin (yellow) and neutravidin (grey) functionalized glass coverslip and interacting with a single DNA-CAR γ receptor. (C) TIRF microscopy images of THP-1 cells show that the DNA-CAR γ (BFP; 5th panel; black in linescan), the receptor DNA bound to the DNA-CAR γ (Cy5; 4th panel; green in linescan), and Syk (mNeonGreen; 3rd panel; cyan in merge and linescan) are recruited to individual 72-ligand origami pegboards (Atto-647; 2nd panel; magenta in merge and linescan). Each diffraction limited magenta spot represents an origami pegboard. The top panels show a single cell (outlined in yellow), and the bottom insets (orange box in top image) show three origami pegboards at higher magnification. The linescan (right, area denoted with a white arrow in merged inset) shows the fluorescence intensity of each of these channels. Intensity was normalized so that 1 is the highest observed intensity and 0 is background for each channel. (D) TIRF microscopy images show DNA-CAR γ expressing THP1s interacting with 72-ligand origami pegboards (pink) and origami pegboards presenting the indicated number of ligands (pegboards labeled in green). Left schematics represent origami pegboard setups for each row of images where red dots denote the presence of a ligand DNA. Middle images depict a single macrophage (outlined in yellow), and right images show the area indicated with an orange box on the left. Examples of DNA-CAR γ -mNeonGreen (grey) recruitment to individual origami pegboards is marked by pink (72L origami pegboard) and green (origami pegboard with the indicated ligand number) arrowheads (right). (E) Quantification of experiment shown in (D). Top graph shows the DNA-CAR γ intensity at the indicated origami pegboard type normalized to the average DNA-CAR γ intensity at 72L origami pegboards in the same well. Each dot represents one origami pegboard and red lines denote the mean \pm SEM of pooled data from three separate replicates. n.s. denotes $p > 0.05$, * indicates $p < 0.05$, and **** indicates $p < 0.0001$ by an ordinary one-way ANOVA with Holm-Sidak's multiple comparison test. A linear regression fit (bottom) of the average fluorescence intensities of each of the origami pegboards suggests that the mean DNA-CAR γ fluorescent intensities are linearly proportional to the number of ligands per DNA origami pegboard. The black dots represent the mean normalized DNA-CAR γ intensity, the red line denotes the linear regression fit, and the grey lines show the 95% confidence intervals.

To ensure a constant total number of ligands and origami pegboards on each bead, we mixed the signaling origami pegboards with 0-ligand “blank” origami pegboards in appropriate ratios (Figure 3a). We confirmed that the surface concentration of origami pegboards on the beads was comparable using fluorescence microscopy (Figure S4). We found that increasing the number of ligands per cluster increased engulfment, but that engulfment plateaued at a cluster size of 8 ligands (Figure 3b). We confirmed that the observed engulfment phenotype was both ligand, receptor, and Fc γ R signaling dependent (Figure 3c, d). Together, these data reveal that Fc γ receptor clustering strongly enhances engulfment, up to a cluster size of 8 ligands.

Spatial organization of ligands in nanoclusters regulates engulfment

Next, we examined whether distance between individual receptor-ligand molecules within a signaling cluster impacts engulfment. For this experiment, we varied the spacing of 4 ligands on the origami pegboard. The 4-ligand tight origami (4T) contains 4 ligands clustered at the center of the pegboard (7 nm by 3.5 nm square), the medium origami (4M) has ligands spaced 21 nm by 17.5 nm apart, and the spread origami (4S) has 4 ligands positioned at the four corners of the pegboard (35 nm by 38.5 nm square) (Figure 4a). We found that the efficiency of macrophage engulfment was approximately 2-fold higher for the 4T functionalized beads when compared to the 4M or 4S beads (Figure 4a). We confirmed via fluorescence microscopy that the concentration of origami pegboards on the surface was similar, and therefore ligand numbers on the beads were similar (Figure S5). DNA CAR constructs that have the FcR γ and α chain transmembrane domains in place of the CD86 transmembrane domain and human THP-1 cells expressing the DNA-CAR γ showed the same ligand spacing dependence (Figure S5). Expression of the various DNA CARs at the cell cortex was comparable, and engulfment of beads functionalized with both the 4T and the 4S origami platforms was dependent on the Fc γ R signaling domain (Figure S5).

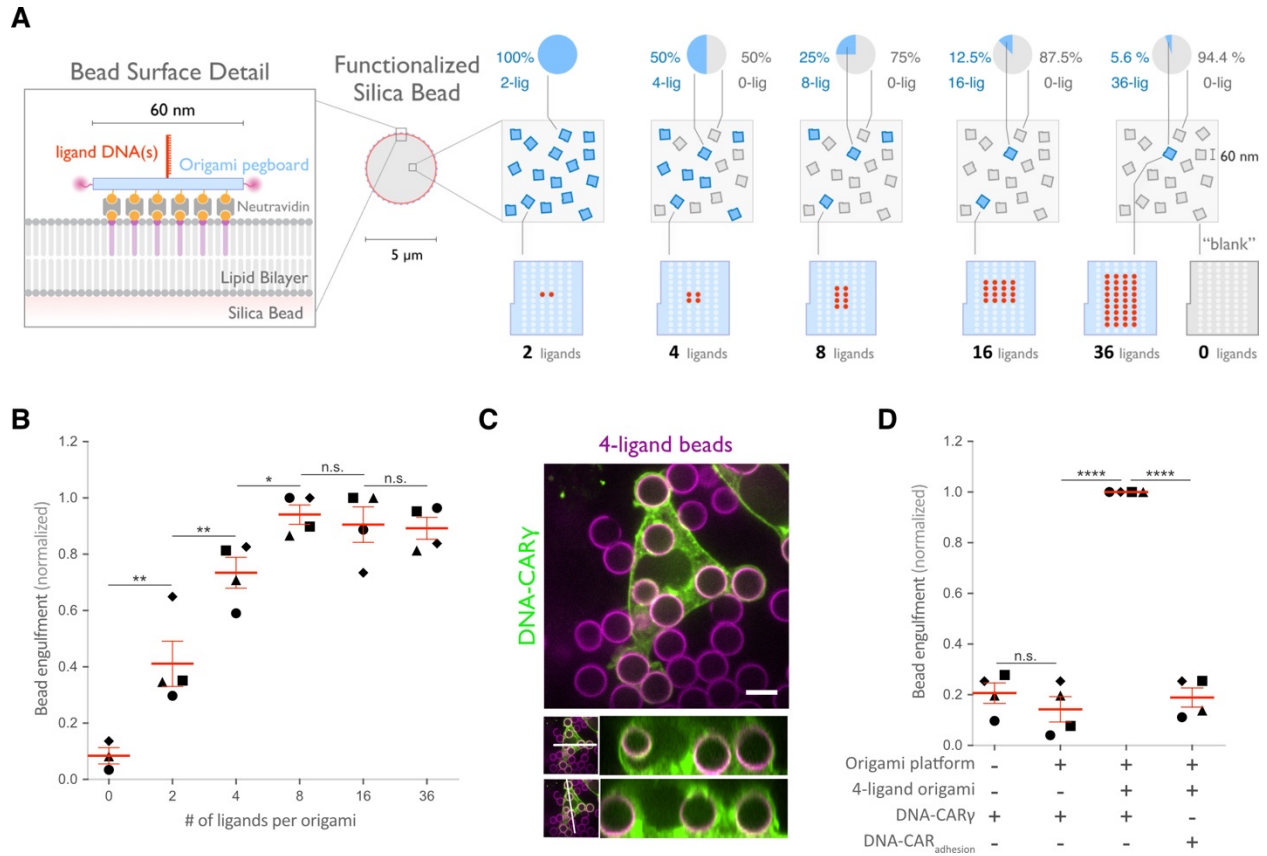


Figure 3.2: DNA origami pegboard induces ligand dependent signaling

(A) Schematic shows the DNA-origami pegboard used in this study (right) and the components used to create it using a one-pot assembly method (left, figure S2). The top of the two-tiered DNA origami pegboard has 72 positions spaced 7 nm and 3.5 nm apart in the x and y dimensions, which can be modified to expose a single-stranded ligand DNA (red) or no ligand (light blue). A fluorophore is attached at each corner of the pegboard for visualization (pink). The bottom tier of the pegboard displays 12 biotin molecules (yellow) used to attach the origami to neutravidin-coated surfaces. Full representation of the DNA origami pegboard assembly is shown in figure S2. (B) Schematic portraying the TIRF microscopy setup used to image THP-1 cells interacting with origami pegboards functionalized to glass coverslips in (C) and (D) (left). On the right is a zoomed-in side view of an origami pegboard functionalized to a biotin (yellow) and neutravidin (grey) functionalized glass coverslip and interacting with a single DNA-CAR γ receptor. (C) TIRF microscopy images of THP-1 cells show that the DNA-CAR γ (BFP; 5th panel; black in linescan), the receptor DNA bound to the DNA-CAR γ (Cy5; 4th panel; green in linescan), and Syk (mNeonGreen; 3rd panel; cyan in merge and linescan) are recruited to individual 72-ligand origami pegboards (Atto-647; 2nd panel; magenta in merge and linescan). Each diffraction limited magenta spot represents an origami pegboard. The top panels show a single cell (outlined in yellow), and the bottom insets (orange box in top image) show three origami pegboards at higher magnification. The linescan (right, area denoted with a white arrow in merged inset) shows the fluorescence intensity of each of these channels. Intensity was normalized so that 1 is the highest observed intensity and 0 is background for each channel. (D) TIRF microscopy images show DNA-CAR γ expressing THP1s interacting with 72-ligand origami pegboards (pink) and origami pegboards presenting the indicated number of ligands (pegboards labeled in green). Left schematics represent origami pegboard setups for each row of images where red dots denote the presence of a ligand DNA. Middle images depict a single macrophage (outlined in yellow), and right images show the area indicated with an

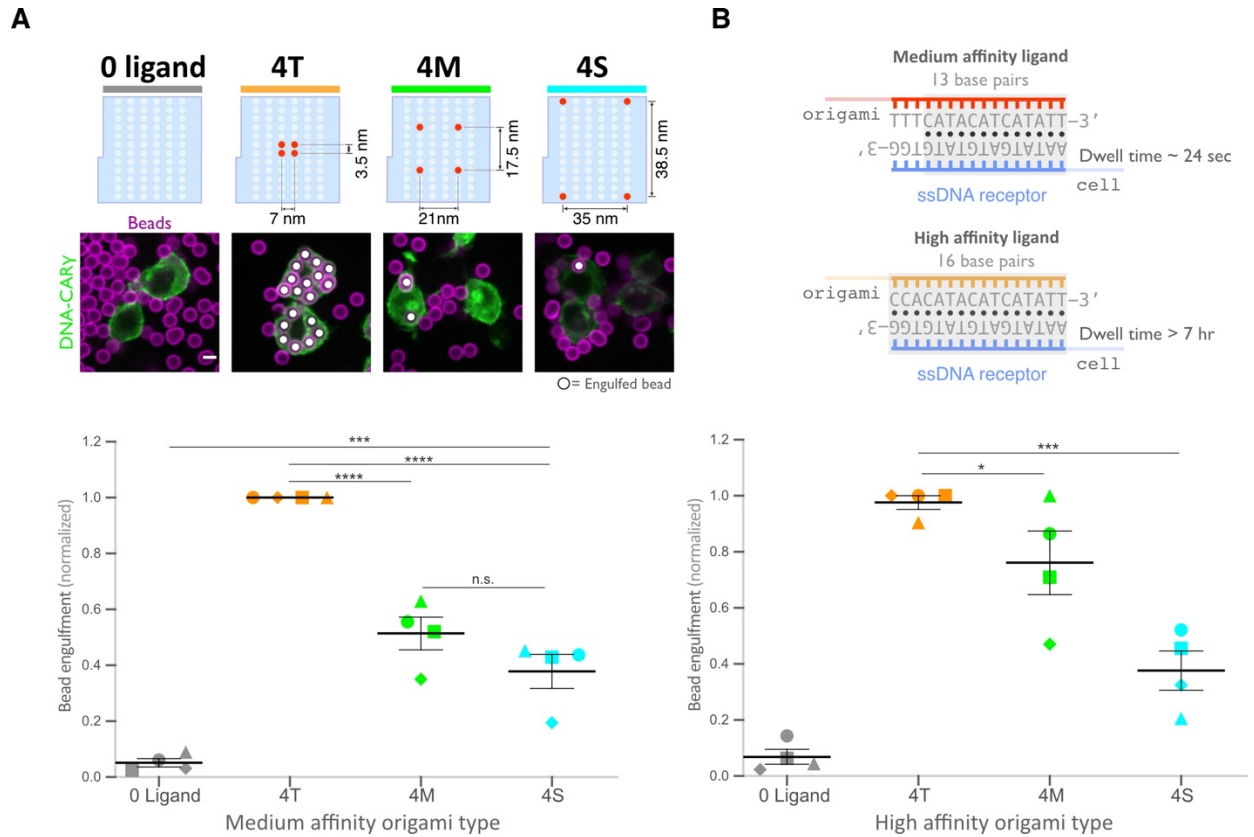
orange box on the left. Examples of DNA-CAR γ -mNeonGreen (grey) recruitment to individual origami pegboards is marked by pink (72L origami pegboard) and green (origami pegboard with the indicated ligand number) arrowheads (right). (E) Quantification of experiment shown in (D). Top graph shows the DNA-CAR γ intensity at the indicated origami pegboard type normalized to the average DNA-CAR γ intensity at 72L origami pegboards in the same well. Each dot represents one origami pegboard and red lines denote the mean \pm SEM of pooled data from three separate replicates. n.s. denotes $p > 0.05$, * indicates $p < 0.05$, and **** indicates $p < 0.0001$ by an ordinary one-way ANOVA with Holm-Sidak's multiple comparison test. A linear regression fit (bottom) of the average fluorescence intensities of each of the origami pegboards suggests that the mean DNA-CAR γ fluorescent intensities are linearly proportional to the number of ligands per DNA origami pegboard. The black dots represent the mean normalized DNA-CAR γ intensity, the red line denotes the linear regression fit, and the grey lines show the 95% confidence intervals.

Together, these results demonstrate that macrophages preferentially engulf targets with tighter ligand clusters.

Tightly spaced ligands could potentially increase phagocytosis by enhancing the avidity of receptor-ligand interactions within each cluster. Such a hypothesis would predict that tightly spaced ligands increase DNA-CAR γ -BFP occupancy at the phagocytic cup. However, when we measured the total fluorescence intensity of receptors at the phagocytic cup, we did not detect a difference in DNA-CAR γ -BFP recruitment to 4T and 4S beads (Figure 6a, b). However, to eliminate any potential contribution of avidity, we created 4T and 4S origami pegboards with very high-affinity 16mer DNA ligands that are predicted to dissociate on a time scale of >7 hr²² (Figure 4b). Using these 16mer high-affinity ligands, we found that 4T origami beads were still preferentially engulfed over 4M or 4S origami beads (Figure 4b, S5). These results suggest that an avidity effect is not the cause of the preferential engulfment of targets having tightly spaced ligands.

Tight ligand spacing enhances engulfment initiation and downstream signaling

We next determined how ligand spacing affects the kinetics of engulfment. Using data from live-cell imaging, we subdivided the engulfment process into three steps: bead binding, engulfment initiation, and engulfment completion (Figure 5a, Supplemental movie 1). To compare engulfment dynamics mediated by 4T and 4S origami pegboards in the same experiment, we labeled each pegboard type with a different colored fluorophore, functionalized a set of beads with each type of pegboard, and added both bead types to macrophages at the same time (Figure 5b, Supplemental movie 2). Macrophages interacted with beads functionalized with the 4T and 4S pegboards with comparable frequency ($46 \pm 7\%$ total bead-cell contacts vs. $54 \pm 7\%$ total bead-cell contacts respectively). However, the probability of engulfment initiation was significantly higher for the 4T ($95 \pm 5\%$ of bead contacts) versus 4S ($61 \pm 9\%$ of bead contacts) beads, and



the probability that initiation events resulted in successful completion of engulfment was higher for 4T ($69 \pm 9\%$ of initiation events) versus 4S ($39 \pm 11\%$ of initiation events) beads (Figure 5a). Initiation events that failed to induce successful engulfment either stalled after progressing partially over the bead or retracted the extended membrane back to the base of the bead. In addition, for beads that were engulfed, the time from contact to engulfment initiation was ~ 300 sec longer for beads functionalized with 4S origami pegboards than beads containing 4T origami pegboards (Figure 5c). However, once initiated, the time from initiation to completion of engulfment did not differ significantly for beads coated with 4T or 4S origami (Figure 5d). Overall, $66 \pm 8\%$ of 4T bead contacts resulted in successful engulfment compared to $24\% \pm 8\%$ for 4S beads (Figure 5e). The DNA-CAR_{adhesion} macrophages rarely met the initiation criteria, suggesting that active signaling from the Fc γ R is required (Figure S6). Together, these data reveal that tighter spacing between ligands within a cluster enhances the probability and kinetics of initiating engulfment, as well as the overall success frequency of completing engulfment, but does not affect the rate of phagosome closure once initiated.

Tightly spaced ligands enhance receptor phosphorylation

We next determined how the 4T or 4S origami pegboards affect signaling downstream of Fc γ R binding by measuring fold enrichment at the phagocytic cup compared to the rest of the cortex of 1) a marker for receptor phosphorylation (the tandem SH2 domains of Syk)^{32,33}, 2) PIP₃ (via recruitment of the PIP₃ binding protein Akt-PH-GFP), and 3) filamentous actin (measured by rhodamine-Phalloidin binding, Figure 6a, b). We found that 4T phagocytic cups recruited more tSH2-Syk than the 4S beads, indicating an increase in receptor phosphorylation by nano-clustered ligands. Generation of PIP₃ and actin filaments at the phagocytic cup also increased at 4T relative to 4S synapses (Figure 6b). This differential recruitment of downstream signaling molecules to 4T versus 4S origami beads was most apparent in early and mid-stage phagocytic cups; late-stage cups showed only a slightly significant difference in tSH2-Syk recruitment and no

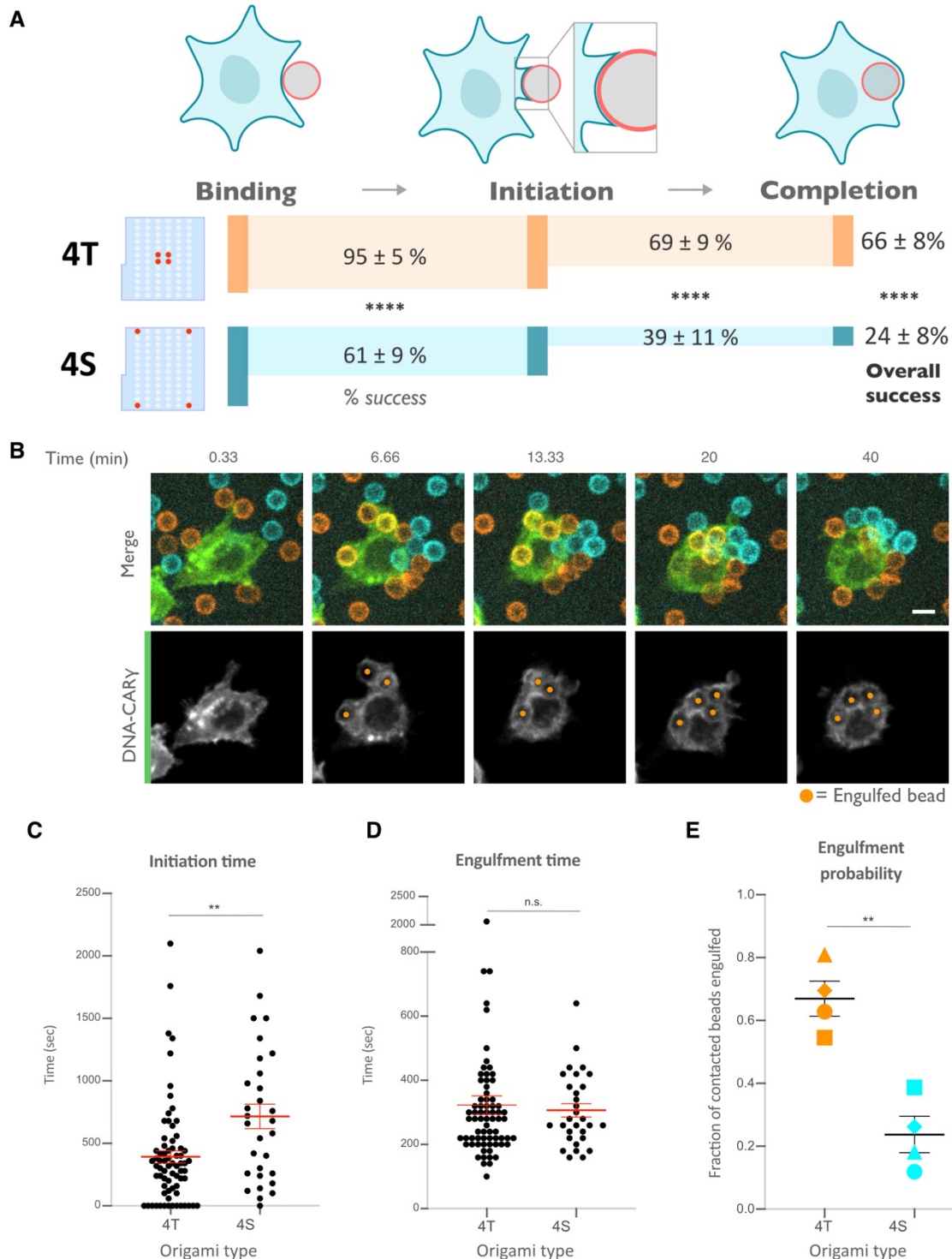


Figure 3.5: Nanoscale ligand clustering controls engulfment initiation

(A) Schematic portraying origami pegboards used to analyze the steps in the engulfment process quantified in (C), (D), and (E). Bead binding is defined as the first frame the macrophage contacts a bead; initiation is the first frame in which the macrophage membrane has begun to extend around the bead, and completion is defined as full internalization. The macrophage membrane was visualized using the DNA CARY, which was present throughout the cell cortex. The % of beads that progress to the next stage of engulfment (% success) is indicated for 4T (orange, origami labeled with Atto550N) and 4S (cyan, origami labeled with

Atto647N) beads. **** denotes $p < 0.0001$ as determined by Fischer's exact test. (B) Still images from a confocal microscopy timelapse showing the macrophage (green) interacting with both the 4T origami pegboard functionalized beads (orange) and the 4S origami pegboard functionalized beads (cyan), but preferentially engulfing the 4T origami pegboard functionalized beads. In the bottom panel (DNA-CAR γ channel), engulfed beads have been indicated by a sphere colored to match its corresponding origami type. (C) Graph depicts quantification of the time from bead contact to engulfment initiation for all beads that were successfully engulfed. Each dot represents one bead with red lines denoting mean \pm SEM. (D) Graph depicts the time from engulfment initiation to completion. Each dot represents one bead with red lines denoting mean \pm SEM. (E) Graph shows the fraction of contacted 4T and 4S beads engulfed (orange and cyan, respectively) by the macrophages. Data represent quantification from 4 independent experiments, denoted by symbol shape, and bars denote the mean \pm SEM. n.s. denotes $p > 0.05$ and ** indicates $p < 0.005$ by Student's T-test comparing the 4T and 4S functionalized beads (C-E).

significant differences in generation of PIP₃ or actin filaments (Figure S7). Together, these data demonstrate that nanoscale ligand spacing affects early downstream signaling events involved in phagocytic cup formation.

We next sought to understand why distributing ligands into tight clusters enhanced receptor phosphorylation and engulfment. One possibility is that the clustering of four complete receptors is needed to drive segregation of the inhibitory phosphatase CD45 and allow sustained phosphorylation of the Fc γ R Immune Receptor Tyrosine-based Activation Motif (ITAM)^{17,26,34,35}. Alternatively, the 4-ligand cluster may be needed to obtain a critical intracellular concentration of Fc γ R ITAM signaling domains. To test for the latter possibility, we designed a synthetic receptor (DNA-CAR-4x γ) that contains four repeats of the intracellular domain of the DNA-CAR γ connected by a GGSG linker between each repeat (Figure 6c). We confirmed that this DNA-CAR-4x γ receptor in which the 3 C-terminal ITAM domains were mutated to phenylalanines (Figure 6c, d). Keeping the number of intracellular ITAMs constant, we compared the engulfment efficiency mediated by two different receptors: 1) the DNA-CAR-4x γ that interacted with beads functionalized with 1-ligand origami, and 2) the DNA-CAR-1x γ -3x Δ ITAM that interacted with beads coated with equivalent amounts of 4T origami (Figure 6c). While the DNA-CAR-1x γ -3x Δ ITAM-expressing macrophages engulfed 4T origami beads, the DNA-CAR-4x γ macrophages failed to engulf the high-affinity 1-ligand origami beads (Figure 6d, Figure S7). To ensure that all four ITAM domains on the DNA-CAR-4x γ were signaling competent, we designed two additional DNA CARs which placed the functional ITAM at the second and fourth position (Figure S7). These receptors were able to induce phagocytosis of 4T origami beads, indicating that the DNA-CAR-4x γ likely contains 4 functional ITAMs. Collectively, these results indicate that the tight clustering of multiple receptors is necessary for engulfment and increasing the number of intracellular signaling modules on a single receptor is not sufficient to surpass the threshold for activation of

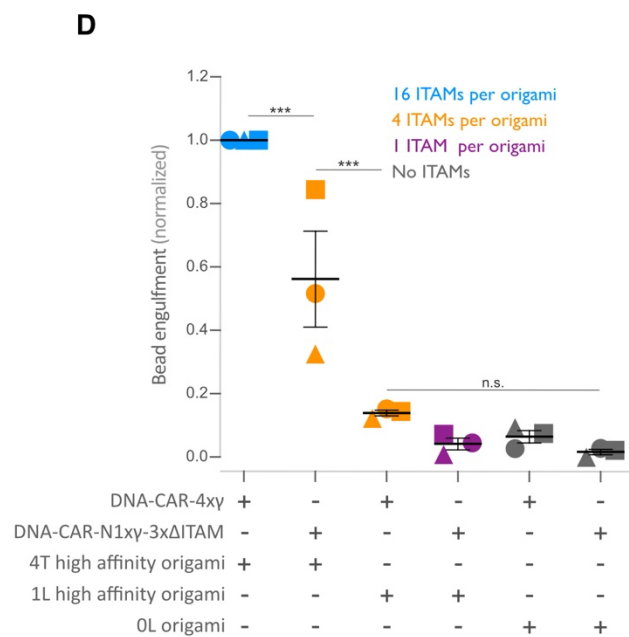
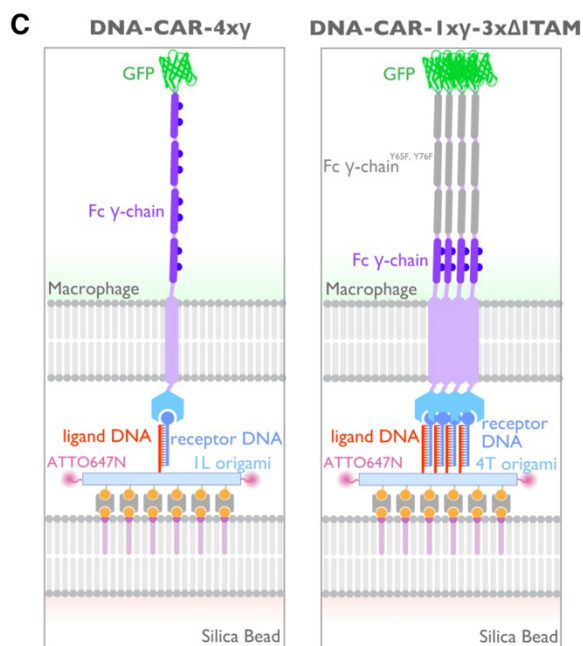
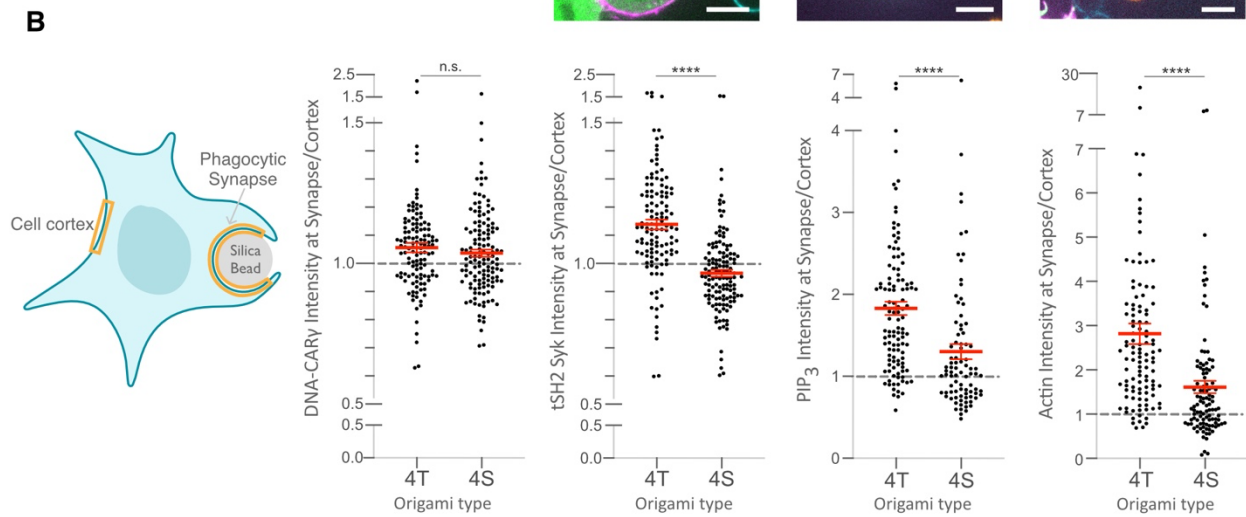
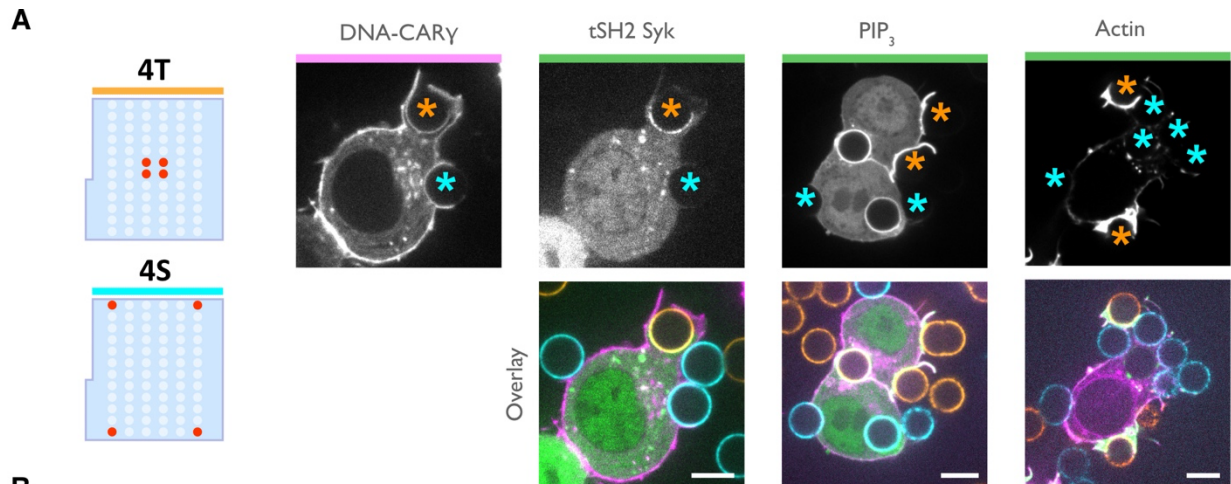


Figure 3.6: Nanoscale ligand spacing controls receptor activation

(A) Beads were functionalized with 4T (orange) or 4S (cyan) origami pegboards at equal amounts, added to macrophages expressing the DNA-CAR γ (magenta) and the indicated signaling reporter protein (green; greyscale on top). Phagocytic synapses were imaged via confocal microscopy. Asterisks indicate whether a 4T (orange) or a 4S (cyan) bead is at the indicated phagocytic synapse in the upper panel. (B) Schematic (left) depicts the areas measured from images shown in (A) to quantify the fluorescence intensity (yellow outlines). Each phagocytic synapse measurement was normalized to the fluorescence intensity of the cell cortex at the same z-plane. Graphs (right) depict the ratio of fluorescence at 4T or 4S functionalized bead synapses to the cortex for the indicated reporter. Each dot represents one bead with red lines denoting mean \pm SEM. (C) Schematic portraying the CAR constructs and origami used in the experiment quantified in (D). The DNA-CAR-4 γ construct (left) consists of four repeats of the intracellular domain of the DNA-CAR γ connected by a GGSG linker. The DNA-CAR-1 γ -3 \times Δ ITAM (right) is identical to the DNA-CAR-4 γ except that the tyrosines composing the ITAM domains (purple circles) are mutated to phenylalanines in the three C-terminal repeats (grey). Cells expressing either of these constructs were fed beads functionalized with either high affinity 1-ligand origami pegboards (left), high affinity 4T origami pegboards (right), or 0 ligand “blank” origami pegboards (not shown), and engulfment was assessed after 45 min. (D) Graph shows the number of beads engulfed per macrophage normalized to the maximum observed eating in that replicate. Each data point represents the mean from an independent experiment, denoted by symbol shape, and bars denote the mean \pm SEM. Blue points represent a condition where 16 ITAMs are available per origami, orange points represent conditions where 4 ITAMs are available per origami, purple points represent a condition where 1 ITAM is available per origami, and grey points represent conditions where no ITAM is available. n.s. denotes $p > 0.05$, *** denotes $p < 0.0005$, and **** denotes $p < 0.00005$ as determined by the Student's T-test (B) or an Ordinary one-way ANOVA with Holm-Sidak's multiple comparison test (D).

engulfment.

3.4 Discussion

Macrophages integrate information from many Fc γ R-antibody interactions to discriminate between highly opsonized targets and background signal from soluble antibody or sparsely opsonized targets. How the macrophage integrates signals from multiple Fc γ R binding events to make an all-or-none engulfment response is not clear. Here, we use DNA origami nanostructures to manipulate and assess how the nanoscale spatial organization of receptor-ligand interactions modulates Fc γ R signaling and the engulfment process. We found that tight ligand clustering increases the probability of initiating phagocytosis by enhancing Fc γ R phosphorylation.

Phagocytosis requires IgG across the entire target surface to initiate local receptor activation and to 'zipper' close the phagocytic cup^{9,34}. Consistent with this zipper model, incomplete opsonization of a target surface, or micron-scale spaces between IgG patches, decreases engulfment^{9,34}. Initially suggested as an alternative to the zipper model, the trigger model proposed that engulfment occurs once a threshold number of receptors interact with IgG^{9,36,37}. While this model has largely fallen out of favor, more recent studies have found a critical IgG threshold needed to activate the final stages of phagocytosis¹⁰. Our data suggest that there may also be a nanoscale density-dependent trigger for receptor phosphorylation and downstream signaling. Taken together, these results suggest that both tight nanoscale IgG-Fc γ R clustering and a uniform distribution of IgG across the target are needed to direct signaling to 'zipper' close the phagocytic cup. Why might macrophages use this local density dependent trigger to dictate engulfment responses? Macrophages constantly encounter background "eat me" signals³⁸. This hyper-local density measurement may buffer macrophages against background stimuli and

weakly opsonized targets that are unlikely to have adjacent bound antibodies, while still robustly detecting and efficiently engulfing highly-opsonized targets.

Our findings are consistent with previous results demonstrating that Fc γ R crosslinking correlates with increased ITAM phosphorylation^{18,20,39,40}. While our data pinpoints a role for ligand spacing in regulating receptor phosphorylation, it is possible that later steps in the phagocytic signaling pathway are also directly affected by ligand spacing. The mechanism by which dense-ligand clustering promotes receptor phosphorylation remains an open question, although our data rule out a couple of models. Specifically, we demonstrate that nanoscale ligand clustering does not noticeably affect the amount of ligand-bound receptor at the phagocytic cup, and that ligand spacing continues to affect engulfment when avidity effects are diminished through the use of high affinity receptor-ligands. Collectively, these data reveal that changes in receptor binding or recruitment caused by increased avidity are unlikely to account for the increased potency of clustered ligands. Our data also exclude the possibility that receptor clustering simply increases the local intracellular concentration of Fc γ R signaling domains, as arranging Fc γ R ITAMs in tandem did not have the same effect as clustering multiple receptor-ligand interactions. However, it remains possible that the geometry of the intracellular signaling domains could be important for activating or localizing downstream signaling, and that tandem ITAMs on the same polypeptide cannot produce the same engulfment signals as ITAMs on separate parallel polypeptides.

One possible model to explain the observed ligand-density dependence of signaling involves the ordering of lipids around the Fc γ receptor. Segregated liquid-ordered and liquid-disordered membrane domains around immune receptor clusters have been reported to promote receptor phosphorylation⁴¹⁻⁴⁶. Fc γ R clusters are associated with liquid-ordered domains^{39,47,48}. Liquid-ordered domains recruit Src family kinases, which phosphorylate Fc γ Rs, while liquid-disordered

domains are enriched in the transmembrane phosphatase CD45, which dephosphorylates Fc γ Rs^{43,44}. Thus, lipid ordering could provide a mechanism that leads to receptor activation if denser receptor-ligand clusters are more efficient in nucleating or associating with ordered lipid domains.

As an alternative model, a denser cluster of ligated receptors may enhance the steric exclusion of the bulky transmembrane proteins like the phosphatases CD45 and CD148^{17,26,49}. CD45 is heavily glycosylated, making the extracellular domain 25-40 nm tall^{12,50,51}. Because of its size, CD45 is excluded from close cell-cell contacts, such as those mediated by IgG-Fc γ R, which have a dimension of 11.5 nm^{26,35,52-55}. IgG bound to antigens ≤ 10.5 nm from the target surface induces CD45 exclusion and engulfment (estimated total intermembrane distance of ≤ 22 nm²⁶). Our DNA origami structure is estimated to generate similar intermembrane spacing, consisting of hybridized receptor-ligand DNA (~ 9.4 nm), the origami pegboard (6 nm) and neutravidin (4 nm)⁵⁶. A higher receptor-ligand density constrains membrane shape fluctuations⁵⁷⁻⁵⁹, and this constraint may increase CD45 exclusion³⁵. Both the lipid ordering and the steric exclusion models predict at least a partial exclusion of the CD45 from the zone of the receptor cluster. However, the dimension of the tight cluster in particular is very small (7 by 3.5 nm) and measurement of protein concentration at this level is currently not easily achieved, even with super-resolution techniques. Overall, our results establish the molecular and spatial parameters necessary for Fc γ R activation and demonstrate that the spatial organization of IgG-Fc γ R interactions alone can affect engulfment decisions.

How does the spacing requirements for Fc γ R nanoclusters compare to other signaling systems? Engineered multivalent Fc oligomers revealed that IgE ligand geometry alters Fc ϵ receptor signaling in mast cells⁶⁰. DNA origami nanoparticles and planar nanolithography arrays have previously examined optimal inter-ligand distance for the T cell receptor, B cell receptor, NK cell

receptor CD16, death receptor Fas, and integrins^{15,61–64}. Some systems, like integrin-mediated cell adhesion, appear to have very discreet threshold requirements for ligand spacing while others, like T cell activation, appear to continuously improve with reduced intermolecular spacing^{62,64}. Our system may be more similar to the continuous improvement observed in T cell activation, as our most spaced ligands (36.5 nm) are capable of activating some phagocytosis, albeit not as potently as the 4T. Interestingly, as the intermembrane distance between T cell and target increases, the requirement for tight ligand spacing becomes more stringent⁶⁴. This suggests that IgG bound to tall antigens may be more dependent on tight nanocluster spacing than short antigens. Planar arrays have also been used to vary inter-cluster spacing, in addition to inter-ligand spacing^{34,64}. Examining the optimal inter-cluster spacing during phagosome closure may be an interesting direction for future studies.

Our study on the spatial requirements of Fc γ R activation could have implications for the design of therapeutic antibodies or chimeric antigen receptors. Antibody therapies that rely on Fc γ R engagement are used to treat cancer, autoimmune and neurodegenerative diseases^{4–8,65}. Multimerizing Fc domains, or targeting multiple antibodies to the same antigen may increase antibody potency⁶⁶. Interestingly, Rituximab, a successful anti-CD20 therapy that potently induces ADCP, has two binding sites on its target antigen⁶⁷. Selecting clustered antigens, or pharmacologically inducing antigen clustering may also increase antibody potency⁶⁸. These results suggest that oligomerization may lead to more effective therapy; however, a systematic study of the spatial parameters that affect Fc γ R activation has not been undertaken²⁶. Our data suggest that antibody engineering strategies that optimize spacing of multiple antibodies through leucine zippers, cysteine bonds, DNA hybridization^{60,63,69} or multimeric scaffolds^{70–73} could lead to stronger Fc γ R activation and potentially more effective therapies.

3.5 Materials and Methods

Cell culture

RAW264.7 macrophages were purchased from the ATCC and cultured in DMEM (Gibco, Catalog #11965–092) supplemented with 1x Penicillin-Streptomycin-L-Glutamine (Corning, Catalog #30–009 CI), 1 mM sodium pyruvate (Gibco, Catalog #11360-070) and 10% heat-inactivated fetal bovine serum (Atlanta Biologicals, Catalog #S11150H). THP1 cells were also purchased from the ATCC and cultured in RPMI 1640 Medium (Gibco, Catalog #11875-093) supplemented with 1x Pen-Strep-Glutamine and 10% heat-inactivated fetal bovine serum. All cells were certified mycoplasma-free and discarded after 20 passages to minimize variation.

Constructs and antibodies

All relevant information can be found in the key resources table, including detailed descriptions of the amino acid sequences for all constructs.

Lentivirus production and infection

Lentiviral infection was used to express constructs described in the key resources table in either RAW264.7 or THP1 cells. Lentivirus was produced by HEK293T cells or Lenti-X 293T cells (Takara Biosciences, Catalog #632180) transfected with pMD2.G (a gift from Didier Trono, Addgene plasmid # 12259 containing the VSV-G envelope protein), pCMV-dR8.91 (since replaced by second generation compatible pCMV-dR8.2, Addgene plasmid #8455), and a lentiviral backbone vector containing the construct of interest (derived from pHRSIN-CSGW, see key resource table) using lipofectamine LTX (Invitrogen, Catalog # 15338–100). The HEK293T media was harvested 60-72 hr post-transfection, filtered through a 0.45 μm filter, and concentrated using Lenti-X (Takara Biosciences, Catalog #631232) via the standard protocol. Concentrated virus was added directly to the cells and the plate was centrifuged at 2200xg for 45

min at 37°C. Cells were analyzed a minimum of 60 hr later. Cells infected with more than one viral construct were FACs sorted (Sony SH800) before use to enrich for double infected cells.

DNA origami preparation

The DNA origami pegboard utilized for all experiments was generated as described in figure S2. The p8064 DNA scaffold was purchased from IDT (Catalog # 1081314). All unmodified oligonucleotides utilized for the origami were purchased from IDT in 96 well plates with standard desalting purification and resuspension at 100 μ M in water. Fluorophore and biotin conjugated oligonucleotides were also purchased from IDT (HPLC purification). All oligonucleotide sequences are listed in table 1, the assembly is schematized in figure S2, and the Cadnano strand diagram for the pegboard with 72 medium-affinity ligands is included in S2. Core staple oligonucleotides (200 nM) (plates 1 and 2), ligand oligonucleotides (200nM) (plates 3-L, 3MA, and 3HA), biotinylated oligonucleotides (200nM), DNA scaffold (20 nM final concentration), and fluorophore-labeled oligonucleotides (200 nM final concentration) were mixed in 1x folding buffer (5 mM Tris pH 8.0, 1 mM EDTA, 5 mM NaCl, 20 mM MgCl₂). Origami folding reaction was performed in a PCR thermocycler (Bio-Rad MJ Research PTC-240 Tetrad), with initial denaturation at 65 °C for 15 min followed by cooling from 60°C to 40°C with a decrease of 1° C per hr. To purify excess oligonucleotides from fully folded DNA origami, the DNA folding reaction was mixed with an equal volume of PEG precipitation buffer (15% (w/v) PEG-8000, 5 mM Tris-Base pH 8.0, 1 mM EDTA, 500 mM NaCl, 20 mM MgCl₂) and centrifuged at 16,000x rcf for 25 min at room temperature. The supernatant was removed, and the pellet was resuspended in 1x folding buffer. PEG purification was repeated a second time and the final pellet was resuspended at the desired concentration in 1x folding buffer and stored at 4°C.

Preparation of benzylguanine-conjugated DNA oligonucleotides

5'-amine modified (5AmMC6) DNA oligonucleotides were ordered from IDT and diluted in 0.15 M HEPES pH 8.5 to a final concentration of 2 mM. N-hydroxysuccinimide ester (BG-GLA-NHS) functionalized benzylguanine was purchased from NEB (Cat #S9151S) and freshly reconstituted in DMSO to a final concentration of 83 mM. To functionalize the oligonucleotides with benzylguanine, the two solutions were mixed so that the molar ratio of oligonucleotide-amine:benzylguanine-NHS is 1:50, and the final concentration of HEPES is between 50 mM and 100 mM. The reaction was left on a rotator overnight at room temperature. To remove excess benzylguanine-NHS ester, the reaction product was purified the next day with illustra NAP-5 Columns (Cytiva, Cat #17085301), using H₂O for elution. The molar concentration of the benzylguanine conjugated oligonucleotides was determined by measuring the absorbance of the purified reaction at 260 nm with a Nanodrop. This reaction was further condensed with the Savant SpeedVac DNA 130 Integrated Vacuum Concentrator System, resuspended in water to a final concentration of 100 μ M, aliquoted, and stored at -20°C until use.

Functionalization of glass surface with DNA origami

96-well glass bottom MatriPlates were purchased from Brooks (Catalog # MGB096-1-2-LG-L). Before use, plates were incubated in 5% (v/v) Hellmanex III solution (Z805939-1EA; Sigma) overnight, washed extensively with Milli-Q water, dried under the flow of nitrogen gas, and covered with sealing tape (ThermoFisher, Cat # 15036). Wells used for experiment were unsealed, incubated with 200 μ L of Biotin-BSA (ThermoFisher, Cat # 29130) at 0.5 mg/mL in PBS pH 7.4 at RT for 2 hr-overnight. Wells were washed 6x with PBS pH 7.4 to remove excess BSA and incubated for 30 min at room temperature with 100 μ L neutravidin at 250 μ g/mL in PBS pH 7.4 for origami quantification and 50 μ g/mL for cellular experiments. Wells were again washed 6x with PBS pH 7.4 supplemented with 20 mM MgCl₂ and incubated for 1-2 hr with the desired amount of DNA origami diluted in PBS pH 7.4 with 20 mM MgCl₂ and 0.1% BSA.

DNA origami quantification

5 wells of a 96-well glass bottom MatriPlate per origami reaction were prepared as described in 'Functionalization of glass surface with DNA origami'. The purified DNA origami reaction was serially diluted into PBS pH 7.4 with 20 mM MgCl₂ and 0.1% BSA and 5 different concentrations were plated and incubated for 1.5 hr before washing 5x with PBS pH 7.4 with 20 mM MgCl₂ and 0.1% BSA. Fluorescent TIRF images were acquired in the channel with which the origami was labeled. 100 sites per well were imaged using the High Content Screening (HCS) Site Generator plugin in uManager⁷⁴. The number of individual DNA origami per μm^2 in each well were quantified using the Spot Counter plugin in Fiji. This was repeated for all concentrations of origami plated. The final concentration of the origami reaction was measured as number of origami/ μm^2 and was calculated from a linear fit including all concentrations in which individual origami could be identified by the plugin.

TIRF imaging

96-well glass bottom MatriPlates were functionalized with DNA origami as described and then washed into engulfment imaging media (20 mM Hepes pH 7.4, 135 mM NaCl, 4 mM KCl, 1 mM CaCl₂, 10 mM glucose) containing 20 mM MgCl₂. ~100,000 dual infected mNeonGreen-DNA-CAR γ and BFP-Syk THP1 cells per well were pelleted via centrifugation, washed into engulfment imaging media, re-pelleted, and resuspended into 50 μL of engulfment imaging media. 1 μL of 100 μM benzylguanine-labeled receptor DNA stock was added per ~50,000 cells pelleted, and the cell-DNA mixture was incubated at room temperature for 15 min. Cells were subsequently washed twice via centrifugation with 10 mL of imaging buffer to remove excess benzylguanine labeled DNA and resuspended in 200 μL per 100,000 cells of imaging buffer containing 20 mM MgCl₂. Cells were then immediately added to each well and imaged. Data was only collected from a central ROI in the TIRF field. The origami fluorescent intensities along the x and y axis were plotted to ensure there was no drop off in signal and thus no uniformity of illumination.

Quantification of receptor and Syk recruitment to individual origami

Cells that expressed both the mNeonGreen tagged DNA-CAR γ receptor and the BFP-tagged Syk and had interactions with the 72-ligand origami were chosen for analysis in Fiji. An ROI was drawn around the perimeter of the cell-glass surface interaction, which was determined by the presence of receptor fluorescence. The 'Spot Intensity in All Channel' plugin in Fiji was used to identify individual origami pegboards, measure fluorescence intensity of the DNA-CAR γ receptor and Syk at each origami pegboard, and subtract local background fluorescence. The intensity at each origami pegboard was normalized to the average intensity measured at 72-ligand origami pegboards in each well.

Supported lipid bilayer coated silica bead preparation

Chloroform-suspended lipids were mixed in the following molar ratios: 96.8% POPC (Avanti, Catalog # 850457), 2.5% biotinyl cap PE (Avanti, Catalog # 870273), 0.5% PEG5000-PE (Avanti, Catalog # 880230, and 0.2% atto390-DOPE (ATTO-TEC GmbH, Catalog # AD 390-161) for labeled lipid bilayers, or 97% POPC, 2.5% biotinyl cap PE, and 0.5% PEG5000-PE for unlabeled lipid bilayers. The lipid mixes were dried under argon gas and desiccated overnight to remove chloroform. The dried lipids were resuspended in 1 mL PBS, pH 7.2 (Gibco, Catalog # 20012050) and stored under argon gas. Lipids were formed into small unilamellar vesicles via ≥ 30 rounds of freeze-thaws and cleared via ultracentrifugation (TLA120.1 rotor, 35,000 rpm / 53,227 x g, 35 min, 4°C). Lipids were stored at 4°C under argon gas in an eppendorf tube for up to two weeks. To form bilayers on beads, 8.6×10^8 silica beads with a 4.89 μm diameter (10 μl of 10% solids, Bangs Labs, Catalog # SS05N) were washed 2x with water followed by 2x with PBS by spinning at 300rcf and decanting. Beads were then mixed with 1mM SUVs in PBS, vortexed for 10 s at medium speed, covered in foil, and incubated in an end-over-end rotator at room temperature for 0.5-2 hr to allow bilayers to form over the beads. The beads were then washed 3x in PBS to remove

excess SUVs, and resuspended in 100uL of 0.2% casein (Sigma, catalog # C5890) in PBS for 15 min at room temperature to block nonspecific binding. Neutravidin (Thermo, Catalog # 31000) was added to the beads at a final concentration of 1 ug/ml for 20-30 minutes, and the beads were subsequently washed 3x in PBS with 0.2% casein and 20mM MgCl₂ to remove unbound neutravidin. The indicated amounts of biotinylated ssDNA or saturating amounts of DNA origami pegboards were added to the beads and incubated for 1 hr at room temperature with end-over-end mixing to allow for coupling. Beads were washed 2 times and resuspended in 100uL PBS with 0.2% casein and 20 mM MgCl₂ to remove uncoupled origami pegboards or ssDNA. When functionalizing SUV-coated beads with anti-biotin AlexaFluor647-IgG (Jackson ImmunoResearch Laboratories Catalog # 200-602-211, Lot # 137445), the IgG was added to the beads at 1uM immediately following the casein blocking step, and beads were incubated for 1 hr at room temperature with end-over-end mixing.

Quantification of ssDNA, IgG, or origami on beads

To estimate the amount of ssDNA bound to each bead, we compared the fluorescence of Atto647-labeled DNA on the bead surface to calibrated fluorescent beads (Quantum AlexaFluor 647, Bangs Lab) using confocal microscopy (Figure S1). To determine saturating conditions of IgG and origami pegboards, we titrated the amount of IgG or origami in the coupling reaction and used confocal microscopy to determine the concentration at which maximum coupling was achieved. A comparable amount of origami pegboard coupling was also confirmed with confocal microscopy for beads used in the same experiment.

Quantification of engulfment

30,000 RAW264.7 macrophages were plated in one well of a 96-well glass bottom MatriPlate (Brooks, Catalog # MGB096-1-2-LG-L) between 12 and 24 hr prior to the experiment. Immediately

before adding beads, 100 μ L of a 1 μ M solution of benzylguanine-conjugated receptor DNA in engulfment imaging media was added, incubated for 10 min at room temperature, and washed out 4 times with engulfment imaging media containing 20 mM $MgCl_2$, making sure to leave \sim 100 μ L of media covering the cells between washes, and finally leaving the cells in \sim 300 μ L of media. \sim 8 x 10⁵ beads were added to the well and engulfment was allowed to proceed for 45 min in the cell incubator. Cells were fixed with 4% PFA for 10 min and washed into PBS. For figures 4c and 6d, 10 nM AlexaFluor647 anti-biotin IgG (Jackson Immuno Labs, Catalog # 200-602-211) diluted into PBS containing 3% BSA was added to each well for 10 minutes to label non-internalized beads. Wells were subsequently washed 3 times with PBS. Images were acquired using the High Content Screening (HCS) Site Generator plugin in μ Manager and at least 100 cells were scored for each condition. When quantifying bead engulfment, cells were selected for analysis based on a threshold of GFP fluorescence, which was held constant throughout analysis for each individual experiment. For figures 3, 4, 6, and S5 the analyzer was blinded during engulfment scoring using the position randomizer plug-in in μ Manager. For the THP1 cells, \sim 100,000 cells per condition were spun down, washed into engulfment imaging media, and coupled to benzylguanine-labeled receptor DNA as described under TIRF imaging. Cells were resuspended into 300 μ L engulfment imaging media containing 20 mM $MgCl_2$ in an Eppendorf tube, \sim 8 x 10⁵ beads were added to the tube, and the tube was inverted 8x before plating the solution into a round-bottomed 96 well plate (Corning, Catalog # 38018). Engulfment was allowed to proceed for 45 min in the cell incubator before the plate was briefly spun and the cells were fixed in 4% PFA for 10 min. Cells were subsequently washed 3x with PBS by briefly centrifuging the plate and removing the media, and finally moved into a 96-well glass bottom MatriPlate for imaging.

Quantification of engulfment kinetics

RAW264.7 macrophages were plated and prepared in wells of a 96-well glass bottom MatriPlate as described in 'Quantification of engulfment'. Using Multi-Dimensional Acquisition in μ Manager,

4 positions in the well were marked for imaging at 20 sec intervals through at least 7 z-planes. $\sim 4 \times 10^5$ Atto647N-labeled 4S origami functionalized beads and $\sim 4 \times 10^5$ Atto550N-labeled 4T origami functionalized beads were mixed in an Eppendorf tube, added to the well, and immediately imaged. Bead contacts were identified by counting the number of beads that came into contact with the cells throughout the imaging time. Initiation events were identified by active membrane extension events around the bead. Engulfment completion was identified by complete internalization of the bead by the macrophage. The initiation time was quantified as the amount of time between bead contact (the first frame in which the bead contacted the macrophage) and engulfment initiation (the first frame in which membrane extension around the bead was visualized) and was only measured for beads that were completely internalized by the end of the imaging time. The engulfment time was quantified as the amount of time between engulfment initiation and engulfment completion (the first frame in which the bead has been fully internalized by the cell).

Quantification of synapse intensity of DNA-CAR γ receptor, tSH2 Syk, PIP₃ reporter, and actin filaments

Phagocytic cups were selected for analysis based on clear initiation of membrane extension around the bead visualized by GFP fluorescence from the DNA-CAR γ receptor. The phagocytic cup and the cell cortex (areas indicated in schematic in figure 6b) were traced with a line (6 pixels wide for DNA-CAR γ receptor and the tSH2 Syk reporter, and 8 pixels wide for the Akt-PH reporter and phalloidin) at the Z-slice with the clearest cross section of the cup.

Microscopy and analysis

Images were acquired on a spinning disc confocal microscope (Nikon Ti-Eclipse inverted microscope with a Yokogawa CSU-X spinning disk unit and an Andor iXon EM-CCD camera) equipped with a 40 \times 0.95 NA air and a 100 \times 1.49 NA oil immersion objective. The microscope

was controlled using μ Manager. For TIRF imaging, images were acquired on the same microscope with a motorized TIRF arm using a Hamamatsu Flash 4.0 camera and the 100x 1.49 NA oil immersion objective.

Statistics

Statistical analysis was performed in Prism 8 (GraphPad, Inc). The statistical test used is indicated in each relevant figure legend.

3.6 Supporting Information

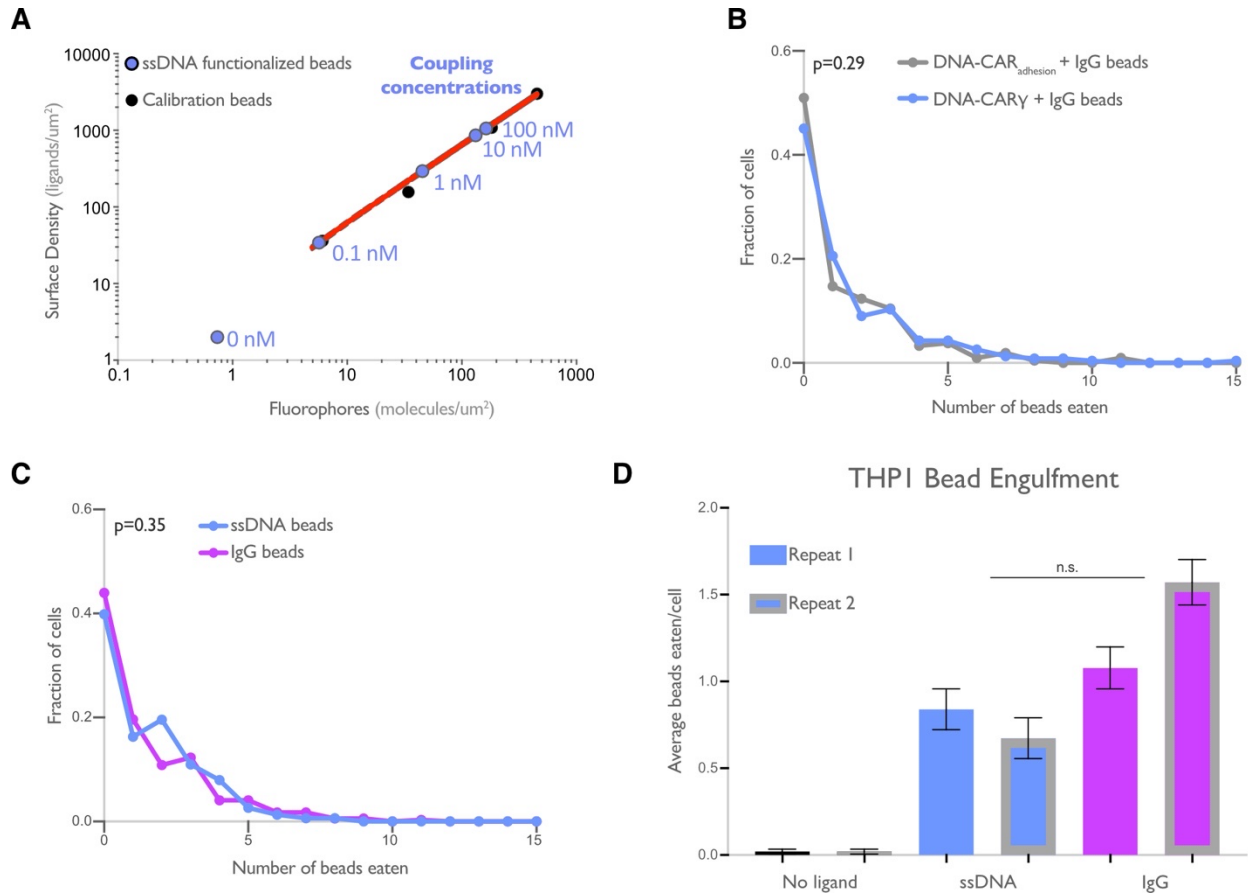


Figure S3.1, related to Figure 1: DNA-based engulfment system reflects endogenous engulfment

(A) Graph depicts the calibration used to determine the surface density of ssDNA on beads used in Figure 1b, c. The intensity of Alexa Fluor 647 fluorescent bead standards (black dots) was measured, and a simple linear regression (red line) was fit to the data. The fluorescence intensity of Alexa Fluor 647-ssDNA coated beads (blue dots) was measured, and the surface density was interpolated using the regression determined from the fluorescent bead standards. The concentration of ssDNA used for each bead coupling condition is indicated next to the blue points on the graph. (B) Macrophages expressing the DNA-CAR γ (blue) or the DNA-CAR_{adhesion} (grey) engulfed similar distributions of IgG functionalized beads. Data is pooled from two independent replicates. (C) Graph depicts the fraction of macrophages engulfing the indicated number of IgG (magenta) or ssDNA (blue) beads from data pooled from the three independent replicates presented in Figure 1d. (D) Graph shows the average number of Neutravidin (black), ligand-DNA (blue), or IgG (magenta) functionalized beads engulfed by the monocyte-like cell line THP1. Lines denote the mean engulfment from each independent replicate and bars denote \pm SEM. P values were calculated using the Mann-Whitney test (B, C) and n.s. denotes $p>0.05$ as determined by the Student's T-test (D).

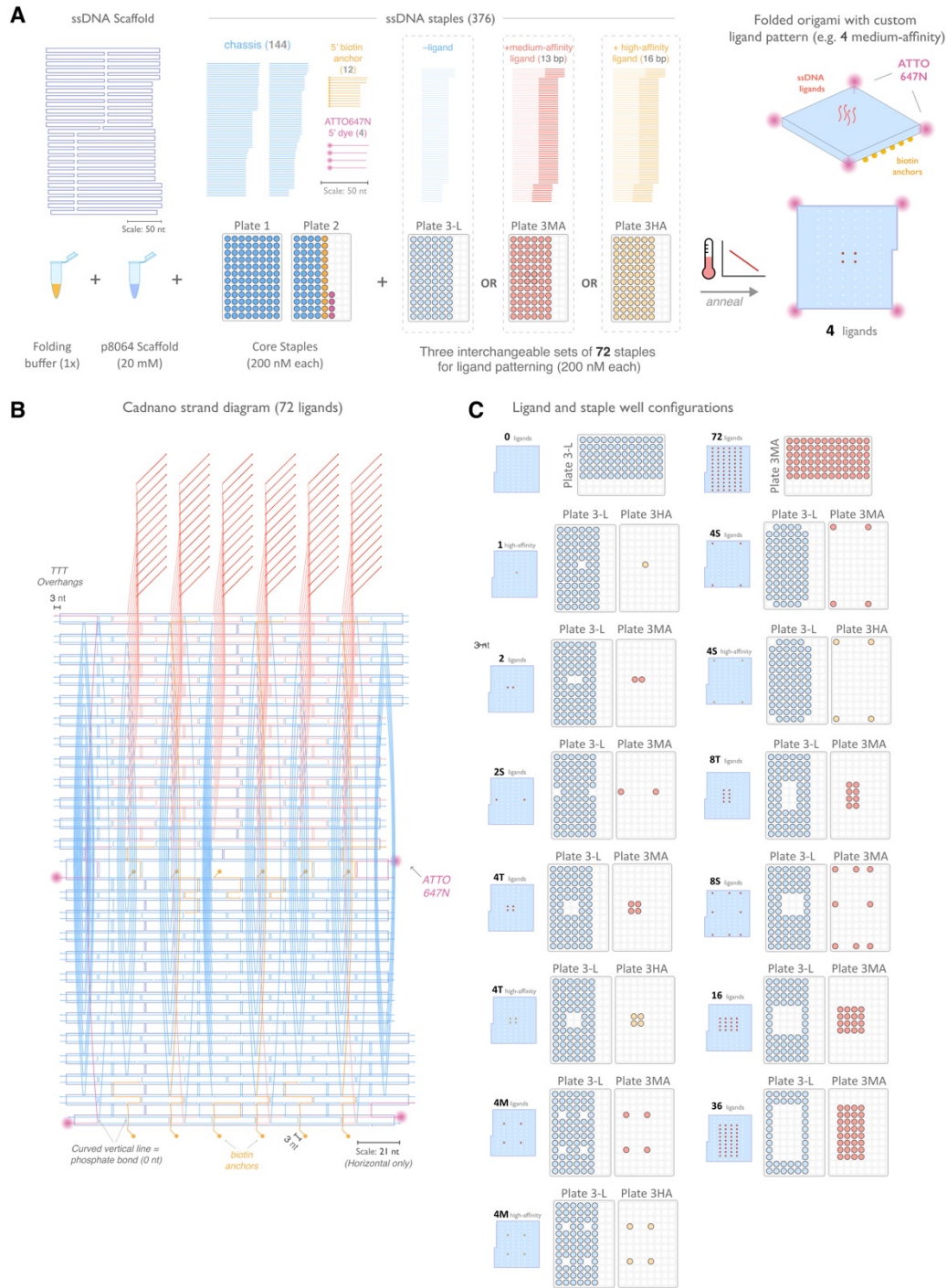


Figure S3.2, related to Figure 2: Design and Assembly of Nanoscale Ligand-Patterning Pegboard built from DNA origami.

(A) 2D schematic of origami scaffold and staples. The p8064 ssDNA scaffold is combined with 160 ssDNA staples that form the chassis, biotin-modified surface anchors, and ATTO647N-labeled dyes, plus a combination of 72 ligand-patterning staples. We used three variants of the ligand-patterning staples: "-ligand" that lacks a 3' single-stranded overhang and terminates flush with the pegboard surface, and a "medium-affinity" (red) and "high-affinity" (yellow) that form 13-bp and 16-bp duplexes with the DNA-CAR

receptors, respectively. Assembly is performed by thermal annealing in a one-pot reaction. (B) Cadnano strand diagram for the pegboard with 72 medium-affinity ligands included. (C) Fourteen pegboard configurations were used in this study. Configurations are labeled by ligand count, spacing, and ligand affinity, and the corresponding plate wells used in each assembly are shown.

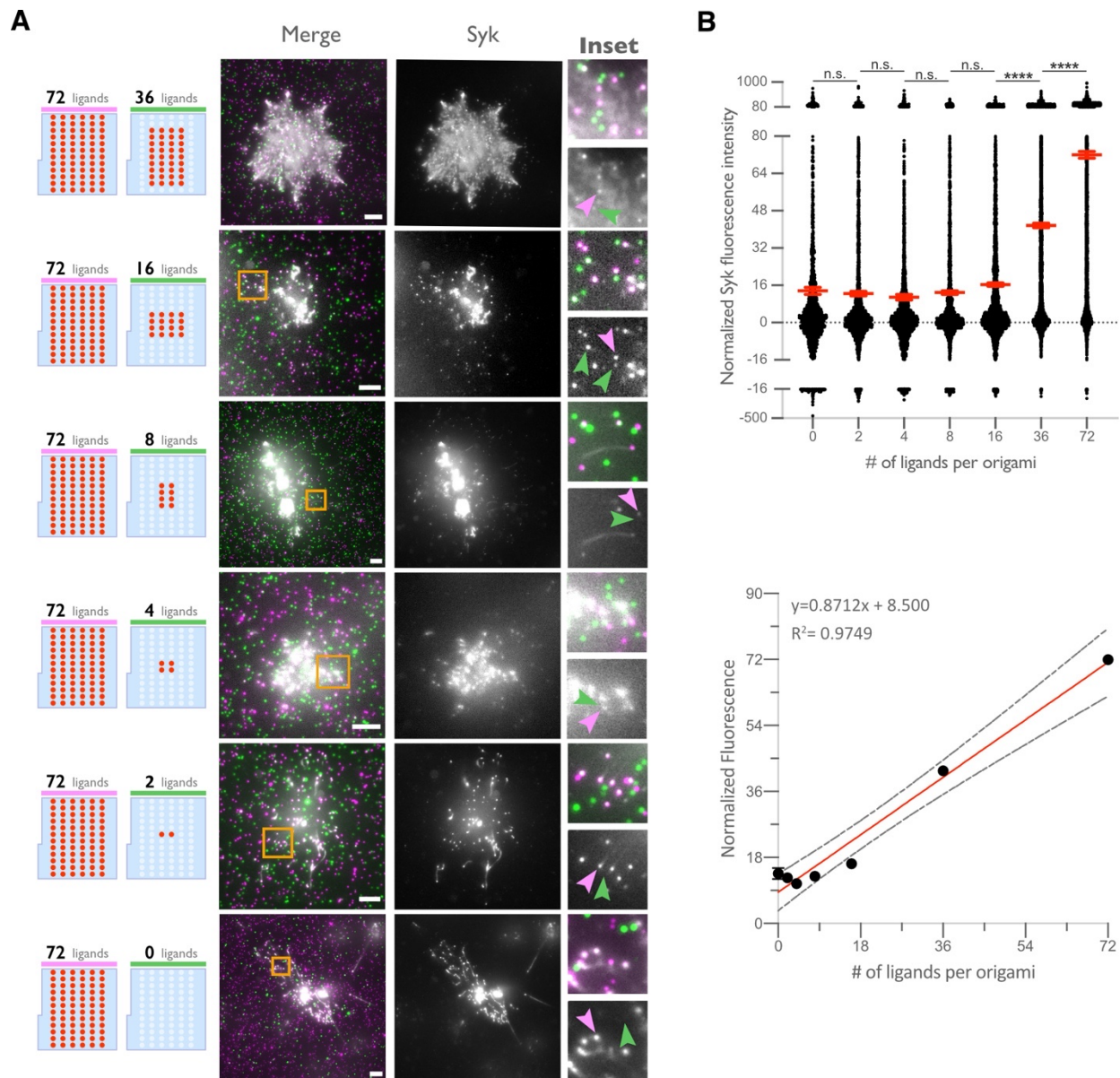


Figure S3.3, related to Figure 2: Syk intensity increases with ligand number in origami cluster

(A) TIRF microscopy images showing DNA-CAR γ -mNeonGreen and Syk-BFP expressing THP1s interacting with 72-ligand origami pegboards (pink) and origami pegboards presenting the indicated number of ligands (green) plated together on a glass surface (schematics shown on the left). Middle images depict a single macrophage, and right images show the area indicated with a yellow box on the left. Examples of Syk-BFP (grey) recruitment to individual origami pegboards is marked by pink (72L origami) and green (indicated ligand number origami) arrowheads (right). (B) Top graph shows the Syk intensity at each indicated origami pegboard type normalized to the average Syk intensity at 72L origami pegboards for each condition. Each dot represents the normalized Syk intensity at one origami and red lines denote the mean \pm SEM of pooled data from three separate replicates. At ligand numbers fewer than 16, we did not detect Syk enrichment over background fluorescence of cytosolic Syk. A linear regression fit (bottom) of the average Syk fluorescence intensity at each origami pegboard type suggests that the mean Syk recruitment is linearly proportional to the number of ligands per DNA origami. n.s. denotes $p>0.05$ and **** indicates $p<0.0001$ by an ordinary one-way ANOVA with Holm-Sidak's multiple comparison test.

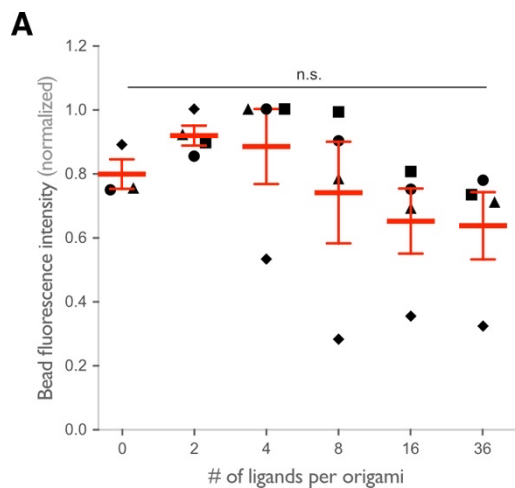


Figure S3.4, related to Figure 3: Origami intensity on beads is comparable across conditions

(A) Graph shows the average Atto647N fluorescence intensity from the beads used in Figure 3a, b measured using confocal microscopy. Each dot represents an independent replicate ($n \geq 100$ cells analyzed per experiment), denoted by symbol shape, with red lines denoting mean \pm SEM. n.s. denotes $p > 0.05$ as determined by an Ordinary one-way ANOVA with Holm-Sidak's multiple comparison test.

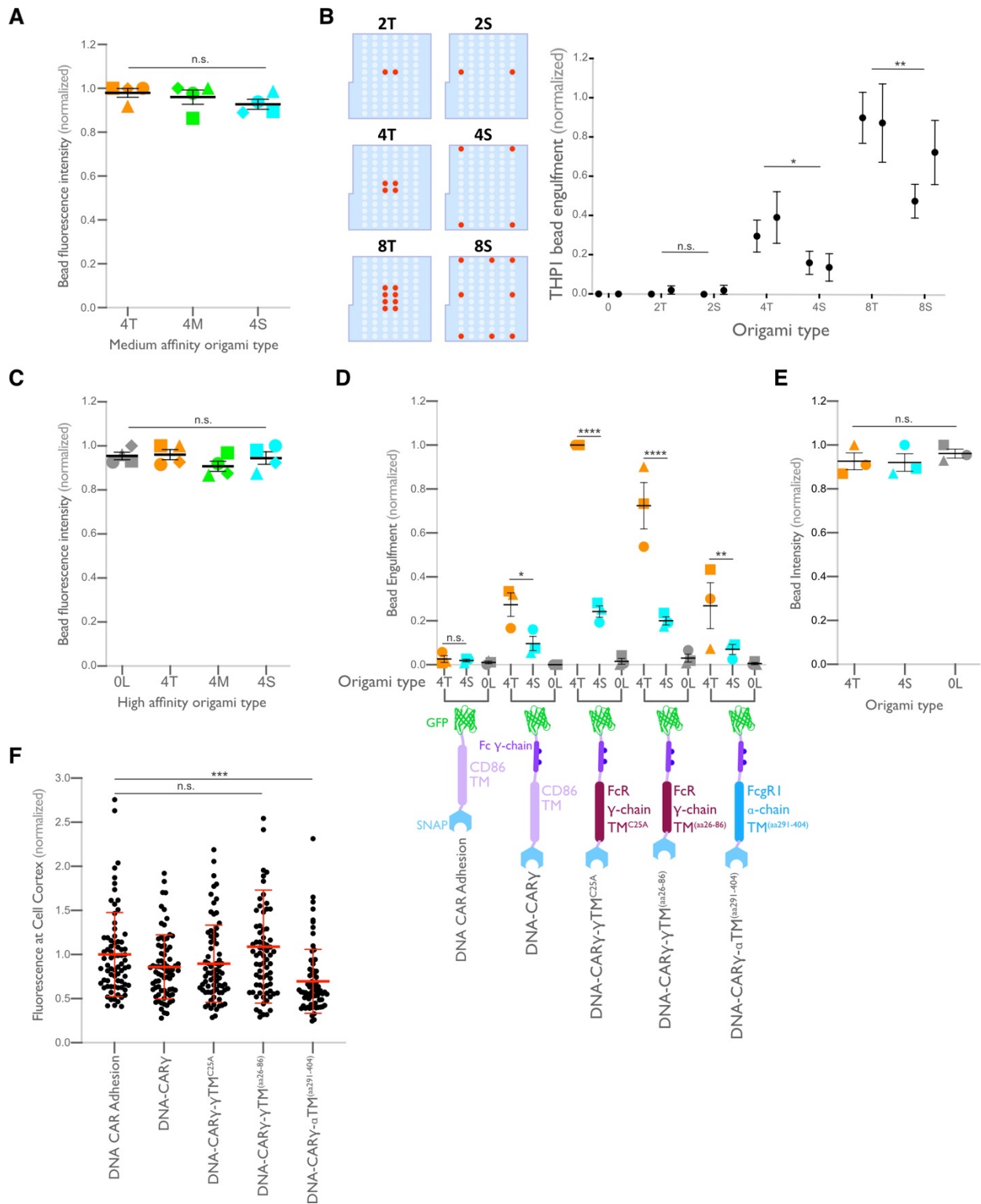


Figure S3.5, related to Figure 4: Ligand clustering enhances engulfment in RAW macrophages expressing DNA CARs with endogenous Fc γ R transmembrane domains and in THP1s

(A) Graph shows the average Atto647N fluorescence intensity from the beads used in Figure 4a measured using confocal microscopy. (B) Beads were functionalized with the indicated ligand-presenting origami pegboards in amounts calculated to equalize the total number of origami pegboards and ligands across conditions. Schematics (left) depict the origami utilized, where the positions presenting a ligand (red dots)

and the positions not occupied by a ligand (light blue) are indicated. Graph (right) depicts the average number of the indicated type of beads internalized per DNA-CAR γ -expressing THP1, normalized to the maximum bead eating in that replicate. (C) Graph shows the average Atto647N647 fluorescence intensity from the beads used in Figure 4b measured using confocal microscopy. (D) Schematics below graph depict the DNA CAR constructs designed with varying transmembrane domains. Beads were functionalized with 4T origami pegboards (orange), 4S origami pegboards (cyan), or 0-ligand 'blank' origami pegboards (grey) and fed to macrophages expressing the DNA CAR receptor depicted below each section of the graph. Graph depicts the number of beads engulfed per macrophage normalized to the maximum observed eating in that replicate. (E) Graph shows the average Atto647N fluorescence intensity from the beads used in (D) measured using confocal microscopy. (F) DNA CAR receptors used in (D) are expressed and trafficked to the membrane at similar levels. Fluorescent intensity at the cell cortex of the DNA CAR-infected macrophage was quantified using the mean intensity of a 2 pixel width linescan at the cell membrane, with the mean intensity of a linescan immediately adjacent to the cell subtracted for local background. The fluorescence intensity was normalized to the average intensity of the DNA CAR_{adhesion} in each experiment. Each dot represents an individual cell and data is pooled from 3 independent experiments, with red lines denoting mean \pm SEM. n.s. denotes $p > 0.05$, * denotes $p < 0.05$, ** denotes $p < 0.005$, *** denotes $p < 0.0005$, and **** indicates $p < 0.0001$ as determined by an Ordinary one-way ANOVA with Holm-Sidak's multiple comparison test (A-F).

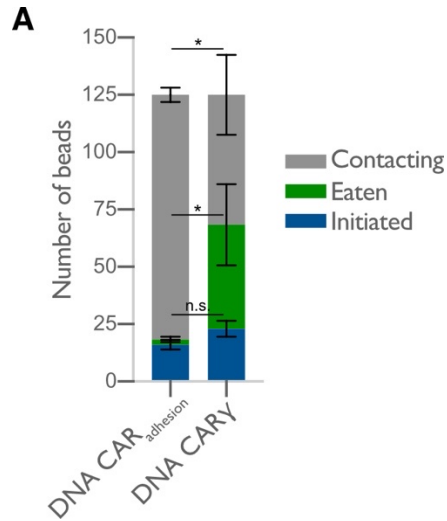


Figure S3.6, related to Figure 5: DNA CAR_{adhesion} fails to induce frequent engulfment initiation attempts

(A) The average number of 4T origami pegboard-functionalized beads contacting (grey), in the initiation stage of engulfment (blue), or fully engulfed (green) by macrophages expressing either the DNA CAR_{adhesion} or the DNA CAR_γ were quantified from fixed still images after 45 minutes of engulfment. 125 beads in contact with DNA CAR expressing macrophages were analyzed in 3 independent replicates. Bars represent the average number of beads identified at each stage and black lines denote \pm SEM between replicates. n.s. denotes $p > 0.05$ and * denotes $p < 0.05$ as determined by an unpaired t-test with Holm-Sidak's multiple comparison test.

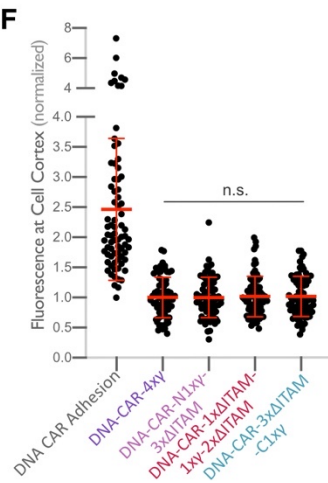
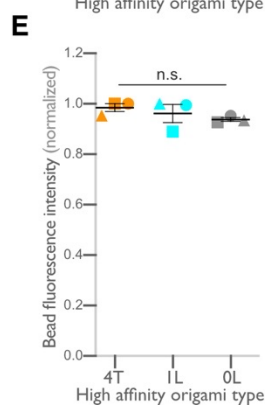
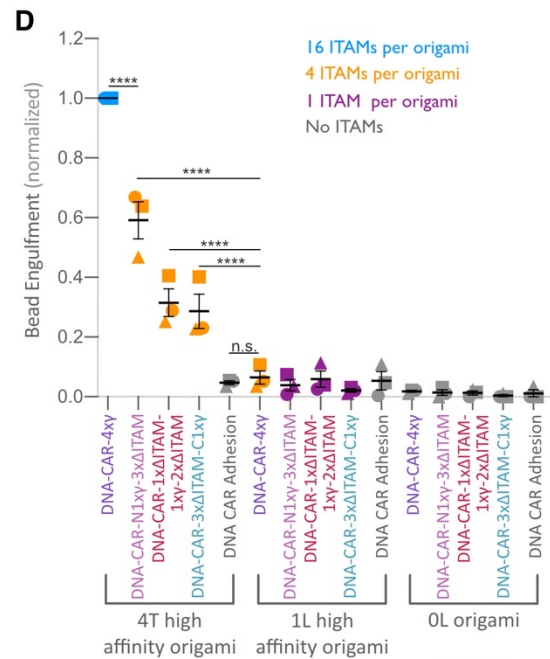
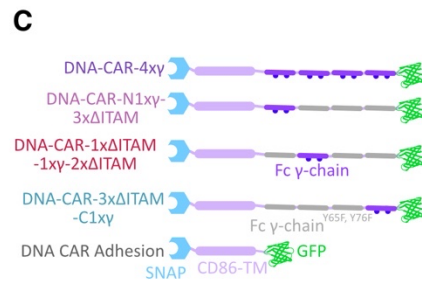
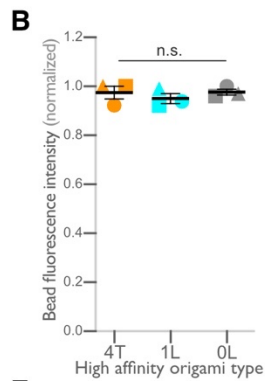
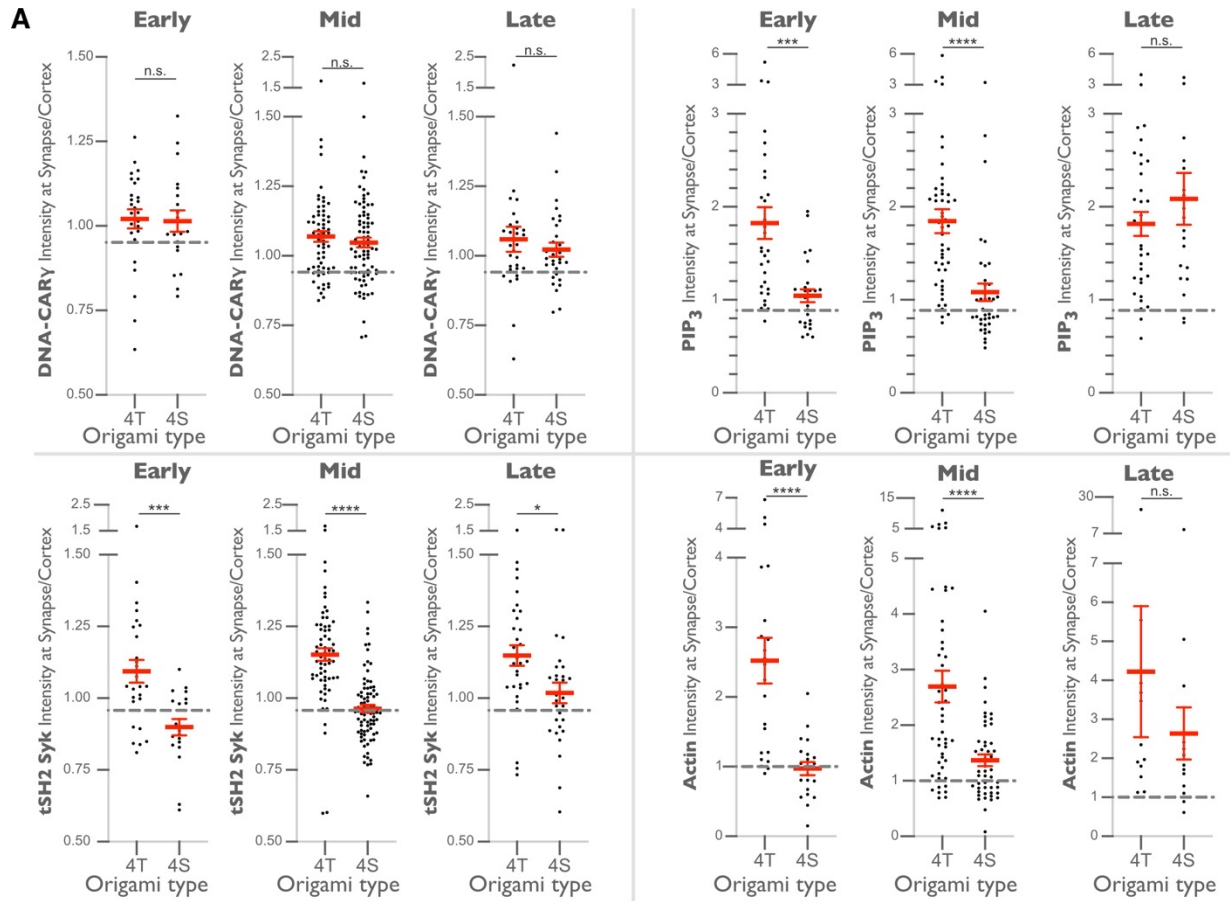


Figure S3.7, related to Figure 6: Differential recruitment of downstream signaling molecules is greater at early and mid-stage phagocytic cups

(A) Data from experiment shown in Figure 6b is separated by early (macrophage membrane extends across <30% of the bead, left), mid (macrophage membrane extends across 30-70% of the bead, middle), and late (macrophage membrane extends across >70% of the bead, right) stage phagocytic cups. Graphs depict the ratio of fluorescence intensity at 4T or 4S functionalized bead synapses compared to the cortex. Each dot represents one bead with red lines denoting mean \pm SEM. n.s. denotes $p > 0.05$, * denotes $p < 0.05$, *** denotes $p < 0.0005$, and **** denotes $p < 0.00005$ by the Student's T-test. (B) Graph shows the average Atto647N fluorescence intensity from the beads used in Figure 6d measured using confocal microscopy. (C) Schematics depict the DNA-CAR-4xy constructs used for experiment quantified in (D). (D) DNA CAR constructs shown in (C) were expressed in RAW macrophages and fed beads functionalized with 4T high affinity origami pegboards, 1 ligand high affinity origami pegboards, or 0 ligand origami pegboards. Graph depicts the number of beads engulfed per macrophage normalized to the maximum observed eating in that replicate. Each data point represents the mean from an independent experiment, denoted by symbol shape, and bars denote the mean \pm SEM. Blue points represent a condition where 16 ITAMs are available per origami, orange points represent conditions where 4 ITAMs are available per origami, purple points represent a condition where 1 ITAM is available per origami, and grey points represent conditions where no ITAM is available. (E) Graph shows the average Atto647N fluorescence intensity from the beads used in (D) measured using confocal microscopy. (F) DNA CAR receptors used in (D) are expressed and trafficked to the membrane at similar levels. Fluorescent intensity at the cell cortex of the DNA CAR infected macrophage was quantified using the mean intensity of a 2 pixel width linescan at the cell membrane, with the mean intensity of a linescan immediately adjacent to the cell subtracted for local background. The fluorescence intensity was normalized to the average intensity of the DNA-CAR-4xy in each experiment. Each dot represents an individual cell and data is pooled from 3 independent experiments, with red lines denoting mean \pm SEM. n.s. denotes $p > 0.05$ and **** indicates $p < 0.0001$ as determined by an Ordinary one-way ANOVA with Holm-Sidak's multiple comparison test (B,D-F).

Table S3.1 Sequences and setup for plates 1+2

Plate Name	Well	Staple ID	Sequence	Length	CN 5' pos	CN 3' pos	Staple Color	Note
Plate1	A1	1	CAGACGAAAAAGAAAGACTGGA TAGCGTAGGCTTGAATACGTAA TGCCACTACGTTT	57	28[4 8]	18[2 0]	#69b 5fc	chassis
Plate1	A2	2	GGTGGCACAATAAAAAGCAATA CCAAAAAGCCTTTCTCATATATT TTAAATGCATTT	57	43[4 2]	48[2 7]	#69b 5fc	chassis
Plate1	A3	3	ATTTTCACATAGTTGTTCCGAAA TCGAGCGGATTGCATCAAATTA TAGTCAGAAGC	56	12[7 6]	33[6 2]	#69b 5fc	chassis
Plate1	A4	4	TACCGATTTCGTCACCAGGAACG GTAATAATAGTAAAATGTTTGT TTGCCAGAGGG	56	16[7 6]	29[6 2]	#69b 5fc	chassis
Plate1	A5	5	GAGGCGAAATATACACAATATA GAGATAGAACCCTGATAGCCCT AAAACACCTCAA	56	18[1 39]	25[1 39]	#69b 5fc	chassis
Plate1	A6	6	GCGAACTTCTGACCTGGTAATG CAATACACGAGCACTGCGCGT CACCCAGAACGTG	56	26[1 53]	33[1 53]	#69b 5fc	chassis
Plate1	A7	7	TACCGCCTCACGCATCCTCGTC TGGCAAGGGTCGAGAACAAGG CAGCAAACGCGC	56	28[1 32]	35[1 32]	#69b 5fc	chassis
Plate1	A8	8	TCACCGTAGGGAAGATAAAGG GACTCCTTGTGTAGGTAAAGAT AGAACCATTTCAA	56	3[42]	47[5 5]	#69b 5fc	chassis
Plate1	A9	9	CCGCCTGTGCGTATTCACAATC CCCGGGCGGTGCCACATCCCC ACCGTCCATCCTC	56	34[1 53]	41[1 53]	#69b 5fc	chassis
Plate1	A10	10	AAGATTATTTAATTCTCCAACCT TTTGATAATTGCATATGCATATA ACAGTTGATT	56	34[4 8]	40[3 5]	#69b 5fc	chassis
Plate1	A11	11	AGTCGGGTGAGCTAGGGGGTT TGGTGCTTATGAGCTCATTGCT TGCCGTCACAGGC	56	35[8 4]	42[8 4]	#69b 5fc	chassis
Plate1	A12	12	ATTTGCCTGAGAGAATGTGCTG CGCCATCGTGGGAGCCATCAA CGGTAATCGTAAA	56	42[1 53]	48[1 40]	#69b 5fc	chassis
Plate1	B1	13	AGAGCCACAGGAGGCATTCCA ACTAAAGTACGGTGTCCCGCC GGCGCGGTTGCGG	56	6[55]	39[8 3]	#69b 5fc	chassis
Plate1	B2	14	TTTGAGCAAGAAACAATGATTA AGCCTGAGCGATGTTGGGAAG GGCGATCGGTTT	55	0[19 3]	45[1 96]	#69b 5fc	chassis

Plate Name	Well	Staple ID	Sequence	Length	CN 5' pos	CN 3' pos	Staple Color	Note
Plate1	B3	15	TTTCGTCAAAAATGAAAATACG ATTTTCGCTATTGGATAGCTCTC ACGGAAAATTT	55	2[19 3]	43[1 96]	#69b 5fc	chassis
Plate1	B4	16	TTTGCCAAAAGGAATTACGAAT GCAGAAGGGAATCAGTGAATAA GGCTTGCCTTT	55	27[2 3]	22[2 0]	#69b 5fc	chassis
Plate1	B5	17	TTTAGCGAGAGGCTTTTGCCGA TAAATAAACGTAGCCGGAACG AGGCGCAGTTT	55	29[2 3]	20[2 0]	#69b 5fc	chassis
Plate1	B6	18	TTTAAATCAGGTCTTTACCAATG ACCTAATAATGCCACGCATAA CCGATATTTT	55	33[2 3]	16[2 0]	#69b 5fc	chassis
Plate1	B7	19	TTTACTTCAAATATCGCGTAGA GGAAAACACAAATAGAAAGGA ACAATAATTT	55	35[2 3]	14[2 0]	#69b 5fc	chassis
Plate1	B8	20	TTTGTACCTTTAATTGCTCAGGT CAGGATATAATACCGTAACACT GAGTTTCTTT	55	37[2 3]	12[2 0]	#69b 5fc	chassis
Plate1	B9	21	TTTGCTCAACATGTTTTAATGAA TATGGGGTCATACCAGGCGGA TAAGTGCCTTT	55	39[2 3]	10[2 0]	#69b 5fc	chassis
Plate1	B10	22	TTTAAGCCTTAAATCAAGACTTG CGGACAGCGGGTAGAACGTCA GCGTGGTGTTT	55	4[19 3]	41[1 96]	#69b 5fc	chassis
Plate1	B11	23	TTTGGGCGCGAGCTGAAAAGC TATATTTTCATCGCAGAGCCGCC ACCAGAACCTTT	55	43[2 3]	6[20]	#69b 5fc	chassis
Plate1	B12	24	TTTAAGAATTAGCAAAAATTTTAT ACATGAATTAGTTTGCCTTTAG CGTCAGATTT	55	45[2 3]	4[20]	#69b 5fc	chassis
Plate1	C1	25	TTTATACTTTTGCGGGAGAACA TTATTACATACGTAAATATTGAC GGAAATTTTT	55	47[2 3]	2[20]	#69b 5fc	chassis
Plate1	C2	26	TTTAAACCAAGTACCGCACTCC AAGAGCAGCAACCGCAAGCGG ACTTATCAAAC	54	6[19 3]	42[1 68]	#69b 5fc	chassis
Plate1	C3	27	ACAAAGTCCCTGAAAGGTCCT CCGGCACCGCTTCACGCCAGG GTTTTTC	49	0[11 8]	44[1 12]	#69b 5fc	chassis
Plate1	C4	28	TCTTACCAGATAACGATTCTCT CGCCATTCAGGCTCTGGCGAA AGGGGG	49	0[16 0]	44[1 54]	#69b 5fc	chassis
Plate1	C5	29	TTGAGAAATAATTAACATACG GGGAGAGGCGGTTGCCCTGAG AGAGTT	49	10[1 39]	34[1 33]	#69b 5fc	chassis

Plate Name	Well	Staple ID	Sequence	Length	CN 5' pos	CN 3' pos	Staple Color	Note
Plate1	C6	30	TAAGGCGCTATATGACGCTGG GTTGTTCCAGTTTGGGTGCCGT AAAGCA	49	12[1 18]	32[1 12]	#69b 5fc	chassis
Plate1	C7	31	TGACCTAACGCGAGCCCTTCAG ACTCCAACGTCAACACTACGTG AACCA	49	12[1 60]	32[1 54]	#69b 5fc	chassis
Plate1	C8	32	TTTTAACCTTGAATTTTTTGGT GTAGCGGTCACGCGTATAACGT GCTT	49	14[1 39]	30[1 33]	#69b 5fc	chassis
Plate1	C9	33	ACATAAAACATTTATGCTTTGTT CTTTGATTAGTAACTATCGGCC TTGC	49	16[1 60]	28[1 54]	#69b 5fc	chassis
Plate1	C10	34	GAAGCGCCAAAATAGATTAAGA GTCCCAGAAATTTGGCCAGCAG TTGGGC	49	2[13 9]	42[1 33]	#69b 5fc	chassis
Plate1	C11	35	ATTGTGTGATGAACGGTCAGTA TTAAATTTAGGAATACCACAAG ATTCA	49	20[7 6]	25[5 5]	#69b 5fc	chassis
Plate1	C12	36	TGCTCATCCGAACTTGTTACTA AAGAGGCGGGTAACAGGGAGA ACCATC	49	22[4 8]	16[4 2]	#69b 5fc	chassis
Plate1	D1	37	ACAAAGCTAAATTGAAAAATCTA CGTTAGGTAGAATTCAACTAGG CATA	49	22[5 5]	27[4 8]	#69b 5fc	chassis
Plate1	D2	38	GAAAAACCCGAGTAGAGCTAAA AAGGAGCTAAATCGTTGAGTTT TGCCC	49	28[1 11]	34[1 05]	#69b 5fc	chassis
Plate1	D3	39	AGCCATTGCAACAGAAAAGGGA CATTCTTTAAAATGATTATCAG ATGA	49	28[1 25]	21[1 32]	#69b 5fc	chassis
Plate1	D4	40	GAGCGTCAATCAGAACATAAAT TTCGTCTCGTCGCCAGCTTACG GCTGG	49	4[11 8]	40[1 12]	#69b 5fc	chassis
Plate1	D5	41	GCACCCAGCGTTTTTCTGCTCA TAACGGAACGTGCAATGCCAAC GGCAG	49	4[16 0]	40[1 54]	#69b 5fc	chassis
Plate1	D6	42	TCCGTTTAAAATCCCGGCGAAC CAGTCACCAGCTTGTGGTGTA GATGG	49	41[1 05]	46[9 8]	#69b 5fc	chassis
Plate1	D7	43	TGGCAGCGTTGTGGTTTACCT TGGGTATGGTGCCGACCGTAC ATTTTT	49	41[1 26]	47[1 32]	#69b 5fc	chassis
Plate1	D8	44	GTAGGAACATGTAGCCATCCCT TTGCTCGTCATAAGGTGCCCCC TGCAT	49	6[13 9]	38[1 33]	#69b 5fc	chassis

Plate Name	Well	Staple ID	Sequence	Length	CN 5' pos	CN 3' pos	Staple Color	Note
Plate1	D9	45	AAGAAAAGTAATTTTCAGTGTCT CTTCGCGTCCGTGAAGCATAAA GTGTA	49	8[11 8]	36[1 12]	#69b 5fc	chassis
Plate1	D10	46	TGCAGAAATAAAGTCAGCCAGT ACCGAGCTCGAATAAATTGTTA TCCGC	49	8[16 0]	36[1 54]	#69b 5fc	chassis
Plate1	D11	47	TTCAGCGCGTTGAAGTTCAGAG AATCCCCCTCAAATGAAAGCCG G	45	14[5 5]	31[7 2]	#69b 5fc	chassis
Plate1	D12	48	CATTAACAAAAGACGTTTACG TAAGAGCAACACTATAATGGAT T	45	18[5 5]	27[7 2]	#69b 5fc	chassis
Plate1	E1	49	ATAGTGGAGCCGCCACGGGAA CGGGCCTTTCATCTTTTCATAAT	44	43[6 1]	5[90]	#69b 5fc	chassis
Plate1	E2	50	TGAAAGCGTAAGAATTAGTCTT TTGGATTATACTTCTGAATTT	43	27[1 54]	21[1 82]	#69b 5fc	chassis
Plate1	E3	51	TAACCACCACCCCCTATGGTA CAATTTCAATTTGAATTAATTT	43	31[1 54]	17[1 82]	#69b 5fc	chassis
Plate1	E4	52	TGGGCGCCAGGGTGTGATTG AAAATTTTTCAAATATATTTT	43	35[1 54]	13[1 82]	#69b 5fc	chassis
Plate1	E5	53	GAATACCCAAAGACGCCAGTTT GAGGAAATATTTAAATTGTA	42	0[76]	47[7 6]	#69b 5fc	chassis
Plate1	E6	54	CGAGGAATTATTTTGC GCATCA GATCGCACTCCAGCGACGTT	42	0[97]	44[9 8]	#69b 5fc	chassis
Plate1	E7	55	ATTAAGACACCCTCTAATGAGA AACCTGTCTGCCCAGCAGG	42	10[9 7]	34[9 8]	#69b 5fc	chassis
Plate1	E8	56	ACCCTCAAAGTTTTCGAAAATTA GCCCCGAGATAGGGGAACCC	42	12[9 7]	32[9 8]	#69b 5fc	chassis
Plate1	E9	57	TGAATTTATTGTATTAAGGGAA GGGAAGAAAGCGACAGGAG	42	14[9 7]	30[9 8]	#69b 5fc	chassis
Plate1	E10	58	TTTTTCAGAGTGAGACGCCTGA CCCATGGTATAGCTGCTCAG	42	15[4 2]	10[4 2]	#69b 5fc	chassis
Plate1	E11	59	TGAATTTGACAGCAGCCGATTA ATCAGTGAGGCCAGCTCATG	42	16[9 7]	28[9 8]	#69b 5fc	chassis
Plate1	E12	60	CAGAGGCTATACCAGAAATACA CCAGTCACACGACCCAGCAG	42	18[9 7]	26[9 8]	#69b 5fc	chassis
Plate1	F1	61	TGGTTTACAGTAGCGTAAACT CACCGGAAACAATCGTAAAA	42	2[97]	42[9 8]	#69b 5fc	chassis
Plate1	F2	62	TTCATTATAATTTACCAGTCAG GACGTAGCACCGCCTGCAA	42	22[7 6]	25[7 6]	#69b 5fc	chassis
Plate1	F3	63	CCTTAACATTTGAGGATTTAGG CCGTCAATAGATAATTGCGA	42	23[9 8]	24[9 8]	#69b 5fc	chassis
Plate1	F4	64	GTGTTGACGCTCAATCGTCTGA CAGGGCCAGAATCCTGAGAA	42	29[8 1]	29[8 0]	#69b 5fc	chassis

Plate Name	Well	Staple ID	Sequence	Length	CN 5' pos	CN 3' pos	Staple Color	Note
Plate1	F5	65	TTTTTATAAAGGGAAGAAAGGA GCCCCCAAAGAACCTGTTT	42	29[8 4]	34[8 4]	#69b 5fc	chassis
Plate1	F6	66	GATTTAGAGCTTGACGGGGCTA AGCAAATCCCTTATAAATC	42	32[8 3]	33[8 3]	#69b 5fc	chassis
Plate1	F7	67	AGCTGCAAAGCCTGTGCCTGTA CTGCGCCCTGCGGAGGTGTC	42	35[1 05]	40[1 05]	#69b 5fc	chassis
Plate1	F8	68	ACTCACATTAATTGCGTTGCCT GCCGTTTTACGGTCATACC	42	36[8 3]	37[8 3]	#69b 5fc	chassis
Plate1	F9	69	GATAGCACGTTTGCAGTGATGA AGGGGCAAATGGTCAATAAC	42	4[76]	42[4 9]	#69b 5fc	chassis
Plate1	F10	70	AACGTCACAAAATCAAAGCCGT CCGGCAAACGCGGCAGCATC	42	4[97]	40[9 8]	#69b 5fc	chassis
Plate1	F11	71	AGGCGTTTTCGCACTCAATTGT CTAAAGTTAAACGATGCTGA	42	40[8 3]	41[8 3]	#69b 5fc	chassis
Plate1	F12	72	AGTGCCAAGCTTTCAGAGGTAT AGGACGACGACAGTATCGGC	42	44[8 3]	45[8 3]	#69b 5fc	chassis
Plate1	G1	73	TTCAAAAGGGTGAGAAAGGCC GTATAAGCAAATAAAAATTTT	42	49[5 6]	48[5 6]	#69b 5fc	chassis
Plate1	G2	74	ACCGCCTAAACAAAAGCGGGG CGGGTCACTGTTGCGCCTGTG	42	6[97]	38[9 8]	#69b 5fc	chassis
Plate1	G3	75	ACCGTTCAGTTAAGAATGCGG CGGGCGGATGGCTTAGAGCT	42	8[76]	38[4 9]	#69b 5fc	chassis
Plate1	G4	76	GAAAGCGTTCGGAACACTCTGT CTGCCAGCACGCGGGGTGCC	42	8[97]	36[9 8]	#69b 5fc	chassis
Plate1	G5	77	GTGCCTTTTTGATGGCATTGAC CACCTGCATTTTGAATCAA	42	9[42]	4[42]	#69b 5fc	chassis
Plate1	G6	78	GGGTTTTCCGGAATAAGCAAAC GAGCTTCAAAGCGAACGCT	41	10[5 5]	35[6 8]	#69b 5fc	chassis
Plate1	G7	79	TTTCGGAATCGTCATAAATATTC ATTAACGAGCTGACTA	40	31[2 3]	33[4 8]	#69b 5fc	chassis
Plate1	G8	80	TTTTATTTTTGAATGGCTATACG TGCCACAGACAATTT	38	26[1 86]	27[1 86]	#69b 5fc	chassis
Plate1	G9	81	TTTGAGTAGAAGAACTCAAATA ACATCACTTGCCTTTT	38	28[1 86]	29[1 86]	#69b 5fc	chassis
Plate1	G10	82	TTTCGCTACAGGGCGCGTAGC CGCGCTTAATGCGCTTT	38	30[1 86]	31[1 86]	#69b 5fc	chassis
Plate1	G11	83	TTTTATCAGGGCGATGGCCAGG GCGAAAACCGTCTTT	38	32[1 86]	33[1 86]	#69b 5fc	chassis
Plate1	G12	84	TTTGTGAGACGGGCAACAGGTT TTTCTTTTACCATTT	38	34[1 86]	35[1 86]	#69b 5fc	chassis
Plate2	H1	85	TTTAGCTGTTTCTGTGTGTCG TAATCATGGTCATTTT	38	36[1 86]	37[1 86]	#69b 5fc	chassis
Plate2	H2	86	TTTGGCATCAGATGCCGGGTCA GCAAATCGTTAACTTT	38	38[1 86]	39[1 86]	#69b 5fc	chassis

Plate Name	Well	Staple ID	Sequence	Length	CN 5' pos	CN 3' pos	Staple Color	Note
Plate2	H3	87	TTTACGACGACAATAAACAAAG TAATTCTGTCCAGTTT	38	8[19 3]	9[19 3]	#69b 5fc	chassis
Plate2	H4	88	CACTGCCCGCTTTCCGATGGTG AGCGTAACGATCTA	36	35[6 9]	13[9 0]	#69b 5fc	chassis
Plate2	H5	89	AAGCAGAAAATTAATGCCGGAA CTAGCATAACCAA	35	0[13 2]	47[1 39]	#69b 5fc	chassis
Plate2	H6	90	ACGCAATGTCAAATCACCATCA GCCCCAGTTAAAA	35	0[90]	47[9 7]	#69b 5fc	chassis
Plate2	H7	91	ATCGTTCGAAAGAAGAGAGCGG AAAGAGTCTGTCCA	35	16[1 18]	29[1 25]	#69b 5fc	chassis
Plate2	H8	92	AAGAAACACAAACAATAACAA CTAATAGATTAGA	35	22[1 39]	24[1 19]	#69b 5fc	chassis
Plate2	H9	93	ACATTATATTAATATCTAAAAT ATCTTACCCTCA	35	22[1 60]	25[1 53]	#69b 5fc	chassis
Plate2	H10	94	AATCTTGTGAATTATTTAAGAA CTGGCTCATTAT	35	22[9 7]	24[7 7]	#69b 5fc	chassis
Plate2	H11	95	AATTAACCGTTGTAATCCAGAA GTAACAGTACCTT	35	29[1 33]	19[1 53]	#69b 5fc	chassis
Plate2	H12	96	CGGGCGCTAGGGCGTAGAATC ATGATGAAACAAAC	35	31[1 12]	17[1 32]	#69b 5fc	chassis
Plate2	A1	97	AGTCCACTATTA AAAAATCAAGA ACATAGCGATAGC	35	33[1 33]	15[1 53]	#69b 5fc	chassis
Plate2	A2	98	TTAATGAATCGGCCGCGTCTCT AAATGCTGATGCA	35	35[1 12]	13[1 32]	#69b 5fc	chassis
Plate2	A3	99	GAGCCGGAGCCTCCCAGACGA AGGTTTCACGCAAC	35	36[1 32]	40[1 26]	#69b 5fc	chassis
Plate2	A4	100	TCACAGTTGAGGATTCCACACC TAGAAAAAGCCTG	35	37[1 33]	11[1 53]	#69b 5fc	chassis
Plate2	A5	101	TAAGAGGTCATTTTAGACCGGA GGTGTATCACCGT	35	37[4 9]	11[6 9]	#69b 5fc	chassis
Plate2	A6	102	CTGGTAATGGGTAATCCAGCGA GGCAGAGGCATTT	35	39[1 12]	9[13 2]	#69b 5fc	chassis
Plate2	A7	103	TTACACTGGTGTGTTTACCTGA CCGACAAAAGGTA	35	39[1 54]	9[17 4]	#69b 5fc	chassis
Plate2	A8	104	CTCCGGCCAGAGCAGGTGGTG AAACCAATCAATAA	35	41[1 33]	7[15 3]	#69b 5fc	chassis
Plate2	A9	105	CCATTAGATACATTGAAGTTTTT GAGGCAGGTCAG	35	41[4 9]	7[69]	#69b 5fc	chassis
Plate2	A10	106	ACGTACAGCGCCATTACATCGT ATAGAAGGCTTAT	35	43[1 12]	5[13 2]	#69b 5fc	chassis
Plate2	A11	107	TAGACTTTCTCCGTTTAAATTAG CGAACCTCCCGA	35	43[1 54]	5[17 4]	#69b 5fc	chassis
Plate2	A12	108	GGTGAAGACGCCAGGCGCAAC GTAACA ACTGGCCT	35	43[1 68]	47[1 74]	#69b 5fc	chassis

Plate Name	Well	Staple ID	Sequence	Length	CN 5' pos	CN 3' pos	Staple Color	Note
Plate2	B1	109	GATAACCGACGGCCCTCAGGA GTAACCGATATTTT	35	43[8 4]	47[9 0]	#69b 5fc	chassis
Plate2	B2	110	GAGGGTAGCTATTTTTGAGAGT CGATGAAAAATAA	35	49[1 40]	47[1 60]	#69b 5fc	chassis
Plate2	B3	111	AATATGATATTCAACCGTTCTAC CCCGGTTGTAA	35	49[9 8]	47[1 18]	#69b 5fc	chassis
Plate2	B4	112	TTGAGGGCACCGACTAACATCT CAATTCTACTA	33	2[55]	43[6 0]	#69b 5fc	chassis
Plate2	B5	113	TTTGCGAACGAGTAGATTTAGT TTGACTGTTTA	33	41[2 3]	42[4 2]	#69b 5fc	chassis
Plate2	B6	114	ATTTACATTGGGTGAGGCGGTG TACAGACCAG	32	27[7 3]	21[9 0]	#69b 5fc	chassis
Plate2	B7	115	CGAACGTGCGGTTTTAGACCTC AGCAGCGAAA	32	31[7 3]	17[9 0]	#69b 5fc	chassis
Plate2	B8	116	TTTTTTAGTTAATTTTCGTTATAC AAATTTT	30	12[1 82]	11[1 82]	#69b 5fc	chassis
Plate2	B9	117	TTTCTTTTTTAATGGTGAGAAGA GTCATTT	30	16[1 82]	15[1 82]	#69b 5fc	chassis
Plate2	B10	118	TTTTAATGGAAGGGTACAATAA CGGATTTT	30	20[1 82]	19[1 82]	#69b 5fc	chassis
Plate2	B11	119	AATAGCAAAGGCTATCAGGTCA TTGCTTT	29	0[17 4]	49[1 89]	#69b 5fc	chassis
Plate2	B12	120	GCCGCCAATACAGGAGTGTACT GGTATTT	29	7[35]	8[20]	#69b 5fc	chassis
Plate2	C1	121	ATTGCGTATATTCCTACCGAAT CTAAAG	28	20[1 18]	25[1 18]	#69b 5fc	chassis
Plate2	C2	122	TACCATACTGATTGTTAATGCAT CAATA	28	20[1 60]	25[1 60]	#69b 5fc	chassis
Plate2	C3	123	ATTTGTAGCGCATAAAGATAAG AGCCAG	28	20[9 7]	25[9 7]	#69b 5fc	chassis
Plate2	C4	124	AGGCAAAGCAAGGCAACAGCC ATATTAT	28	45[1 40]	3[15 3]	#69b 5fc	chassis
Plate2	C5	125	TTTAAACGTAGAAAAGACCCTG TATTT	27	1[20]	46[2 3]	#69b 5fc	chassis
Plate2	C6	126	TTTGTGCGAGAGGGTTGATTAGA GATTT	27	11[2 0]	36[2 3]	#69b 5fc	chassis
Plate2	C7	127	TTTGTCCACCAGTACAGCCCGAA AGTTT	27	13[2 0]	34[2 3]	#69b 5fc	chassis
Plate2	C8	128	TTTAGGAATTGCGAAATAAATC AATTT	27	15[2 0]	32[2 3]	#69b 5fc	chassis
Plate2	C9	129	TTTATTCGGTCGCTGCCAATAC TGTTT	27	17[2 0]	30[2 3]	#69b 5fc	chassis
Plate2	C10	130	TTTAAGGCACCAACCAACCAAA ATTTT	27	19[2 0]	28[2 3]	#69b 5fc	chassis

Plate Name	Well	Staple ID	Sequence	Length	CN 5' pos	CN 3' pos	Staple Color	Note
Plate2	C11	131	TTTACGGTCAATCATATACATAA CTTT	27	21[2 0]	26[2 3]	#69b 5fc	chassis
Plate2	C12	132	TTTCTGACGAGAAACGAACTAA CGTTT	27	23[2 0]	24[2 3]	#69b 5fc	chassis
Plate2	D1	133	TTTATTCATTAAGGGGCAAGG CATT	27	3[20]	44[2 3]	#69b 5fc	chassis
Plate2	D2	134	TTTCTGGTCTGGTCAACGGGTA TTTTT	27	40[1 96]	7[19 3]	#69b 5fc	chassis
Plate2	D3	135	TTTAGAGACGCAGAAGAGGTTT TGTTT	27	42[1 96]	5[19 3]	#69b 5fc	chassis
Plate2	D4	136	TTTTGCGGGCCTCTTTTTGTTTA ATTT	27	44[1 96]	3[19 3]	#69b 5fc	chassis
Plate2	D5	137	TTTCAACATTAATGCAATAATA ATTT	27	46[1 96]	1[19 3]	#69b 5fc	chassis
Plate2	D6	138	TTTCTGTAGCGCTTTTTTCATT GTTT	27	5[20]	42[2 3]	#69b 5fc	chassis
Plate2	D7	139	TTTACCACCAGAGCCCCAATT CTTTT	27	7[20]	40[2 3]	#69b 5fc	chassis
Plate2	D8	140	TTTATAAGTTTTAACAATGCTGT ATTT	27	9[20]	38[2 3]	#69b 5fc	chassis
Plate2	D9	141	TAACCCTATACACTAAAACAC	21	28[6 2]	19[6 9]	#69b 5fc	chassis
Plate2	D10	142	TTAAACAAATCTCCAAAAAAA	21	32[6 2]	15[6 9]	#69b 5fc	chassis
Plate2	D11	143	GCGGCCATGCCCCCTGCCTAT	21	38[8 3]	9[90]	#69b 5fc	chassis
Plate2	D12	144	GTAGCATTGAGCCATTGTTGGG	21	44[6 2]	3[69]	#69b 5fc	chassis
Plate2	E1	145	????TCTGGTCAAGGTTCTTTT GCCCGAACGTTATT???	40	50[1 64]	23[1 82]	#f793 1e	biotin anchor
Plate2	E2	146	????CAGTGCCACGCTGAAACA GAGCAGATTCCTACATT	39	50[8 0]	28[8 4]	#f793 1e	biotin anchor
Plate2	E3	147	????CGCAAGGGCTAAATCGGT TGTAAGCCTCAGAGCA	39	52[5 9]	45[6 2]	#f793 1e	biotin anchor
Plate2	E4	148	????CAGCAAATGAAAAACGAAC CACAGTAAT	32	50[1 01]	27[1 11]	#f793 1e	biotin anchor
Plate2	E5	149	????CATCACCTTGCTGAATCGC CAGGCCAAC	32	50[1 22]	27[1 32]	#f793 1e	biotin anchor
Plate2	E6	150	????ATATCAATAGGAGCATTTCG ACAACCTCGT	32	50[1 43]	23[1 53]	#f793 1e	biotin anchor
Plate2	E7	151	????TCAGTTGTGGGAAGGGCT TGAGATGGTT	32	50[5 9]	23[6 9]	#f793 1e	biotin anchor
Plate2	E8	152	????TTCGCATTAATTTTTGATA ATCAGAAA	32	52[1 01]	48[9 8]	#f793 1e	biotin anchor

Plate Name	Well	Staple ID	Sequence	Length	CN 5' pos	CN 3' pos	Staple Color	Note
Plate2	E9	153	????ATCAGCTATGGGATCAAAG TCAGAGGGT	32	52[1 22]	1[13 2]	#f793 1e	biotin anchor
Plate2	E10	154	????TAGGAACACAAACGGCGG ATTGGAACC	32	52[1 43]	45[1 39]	#f793 1e	biotin anchor
Plate2	E11	155	????TTCGCGTCCCGTCGCCAC AAGAATTGAG	32	52[1 64]	1[17 4]	#f793 1e	biotin anchor
Plate2	E12	156	????AACGTTATGCATCTACCAC GGAATAAGT	32	52[8 0]	1[90]	#f793 1e	biotin anchor
Plate2	F1	157	?????GAACAACATTATTACAATA AAACACCAGAACGAGTAG	42	25[2 1]	23[4 8]	#730 0de	no dye
Plate2	F2	158	?????GTTGAAAGGAATTGAGAG TTGGCAAATCAACA???	40	24[1 88]	25[1 86]	#730 0de	no dye
Plate2	F3	159	?????CTGAGAGTCTGGTCCTGT AGCCAGCTTTCAT???	39	48[1 91]	47[1 96]	#730 0de	no dye
Plate2	F4	160	?????ATGCCTGAGTAATATTAC GCAGTATGTTAGC???	39	49[2 5]	0[20]	#730 0de	no dye
Plate2	F5		empty					
Plate2	F6		empty					
Plate2	F7		empty					
Plate2	F8		empty					
Plate2	F9		empty					
Plate2	F10		empty					
Plate2	F11		empty					
Plate2	F12		empty					
Plate2	G1		empty					
Plate2	G2		empty					
Plate2	G3		empty					
Plate2	G4		empty					
Plate2	G5		empty					
Plate2	G6		empty					
Plate2	G7		empty					
Plate2	G8		empty					
Plate2	G9		empty					
Plate2	G10		empty					
Plate2	G11		empty					
Plate2	G12		empty					
Plate2	H1		empty					
Plate2	H2		empty					
Plate2	H3		empty					

Plate Name	Well	Staple ID	Sequence	Length	CN 5' pos	CN 3' pos	Staple Color	Note
Plate2	H4		empty					
Plate2	H5		empty					
Plate2	H6		empty					
Plate2	H7		empty					
Plate2	H8		empty					
Plate2	H9		empty					
Plate2	H10		empty					
Plate2	H11		empty					
Plate2	H12		empty					
			SEPARATE TUBE ORDER					
	Tube Name	Staple ID	Sequence	Length	CN 5' pos	CN 3' pos	Staple Color	Note
	DyeTube1	157+dye	/5ATTO647NN/TTTCTGAGAGTC TGGTCCTGTAGCCAGCTTTCAT TTT	42	25[21]	23[48]	#7300de	+ATTO 847N dye
	DyeTube2	158+dye	/5ATTO647NN/TTTATGCCTGAG TAATATTACGCAGTATGTTAGCT TT	40	24[188]	25[186]	#7300de	+ATTO 847N dye
	DyeTube3	159+dye	/5ATTO647NN/TTTGTTGAAAGG AATTGAGAGTTGGCAAATCAAC ATTT	39	48[191]	47[196]	#7300de	+ATTO 847N dye
	DyeTube4	160+dye	/5ATTO647NN/TTTGAACAACAT TATTACAATAAAACACCAGAAC GAGTAG	39	49[25]	0[20]	#7300de	+ATTO 847N dye

Table S3.2 Sequences and setup for plates 3: No ligand

Plate 3-L (No Ligand)						
Plate	Well	Sequence	Length	CN 5' pos	CN 3' pos	CN Color
Plate3-L	A1	CGACATTAGAAACGCAAAAGAACTGGCA	28	2[69]	51[76]	#cee7fe
Plate3-L	A2	AAAACAGGAAGATTGGAGACAAATAACG	28	48[90]	51[97]	#cee7fe
Plate3-L	A3	GTCACAATCAATCATACCAGAAGGAAAC	28	1[98]	51[118]	#cee7fe

Plate 3-L (No Ligand)						
Plate	Well	Sequence	Length	CN 5' pos	CN 3' pos	CN Color
Plate3-L	A4	TGTC AATCATATGTAGCTGATTAGCCGA	28	48[132]	51[139]	#cee7fe
Plate3-L	A5	AACATAAATCAGAGGAAGCCCTTTTTAA	28	2[153]	51[160]	#cee7fe
Plate3-L	A6	AGCAAACAAGAGAAATCTACAATAGCTA	28	48[174]	51[181]	#cee7fe
Plate3-L	A7	TGATTAATGGCAACATATAACAACCGA	28	0[55]	53[76]	#cee7fe
Plate3-L	A8	CCAATGAAAATCACCCAGCGCCAAAGAC	28	4[90]	53[97]	#cee7fe
Plate3-L	A9	TTAACTGAAAGAAAATTCATA	21	2[118]	53[118]	#cee7fe
Plate3-L	A10	TTACCAACCAGTTAATTAGACGGGAGAA	28	4[132]	53[139]	#cee7fe
Plate3-L	A11	GAAAAGTAATTGAGCGCTAATAAACAGG	28	0[139]	53[160]	#cee7fe
Plate3-L	A12	TTAGTTGATAAGAAAGCAGCCTTTACAG	28	4[174]	53[181]	#cee7fe
Plate3-L	B1	GAACCGCTTATTAGGCACCGTAATCAGT	28	6[69]	55[76]	#cee7fe
Plate3-L	B2	AAAAGGGAATTAGAGCCAGCAAACCATC	28	2[76]	55[97]	#cee7fe
Plate3-L	B3	ACCGGAACCAGACATTAGCAAGGCCGGA	28	5[98]	55[118]	#cee7fe
Plate3-L	B4	ACCATTACCATTTCCAGAGCCTAATTTGCGCTAAC	35	3[98]	55[139]	#cee7fe
Plate3-L	B5	TTTTTATACGCGAGGCTACAATTTTATC	28	6[153]	55[160]	#cee7fe
Plate3-L	B6	AGAGAATTTATCCCAATCCAATTTTTAGCGACACGGTCATAGCCCCCACCCTC	28	2[160]	55[181]	#cee7fe
Plate3-L	B7	CAGTCTCTATTACCCCTCAGAGCCGCC	28	4[55]	57[76]	#cee7fe
Plate3-L	B8	AATAGCAAGGCCACCACCGGA	21	6[118]	57[97]	#cee7fe
Plate3-L	B9	GATAAGTTTACGAGTCATTACCGCGCCC	28	8[90]	57[118]	#cee7fe
Plate3-L	B10	CTGAATCCCGGTATTCTAAGATTTTCATC	28	8[132]	57[139]	#cee7fe
Plate3-L	B11	ACATGTTTTATCATTTCATCGAGAACAAG	28	4[139]	57[160]	#cee7fe
Plate3-L	B12	GGATTAGGTATAAACAGTAAGCGTCATA	28	8[174]	57[181]	#cee7fe
Plate3-L	C1	GGATTAGGTATAAACAGTAAGCGTCATA	28	10[69]	59[76]	#cee7fe

Plate 3-L (No Ligand)						
Plate	Well	Sequence	Length	CN 5' pos	CN 3' pos	CN Color
Plate3-L	C2	ACCTCAACGATTGGCCTTGATGAATTT	28	6[76]	59[97]	#cee7fe
Plate3-L	C3	CCTATTATTCTGATATAAAGCCAGAATG	28	9[98]	59[118]	#cee7fe
Plate3-L	C4	TAAATCCTCATTAAATATCCCATCCTAATCCTGAAC	35	7[98]	59[139]	#cee7fe
Plate3-L	C5	ACAGTAGAGAGAATCGCGCCTGTTTATC	28	10[153]	59[160]	#cee7fe
Plate3-L	C6	CAAGCCGTCGGCTGTCTTTCCCAGCTAACATGGCTGAGTAACAGTGCCCGATTAGC	28	6[160]	59[181]	#cee7fe
Plate3-L	C7	GAGCCACGTACCGCGGCTGAGACTCCTC	28	8[55]	61[76]	#cee7fe
Plate3-L	C8	GAGCCACGTACCGCGGCTGAGACTCCTC	28	12[90]	61[97]	#cee7fe
Plate3-L	C9	AACGCCAACAAACATGAAAGT	21	10[118]	61[118]	#cee7fe
Plate3-L	C10	GACCGTGCGGAATCTCGCCATATTTAAC	28	12[132]	61[139]	#cee7fe
Plate3-L	C11	AACAATATCGAGCCAGTAATAGGCTTAA	28	8[139]	61[160]	#cee7fe
Plate3-L	C12	TTTTCTTACCAGTATAAAGCCA CAACTTTCAGCCCTGGGATAGCAAGCC C	22	10[182]	61[181]	#cee7fe
Plate3-L	D1	CAACTTTCAGCCCTGGGATAGCAAGCC C	28	14[69]	63[76]	#cee7fe
Plate3-L	D2	AAGAGAACTCAGGAGGTTTACACCCTC	28	10[76]	63[97]	#cee7fe
Plate3-L	D3	GTCGTCTTTCCAAATTCTCAGAACCGCC	28	13[98]	63[118]	#cee7fe
Plate3-L	D4	AGAACCGCCACCAAATAAGAATAAACAC TGATAAA	35	11[98]	63[139]	#cee7fe
Plate3-L	D5	CTGAGAGACAAAGAAATTTAATGGTTTG	28	14[153]	63[160]	#cee7fe
Plate3-L	D6	ACGCTCATTTAGTATCATATGCATCTTC	28	10[160]	63[181]	#cee7fe
Plate3-L	D7	AATAGGATAGCATTCCACAGACAACAGT	28	12[55]	65[76]	#cee7fe
Plate3-L	D8	CTTAAACGCCTTTATCTGTATGGGATTT	28	16[90]	65[97]	#cee7fe
Plate3-L	D9	GGGTTATATGACGTTAGTAAA	21	14[118]	65[118]	#cee7fe
Plate3-L	D10	CCTTGCTTTAGAATCTCCGGCTTAGGTT	28	16[132]	65[139]	#cee7fe
Plate3-L	D11	AAATACCAATCCAATCGCAAGACTACCT	28	12[139]	65[160]	#cee7fe

Plate 3-L (No Ligand)						
Plate	Well	Sequence	Length	CN 5' pos	CN 3' pos	CN Color
Plate3-L	D12	TTTATAGTGAATTTATCAAAAT	22	14[182]	65[181]	#cee7fe
Plate3-L	E1	CATGAGGTGCGGGAAGTTGCGCCGACA A	28	18[69]	67[76]	#cee7fe
Plate3-L	E2	TGCTAAAAGGCTCCAAAAGGAAGCTTGA	28	14[76]	67[97]	#cee7fe
Plate3-L	E3	TCGGAACGAGGGCACTTTGCTTTTCGAG G	28	17[98]	67[118]	#cee7fe
Plate3-L	E4	CGGTTTATCAGCATTAAATTTTCCCT CTGTAA	35	15[98]	67[139]	#cee7fe
Plate3-L	E5	TACAAAATTAATTTCAATATATGTGAG	28	18[153]	67[160]	#cee7fe
Plate3-L	E6	CATAGGTTTAGATTAAGACGCAAACAGT	28	14[160]	67[181]	#cee7fe
Plate3-L	E7	TGACAACCTAAAGGCCGCTTTAAGTTTC	28	16[55]	69[76]	#cee7fe
Plate3-L	E8	TCATCGCCAGCGATTTTGAGGACTAAAG	28	20[90]	69[97]	#cee7fe
Plate3-L	E9	TTACCTGAGTAGCAACGGCTA	21	18[118]	69[118]	#cee7fe
Plate3-L	E10	ACAGAAATCAGATGATTATTCATTTCAA	28	20[132]	69[139]	#cee7fe
Plate3-L	E11	TGAATAAATCAAGAAAACAAATCGCGCA	28	16[139]	69[160]	#cee7fe
Plate3-L	E12	TTTTCGCCTGATTGCTTTGAAT	22	18[182]	69[181]	#cee7fe
Plate3-L	F1	CCCAAATGAGGACACGAAATCCGCGAC C	28	22[69]	71[76]	#cee7fe
Plate3-L	F2	ACTTTTTTTCATCTTTGACCCCCTGATAA GGCTGGCTGACCTCAGAGTACAACGGA	28	18[76]	71[97]	#cee7fe
Plate3-L	F3	G	28	21[98]	71[118]	#cee7fe
Plate3-L	F4	AGCGCGAAACAAATTTTCAGGTTTAACG TAAAGAA	35	19[98]	71[139]	#cee7fe
Plate3-L	F5	CATTTTGTATAATCTCAAATTATTTGC	28	22[153]	71[160]	#cee7fe
Plate3-L	F6	ACCAAGTTTACATCGGGAGAATAGAACC	28	18[160]	71[181]	#cee7fe
Plate3-L	F7	TGCTCCAGACCAACTTTGAAACAACGTA	28	20[55]	73[76]	#cee7fe
Plate3-L	F8	AACTTTAATCATTGACAAGAACCGGATA	28	23[77]	73[97]	#cee7fe
Plate3-L	F9	GAATTATCATTATCAAGAGT	21	22[118]	73[118]	#cee7fe

Plate 3-L (No Ligand)						
Plate	Well	Sequence	Length	CN 5' pos	CN 3' pos	CN Color
Plate3-L	F10	AAGTATTAGACTTTCCACCAGAAGGAGCG	28	23[119]	73[139]	#cee7fe
Plate3-L	F11	ACGTAAATGGCAATTCATCAACGGAACA	28	20[139]	73[160]	#cee7fe
Plate3-L	F12	TTTAATTTTAAAAGTTTGAGTA	22	22[182]	73[181]	#cee7fe
Plate3-L	G1	empty				
Plate3-L	G2	empty				
Plate3-L	G3	empty				
Plate3-L	G4	empty				
Plate3-L	G5	empty				
Plate3-L	G6	empty				
Plate3-L	G7	empty				
Plate3-L	G8	empty				
Plate3-L	G9	empty				
Plate3-L	G10	empty				
Plate3-L	G11	empty				
Plate3-L	G12	empty				
Plate3-L	H1	empty				
Plate3-L	H2	empty				
Plate3-L	H3	empty				
Plate3-L	H4	empty				
Plate3-L	H5	empty				
Plate3-L	H6	empty				
Plate3-L	H7	empty				
Plate3-L	H8	empty				
Plate3-L	H9	empty				
Plate3-L	H10	empty				
Plate3-L	H11	empty				
Plate3-L	H12	empty				

Table S3.3 Sequences and setup for plates 3: High-affinity ligand

Plate 3HA (high-affinity 16-bp ligand)						
5T + Ligand:		TTTTTCCACATACATCATATT				
Plate	Well	Sequence	Length	CN 5' pos	CN 3' pos	CN Color
Plate3HA	A1	CGACATTAGAAACGCAAAAGAACTGG CATTTTTCCACATACATCATATT	49	2[69]	51[76]	#ccFB B040
Plate3HA	A2	AAAACAGGAAGATTGGAGACAAATAAC GTTTTTCCACATACATCATATT	49	48[90]	51[97]	#ccFB B040
Plate3HA	A3	GTCACAATCAATCATACCAGAAGGAAA CTTTTTCCACATACATCATATT	49	1[98]	51[118]	#ccFB B040
Plate3HA	A4	TGTCAATCATATGTAGCTGATTAGCCG ATTTTTCCACATACATCATATT	49	48[132]	51[139]	#ccFB B040
Plate3HA	A5	AACATAAATCAGAGGAAGCCCTTTTA ATTTTTCCACATACATCATATT	49	2[153]	51[160]	#ccFB B040
Plate3HA	A6	AGCAAACAAGAGAAATCTACAATAGCT ATTTTTCCACATACATCATATT	49	48[174]	51[181]	#ccFB B040
Plate3HA	A7	TGATTAATGGCAACATATAACAACCG ATTTTTCCACATACATCATATT	49	0[55]	53[76]	#ccFB B040
Plate3HA	A8	CCAATGAAAATCACCCAGCGCCAAAG ACTTTTTCCACATACATCATATT	49	4[90]	53[97]	#ccFB B040
Plate3HA	A9	TTAACTGAAAGAAAATTCATATTTTTCC ACATACATCATATT	42	2[118]	53[118]	#ccFB B040
Plate3HA	A10	TTACCAACCAGTTAATTAGACGGGAGA ATTTTTCCACATACATCATATT	49	4[132]	53[139]	#ccFB B040
Plate3HA	A11	GAAAAGTAATTGAGCGCTAATAAACAG GTTTTTCCACATACATCATATT	49	0[139]	53[160]	#ccFB B040
Plate3HA	A12	TTAGTTGATAAGAAAGCAGCCTTTACA GTTTTTCCACATACATCATATT	49	4[174]	53[181]	#ccFB B040
Plate3HA	B1	GAACCGCTTATTAGGCACCGTAATCA GTTTTTCCACATACATCATATT	49	6[69]	55[76]	#ccFB B040
Plate3HA	B2	AAAAGGGAATTAGAGCCAGCAAACCA TCTTTTTCCACATACATCATATT	49	2[76]	55[97]	#ccFB B040
Plate3HA	B3	ACCGGAACCAGACATTAGCAAGGCCG GATTTTTCCACATACATCATATT	49	5[98]	55[118]	#ccFB B040
Plate3HA	B4	ACCATTACCATTTCCAGAGCCTAATTT GCGCTAACTTTTTCCACATACATCATA TT	56	3[98]	55[139]	#ccFB B040
Plate3HA	B5	TTTTTATACGCGAGGCTACAATTTTAT CTTTTTCCACATACATCATATT	49	6[153]	55[160]	#ccFB B040
Plate3HA	B6	AGAGAATTTATCCCAATCCAATTTTT TTTTTCCACATACATCATATT	49	2[160]	55[181]	#ccFB B040
Plate3HA	B7	AGCGACACGGTCATAGCCCCCACCC TCTTTTTCCACATACATCATATT	49	4[55]	57[76]	#ccFB B040
Plate3HA	B8	CAGTCTCTATTCACCCCTCAGAGCCG CCTTTTTCCACATACATCATATT	49	8[90]	57[97]	#ccFB B040

Plate 3HA (high-affinity 16-bp ligand)						
5T + Ligand:		TTTTTCCACATACATCATATT				
Plate3HA	B9	AATAGCAAGGCCACCACCGGATTTTTCCACATACATCATATT	42	6[118]	57[118]	#ccFB B040
Plate3HA	B10	GATAAGTTTACGAGTCATTACCGCGCCCTTTTTCCACATACATCATATT	49	8[132]	57[139]	#ccFB B040
Plate3HA	B11	CTGAATCCCGGTATTCTAAGATTTTCATCTTTTTCCACATACATCATATT	49	4[139]	57[160]	#ccFB B040
Plate3HA	B12	ACATGTTTTATCATTTCATCGAGAACAA GTTTTTCCACATACATCATATT	49	8[174]	57[181]	#ccFB B040
Plate3HA	C1	GGATTAGGTATAAACAGTAAGCGTCATATTTTTCCACATACATCATATT	49	10[69]	59[76]	#ccFB B040
Plate3HA	C2	ACCCTCAACGATTGGCCTTGATGAATT TTTTTCCACATACATCATATT	49	6[76]	59[97]	#ccFB B040
Plate3HA	C3	CCTATTATTCTGATATAAAGCCAGAAT GTTTTTCCACATACATCATATT	49	9[98]	59[118]	#ccFB B040
Plate3HA	C4	TAAATCCTCATTAAATATCCCATCCTAAT CCTGAACTTTTTCCACATACATCATATT	56	7[98]	59[139]	#ccFB B040
Plate3HA	C5	ACAGTAGAGAGAATCGCGCCTGTTTATCTTTTTCCACATACATCATATT	49	10[153]	59[160]	#ccFB B040
Plate3HA	C6	CAAGCCGTCGGCTGTCTTTCCAGCTAATTTTTCCACATACATCATATT	49	6[160]	59[181]	#ccFB B040
Plate3HA	C7	CATGGCTGAGTAACAGTGCCCGATTA GCTTTTTCCACATACATCATATT	49	8[55]	61[76]	#ccFB B040
Plate3HA	C8	GAGCCACGTACCGCGGCTGAGACTCCTTTTTCCACATACATCATATT	49	12[90]	61[97]	#ccFB B040
Plate3HA	C9	AACGCCAACAAACATGAAAGTTTTTTCACATACATCATATT	42	10[118]	61[118]	#ccFB B040
Plate3HA	C10	GACCGTGCGGAATCTCGCCATATTTAACTTTTTCCACATACATCATATT	49	12[132]	61[139]	#ccFB B040
Plate3HA	C11	AACAATATCGAGCCAGTAATAGGCTTAATTTTTCCACATACATCATATT	49	8[139]	61[160]	#ccFB B040
Plate3HA	C12	TTTTCTTACCAGTATAAAGCCATTTTTCCACATACATCATATT	43	10[182]	61[181]	#ccFB B040
Plate3HA	D1	CAACTTTCAGCCCTGGGATAGCAAGCCCTTTTTCCACATACATCATATT	49	14[69]	63[76]	#ccFB B040
Plate3HA	D2	AAGAGAAACTCAGGAGTTTACACCCCTTTTTCCACATACATCATATT	49	10[76]	63[97]	#ccFB B040
Plate3HA	D3	GTCGTCTTCCAAATTCTCAGAACCGCCTTTTTCCACATACATCATATT	49	13[98]	63[118]	#ccFB B040
Plate3HA	D4	AGAACCGCCACCAAATAAGAATAAACACTGATAAATTTTTCCACATACATCATATT	56	11[98]	63[139]	#ccFB B040
Plate3HA	D5	CTGAGAGACAAAGAAATTTAATGGTTGTTTTTCCACATACATCATATT	49	14[153]	63[160]	#ccFB B040
Plate3HA	D6	ACGCTCATTTAGTATCATATGCATCTCTTTTTCCACATACATCATATT	49	10[160]	63[181]	#ccFB B040

Plate 3HA (high-affinity 16-bp ligand)						
5T + Ligand:		TTTTTCCACATACATCATATT				
Plate3HA	D7	AATAGGATAGCATTCCACAGACAACAG TTTTTCCACATACATCATATT	49	12[55]	65[76]	#ccFB B040
Plate3HA	D8	CTTAAACGCCTTTATCTGTATGGGATT TTTTTCCACATACATCATATT	49	16[90]	65[97]	#ccFB B040
Plate3HA	D9	GGGTTATATGACGTTAGTAAATTTTTTC CACATACATCATATT	42	14[11 8]	65[11 8]	#ccFB B040
Plate3HA	D10	CCTTGCTTTAGAATCTCCGGCTTAGGT TTTTTCCACATACATCATATT	49	16[13 2]	65[13 9]	#ccFB B040
Plate3HA	D11	AAATACCAATCCAATCGCAAGACTACC TTTTTCCACATACATCATATT	49	12[13 9]	65[16 0]	#ccFB B040
Plate3HA	D12	TTTATAGTGAATTTATCAAAATTTTTTC CACATACATCATATT	43	14[18 2]	65[18 1]	#ccFB B040
Plate3HA	E1	CATGAGGTGCGGGAAGTTGCGCCGAC AATTTTTCCACATACATCATATT	49	18[69]	67[76]	#ccFB B040
Plate3HA	E2	TGCTAAAAGGCTCCAAAAGGAAGCTT GATTTTTCCACATACATCATATT	49	14[76]	67[97]	#ccFB B040
Plate3HA	E3	TCGGAACGAGGGCACTTTGCTTTCGA GGTTTTTCCACATACATCATATT	49	17[98]	67[11 8]	#ccFB B040
Plate3HA	E4	CGGTTTATCAGCATTAAATTTTTCCC TCTGTAATTTTTCCACATACATCATATT	56	15[98]	67[13 9]	#ccFB B040
Plate3HA	E5	TACAAAATTAATTTCAATATATGTGAG TTTTTCCACATACATCATATT	49	18[15 3]	67[16 0]	#ccFB B040
Plate3HA	E6	CATAGGTTTAGATTAAGACGCAAACAG TTTTTCCACATACATCATATT	49	14[16 0]	67[18 1]	#ccFB B040
Plate3HA	E7	TGACAACCTAAAGGCCGCTTTAAGTTT CTTTTTCCACATACATCATATT	49	16[55]	69[76]	#ccFB B040
Plate3HA	E8	TCATCGCCAGCGATTTTGAGGACTAAA GTTTTTCCACATACATCATATT	49	20[90]	69[97]	#ccFB B040
Plate3HA	E9	TTACCTGAGTAGCAACGGCTATTTTTTC CACATACATCATATT	42	18[11 8]	69[11 8]	#ccFB B040
Plate3HA	E10	ACAGAAATCAGATGATTATTCATTTCA ATTTTTCCACATACATCATATT	49	20[13 2]	69[13 9]	#ccFB B040
Plate3HA	E11	TGAATAAATCAAGAAAACAAATCGCGC ATTTTTCCACATACATCATATT	49	16[13 9]	69[16 0]	#ccFB B040
Plate3HA	E12	TTTTCGCCTGATTGCTTTGAATTTTTTC CACATACATCATATT	43	18[18 2]	69[18 1]	#ccFB B040
Plate3HA	F1	CCCAAATGAGGACACGAAATCCGCGA CCTTTTTCCACATACATCATATT	49	22[69]	71[76]	#ccFB B040
Plate3HA	F2	ACTTTTTTCATCTTTGACCCCCTGATAA TTTTTCCACATACATCATATT	49	18[76]	71[97]	#ccFB B040
Plate3HA	F3	GGCTGGCTGACCTCAGAGTACAACGG AGTTTTTCCACATACATCATATT	49	21[98]	71[11 8]	#ccFB B040
Plate3HA	F4	AGCGCGAAACAAATTTTCAGTTTAAAC GTAAAGAATTTTTCCACATACATCATAT T	56	19[98]	71[13 9]	#ccFB B040

Plate 3HA (high-affinity 16-bp ligand)						
5T + Ligand:		TTTTTCCACATACATCATATT				
Plate3HA	F5	CATTTTGTATAATCTCAAAATTATTTGC TTTTTCCACATACATCATATT	49	22[15 3]	71[16 0]	#ccFB B040
Plate3HA	F6	ACCAAGTTTACATCGGGAGAATAGAAC CTTTTTCCACATACATCATATT	49	18[16 0]	71[18 1]	#ccFB B040
Plate3HA	F7	TGCTCCAGACCAACTTTGAAACAACGT ATTTTTCCACATACATCATATT	49	20[55]	73[76]	#ccFB B040
Plate3HA	F8	AACTTTAATCATTGACAAGAACCGGAT ATTTTTCCACATACATCATATT	49	23[77]	73[97]	#ccFB B040
Plate3HA	F9	GAATTATCATTCAAGAGTTTTTTCC ACATACATCATATT	42	22[11 8]	73[11 8]	#ccFB B040
Plate3HA	F10	AAGTATTAGACTTTCCACCAGAAGGAGC GTTTTTCCACATACATCATATT	49	23[11 9]	73[13 9]	#ccFB B040
Plate3HA	F11	ACGTAAATGGCAATTCATCAACGGAAC ATTTTTCCACATACATCATATT	49	20[13 9]	73[16 0]	#ccFB B040
Plate3HA	F12	TTTAATTTTAAAAGTTTGAGTATTTTC CACATACATCATATT	43	22[18 2]	73[18 1]	#ccFB B040
Plate3HA	G1	empty				
Plate3HA	G2	empty				
Plate3HA	G3	empty				
Plate3HA	G4	empty				
Plate3HA	G5	empty				
Plate3HA	G6	empty				
Plate3HA	G7	empty				
Plate3HA	G8	empty				
Plate3HA	G9	empty				
Plate3HA	G10	empty				
Plate3HA	G11	empty				
Plate3HA	G12	empty				
Plate3HA	H1	empty				
Plate3HA	H2	empty				
Plate3HA	H3	empty				
Plate3HA	H4	empty				
Plate3HA	H5	empty				
Plate3HA	H6	empty				
Plate3HA	H7	empty				
Plate3HA	H8	empty				
Plate3HA	H9	empty				
Plate3HA	H10	empty				
Plate3HA	H11	empty				

Plate 3HA (high-affinity 16-bp ligand)					
5T + Ligand:		TTTTTCCACATACATCATATT			
Plate3HA	H12	empty			

Table S3.4 Sequences and setup for plates 3: Medium-affinity ligand

Plate 3MA (mid-affinity 13-bp ligand)						
7T + Ligand:		TTTTTTTTTCATACATCATATT				
Plate	Well	Sequence	Length	CN 5' pos	CN 3' pos	CN Color
Plate3MA	A1	CGACATTAGAAAACGCAAAGAAGCTGG CATTTTTTTTTTCATACATCATATT	49	2[69]	51[76]	#ccFD 3500
Plate3MA	A2	AAAACAGGAAGATTGGAGACAAATAAC GTTTTTTTTTCATACATCATATT	49	48[90]	51[97]	#ccFD 3500
Plate3MA	A3	GTCACAATCAATCATACCAGAAGGAAA CTTTTTTTTTTCATACATCATATT	49	1[98]	51[118]	#ccFD 3500
Plate3MA	A4	TGTCAATCATATGTAGCTGATTAGCCG ATTTTTTTTTTCATACATCATATT	49	48[132]	51[139]	#ccFD 3500
Plate3MA	A5	AACATAAATCAGAGGAAGCCCTTTTTA ATTTTTTTTTTCATACATCATATT	49	2[153]	51[160]	#ccFD 3500
Plate3MA	A6	AGCAAACAAGAGAAATCTACAATAGCT ATTTTTTTTTTCATACATCATATT	49	48[174]	51[181]	#ccFD 3500
Plate3MA	A7	TGATTAATGGCAACATATAAACAACCG ATTTTTTTTTTCATACATCATATT	49	0[55]	53[76]	#ccFD 3500
Plate3MA	A8	CCAATGAAAATCACCCAGCGCCAAAG ACTTTTTTTTTTCATACATCATATT	49	4[90]	53[97]	#ccFD 3500
Plate3MA	A9	TTAACTGAAAGAAAATTCATATTTTTTT TCATACATCATATT	42	2[118]	53[118]	#ccFD 3500
Plate3MA	A10	TTACCAACCAGTTAATTAGACGGGAGA ATTTTTTTTTTCATACATCATATT	49	4[132]	53[139]	#ccFD 3500
Plate3MA	A11	GAAAAGTAATTGAGCGCTAATAAACAG GTTTTTTTTTCATACATCATATT	49	0[139]	53[160]	#ccFD 3500
Plate3MA	A12	TTAGTTGATAAGAAAGCAGCCTTTACA GTTTTTTTTTCATACATCATATT	49	4[174]	53[181]	#ccFD 3500
Plate3MA	B1	GAACCGCTTATTAGGCACCGTAATCA GTTTTTTTTTCATACATCATATT	49	6[69]	55[76]	#ccFD 3500
Plate3MA	B2	AAAAGGGAATTAGAGCCAGCAAACCA TCTTTTTTTTTTCATACATCATATT	49	2[76]	55[97]	#ccFD 3500
Plate3MA	B3	ACCGGAACCAGACATTAGCAAGGCCG GATTTTTTTTTTCATACATCATATT	49	5[98]	55[118]	#ccFD 3500
Plate3MA	B4	ACCATTACCATTTCCAGAGCCTAATTT GCGCTAACTTTTTTTTTTCATACATCATAT T	56	3[98]	55[139]	#ccFD 3500

Plate 3MA (mid-affinity 13-bp ligand)						
7T + Ligand:		TTTTTTTTTCATACATCATATT				
Plate3MA	B5	TTTTTATACGCGAGGCTACAATTTTAT CTTTTTTTTCATACATCATATT	49	6[153]	55[160]	#ccFD 3500
Plate3MA	B6	AGAGAATTTATCCCAATCCAACATTTTT TTTTTTTTTCATACATCATATT	49	2[160]	55[181]	#ccFD 3500
Plate3MA	B7	AGCGACACGGTCATAGCCCCCACCC TCTTTTTTTTCATACATCATATT	49	4[55]	57[76]	#ccFD 3500
Plate3MA	B8	CAGTCTCTATTACCCCTCAGAGCCG CCTTTTTTTTCATACATCATATT	49	8[90]	57[97]	#ccFD 3500
Plate3MA	B9	AATAGCAAGGCCACCACCGGATTTTTT TTCATACATCATATT	42	6[118]	57[118]	#ccFD 3500
Plate3MA	B10	GATAAGTTTACGAGTCATTACCGCGCC CTTTTTTTTCATACATCATATT	49	8[132]	57[139]	#ccFD 3500
Plate3MA	B11	CTGAATCCCGGTATTCTAAGATTTTCAT CTTTTTTTTCATACATCATATT	49	4[139]	57[160]	#ccFD 3500
Plate3MA	B12	ACATGTTTTATCATTTCATCGAGAACAA GTTTTTTTTTCATACATCATATT	49	8[174]	57[181]	#ccFD 3500
Plate3MA	C1	GGATTAGGTATAAACAGTAAGCGTCAT ATTTTTTTTCATACATCATATT	49	10[69]	59[76]	#ccFD 3500
Plate3MA	C2	ACCCTCAACGATTGGCCTTGATGAATT TTTTTTTTTCATACATCATATT	49	6[76]	59[97]	#ccFD 3500
Plate3MA	C3	CCTATTATTCTGATATAAAGCCAGAAT GTTTTTTTTTCATACATCATATT	49	9[98]	59[118]	#ccFD 3500
Plate3MA	C4	TAAATCCTCATTAATATCCCATCCTAAT CCTGAACTTTTTTTTCATACATCATATT	56	7[98]	59[139]	#ccFD 3500
Plate3MA	C5	ACAGTAGAGAGAATCGCGCCTGTTTAT CTTTTTTTTCATACATCATATT	49	10[153]	59[160]	#ccFD 3500
Plate3MA	C6	CAAGCCGTCGGCTGTCTTTCCAGCT AATTTTTTTTCATACATCATATT	49	6[160]	59[181]	#ccFD 3500
Plate3MA	C7	CATGGCTGAGTAACAGTGCCCGATTA GCTTTTTTTTCATACATCATATT	49	8[55]	61[76]	#ccFD 3500
Plate3MA	C8	GAGCCACGTACCGCGGCTGAGACTCC TCTTTTTTTTCATACATCATATT	49	12[90]	61[97]	#ccFD 3500
Plate3MA	C9	AACGCCAACAAACATGAAAGTTTTTTTT TTCATACATCATATT	42	10[118]	61[118]	#ccFD 3500
Plate3MA	C10	GACCGTGCGGAATCTCGCCATATTTAA CTTTTTTTTCATACATCATATT	49	12[132]	61[139]	#ccFD 3500
Plate3MA	C11	AACAATATCGAGCCAGTAATAGGCTTA ATTTTTTTTCATACATCATATT	49	8[139]	61[160]	#ccFD 3500
Plate3MA	C12	TTTTCTTACCAGTATAAAGCCATTTTTT TTCATACATCATATT	43	10[182]	61[181]	#ccFD 3500
Plate3MA	D1	CAACTTTCAGCCCTGGGATAGCAAGC CCTTTTTTTTCATACATCATATT	49	14[69]	63[76]	#ccFD 3500
Plate3MA	D2	AAGAGAACTCAGGAGGTTTACACCC TCTTTTTTTTCATACATCATATT	49	10[76]	63[97]	#ccFD 3500

Plate 3MA (mid-affinity 13-bp ligand)						
7T + Ligand:		TTTTTTTTTCATACATCATATT				
Plate3MA	D3	GTCGTCTTCCAAATTCTCAGAACCGC CTTTTTTTTCATACATCATATT	49	13[98]	63[11 8]	#ccFD 3500
Plate3MA	D4	AGAACCGCCACCAAATAAGAATAAACA CTGATAAATTTTTTTTCATACATCATAT T	56	11[98]	63[13 9]	#ccFD 3500
Plate3MA	D5	CTGAGAGACAAAGAAATTTAATGGTTT GTTTTTTTTTCATACATCATATT	49	14[15 3]	63[16 0]	#ccFD 3500
Plate3MA	D6	ACGCTCATTTAGTATCATATGCATCTT CTTTTTTTTCATACATCATATT	49	10[16 0]	63[18 1]	#ccFD 3500
Plate3MA	D7	AATAGGATAGCATTCCACAGACAACAG TTTTTTTTTCATACATCATATT	49	12[55]	65[76]	#ccFD 3500
Plate3MA	D8	CTTAAACGCCTTTATCTGTATGGGATT TTTTTTTTTCATACATCATATT	49	16[90]	65[97]	#ccFD 3500
Plate3MA	D9	GGGTTATATGACGTTAGTAAATTTTTTT TCATACATCATATT	42	14[11 8]	65[11 8]	#ccFD 3500
Plate3MA	D10	CCTTGCTTTAGAATCTCCGGCTTAGGT TTTTTTTTTCATACATCATATT	49	16[13 2]	65[13 9]	#ccFD 3500
Plate3MA	D11	AAATACCAATCCAATCGCAAGACTACC TTTTTTTTTCATACATCATATT	49	12[13 9]	65[16 0]	#ccFD 3500
Plate3MA	D12	TTTATAGTGAATTTATCAAAATTTTTTT TCATACATCATATT	43	14[18 2]	65[18 1]	#ccFD 3500
Plate3MA	E1	CATGAGGTGCGGGAAGTTGCGCCGAC AATTTTTTTTCATACATCATATT	49	18[69]	67[76]	#ccFD 3500
Plate3MA	E2	TGCTAAAAGGCTCCAAAAGGAAGCTT GATTTTTTTTCATACATCATATT	49	14[76]	67[97]	#ccFD 3500
Plate3MA	E3	TCGGAACGAGGGCACTTTGCTTTCGA GGTTTTTTTCATACATCATATT	49	17[98]	67[11 8]	#ccFD 3500
Plate3MA	E4	CGGTTTATCAGCATTAATTAATTTTCCC TCTGTAATTTTTTTTCATACATCATATT	56	15[98]	67[13 9]	#ccFD 3500
Plate3MA	E5	TACAAAAATTAATTTCAATATATGTGAG TTTTTTTTTCATACATCATATT	49	18[15 3]	67[16 0]	#ccFD 3500
Plate3MA	E6	CATAGGTTTAGATTAAGACGCAAACAG TTTTTTTTTCATACATCATATT	49	14[16 0]	67[18 1]	#ccFD 3500
Plate3MA	E7	TGACAACTTAAAGGCCGCTTTAAGTTT CTTTTTTTTCATACATCATATT	49	16[55]	69[76]	#ccFD 3500
Plate3MA	E8	TCATCGCCAGCGATTTTGAGGACTAAA GTTTTTTTTTCATACATCATATT	49	20[90]	69[97]	#ccFD 3500
Plate3MA	E9	TTACCTGAGTAGCAACGGCTATTTTTT TTCATACATCATATT	42	18[11 8]	69[11 8]	#ccFD 3500
Plate3MA	E10	ACAGAAATCAGATGATTATTCATTTCA ATTTTTTTTCATACATCATATT	49	20[13 2]	69[13 9]	#ccFD 3500
Plate3MA	E11	TGAATAAATCAAGAAAACAAATCGCGC ATTTTTTTTCATACATCATATT	49	16[13 9]	69[16 0]	#ccFD 3500
Plate3MA	E12	TTTTCGCCTGATTGCTTTGAATTTTTTT TTCATACATCATATT	43	18[18 2]	69[18 1]	#ccFD 3500

Plate 3MA (mid-affinity 13-bp ligand)						
7T + Ligand:		TTTTTTTTTCATACATCATATT				
Plate3MA	F1	CCCAAATGAGGACACGAAATCCGCGA CCTTTTTTTTTTCATACATCATATT	49	22[69]	71[76]	#ccFD 3500
Plate3MA	F2	ACTTTTTTTCATCTTTGACCCCCTGATAA TTTTTTTTTCATACATCATATT	49	18[76]	71[97]	#ccFD 3500
Plate3MA	F3	GGCTGGCTGACCTCAGAGTACAACGG AGTTTTTTTTTCATACATCATATT	49	21[98]	71[118]	#ccFD 3500
Plate3MA	F4	AGCGCGAAACAAATTTTCAGGTTTAAC GTAAAGAATTTTTTTTTTCATACATCATAT T	56	19[98]	71[139]	#ccFD 3500
Plate3MA	F5	CATTTTGTATAATCTCAAATTTATTTGC TTTTTTTTTCATACATCATATT	49	22[153]	71[160]	#ccFD 3500
Plate3MA	F6	ACCAAGTTTACATCGGGAGAATAGAAC CTTTTTTTTTTCATACATCATATT	49	18[160]	71[181]	#ccFD 3500
Plate3MA	F7	TGCTCCAGACCAACTTTGAAACAACGT ATTTTTTTTTTCATACATCATATT	49	20[55]	73[76]	#ccFD 3500
Plate3MA	F8	AACTTTAATCATTGACAAGAACCGGAT ATTTTTTTTTTCATACATCATATT	49	23[77]	73[97]	#ccFD 3500
Plate3MA	F9	GAATTATCATTCATCAAGAGTTTTTTTTT TCATACATCATATT	42	22[118]	73[118]	#ccFD 3500
Plate3MA	F10	AAGTATTAGACTTTACCAGAAGGAGC GTTTTTTTTTCATACATCATATT	49	23[119]	73[139]	#ccFD 3500
Plate3MA	F11	ACGTAAATGGCAATTCATCAACGGAAC ATTTTTTTTTTCATACATCATATT	49	20[139]	73[160]	#ccFD 3500
Plate3MA	F12	TTTAATTTTAAAAGTTTGAGTATTTTTTT TCATACATCATATT	43	22[182]	73[181]	#ccFD 3500
Plate3MA	G1	empty				
Plate3MA	G2	empty				
Plate3MA	G3	empty				
Plate3MA	G4	empty				
Plate3MA	G5	empty				
Plate3MA	G6	empty				
Plate3MA	G7	empty				
Plate3MA	G8	empty				
Plate3MA	G9	empty				
Plate3MA	G10	empty				
Plate3MA	G11	empty				
Plate3MA	G12	empty				
Plate3MA	H1	empty				
Plate3MA	H2	empty				
Plate3MA	H3	empty				
Plate3MA	H4	empty				

Plate 3MA (mid-affinity 13-bp ligand)					
7T + Ligand:		TTTTTTTTCATACATCATATT			
Plate3MA	H5	empty			
Plate3MA	H6	empty			
Plate3MA	H7	empty			
Plate3MA	H8	empty			
Plate3MA	H9	empty			
Plate3MA	H10	empty			
Plate3MA	H11	empty			
Plate3MA	H12	empty			

Table S3.5 Key resources

REAGENT or RESOURCE	SOURCE	IDENTIFIER	ADDITIONAL INFO
Antibodies			
AlexaFluor 647 anti-biotin IgG	Jackson Immuno Labs	Cat# 200-602-211	
AlexaFluor 488 anti-biotin IgG	Jackson Immuno Labs	Cat# 200-542-211	
Oligonucleotides			
Receptor DNA strand	this paper	Benzylguanine-5'-AATATGATGTATGTGG -3'	Oligonucleotide was ordered from IDT with a 5' terminal amine. Conjugation to benzylguanine was performed as described (Farlow et al., 2013).
DNA ligand strand	IDT	Biotin-5'- TTTT-TTTCATACATCATATT - 3'-Atto647	

REAGENT or RESOURCE	SOURCE	IDENTIFIER	ADDITIONAL INFO
p8064 DNA scaffold	IDT	Cat # 1081314	
All other oligonucleotides used for origami pegboard are listed in Table 1			
Chemicals, Peptides, and Recombinant Proteins			
Alexa Fluor 488 Phalloidin	Thermo/Molecular Probes	Cat# A12379	
Biotinyl Cap PE	Avanti	Cat# 870273	
POPC	Avanti	Cat# 850457	
PEG5000-PE	Avanti	Cat# 880230	
Atto390 DOPE	ATTO-TEC GmbH	Cat# AD 390-161	
Lipofectamine LTX	ThermoFisher	Cat#15338030	
Lenti-X Concentrator	Takara Biosciences	Cat# 631231	
Pierce Biotinylated Bovine Serum Albumin (Biotin-LC-BSA)	ThermoScientific	Cat#29130	
Neutravidin	ThermoScientific	Cat# 31050	
Experimental Models: Cell Lines			
Lenti-X 293T cell line	Takara Biosciences	Cat# 632180	For lentivirus production
HEK293T cells	UCSF Cell Culture Facility		For lentivirus production
Raw264.7 Macrophages	ATCC	Cat# ATCC® TIB-71™	
THP1 Monocytes	ATCC	Cat# ATCC® TIB-202™	
Recombinant DNA			

REAGENT or RESOURCE	SOURCE	IDENTIFIER	ADDITIONAL INFO
pHR-DNA-CAR γ	this paper	In PhR vector. Signal peptide: (MQSGTHWRVGLGLCLLSVGVWG QD) Derived from CD3 ϵ Extracellular: HA tag plus a linker (LPETGGGGGG), SNAPf (from the pSNAPf plasmid, New England Biolabs) Linker: GGSGGSGGS, TM and intracellular: CD86TM (aa 236-271), cytoplasmic domain (aa 45-86) of the Fc γ -chain UniProtKB - P20491 (FCERG_MOUSE) linker: GSGS, Fluorophore: mGFP or BFP	
pHR-Syk-BFP	adapted from DOI: 10.1016/j.immuni.2020.07.008	CDS: aa1-629 UniProtKB - P48025 (KSYK_MOUSE), Linker: ADPVAT, Fluorophore: BFP	
pHR-DNA-CARadhesion	DOI: 10.1016/j.immuni.2020.07.008	In PhR vector. Signal peptide: (MQSGTHWRVGLGLCLLSVGVWG QD) Derived from CD3 ϵ Extracellular: HA tag plus a linker (LPETGGGGGG), SNAPf (from the pSNAPf plasmid, New England Biolabs) Linker: GGSGGSGGS, TM and intracellular: CD86TM (aa 236-271), linker: SADASGG, Fluorophore: eGFP	
pHR-mNeonGreen-tSH2 Syk	adapted from DOI: 10.1016/j.cell.2018.05.059	CDS: aa2-261 UniProtKB - P48025 (KSYK_MOUSE), Linker: GGGSGGGG, Fluorophore: mNeonGreen	
pHR-Akt PH domain	this paper	CDS: aa1-164 UniProtKB - P31749 (AKT1_HUMAN), Linker: HMTSPVAT, Fluorophore: mGFP	

REAGENT or RESOURCE	SOURCE	IDENTIFIER	ADDITIONAL INFO
pHR-DNA-CAR _{4xγ}	this paper	<p>In PhR vector. Signal peptide: (MQSGTHWRV LGLCLLSVGVWG QD) Derived from CD3ε</p> <p>Extracellular: HA tag plus a linker (LPETGGGGGG), SNAPf (from the pSNAPf plasmid, New England Biolabs) Linker: GSGSGSGGS, TM and intracellular: CD86TM (aa 236-271), 4 repeats of the cytoplasmic domain (aa 45-86) of the Fc γ-chain UniProtKB - P20491 (FCERG_MOUSE) with a GSGS linker between each repeat, Linker: GSGS, Fluorophore: mGFP</p>	
pHR-DNA-CAR-1xγ-3xΔITAM	this paper	<p>In PhR vector. Signal peptide: (MQSGTHWRV LGLCLLSVGVWG QD) Derived from CD3ε</p> <p>Extracellular: HA tag plus a linker (LPETGGGGGG), SNAPf (from the pSNAPf plasmid, New England Biolabs) Linker: GSGSGSGGS, TM and intracellular: CD86TM (aa 236-271), the cytoplasmic domain (aa 45-86) of the Fc γ-chain UniProtKB - P20491 (FCERG_MOUSE) followed by 3 repeats of the cytoplasmic domain (aa 45-86) of the Fc γ-chain UniProtKB - P20491 (FCERG_MOUSE) with aa65 and aa76 mutated from YtoF and a GSGS linker between each repeat, Linker: GSGS, Fluorophore: mGFP</p>	

REAGENT or RESOURCE	SOURCE	IDENTIFIER	ADDITIONAL INFO
pHR-DNA-CAR γ human	this paper	In PhR vector. Signal peptide: (MQSGTHWRV LGLCLLSVGVWG QD) Derived from CD3 ϵ Extracellular: HA tag plus a linker (LPETGGGGGG), SNAPf (from the pSNAPf plasmid, New England Biolabs) Linker: GGSGGSGGS, TM and intracellular: CD86 TM (aa 236-271), cytoplasmic domain (aa 45-86) of the Fc γ -chain UniProtKB - P30273 (FCERG_HUMAN) linker: GSGS, Fluorophore: mGFP or BFP	
pMD2.G lentiviral plasmid	D. Stainier, Max Planck; VSV-G envelope	Addgene 12259	
pCMV-dR8.91	DOI: 10.1038/nature11220.	Current Addgene 8455	
pHRSIN-CSGW	DOI: 10.1038/nature11220.		
Software and Algorithms			
ImageJ	NIH		
Affinity Designer			
Fiji	https://fiji.sc/		
Prism	GraphPad	8	
Micromanager	DOI:10.14440/jbm.2014.36		
Other			
5 μ m silica microspheres	Bangs	Cat# SS05N	
MatriPlate	Brooks	Cat# MGB096-1-2-LG-L	
96 well round bottomed plates	Corning	Cat# 38018	
Illustra NAP-5 columns	Cytiva	Cat# 17085301	

3.7 Acknowledgements

We thank N. Stuurman for help with microscopy and developing the 'image randomizer' plug-in for blinding our analysis as well as the 'Spot Intensity in All Channel' plugin for quantification of our TIRF experiments. We also thank K. McKinley, T. Skokan, C. Gladkova, J. Sheu-Gruttadauria for discussions and critical feedback on this manuscript. M.A.M. was supported by the National Institute of General Medical Sciences of the National Institutes of Health under award number F32GM120990. Funding was provided by the Howard Hughes Medical Institute to R.D.V.

3.8 Author Contributions

N.K., R.D.V., and M.A.M. designed research; N.K. performed research; N.K., R.D., S.D. and M.A.M. contributed new reagents/analytic tools; N.K. analyzed data; and N.K., R.D.V., and M.A.M wrote the paper.

3.9 References

1. Erwig, L. P. & Gow, N. A. R. Interactions of fungal pathogens with phagocytes. *Nature Reviews Microbiology* **14**, 163–176 (2016).
2. Dilillo, D. J., Tan, G. S., Palese, P. & Ravetch, J. V. Broadly neutralizing hemagglutinin stalk-specific antibodies require FcR interactions for protection against influenza virus in vivo. *Nat. Med.* **20**, 143–151 (2014).
3. Nimmerjahn, F. & Ravetch, J. V. Fcγ receptors as regulators of immune responses. *Nat. Rev. Immunol.* (2008). doi:10.1038/nri2206
4. Uchida, J. *et al.* The innate mononuclear phagocyte network depletes B lymphocytes through Fc receptor-dependent mechanisms during anti-CD20 antibody immunotherapy. *J. Exp. Med.* **199**, 1659–1669 (2004).
5. Weiskopf, K. *et al.* Engineered SIRPα variants as immunotherapeutic adjuvants to anticancer antibodies. *Science (80-.)*. **341**, 88–91 (2013).
6. Chao, M. P. *et al.* Anti-CD47 Antibody Synergizes with Rituximab to Promote Phagocytosis and Eradicate Non-Hodgkin Lymphoma. *Cell* **142**, 699–713 (2010).
7. Weiskopf, K. & Weissman, I. L. Macrophages are critical effectors of antibody therapies for cancer. *mAbs* **7**, 303–310 (2015).
8. Watanabe, M. *et al.* Antibody dependent cellular phagocytosis (ADCP) and antibody dependent cellular cytotoxicity (ADCC) of breast cancer cells mediated by bispecific antibody, MDX-210. *Breast Cancer Res. Treat.* **53**, 199–207 (1999).
9. Griffin, F. M., Griffin, J. A., Leider, J. E. & Silverstein, S. C. Studies on the mechanism of phagocytosis. I. Requirements for circumferential attachment of particle-bound ligands to specific receptors on the macrophage plasma membrane. *J. Exp. Med.* **142**, 1263–1282 (1975).
10. Zhang, Y., Hoppe, A. D. & Swanson, J. A. Coordination of Fc receptor signaling regulates

- cellular commitment to phagocytosis. *Proc. Natl. Acad. Sci. U. S. A.* **107**, 19332–19337 (2010).
11. Ma, Y., Lim, Y., Benda, A., Goyette, J. & Gaus, K. Clustering of CD3 ζ is sufficient to initiate T cell receptor signaling. (2020). doi:10.1101/2020.02.17.953463
 12. Davis, S. J. & van der Merwe, P. A. The kinetic-segregation model: TCR triggering and beyond. *Nat. Immunol.* **7**, 803–809 (2006).
 13. Holowka, D. & Baird, B. Antigen-Mediated IGE Receptor Aggregation and Signaling: A Window on Cell Surface Structure and Dynamics. *Annu. Rev. Biophys. Biomol. Struct.* **25**, 79–112 (1996).
 14. Kato, Y. *et al.* Multifaceted Effects of Antigen Valency on B Cell Response Composition and Differentiation *In Vivo*. (2020). doi:10.1016/j.immuni.2020.08.001
 15. Veneziano, R. *et al.* Role of nanoscale antigen organization on B-cell activation probed using DNA origami. *bioRxiv* 2020.02.16.951475 (2020). doi:10.1101/2020.02.16.951475
 16. Berger, R. M. L. *et al.* Nanoscale Organization of FasL on DNA Origami as a Versatile Platform to Tune Apoptosis Signaling in Cells. doi:10.1101/2020.07.05.187203
 17. Goodridge, H. S., Underhill, D. M. & Touret, N. Mechanisms of Fc Receptor and Dectin-1 Activation for Phagocytosis. *Traffic* **13**, 1062–1071 (2012).
 18. Sobota, A. *et al.* Binding of IgG-Opsonized Particles to Fc γ R Is an Active Stage of Phagocytosis That Involves Receptor Clustering and Phosphorylation. *J. Immunol.* **175**, 4450–4457 (2005).
 19. Lopes, F. B. *et al.* Membrane nanoclusters of Fc γ RI segregate from inhibitory SIRP α upon activation of human macrophages. *J. Cell Biol.* jcb.201608094 (2017). doi:10.1083/jcb.201608094
 20. Lin, J. *et al.* TIRF imaging of Fc gamma receptor microclusters dynamics and signaling on macrophages during frustrated phagocytosis. *BMC Immunol.* **17**, 5 (2016).
 21. Jaumouillé, V. *et al.* Actin cytoskeleton reorganization by syk regulates fcy receptor

- responsiveness by increasing its lateral mobility and clustering. *Dev. Cell* **29**, 534–546 (2014).
22. Taylor, M. J., Husain, K., Gartner, Z. J., Mayor, S. & Vale, R. D. A DNA-Based T Cell Receptor Reveals a Role for Receptor Clustering in Ligand Discrimination. *Cell* **169**, 108-119.e20 (2017).
 23. Morrissey, M. A. *et al.* Chimeric antigen receptors that trigger phagocytosis. *Elife* (2018). doi:10.7554/eLife.36688
 24. Li, P. *et al.* Affinity and kinetic analysis of Fc γ receptor IIIa (CD16a) binding to IgG ligands. *J. Biol. Chem.* **282**, 6210–6221 (2007).
 25. Morrissey, M. A., Kern, N. & Vale, R. D. CD47 Ligation Repositions the Inhibitory Receptor SIRPA to Suppress Integrin Activation and Phagocytosis. *Immunity* **53**, 290-302.e6 (2020).
 26. Bakalar, M. H. *et al.* Size-Dependent Segregation Controls Macrophage Phagocytosis of Antibody-Opsonized Targets. *Cell* (2018). doi:10.1016/j.cell.2018.05.059
 27. Rothmund, P. W. K. Folding DNA to create nanoscale shapes and patterns. *Nature* **440**, 297–302 (2006).
 28. Seeman, N. C. Nanomaterials Based on DNA. *Annu. Rev. Biochem.* **79**, 65–87 (2010).
 29. Hong, F., Zhang, F., Liu, Y. & Yan, H. *DNA Origami: Scaffolds for Creating Higher Order Structures. Chemical Reviews* **117**, (2017).
 30. Shaw, A. *et al.* Binding to nanopatterned antigens is dominated by the spatial tolerance of antibodies. *Nat. Nanotechnol.* **14**, 184–190 (2019).
 31. Duchemin, A. M., Ernst, L. K. & Anderson, C. L. Clustering of the high affinity Fc receptor for immunoglobulin G (Fc γ RI) results in phosphorylation of its associated γ -chain. *J. Biol. Chem.* **269**, 12111–12117 (1994).
 32. Bakalar, M. H. *et al.* Size-Dependent Segregation Controls Macrophage Phagocytosis of Antibody-Opsonized Targets. *Cell* **174**, 131-142.e13 (2018).

33. Morrissey, M. A. *et al.* Chimeric antigen receptors that trigger phagocytosis. *Elife* **7**, (2018).
34. Freeman, S. A. *et al.* Integrins Form an Expanding Diffusional Barrier that Coordinates Phagocytosis. *Cell* **164**, 128–140 (2016).
35. Schmid, E. M. *et al.* Size-dependent protein segregation at membrane interfaces. *Nat. Phys.* **12**, 704–711 (2016).
36. Swanson, J. A. & Baer, S. C. Phagocytosis by zippers and triggers. *Trends Cell Biol.* **5**, 89–93 (1995).
37. Ben M'Barek, K. *et al.* Phagocytosis of immunoglobulin-coated emulsion droplets. *Biomaterials* **51**, 270–277 (2015).
38. Gonzalez-Quintela, A. *et al.* Serum levels of immunoglobulins (IgG, IgA, IgM) in a general adult population and their relationship with alcohol consumption, smoking and common metabolic abnormalities. *Clin. Exp. Immunol.* **151**, 42–50 (2008).
39. Kwiatkowska, K. & Sobota, A. The clustered Fcγ receptor II is recruited to Lyn-containing membrane domains and undergoes phosphorylation in a cholesterol-dependent manner. *Eur. J. Immunol.* **31**, 989–998 (2001).
40. Huang, M. M. *et al.* Activation of FcγRII induces tyrosine phosphorylation of multiple proteins including FcγRII. *J. Biol. Chem.* **267**, 5467–5473 (1992).
41. Simons, K. & Ikonen, E. Functional rafts in cell membranes. *Nature* **387**, 569–572 (1997).
42. Eggeling, C. *et al.* Direct observation of the nanoscale dynamics of membrane lipids in a living cell. *Nature* **457**, 1159–1162 (2009).
43. Stone, M. B., Shelby, S. A., Nñez, M. F., Wisser, K. & Veatch, S. L. Protein sorting by lipid phase-like domains supports emergent signaling function in b lymphocyte plasma membranes. *Elife* **6**, 1–33 (2017).
44. Sohn, H. W., Tolar, P., Jin, T. & Pierce, S. K. Fluorescence resonance energy transfer in living cells reveals dynamic membrane changes in the initiation of B cell signaling. *Proc.*

- Natl. Acad. Sci. U. S. A.* **103**, 8143–8148 (2006).
45. Dinic, J., Riehl, A., Adler, J. & Parmryd, I. The T cell receptor resides in ordered plasma membrane nanodomains that aggregate upon patching of the receptor. *Sci. Rep.* **5**, 1–9 (2015).
 46. Kabouridis, P. S. Lipid rafts in T cell receptor signalling (review). *Molecular Membrane Biology* **23**, 49–57 (2006).
 47. Beekman, J. M., van der Linden, J. A., van de Winkel, J. G. J. & Leusen, J. H. W. FcγRI (CD64) resides constitutively in lipid rafts. *Immunol. Lett.* **116**, 149–155 (2008).
 48. Katsumata, O. *et al.* Association of FcγRII with Low-Density Detergent-Resistant Membranes Is Important for Cross-Linking-Dependent Initiation of the Tyrosine Phosphorylation Pathway and Superoxide Generation. *J. Immunol.* **167**, 5814–5823 (2001).
 49. Zhu, J. W., Brdicka, T., Katsumoto, T. R., Lin, J. & Weiss, A. Structurally Distinct Phosphatases CD45 and CD148 Both Regulate B Cell and Macrophage Immunoreceptor Signaling. *Immunity* **28**, 183–196 (2008).
 50. McCall, M. N., Shotton, D. M. & Barclay, A. N. Expression of soluble isoforms of rat CD45. Analysis by electron microscopy and use in epitope mapping of anti-CD45R monoclonal antibodies. *Immunology* **76**, 310–7 (1992).
 51. Woollett, G. R., Williams, A. F. & Shotton, D. M. Visualisation by low-angle shadowing of the leucocyte-common antigen. A major cell surface glycoprotein of lymphocytes. *EMBO J.* **4**, 2827–2830 (1985).
 52. Burroughs, N. J. *et al.* Boltzmann energy-based image analysis demonstrates that extracellular domain size differences explain protein segregation at immune synapses. *PLoS Comput. Biol.* **7**, (2011).
 53. Lu, J., Ellsworth, J. L., Hamacher, N., Oak, S. W. & Sun, P. D. Crystal structure of Fcγ receptor I and its implication in high affinity γ-immunoglobulin binding. *J. Biol. Chem.* **286**,

- 40608–40613 (2011).
54. Carbone, C. B. *et al.* In vitro reconstitution of T cell receptor-mediated segregation of the CD45 phosphatase. *Proc. Natl. Acad. Sci. U. S. A.* **114**, E9338–E9345 (2017).
 55. Chung, M., Koo, B. J. & Boxer, S. G. Formation and analysis of topographical domains between lipid membranes tethered by DNA hybrids of different lengths. *Faraday Discuss.* **161**, 333–45; discussion 419–59 (2013).
 56. Rosano, C., Arosio, P. & Bolognesi, M. The X-ray three-dimensional structure of avidin. *Biomol. Eng.* **16**, 5–12 (1999).
 57. Krobath, H., Rózycki, B., Lipowsky, R. & Weikl, T. R. Binding cooperativity of membrane adhesion receptors. *Soft Matter* **5**, 3354–3361 (2009).
 58. Rózycki, B., Lipowsky, R. & Weikl, T. R. Segregation of receptor-ligand complexes in cell adhesion zones: Phase diagrams and the role of thermal membrane roughness. *New J. Phys.* **12**, (2010).
 59. Krobath, H., Rózycki, B., Lipowsky, R. & Weikl, T. R. Line tension and stability of domains in cell-adhesion zones mediated by long and short receptor-ligand complexes. *PLoS One* **6**, (2011).
 60. Sil, D., Lee, J. B., Luo, D., Holowka, D. & Baird, B. Trivalent Ligands with Rigid DNA Spacers Reveal Structural Requirements For IgE Receptor Signaling in RBL Mast Cells. *ACS Chem. Biol.* **2**, 674–684 (2007).
 61. Berger, R. M. L. *et al.* Nanoscale Organization of FasL on DNA Origami as a Versatile Platform to Tune Apoptosis Signaling in Cells. *bioRxiv* 2020.07.05.187203 (2020).
doi:10.1101/2020.07.05.187203
 62. Arnold, M. *et al.* Activation of integrin function by nanopatterned adhesive interfaces. *ChemPhysChem* **5**, 383–388 (2004).
 63. Delcassian, D. *et al.* Nanoscale ligand spacing influences receptor triggering in T cells and NK cells. *Nano Lett.* **13**, 5608–5614 (2013).

64. Cai, H. *et al.* Full control of ligand positioning reveals spatial thresholds for T cell receptor triggering. *Nat. Nanotechnol.* **13**, 610–617 (2018).
65. Nimmerjahn, F. & Ravetch, J. V. Translating basic mechanisms of IgG effector activity into next generation cancer therapies. *IECON Proc. (Industrial Electron. Conf.* **2005**, 1104–1109 (2005).
66. Zhang, X. *et al.* Anti-CD20 Antibody with Multimerized Fc Domains: A Novel Strategy To Deplete B Cells and Augment Treatment of Autoimmune Disease. *J. Immunol.* **196**, 1165–1176 (2016).
67. Zhao, K. *et al.* Structure of CD20 in complex with the therapeutic monoclonal antibody rituximab. *Science (80-.).* **367**, 1218–1223 (2020).
68. Chew, H. Y. *et al.* Endocytosis Inhibition in Humans to Improve Responses to ADCC-Mediating Antibodies. *Cell* **180**, 895-914.e27 (2020).
69. Seifert, O. *et al.* Tetravalent Antibody-scTRAIL Fusion Proteins with Improved Properties. *Mol. Cancer Ther.* **13**, 101–111 (2014).
70. Huang, X. *et al.* DNA scaffolds enable efficient and tunable functionalization of biomaterials for immune cell modulation. *Nat. Nanotechnol.* (2020). doi:10.1038/s41565-020-00813-z
71. Ueda, G. *et al.* Tailored design of protein nanoparticle scaffolds for multivalent presentation of viral glycoprotein antigens. *Elife* **9**, 1–30 (2020).
72. Fallas, J. A. *et al.* Computational design of self-assembling cyclic protein homo-oligomers. *Nat. Chem.* **9**, 353–360 (2017).
73. Divine, R. *et al.* Designed proteins assemble antibodies into modular nanocages. *bioRxiv* (2020). doi:10.1101/2020.12.01.406611
74. Stuurman, N., Edelstein, A., Amodaj, N., Hoover, K. & Vale, R. Computer control of microscopes using manager. *Current Protocols in Molecular Biology* **CHAPTER**, Unit14.20 (2010).

Concluding Thoughts

4.1 Looking Forward

The work presented in this thesis provides a much clearer picture of how the molecular-scale organization of Fc γ R nanoclusters regulate macrophage activation and an increased understanding of the steric exclusion mechanisms driving CD45 segregation from TCR clusters. However, the mechanisms underlying how both T cells and macrophages use this spatial information to make such specific yet robust activation decisions are not yet fully understood. Additionally, how parameters like receptor-ligand size, mobility, or affinity regulate the organization of proteins at different immunological synapses, and how spatial regulation cooperates with other immune cell regulation mechanisms remain open questions.

The work presented in chapter 3 of this dissertation demonstrates that tight Fc γ R clustering promotes receptor phosphorylation and phagocytosis. As the exclusion of phosphatases CD45 and CD148 has been demonstrated to be essential for Fc γ R phosphorylation and phagocytosis,¹ we suggest that the increased receptor phosphorylation in tight clusters is driven by an increase in the exclusion of these phosphatases. Although this model fits within the current literature, the scale at which we are currently able to form this pre-defined spacing remains below the diffraction limit of fluorescence microscopes. Therefore, we could not directly visualize and measure CD45 or CD148 exclusion from these nanoclusters with current technologies. As DNA origami technology advances, increasing the size of the origami pegboards to be able to maintain this same level of precision on the spacing but over a larger area would allow us to directly test and visualize this hypothesis. Alternatively, slight improvements in ultra-high resolution imaging techniques could enable this farther analysis.

The work shown in chapter 2 of this dissertation demonstrates that CD45 exclusion can be driven

from nanoscale TCR-pMHC clusters merely based on the size of the extracellular domain of the phosphatase. Given that the TCR shares many properties with the Fc γ R, we hypothesize that this increase in CD45 exclusion from tight clusters compared to more sparse clusters could be due to an increase in this steric exclusion. Data mostly in the TCR field has shown that higher-receptor ligand densities result in less deformations in the intermembrane space,^{2,3} and thus could increase the extent of phosphatase exclusion from the receptors. Alternatively, we suggest a mechanism in which the lipid organization around tight clusters enhances receptor phosphorylation. It has been shown both for the TCR and the Fc γ R that receptor clusters associate with or induce the formation of ordered lipid domains that are enriched in Src-family kinases.⁴⁻⁸ These ordered lipid domains then act as phosphorylation hotspots, as phosphatases like CD45 are excluded from the domains, farther enhancing the likelihood that receptors within these domains are phosphorylated.^{9,10} Work by Bag et al recently demonstrated that a combination of lipid-based, protein-based, and steric interactions drove Fc ϵ receptor (Fc ϵ R) phosphorylation and signaling in mast cells.⁸ As the Fc ϵ R contains the same common cytosolic γ chain as the Fc γ R, it is highly likely that tight nanoclustering of IgG-Fc γ R interactions promotes many of these factors and that they synergistically promote receptor phosphorylation.

Future work separately manipulating the lipid ordering, extent of steric exclusion of phosphatases, and protein-protein interactions in a well-controlled system could help our understanding of the relative roles of each of these parameters for both Fc γ R and TCR signaling. Additionally, a better quantitative understanding of how each parameter may be regulated by changes in protein size, affinity of interactions, and identity of transmembrane domains to modulate cellular activation thresholds will significantly increase our understanding of how immune cells integrate all of the extracellular information they receive to make their critical all-or-none-activation decisions. This in depth knowledge of the endogenous systems will enable rational design of new engineered

chimeric antigen receptors for cell based therapies as well as antibody based immunotherapies.

Lastly, much of this work focuses on the nanoscale spatial organization of receptor-ligand and surrounding protein interactions, as these play a large role in dictating receptor activation. However, immune cells also take in and integrate information about the larger-scale spacing of proteins throughout the entire immunological synapse when making activation decisions. For example, the micron-scale spacing between individual TCR clusters as well as Fc γ R clusters has been shown to regulate T cell and macrophage activation.^{11,12} Again, expanding DNA origami platforms in a manner that would enable both the control of inter-ligand spacing within clusters as well as inter-cluster spacing would enable the precise study of both of these parameters are integrated in cellular decisions. Alternatively, this current hurdle would be overcome if nanolithography techniques evolve to match the precision that DNA origami patterning provides or enable patterning of 3 dimensional surfaces. Either of these technological advances would especially prove helpful for the study of phagocytosis, as phagocytosis is a process that must be spatially controlled in all 3 dimensions to proceed successfully, and thus study of this process on 3 dimensional targets is essential.

As our understanding of TCR and Fc γ R signaling advances, we have uncovered paradigms that are generalizable between these and many other immune receptors. Farther study of these receptors will keep improving our understanding of the basic biophysical parameters that regulate their activation, but also progress our knowledge of how each individual receptor may have evolved to function optimally within each type of immune cell or for each of its intended functions.

4.2 References

1. Zhu, J. W., Brdicka, T., Katsumoto, T. R., Lin, J. & Weiss, A. Structurally Distinct Phosphatases CD45 and CD148 Both Regulate B Cell and Macrophage Immunoreceptor Signaling. *Immunity* **28**, 183–196 (2008).
2. Krobath, H., Rózycki, B., Lipowsky, R. & Weikl, T. R. Line tension and stability of domains in cell-adhesion zones mediated by long and short receptor-ligand complexes. *PLoS One* **6**, (2011).
3. Rózycki, B., Lipowsky, R. & Weikl, T. R. Segregation of receptor-ligand complexes in cell adhesion zones: Phase diagrams and the role of thermal membrane roughness. *New J. Phys.* **12**, (2010).
4. Dinic, J., Riehl, A., Adler, J. & Parmryd, I. The T cell receptor resides in ordered plasma membrane nanodomains that aggregate upon patching of the receptor. *Sci. Rep.* **5**, 1–9 (2015).
5. Beekman, J. M., van der Linden, J. A., van de Winkel, J. G. J. & Leusen, J. H. W. FcγRI (CD64) resides constitutively in lipid rafts. *Immunol. Lett.* **116**, 149–155 (2008).
6. Katsumata, O. *et al.* Association of FcγRII with Low-Density Detergent-Resistant Membranes Is Important for Cross-Linking-Dependent Initiation of the Tyrosine Phosphorylation Pathway and Superoxide Generation. *J. Immunol.* **167**, 5814–5823 (2001).
7. Kwiatkowska, K. & Sobota, A. The clustered Fcγ receptor II is recruited to Lyn-containing membrane domains and undergoes phosphorylation in a cholesterol-dependent manner. *Eur. J. Immunol.* **31**, 989–998 (2001).
8. Bag, N., Wagenknecht-Wiesner, A., Lee, A., Shi, S. & Holowka, D. A. Lipid-based, protein-based, and steric interactions synergize to facilitate transmembrane signaling stimulated by antigen-clustering of IgE receptors. *Bioarxiv*

doi:10.1101/2020.12.26.424347

9. Sohn, H. W., Tolar, P., Jin, T. & Pierce, S. K. Fluorescence resonance energy transfer in living cells reveals dynamic membrane changes in the initiation of B cell signaling. *Proc. Natl. Acad. Sci. U. S. A.* **103**, 8143–8148 (2006).
10. Stone, M. B., Shelby, S. A., Nññez, M. F., Wisser, K. & Veatch, S. L. Protein sorting by lipid phase-like domains supports emergent signaling function in b lymphocyte plasma membranes. *Elife* **6**, 1–33 (2017).
11. Cai, H. *et al.* Full control of ligand positioning reveals spatial thresholds for T cell receptor triggering. *Nat. Nanotechnol.* **13**, 610–617 (2018).
12. Freeman, S. A. *et al.* Integrins Form an Expanding Diffusional Barrier that Coordinates Phagocytosis. *Cell* **164**, 128–140 (2016).

Publishing Agreement

It is the policy of the University to encourage open access and broad distribution of all theses, dissertations, and manuscripts. The Graduate Division will facilitate the distribution of UCSF theses, dissertations, and manuscripts to the UCSF Library for open access and distribution. UCSF will make such theses, dissertations, and manuscripts accessible to the public and will take reasonable steps to preserve these works in perpetuity.

I hereby grant the non-exclusive, perpetual right to The Regents of the University of California to reproduce, publicly display, distribute, preserve, and publish copies of my thesis, dissertation, or manuscript in any form or media, now existing or later derived, including access online for teaching, research, and public service purposes.

DocuSigned by:

BBB26C31ED0148F... Author Signature

3/6/2021
Date